METALLIC MICRONUTRIENT HOMEOSTASIS IN PLANTS

EDITED BY: Manuel González-Guerrero, Hannetz Roschzttardtz and Diego Fabian Gomez-Casati

PUBLISHED IN: Frontiers in Plant Science

frontiers Research Topics

ISSN 1664-8714
ISBN 978-2-88963-235-0
DOI 10.3389/978-2-88963-235-0

About Frontiers

Frontiers is more than just an open-access publisher of scholarly articles: it is a pioneering approach to the world of academia, radically improving the way scholarly research is managed. The grand vision of Frontiers is a world where all people have an equal opportunity to seek, share and generate knowledge. Frontiers provides immediate and permanent online open access to all its publications, but this alone is not enough to realize our grand goals.

Frontiers Journal Series

The Frontiers Journal Series is a multi-tier and interdisciplinary set of open-access, online journals, promising a paradigm shift from the current review, selection and dissemination processes in academic publishing. All Frontiers journals are driven by researchers for researchers; therefore, they constitute a service to the scholarly community. At the same time, the Frontiers Journal Series operates on a revolutionary invention, the tiered publishing system, initially addressing specific communities of scholars, and gradually climbing up to broader public understanding, thus serving the interests of the lay society, too.

Dedication to Quality

Each Frontiers article is a landmark of the highest quality, thanks to genuinely collaborative interactions between authors and review editors, who include some of the world's best academicians. Research must be certified by peers before entering a stream of knowledge that may eventually reach the public - and shape society; therefore, Frontiers only applies the most rigorous and unbiased reviews.
Frontiers revolutionizes research publishing by freely delivering the most outstanding research, evaluated with no bias from both the academic and social point of view. By applying the most advanced information technologies, Frontiers is catapulting scholarly publishing into a new generation.

What are Frontiers Research Topics?

Frontiers Research Topics are very popular trademarks of the Frontiers Journals Series: they are collections of at least ten articles, all centered on a particular subject. With their unique mix of varied contributions from Original Research to Review Articles, Frontiers Research Topics unify the most influential researchers, the latest key findings and historical advances in a hot research area! Find out more on how to host your own Frontiers Research Topic or contribute to one as an author by contacting the Frontiers Editorial Office: researchtopics@frontiersin.org

METALLIC MICRONUTRIENT HOMEOSTASIS IN PLANTS

Topic Editors:
Manuel González-Guerrero, Polytechnic University of Madrid, Spain
Hannetz Roschzttardtz, Pontificia Universidad Católica, Chile
Diego Fabian Gomez-Casati, National University of Rosario, Argentina

Citation: González-Guerrero, M., Roschzttardtz, H., Gomez-Casati, D. F., eds. (2019). Metallic Micronutrient Homeostasis in Plants. Lausanne: Frontiers Media SA.
doi: 10.3389/978-2-88963-235-0

Table of Contents

frontiers in Plant Science

EDITORIAL
published: 17 July 2019
doi: 10.3389/fpls.2019.00927

Editorial: Metallic Micronutrient Homeostasis in Plants

Hannetz Roschzttardtz[1], Manuel González-Guerrero[2]* and Diego F. Gomez-Casati[3]**

[1] Facultad de Ciencias Biológicas, Pontificia Universidad Católica de Chile, Santiago, Chile, [2] Centro de Biotecnología y Genómica de Plantas (UPM-INIA), Universidad Politécnica de Madrid, Madrid, Spain, [3] Centro de Estudios Fotosintéticos y Bioquímicos (CEFOBI-CONICET), Universidad Nacional de Rosario, Rosario, Argentina

Keywords: metals, plant nutrition, metal accumulation, frataxin, nodule, medicago

Editorial on the Research Topic

Metallic Micronutrient Homeostasis in Plants

Transition elements, such as copper, iron, or zinc, are essential nutrients for plants. They participate in every biological process. However, intracellular metal levels must be maintained within a narrow physiological concentration. Too little, and not enough cofactors are available to the cell; too much, and Fenton-type reactions and mismetallation events will disrupt many cellular processes. As a result, plants have developed complex systems to control metal uptake and to deliver them to all tissues and cells. In this Research Topic, we have collected some of the most recent work furthering our understanding of Metallic Micronutrient Homeostasis in Plants.

Plant dependence on metals contrasts to the common low bioavailability of these nutrients in many soil types. Growing evidence indicates that plants have optimized the use of metals facilitating their relocation from one cellular compartment to another, depending on their need in different physiological processes. In this Topic, Zhang and Krämer have reanalyzed available bioinformatic data to show that there is a diurnal regulation of the translation of proteins involved in Fe-S metabolism in *Arabidopsis thaliana*, including that of frataxin, a protein involved in iron transfer in Fe-S protein biogenesis, and also in copper control in mitochondria and chloroplasts, as reviewed in this issue by Gomez-Casati et al. Iron is not the only metal micronutrient that is regulated by day-night cycles. Copper homeostasis is also controlled in this way, the likely consequence of plastocyanin synthesis for photosynthesis, and the toxic effect of copper in Fe-S synthesis. Andrés-Colás et al. showed that copper transporter COPT3 transcription is controlled in this way, in a process that is dependent of copper availability to the plant and on transcription factor TCP16.

The study of metal (re)distribution in plants can be greatly assisted by metal-imaging methods. Using X-ray fluorescence approaches, Vigani et al. showed how iron deficiency affects zinc distribution in leaves. With a similar approach, Ibeas et al. have determined the iron distribution in *Chenopodium quinoa* seeds and used it to validate the Perls-DAB histochemical method to visualize iron. This approach not only led to illustrate how iron distribution in seeds changed during dicot evolution but showed how subcellular iron distribution changes during embryo development (Ibeas et al.). Metal imaging approaches are also important to evaluate how metal nanoparticles could enter into trophic chains through plants, and the physiological effects that might cause there (Mosa et al.).

The evolving metal distribution in a cell and an organism could also reflect how some metalloenzymes are expressed with different demand for metal cofactors. For this, we would need high throughput metalloproteomics methods to identify the precise nature of the accepting metalloprotein to put into context many of the observed phenotypes. For instance, symbiotic nitrogen fixation requires one or several zinc-proteins that although dependent on zinc transfer into the endoplasmic reticulum of nodule cells, exert their effect in nitrogen-fixing symbiosomes and in nodule development (León-Mediavilla et al.).

OPEN ACCESS

Edited and reviewed by:
Felipe Klein Ricachenevsky, Universidade Federal de Santa Maria, Brazil

****Correspondence:***
Hannetz Roschzttardtz
hroschzttardtz@bio.puc.cl
Manuel González-Guerrero
manuel.gonzalez@upm.es
Diego F. Gomez-Casati
gomezcasati@cefobi-conicet.gov.ar

Specialty section:
This article was submitted to Plant Nutrition, a section of the journal Frontiers in Plant Science

Received: *13 June 2019*
Accepted: *02 July 2019*
Published: *17 July 2019*

Citation:
Roschzttardtz H, González-Guerrero M and Gomez-Casati DF (2019) Editorial: Metallic Micronutrient Homeostasis in Plants. Front. Plant Sci. 10:927. doi: 10.3389/fpls.2019.00927

Hormones have been known to control metal homeostasis, but the precise mechanisms of how hormone levels are controlled by metals still remains elusive. In this topic, García et al. reported how long-distance iron trafficking mediated by OPT3 could control ethylene metabolism as well as GSNO levels. In addition, micronutrients such as silicon, modulate hormone levels to overcome abiotic stress such as chilling and also improve the nutrition by metals (particularly zinc and manganese) (Moradtalab et al.).

In summary, the work shown in this Research Topic illustrates our advances in defining how cells and organisms control and redistribute essential metal nutrients. This distribution is affected by biotic and abiotic interactions, hormones and responds to different physiological states of plant development. The work also illustrates the need to have new methods to determine and visualize metals, as well-new developments in metalloproteomics and in metal-speciation analyses.

AUTHOR CONTRIBUTIONS

All authors listed have made a substantial, direct and intellectual contribution to the work, and approved it for publication.

Conflict of Interest Statement: The authors declare that the research was conducted in the absence of any commercial or financial relationships that could be construed as a potential conflict of interest.

frontiers in Plant Science

ORIGINAL RESEARCH
published: 22 December 2017
doi: 10.3389/fpls.2017.02186

Dynamic Subcellular Localization of Iron during Embryo Development in Brassicaceae Seeds

*Miguel A. Ibeas[1], Susana Grant-Grant[1], Nathalia Navarro[1], M. F. Perez[2] and Hannetz Roschzttardtz[1]**

[1] Departamento de Genética Molecular y Microbiología, Pontificia Universidad Católica de Chile, Santiago, Chile,
[2] Departamento de Ecología, Pontificia Universidad Católica de Chile, Santiago, Chile

Iron is an essential micronutrient for plants. Little is know about how iron is loaded in embryo during seed development. In this article we used Perls/DAB staining in order to reveal iron localization at the cellular and subcellular levels in different Brassicaceae seed species. In dry seeds of *Brassica napus, Nasturtium officinale, Lepidium sativum, Camelina sativa*, and *Brassica oleracea* iron localizes in vacuoles of cells surrounding provasculature in cotyledons and hypocotyl. Using *B. napus* and *N. officinale* as model plants we determined where iron localizes during seed development. Our results indicate that iron is not detectable by Perls/DAB staining in heart stage embryo cells. Interestingly, at torpedo development stage iron localizes in nuclei of different cells type, including integument, free cell endosperm and almost all embryo cells. Later, iron is detected in cytoplasmic structures in different embryo cell types. Our results indicate that iron accumulates in nuclei in specific stages of embryo maturation before to be localized in vacuoles of cells surrounding provasculature in mature seeds.

Keywords: embryo development, iron, Brassicaceae, nucleus, perls/DAB

OPEN ACCESS

Edited by:
Felipe Klein Ricachenevsky, Universidade Federal de Santa Maria, Brazil

Reviewed by:
Ricardo Fabiano Hettwer Giehl, Leibniz-Institut für Pflanzengenetik und Kulturpflanzenforschung (IPK), Germany
Sebastien Thomine, Centre National de la Recherche Scientifique (CNRS), France

****Correspondence:***
Hannetz Roschzttardtz
hroschzttardtz@bio.puc.cl

Specialty section:
This article was submitted to Plant Nutrition, a section of the journal Frontiers in Plant Science

Received: *04 September 2017*
Accepted: *12 December 2017*
Published: *22 December 2017*

Citation:
Ibeas MA, Grant-Grant S, Navarro N, Perez MF and Roschzttardtz H (2017) Dynamic Subcellular Localization of Iron during Embryo Development in Brassicaceae Seeds. Front. Plant Sci. 8:2186. doi: 10.3389/fpls.2017.02186

INTRODUCTION

Nutrient reserves in the seed must be sufficient to sustain plant establishment until the root system has developed enough to provide nutrients from the soils. High nutrient content of seeds is particularly important for plants growing in unfavorable nutritional conditions and has been related to higher seed viability and seedling vigor. Besides its impact on plant growth, nutrient levels in seeds are an important consideration for human and/or livestock seed-based nutrition (Roschzttardtz et al., 2017).

Iron is an essential micronutrient for plant growth and development. Despite its importance, the prevalent low iron bioavailability in the soils of main agricultural areas of the world limits plant productivity, fertility, and germination rates (Guerinot and Yi, 1994). As a consequence, iron contents in seeds is diminished which results in negative impacts in human and animal health, since seeds are a main source of food for humans and animals (Fan et al., 2008; DeFries et al., 2015). In humans, iron deficiency in women and children under 2 years is a serious and growing public health problem and a major concern for the World Health Organization. Therefore, understanding seed iron distribution and storage at the physiological and molecular level is key to design biotechnological applications to improve iron content of staple seeds.

Different approaches have been used in order to study where iron localizes in plant organs and at subcellular level. In plant, iron accumulates in different compartments depending of the tissue and

cell type. Among these are apoplast in root vasculature, plastids in leaves and pollen grain, vacuoles in embryos, and nuclei in different cell types (Roschzttardtz et al., 2009, 2011, 2013; Lanquar et al., 2010).

Regarding seeds, it has been described that iron accumulates in embryo during maturation stage of seed development (Roschzttardtz et al., 2009). So far, VACUOLAR IRON TRANSPORTER1 (VIT1) is the only player described involved in the iron loading into the vacuoles of endodermis cell layer in Arabidopsis embryos. Mutants in *VIT1* mislocalize iron, which accumulates in vacuoles of cortex cells in hypocotyl and subepidermal cells of abaxial side of cotyledons (Kim et al., 2006; Roschzttardtz et al., 2009; Eroglu et al., 2017). Interestingly, *vit1* mutants do not grow correctly in iron deficient conditions, suggesting that iron localization in seed has an important role in seed physiology. In the absence of functional VIT1 or during germination, the manganese and iron transporter MTP8 is responsible for loading iron in the vacuoles of subepidermal cells of cotyledons (Eroglu et al., 2017).

Little is known about the mechanism involved in iron loading in embryo during seed development. Recently Grillet et al. (2014) described that ascorbate efflux from Pea embryos is required for iron loading in seeds.

In this article we used, as model plants, species belonging to the Brassicaceae family in order to describe the subcellular compartments where iron accumulates in embryo during seed development. One of our models, *Brassica napus* L., is one of the most important oil crops almost all over the world. The tetraploid *B. napus* is a hybrid derived from *Brassica oleracea* and *Brassica rapa* and it shares more than 86% similarity in protein coding sequence with *Arabidopsis thaliana* (Cavell et al., 1998; Parkin et al., 2005). Furthermore, rapseed is not only important for vegetal oil, but also a major source for industrial materials such as biofuel (Chen et al., 2017).

Our results show that iron is accumulated first in nuclei of integument cells, endosperm and embryo cells in the early maturation stage of seed development before being located in vacuoles of endodermis cells. Some differences in iron localization were also observed in mature embryos of *Brassica napus*, *Nasturtium officinale*, *Lepidium sativum*, *Brassica oleracea* and *Camelina sativa* compared with *Arabidopsis thaliana*.

MATERIALS AND METHODS

Plant Material and Growth Conditions

Brassica napus, Nasturtium officinale, Camelina sativa, *Lepidium sativum,* and *Brassica oleracea* seeds were purchased at a local market. *B. napus* and *N. officinale* plants were grown on soil in a greenhouse at 23°C under long-day conditions (16-h/8-h day/night cycle).

Histochemical Staining of Iron with the Perls/DAB Procedure

Iron staining was performed according to Roschzttardtz et al. (2009). *Brassica napus, Nasturtium officinale, Camelina sativa, Brassica oleracea,* and *Lepidium sativum* dry seeds or seeds from *B. Napus* and *N. officinale* at different developmental stage were vacuum infiltrated with fixation solution (2% w/v paraformaldehyde in 1 mM phosphate buffer pH 7.0) for 45 min and incubated for 16 h in the same solution. The fixated seeds were dehydrated with ascendant concentration of ethanol (50, 70, 80, 90, 95, and 100%), later were incubated 12 h with a solution of butanol/ethanol 1:1 (v/v), and finally were incubated 12 h with 100% butanol. Then, the seeds were embedded in the Technovit 7100 resin (Kulzer) according to the manufacturer's instructions and thin sections (3 μm) were cut and were deposited on glass slides. For Perls/DAB staining, slides were incubated with 2% (v/v) HCl and 2% (w/v) K-ferrocyanide (Sigma–Aldrich) for 45 min For the DAB intensification, each glass slide was washed with distilled water, later were incubated in a methanol solution containing 0.01 M NaN_3 (Sigma–Aldrich) and 0.3% (v/v) H_2O_2 (Merck) for 1 h, and then washed with 0.1 M phosphate buffer (pH 7.4). For the intensification reaction, the glass slides were incubated between 10 and 30 min in a 0.1 M phosphate buffer (pH 7.4) solution containing 0.025% (v/v) H_2O_2, and 0.005% (w/v) $CoCl_2{}^*6H_2O$ (intensification solution). To stop the reaction each slide was rinsed with distilled water.

Iron Quantification

A microwave-assisted acid digestion was performed using 6.0 mL of concentrated HNO_3 (Winkler) and 1.0 mL of 30% (v/v) H_2O_2 added over 10–20 mg of seeds of each genotype. The colorless digestate were filled up to 15 mL using deionized water. The iron content of each genotype was measured in triplicate using inductively coupled plasma mass spectrometry (ICP-MS).

Microscopy and Staining with DAPI, Perls/DAB and Toluidine Blue

Thin sections were first stained with DAPI in order to visualize nuclei (Roschzttardtz et al., 2013), the same section was stained by Perls/DAB, as described above. Then were stained with toluidine blue. Each slide was incubated in a 0.5% (w/v) solution of toluidine blue for 2 min and rinsed with distilled water. The samples were observed and photographed with a Nikon Eclipse 80i microscope.

RESULTS

Iron Concentration and Distribution in Dry Seeds of Close Related Species to *Arabidopsis thaliana*

To evaluate iron concentration and distribution in dry seeds from closely related Arabidopsis species, first we determine iron content in dry seeds from *Arabidopsis thaliana, Brassica napus* and *Nasturtium officinale* (**Figure 1A**). Dry seeds were isolated, and a microwave-assisted acid digestion was performed. **Figure 1B** show iron concentration of each species determined by inductively coupled plasma mass spectrometry (ICP-MS). Iron concentration in *Arabidopsis thaliana* and *Brassica napus* dry seeds (70.4 and 64.6 μg of iron/g of seeds, respectively) was lower compared to *Nasturtium officinale* (116.6 μg of iron/g of seeds),

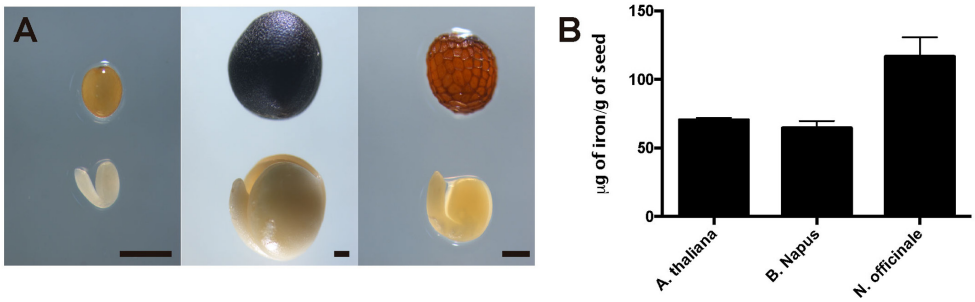

FIGURE 1 | Iron concentration in Brassicaceae seeds. **(A)** Differences in size and form of Brassicales mature seeds and embryos used in this study. The left panel shows *Arabidopsis thaliana*, the middle panel shows *Brassica napus* and the right panel shows *Nasturtium officinale*. The bar scale represents 500 µm. **(B)** Iron content in mature seeds determined by ICP-MS. Values are the mean of three biological replicates (±SD).

suggesting that there is no relation between iron concentration and seed size, as *Brassica napus* have the biggest seeds (**Figure 1A**) but also have a similar iron content as *Arabidopsis thaliana*.

In order to determine where iron localizes in dry seed embryos from species closely related to *Arabidopsis thaliana*, we analyzed seven different plant species: *Brassica napus, Nasturtium officinale, Camelina sativa*, *Arabidopsis thaliana*, *Lepidium sativum, Brassica oleracea and Brassica oleracea* var. capitate (**Figure 2** and Supplementary Figure S2). Embryos from dry seeds were isolated and fixed. Thin sections of different embryo regions were analyzed, in particular, cotyledon and hypocotyl. **Figure 2** and Supplementary Figure S2 show Perls/DAB staining revealing iron distribution in embryos from these species. Cotyledons accumulate iron in vacuoles of cells surrounding provasculature (**Figures 2A–D** and Supplementary Figures S2A,B) as has been described before for *Arabidopsis thaliana* (Roschzttardtz et al., 2009). Provasculature complexity in cotyledon is clearly higher than Arabidopsis (Roschzttardtz et al., 2014, 2017). Iron accumulation was not observed in other cell types like protodermis and cortex cells in dry seed embryos (**Figures 2A–D** and Supplementary Figures S2A,B).

Interestingly, transversal sections of hypocotyl show differences in the number of cell layer where iron accumulates compared to Arabidopsis hypocotyl, where only one cell layer accumulates iron (Roschzttardtz et al., 2009). We found that at least two-cell layers accumulate iron in the hypocotyl of *Brassica napus, Nasturtium officinale, Camelina sativa, Lepidium sativum* and *Brassica oleracea* dry seed embryos (**Figures 2E–G** and Supplementary Figure S2C,D, respectively). Despite the differences in the number of cell layers where iron accumulates in dry seeds of *Brassica napus, Nasturtium officinale, Camelina sativa, Lepidium sativum* and *Brassica oleracea* compared to *Arabidopsis thaliana*, at subcellular level iron is stored in the vacuoles in cells surrounding provasculature (**Figures 2A–D** and Supplementary Figures S2A,B).

Analyses of embryonic root tips indicate that iron accumulates in different cells identified as endodermis-cortex cells (Supplementary Figure S3).

Supplementary Figure S1 shows the phylogenetic tree of the 5 species of Brassicaceae family used in this study. Interestingly, iron localization in vacuoles is a conserved trait in the analyzed plant species. As indicated above, differences were only observed in the number of cell layers that accumulate iron in the hypocotyls.

Iron Distribution during *Brassica napus* Seed Development

As we showed, iron accumulates in vacuoles in embryos of seven species of Brassicaceae (**Figure 2** and Supplementary Figure S2). We used *Brassica napus* plants as model to study where iron localizes during seed development. *B. napus* produces bigger seeds compared with Arabidopsis plants allowing to study with more details different seed regions during its development (**Figure 1A**). In a phylogenetic point of view, *B. napus* is the more distant specie to *A. thaliana* used in this study. The fact that iron localizes in vacuoles of mature *B. napus* seeds is a strong indication that it is a conserved trait. Using *A. thaliana* as plant model it has been described that iron accumulates in embryo during seed maturation stages (Roschzttardtz et al., 2009), for this reason we analyzed three different stages of seed maturation, torpedo, bent cotyledon and mature stage before seed desiccation. In order to describe seed structures where iron accumulates before to be loaded into the embryo, we used in our analysis whole seeds including seed coat, endosperm and embryo. Whole seeds of *B. napus* containing embryos in different maturation stages as indicated above, were fixed and embedded in Technovit resin according to Section "Material and Methods."

The analysis of seeds with torpedo embryo stages revealed that iron localizes mainly in nuclei of integument cells, free cell endosperm and in different cell layers in the embryo (**Figure 3**). At this embryo stage, Perls/DAB and Toluidine blue staining show that in protodermal, cortex, endodermis and provasculature cells iron is localized in nuclei (**Figures 3A,B**). As vacuoles look empty after both staining, our results suggest that vacuoles of embryo cells are not an important compartment for iron storage at this developmental stage. Interestingly, strong iron staining was observed in nuclei (one to three iron pools were observed) of the free cell endosperm surrounding the embryo (**Figures 3C,D**).

Later, in seeds containing bent cotyledon embryo stage, integuments no longer contain iron inside the nuclei (**Figures 4A,B**). In the embryo, the number of cells containing

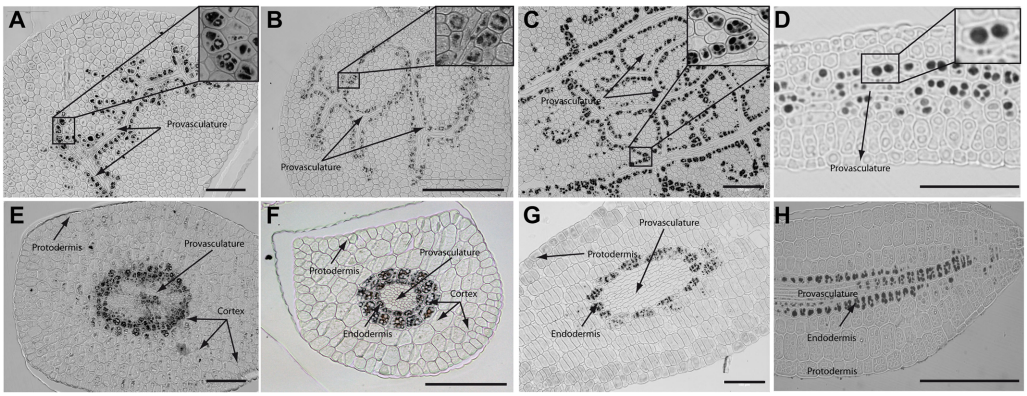

FIGURE 2 | Iron distribution in *Brassica napus, Nasturtium officinale, Camelina sativa,* and *Arabidopsis thaliana* dry seed embryos. Embryos were dissected from dry seeds and thin sections were obtained and stained with Perls/DAB in order to reveal iron accumulation. *Brassica napus* sections are shown in **(A,E)**; *Nasturtium officinale* sections are shown in **(B,F)**; *Camelina sativa* sections are shown in **(C,G)** and *Arabidopsis thaliana* sections are shown in **(D,H)**. Cotyledons and hypocotyl are shown in **(A–D)** and **(E–H)** respectively. In panel A to D a zoom is shown in order to indicate iron accumulation into the vacuoles. Bars in panels correspond to 100 μm.

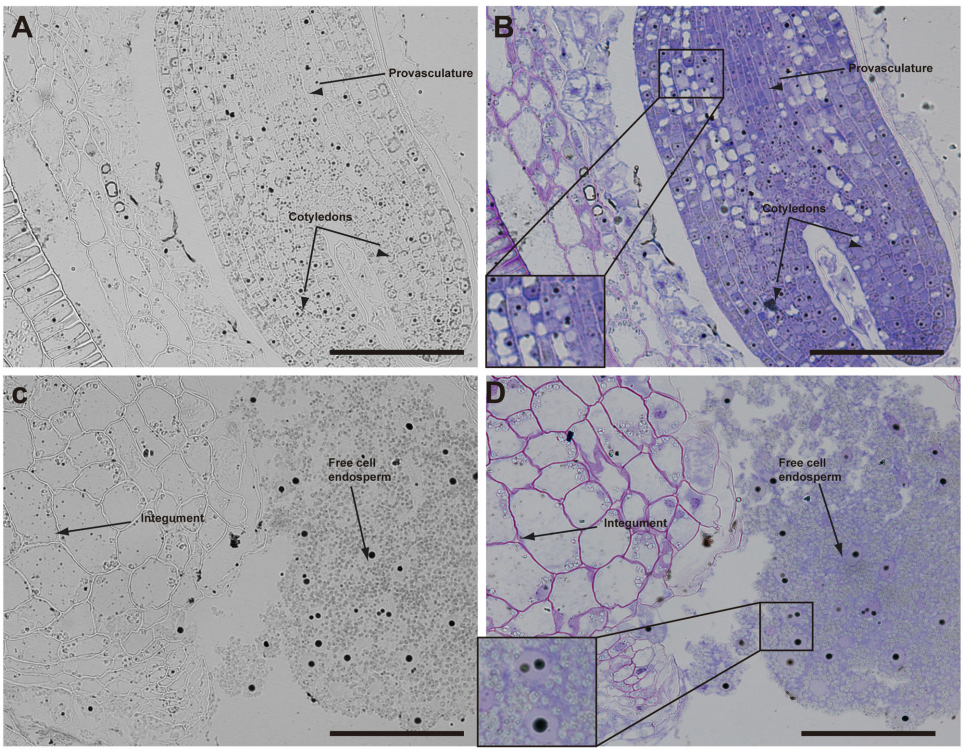

FIGURE 3 | Iron distribution in *Brassica napus* seeds in torpedo embryo stage. *Brassica napus* seeds at torpedo stage dissected from siliques were embedded in Technovit resin and sectioned (3 μm) and then stained with Perls/DAB **(A–D)** and then with Toluidine blue **(B,D)**. In **(B,D)** a zoom is shown in order to indicate iron accumulation into the nuclei of the cells **(B)** and free cell endosperm **(D)**. The scale bar represents 100 μm.

iron in nuclei decreases. In embryonic root tips and cotyledons, iron is localized in structures surrounding the nuclei (**Figures 4A,B,E,F**), while vacuoles are starting to load iron in the hypocotyl endodermis cell layer (**Figures 4C,D**).

In mature seeds before desiccation, iron does not localize in nuclei (**Figure 5**) and vacuoles are the principal compartments for iron storage (**Figures 5B,D**). At this late stage of seed development, cells adjacent to provasculature load iron and protodermis and cortex cells have not detectable iron as the previous seed developmental stages (**Figure 5**).

In order to determine whether iron is accumulated in nuclei before torpedo stages, we use *N. officinale* developing

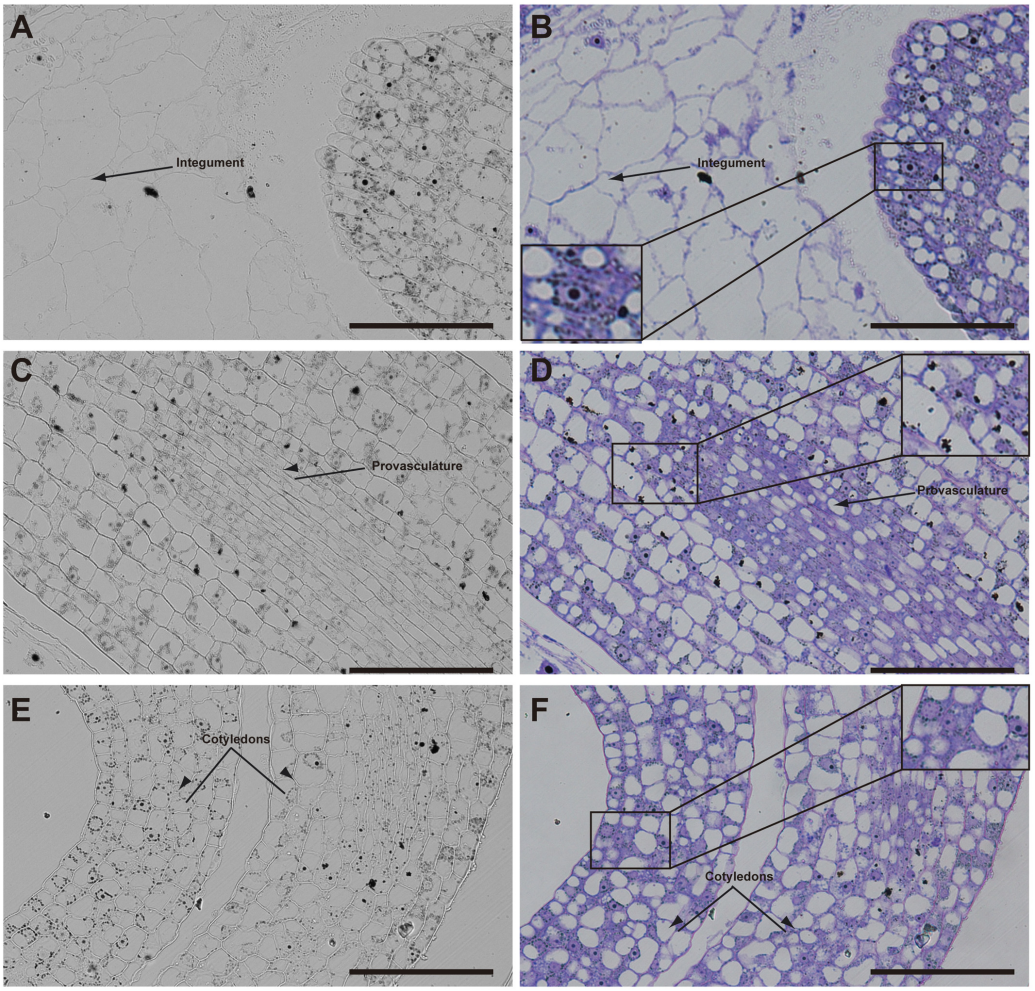

FIGURE 4 | Iron distribution in *Brassica napus* seeds in bent cotyledon embryo stage. *Brassica napus* seeds at the bent cotyledon stage dissected from siliques were embedded in Technovit resin and sectioned (3 μm) and stained with Perls/DAB **(A–F)** and then with Toluidine blue **(D–F)**. In **(D–F)** a zoom is shown in order to indicate iron accumulation into and around the nuclei **(B)**, cellular structures surrounding the nuclei **(B,F)** and iron accumulation inside vacuoles **(D)**. The scale bar represents 100 μm.

embryos. Our results indicate that in the heart stage of embryo development iron is not detectable by Perls/DAB staining in embryo cells. This result strongly supports the conclusion that iron localizes in nuclei of embryo cells in the torpedo stage (Supplementary Figure S5). Similar stages of seed maturation were analyzed using *N. officinale*. No differences in iron distribution were observed compared to *B. napus* (Supplementary Figure S4).

Iron Distribution at Subcellular Level during Seed Maturation

In order to confirm the subcellular compartments accumulating iron during development we performed consecutively staining with DAPI, Perls/DAB and toluidine blue on the same sections of different developmental stages of *B. napus* embryos. Iron accumulates in nuclei of different cell types in early maturation stages of seed development (**Figures 6A–E**). In bent cotyledon stage, iron is not longer detected in nuclei and accumulates in cytoplasmic structures (**Figures 6K–O**). Finally in mature stages, vacuoles of cells surrounding provasculature start to accumulate iron (**Figures 6P–T**). Details of unique cells are shown in **Figure 6**, indicating unambiguously were iron localizes in different cases, nuclei, cytoplasmic structures or vacuoles.

DISCUSSION

During seed development embryo accumulates nutrients that will be used in the transition of heterotrophy to autotrophy metabolism during germination and post germination stage of development. In the case of iron, the principal transporter expressed in root involved in iron acquisition in Arabidopsis *IRT1* is expressed 3–4 days after germination (Lanquar et al., 2010). Before roots are able to acquire iron from the soil, iron that was stored during seed development is remobilized from

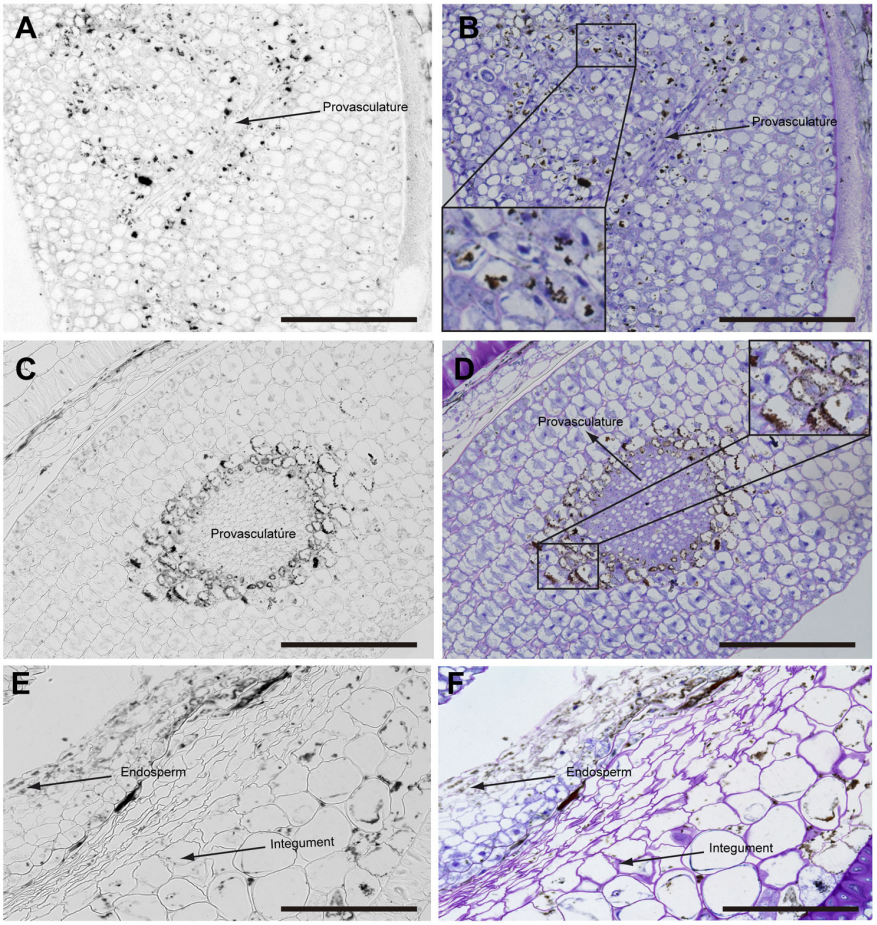

FIGURE 5 | Iron distribution in *Brassica napus* seeds in mature embryo stage before seed desiccation. *Brassica napus* seeds at the mature embryo before seed desiccation stage dissected from siliques were embedded in Technovit resin and sectioned (3 μm) and stained with Perls/DAB **(A–F)** and then with Toluidine blue **(B,D,F)**. Cotyledons, hypocotyl and endosperm-seed coat are shown in **(A–F)**, respectively. In **(B,D)** a zoom are shown in order to indicate iron accumulation in the vacuoles. The scale bar represents 100 μm.

vacuoles of endodermis and bundle sheath cells (Roschzttardtz et al., 2009; Lanquar et al., 2010; Mary et al., 2015). When iron is not correctly localized as in *vit1* mutants or not remobilized as in *nramp3 nramp4* double mutant, germinated seeds have difficulties to growth in iron deficiency conditions (Kim et al., 2006; Lanquar et al., 2010; Mary et al., 2015). This indicates that iron storage and localization in embryos is pivotal for seed physiology (Kim et al., 2006).

In this article, different stages of seed maturation were analyzed by a histochemical approach (Perls/DAB staining) in order to reveal iron localization. Perls/DAB method is specific and very sensitive for iron detection and can detect both Fe^{2+} and Fe^{3+} forms (Roschzttardtz et al., 2009). Other methods more quantitative have been used to reveal iron localization in seeds, indicating that an Arabidopsis embryo contains a fraction of the total iron of a seed (Schnell Ramos et al., 2013). Despite of not being a quantitative method, Perls/DAB staining allows to obtain information at subcellular level of any plant tissues and stages of plant development (Roschzttardtz et al., 2013).

Our analysis showed that iron was not localized in an unique subcellular compartment during seed development. In early maturation stages (embryo in torpedo stage) iron was localized principally in nuclei of integument, endosperm and embryo cells. This result is very surprising, indicating that vacuoles are not the only relevant subcellular compartment for iron storage during seed development (**Figures 3**, **4**). Interestingly, Perls/DAB did not detect iron in embryo at heart stage, suggesting strongly that iron is accumulated in nuclei not before torpedo stages (Supplementary Figure S5). Later iron seems to be gradually concentrated in structures surrounding nuclei (possibly mitochondria or endoplasmic reticulum) before to be loaded into the vacuoles of endodermis cells (**Figure 5**). The micronutrient manganese has been detected in endoplasmic reticulum during seed development, but more studies may be performed in order to identify the nature of the structures where iron is detected before to be mobilized to the vacuoles (Otegui et al., 2002). A model of iron dynamic during embryo loading is shown in **Figure 7**. The presence of iron in nuclei of pea embryos was

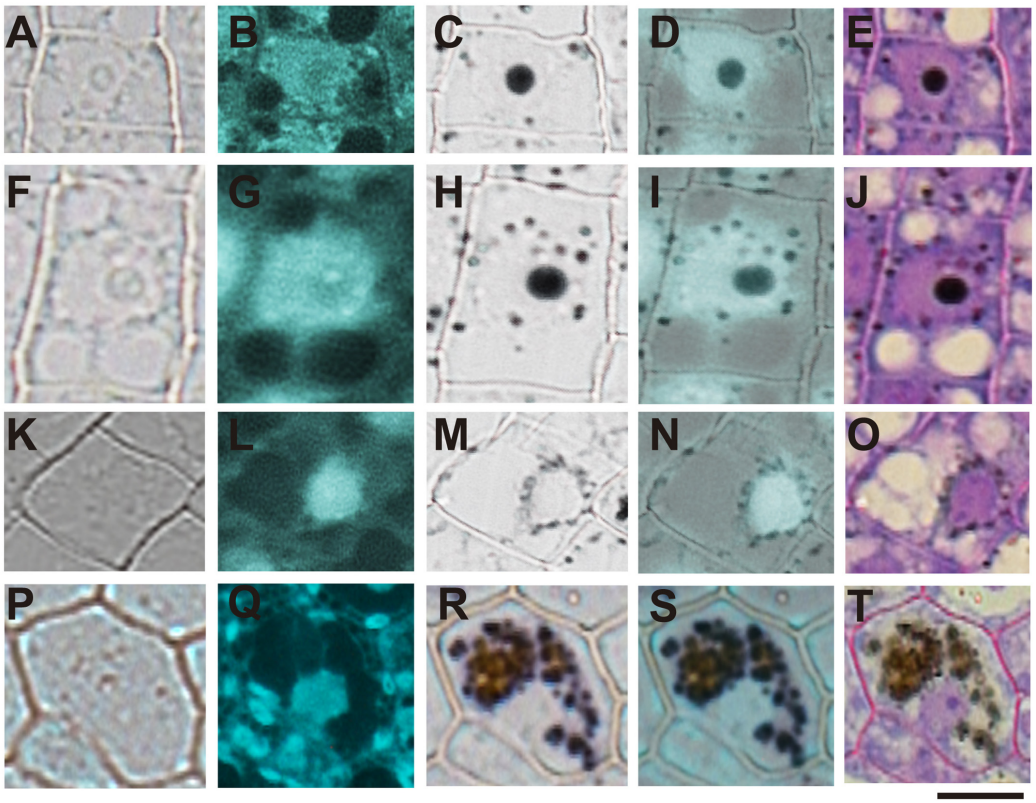

FIGURE 6 | Iron transit across different subcellular compartments during seed development. Iron accumulates in nuclei of different cell type in early maturation stages of seed development **(A–E)**. In bent cotyledon stage, iron is detected in nuclei and cytoplasmic structures **(F–J)**, later is not longer detected in nuclei but accumulates only in cytoplasmic structures **(K–O)**, and finally in mature stages vacuoles of cells surrounding provasculature start to accumulate iron **(P–T)**. DAPI staining was used in order to visualize nuclei **(B,G,L,Q)**. Perls/DAB staining was used to reveal iron pools inside the cells **(C,H,M,R)**. Merge between DAPI and Perls/DAB staining are shown in **(D,I,N,S)** and Toluidine blue staining was used to reveal different cell structures **(E,J,O,T)**. **(A,F,K,P)** show controls cells without staining. The subsequent staining was performed over the same sections. The scale bar represents 20 μm.

previously reported in Roschzttardtz et al. (2011), however, in this present study we shown that iron localizes in nuclei only during torpedo stages in Brassicaceae seeds. These results open interesting questions about the role of nuclei at this embryo stage of development. Our results suggest that nuclei may be a reservoir of iron during seed development or that iron may have unknown functions in nuclei of embryos in torpedo stage. Very recently, a specific role of iron in promoting meristematic cell division in adventitious root formation has been proposed (Hilo et al., 2017), however, the molecular role of iron in nuclei remains unknown.

Regarding iron distribution, we found that species closely related to *Arabidopsis thaliana* have some differences in dry seed embryos. For instance, iron is accumulated into the vacuoles of two-cell layer in mature embryos of *Lepidium sativum* showing a clear difference with Arabidopsis mature embryos, where only one cell layer accumulates iron (**Figure 2**; Roschzttardtz et al., 2009). A study reporting iron localization in dry seeds of 13 genoypes of three Phaseolus species has shown that large concentrations of iron are accumulated in the cytoplasm of cells surrounding the provascular bundles (Cvitanich et al., 2010). In the case of monocots, the highest iron concentration occurs in scutellum and outer regions of the embryo while a very low Fe is detected in the outermost layers of the endosperm and the single-layered aleurone that surrounds the endosperm

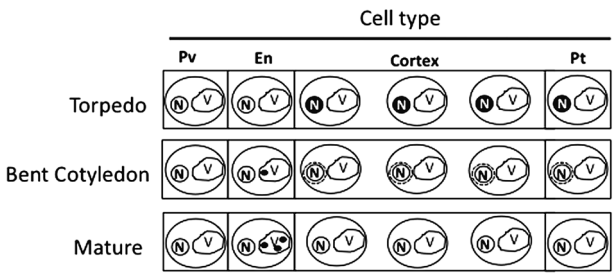

FIGURE 7 | Model of iron distribution during seed development. At the torpedo stage iron accumulates mainly in nuclei of different cell types. In bent cotyledon stage, iron is not longer detected in nuclei and accumulates in unknown cytoplasmic structures (possibly endoplasmic reticulum or mitochondria), later in mature stages vacuoles of cells surrounding provasculature start to accumulate iron. Pv, provasculature; En, endodermis; Pt, protodermis. N, nuclei; V, vacuole.

(Johnson et al., 2011). This suggests that different mechanisms of iron acquisition may play important roles in different seed species. In our group, we are interested in elucidating the molecular mechanisms that may explain these differences.

AUTHOR CONTRIBUTIONS

MI, SG-G, NN, and HR performed experiments and designed the research. MP was involved in the phylogenetic tree analysis. All authors participated in manuscript preparation.

FUNDING

This work was funded by FONDECYT 1160334 (Chilean Government) and INTER 6809 (Pontificia Universidad Católica de Chile-VRI) to HR, and Millennium Nucleus Center for Plant Systems and Synthetic Biology (NC130030). Ph.D. students work was supported by Conicyt-Chile grants 21160350 (to MI) and 21170951 (to SG-G).

ACKNOWLEDGMENT

The authors are greatly indebted to Xavier Jordana and María Isabel Gómez for their continued support and encouragement.

SUPPLEMENTARY MATERIAL

The Supplementary Material for this article can be found online at: https://www.frontiersin.org/articles/10.3389/fpls.2017.02186/full#supplementary-material

REFERENCES

Cavell, A., Lydiate, D., Parkin, I., Dean, C., and Trick, M. (1998). Collinearity between a 30-centimorgan segment of *Arabidopsis thaliana* chromosome 4 and duplicated regions within the *Brassica napus* genome. *Genome* 41, 62–69. doi: 10.1139/g97-097

Chen, B. Y., Zhao, B. C., Li, M. F., Liu, Q. Y., and Sun, R. C. (2017). Fractionation of rapeseed straw by hydrothermal/dilute acid pretreatment combined with alkali post-treatment for improving its enzymatic hydrolysis. *Bioresour. Technol.* 225, 127–133. doi: 10.1016/j.biortech.2016.11.062

Cvitanich, C., Przybyłowicz, W. J., Urbanski, D. F., Jurkiewicz, A. M., Mesjasz-Przybyłowicz, J., Blair, M. W., et al. (2010). Iron and ferritin accumulate in separate cellular locations in *Phaseolus* seeds. *BMC Plant Biol.* 10:26. doi: 10.1186/1471-2229-10-26

DeFries, R., Fanzo, J., Remans, R., Palm, C., Wood, S., and Anderman, T. L. (2015). Global nutrition. Metrics for land-scarce agriculture. *Science* 349, 238–240. doi: 10.1126/science.aaa5766

Eroglu, S., Giehl, R. F. H., Meier, B., Takahashi, M., Terada, Y., Ignatyev, K., et al. (2017). Metal tolerance protein 8 mediates manganese homeostasis and iron reallocation during seed development and germination. *Plant Physiol.* 174, 1633–1647. doi: 10.1104/pp.16.01646

Fan, M., Zhao, F., Fairweather-Tait, S., Poulton, P., Dunham, S., and McGrath, S. (2008). Evidence of decreasing mineral density in wheat grain over the last 160 years. *J. Trace Elem. Med. Biol.* 22, 315–324. doi: 10.1016/j.jtemb.2008.07.002

Grillet, L., Ouerdane, L., Flis, P., Hoang, M., Isaure, M., Lobinski, R., et al. (2014). Ascorbate efflux as a new strategy for iron reduction and transport in plants. *J. Biol. Chem.* 289, 2515–2525. doi: 10.1074/jbc.M113.514828

Guerinot, M., and Yi, Y. (1994). Iron: nutritious, noxious, and not readily available. *Plant Physiol.* 104, 815–820. doi: 10.1104/pp.104.3.815

Guo, X., Liu, J., Hao, G., Zhang, L., Mao, K., Wang, X., et al. (2017). Plastome phylogeny and early diversification of Brassicaceae. *BMC Genomics* 18:176. doi: 10.1186/s12864-017-3555-3

Hilo, A., Shahinnia, F., Druege, U., Franken, P., Melzer, M., Rutten, T., et al. (2017). A specific role of iron in promoting meristematic cell division during adventitious root formation. *J. Exp. Bot.* 68, 4233–4247. doi: 10.1093/jxb/erx248

Johnson, A., Kyriacou, B., Callahan, D., Carruthers, L., Stangoulis, J., Lombi, E., et al. (2011). Constitutive overexpression of the *OsNAS* gene family reveals single-gene strategies for effective iron- and zinc-biofortification of rice endosperm. *PLOS ONE* 6:e24476. doi: 10.1371/journal.pone.0024476

Kim, S., Punshon, T., Lanzirotti, A., Li, L., Alonso, J., Ecker, J., et al. (2006). Localization of iron in *Arabidopsis* seed requires the vacuolar membrane transporter VIT1. *Science* 314, 1295–1298. doi: 10.1126/science.1132563

Lanquar, V., Ramos, M. S., Lelievre, F., Barbier-Brygoo, H., Krieger-Liszkay, A., and Kramer, U. (2010). Export of vacuolar manganese by AtNRAMP3 and AtNRAMP4 is required for optimal photosynthesis and growth under manganese deficiency. *Plant Physiol.* 152, 1986–1999. doi: 10.1104/pp.109.150946

Mary, V., Schnell, M., Gillet, C., Socha, A., Giraudat, J., Agorio, A., et al. (2015). Bypassing iron storage in endodermal vacuoles rescues the iron mobilization defect in the natural resistance associated-macrophage protein3natural resistance associated-macrophage protein4 double mutant. *Plant Physiol.* 169, 748–759. doi: 10.1104/pp.15.00380

Otegui, M. S., Capp, R., and Staehelin, L. A. (2002). Developing seeds of arabidopsis store different minerals in two types of vacuoles and in the endoplasmic reticulum. *Plant Cell* 14, 1311–1327. doi: 10.1105/tpc.010486

Parkin, I., Sigrun, M., Andrew, G., Lewis, L., Martin, T., Thomas, C., et al. (2005). Segmental structure of the *Brassica napus* genome based on comparative analysis with *Arabidopsis thaliana*. *Genetics* 171, 765–781. doi: 10.1534/genetics.105.042093

Roschzttardtz, H., Bustos, S., Coronas, M. F., Ibeas, M. A., Grant-Grant, S., and Vargas-Pérez, J. (2017). Increasing provasculature complexity in the arabidopsis embryo may increase total iron content in seeds: a hypothesis. *Front. Plant Sci.* 8:960. doi: 10.3389/fpls.2017.00960

Roschzttardtz, H., Conejero, G., Curie, C., and Mari, S. (2009). Identification of the endodermal vacuole as the iron storage compartment in the Arabidopsis embryo[1]. *Plant Physiol.* 151, 1329–1338. doi: 10.1104/pp.109.144444

Roschzttardtz, H., Conéjéro, G., Divol, F., Alcon, C., Verdeil, J.-L., Curie, C., and Mari, S. (2013). New insights into fe localization in plant tissues. *Front. Plant Sci.* 4:350. doi: 10.3389/fpls.2013.00350

Roschzttardtz, H., Grillet, L., Isaure, M. P., Conejero, G., Ortega, R., and Curie, C. (2011). Plant cell nucleolus as a hot spot for iron. *J. Biol. Chem.* 286, 27863–27866. doi: 10.1074/jbc.C111.269720

Roschzttardtz, H., Paez-Valencia, J., Dittakavi, T., Jali, S., Reyes, F., Baisa, G., et al. (2014). The *VASCULATURE COMPLEXITY AND CONNECTIVITY (VCC)* gene encodes a plant-specific protein required for embryo provasculature development. *Plant Physiol.* 166, 889–902. doi: 10.1104/pp.114.246314

Schnell Ramos, M., Khodja, H., Mary, V., and Thomine, S. (2013). Using μPIXE for quantitative mapping of metal concentration in *Arabidopsis thaliana* seeds. *Front. Plant Sci.* 4:168. doi: 10.3389/fpls.2013.00168

Conflict of Interest Statement: The authors declare that the research was conducted in the absence of any commercial or financial relationships that could be construed as a potential conflict of interest.

frontiers in Plant Science

ORIGINAL RESEARCH
published: 26 April 2018
doi: 10.3389/fpls.2018.00420

Silicon Improves Chilling Tolerance During Early Growth of Maize by Effects on Micronutrient Homeostasis and Hormonal Balances

Narges Moradtalab[1], Markus Weinmann[1], Frank Walker[2], Birgit Höglinger[2], Uwe Ludewig[1] and Guenter Neumann[1]*

[1] Institute of Crop Science (340h), University of Hohenheim, Stuttgart, Germany, [2] Institute of Phytomedicine (360), University of Hohenheim, Stuttgart, Germany

OPEN ACCESS

Edited by:
Manuel González-Guerrero, Universidad Politécnica de Madrid (UPM), Spain

Reviewed by:
Yongchao Liang, Zhejiang University, China
Julia Quintana González, Ruhr University Bochum, Germany

****Correspondence:***
Narges Moradtalab
n.moradtalab@uni-hohenheim.de

Specialty section:
This article was submitted to Plant Nutrition, a section of the journal Frontiers in Plant Science

Received: *18 December 2017*
Accepted: *16 March 2018*
Published: *26 April 2018*

Citation:
Moradtalab N, Weinmann M, Walker F, Höglinger B, Ludewig U and Neumann G (2018) Silicon Improves Chilling Tolerance During Early Growth of Maize by Effects on Micronutrient Homeostasis and Hormonal Balances. Front. Plant Sci. 9:420. doi: 10.3389/fpls.2018.00420

Low soil temperature in spring is a major constraint for the cultivation of tropical and subtropical crops in temperate climates, associated with inhibition of root growth and activity, affecting early growth and frequently plant performance and final yield. This study was initiated to investigate the physiological base of cold-protective effects induced by supplementation with silicon (Si), widely recommended as a stress-protective mineral nutrient. Maize was used as a cold-sensitive model plant, exposed to chilling stress and low root-zone temperature (RZT) during early growth in a lab to field approach. In a pot experiment, 2–weeks exposure of maize seedlings to low RZT of 12–14°C, induced leaf chlorosis and necrosis, inhibition of shoot and root growth and micronutrient limitation (particularly Zn and Mn). These phenotypes were mitigated by seed treatments with the respective micronutrients, but surprisingly, also by Si application. Both, silicon and micronutrient treatments were associated with increased activity of superoxide dismutase in shoot and roots (as a key enzyme for detoxification of reactive oxygen species, depending on Zn and Mn as cofactors), increased tissue concentrations of phenolics, proline, and antioxidants, but reduced levels of H_2O_2. These findings suggest that mitigation of oxidative stress is a major effect of Zn, Mn, and Si applied as cold stress protectants. In a soil–free culture system without external nutrient supply, Si significantly reduced large leaching losses of Zn and Mn from germinating seeds exposed to low-temperature stress. Silicon also increased the translocation of micronutrient seed reserves to the growing seedling, especially the Zn shoot translocation. In later stages of seedling development (10 days after sowing), cold stress reduced the root and shoot contents of important hormonal growth regulators (indole acetic acid, gibberellic acid, zeatin). Silicon restored the hormonal balances to a level comparable with non-stressed plants and stimulated the production of hormones involved in stress adaptation

(abscisic, salicylic, and jasmonic acids). Beneficial effects of Si seed treatments on seedling establishment and the nutritional status of Zn and Mn were also measured for a field-grown silage maize, exposed to chilling stress by early sowing. This translated into increased final biomass yield.

Keywords: silicon, micronutrients, germination, chilling stress, maize, oxidative stress

INTRODUCTION

In the context of global warming, there is an increasing trend for the cultivation of crops with tropical and subtropical origins, such as maize, soybean, *Miscanthus* or *Sorghum* also in temperate climates, e.g., in Central Europe. Under these conditions, early sowing is required for efficient use of the comparatively shorter vegetation periods and to escape from detrimental effects of summer drought (Hund et al., 2004). However, low temperature and cold and wet soils during early spring represent major constraints for the cultivation of tropical crops bearing the risk of poor germination, impaired seedling establishment, and reduced nutrient acquisition due to limited root growth and activity. This is frequently associated with poor vegetative plant development, reduced stress resistance and finally reduced crop yield (Duncan and Hesketh, 1968; Muldoon et al., 1984; Imran et al., 2013), although under favorable conditions short cold periods can be tolerated and later compensated until final harvest (Saeidnejad et al., 2012). In plant species, such as maize, with optimum temperatures of 25–30°C for germination and plant growth, even moderately low soil temperatures <15°C are already detrimental (Cutforth et al., 1986; Kasper and Bland, 1992).

Due to root growth limitation and slow diffusion rates, plant availability, and acquisition of sparingly soluble nutrients, such as P, NH_4^+, K, Fe, Zn, Mn, and Cu, is particularly affected by low soil temperatures (Duncan and Hesketh, 1968; Kramer and Boyer, 1995; Wan et al., 2001). Therefore, placement of these nutrients close to the seedling roots or as seed treatments are among the most widespread practical measures to counteract detrimental effects of low soil temperatures on seedling establishment and early growth of maize (Imran et al., 2013; Bradáčová et al., 2016; Nkebiwe et al., 2016). Meanwhile, starter applications of ammonium phosphates by shallow subsurface placement below the seeds (Nkebiwe et al., 2016) belong to the standard fertilization strategies employed for maize production systems in temperate climates. Micronutrients with stress-protective functions, such as Zn and Mn, are frequently applied as foliar sprays. However, this is not possible in the seedling stage and usually, the formulations are more expensive than soil fertilizers. More cost-effective placement strategies including seed dressings are increasingly employed to promote stress resistance, early growth, and crop establishment (Farooq et al., 2012; Bradáčová et al., 2016). Similar stress-protective effects have been recorded also for amendments with Si (Liang et al., 2015).

When plants are exposed to environmental stress factors, such as chilling, drought or salinity, an imbalance between production and detoxification of reactive oxygen species (ROS) promotes accumulation of ROS, which induces oxidative damage to cellular components (Gong et al., 2005). Many studies have highlighted a role of Si in the suppression of oxidative damage in various plant species under a wide range of stress conditions. Protective effects have been reported against drought stress in wheat (Gong et al., 2005, 2008; Pei et al., 2010), salinity and boron toxicity in tomato, spinach (Al-aghabary et al., 2005; Gunes et al., 2007), cotton (Gossett et al., 1994), and barley (Liang et al., 2003; Inal et al., 2009), or low temperature stress in wheat (Liang et al., 2008) and cucumber (Liu et al., 2009). Mitigation of oxidative stress by Si treatments has been related to increased expression of enzymatic ROS detoxification systems, such as superoxide dismutases, catalases, peroxidases, ascorbate peroxidase, and increased accumulation of antioxidants (phenolics, proline, ascorbic acid), similar to the effects mediated by stress-protective micronutrients, such as Zn, Mn, Fe, and Cu (Cakmak, 2000; Datnoff et al., 2007). However, the links between Si application and induction of the protective mechanisms against oxidative stress are still largely unknown.

Therefore, this study was designed to investigate more in detail the physiological background of Si effects on cold stress mitigation during early growth of maize. We hypothesized that the protective role of silicon is related to the homeostasis of cold stress-protective micronutrients, such as Zn and Mn (Imran et al., 2013; Bradáčová et al., 2016). In a comparative investigation, Zn, Mn, and Si were applied as seed treatments or by starter fertigation to maize plants, subsequently exposed to low temperatures of 12–14°C on a silty loam soil taken from a field site of maize cultivation and also in a soil-free culture system. Plant growth, symptoms of oxidative leaf damage and the mineral nutritional status in different plant organs were documented in relation with the expression of various physiological stress indicators (production of H_2O_2, activities of superoxide dismutase and peroxidase, accumulation of antioxidants, phenolics, and proline) and with changes in hormonal balances. Finally, a preliminary field experiment was conducted on the same soil, where low-temperature stress was provoked due to early sowing at the mid of April. This allowed evaluating the expression of micronutrient and Si effects and their impact on final yield under practical conditions.

Abbreviations: Zn, zinc; Si, silicon, Mn, manganese, IAA, indole acetic acid; SA, salicylic acid; JA, jasmonic acid; GA, gibberellin; COR, cold response; RZT, root zone temperature; DAS, days after sowing, ROS, reactive oxygen species; SOD, superoxide dismutase; POD, peroxidase.

MATERIALS AND METHODS

Plant Cultivation

Soil Culture Experiment

Zea mays L cv. Colisee was used as test plant. Soil material (silty-loam, pH 6.9) was derived from the Ap horizon of a maize cultivation field site at the Hohenheim University experimental station Ihinger Hof, Renningen, Germany (Supplementary Table 1). After sieving with 2 mm mesh size, fertilization was performed with $Ca(NO_3)_2$, 100 mg N kg^{-1} DM; $Ca(H_2PO_4)_2$, 80 mg P kg^{-1} DM; K_2SO_4, 150 mg K kg^{-1}DM and $MgSO_4$, 50 mg Mg kg^{-1} DM. For improvement of the soil structure, the fertilized soil was mixed with quartz sand (ratio 2:1). Plastic pots were filled with 1,800 ml of this soil substrate and inserted into a cooling system, designed to control the root zone temperature of plants. An immersion water bath circulator (Thermomix 1480/Frigomix 1497, Braun, Melsungen, Germany) was connected to the cooling system, equipped with a closed pipe system which was installed into moist peat substrate to circulate the refrigerating fluid through the moist peat layer surrounding the culture vessels (Bradáčová et al., 2016). The plants were regularly watered to 70% of substrate water holding capacity (WHC) with deionized water and cultivated for 2 weeks at a root zone temperature of 20–22°C, 2 weeks at low root zone temperature (12–14°C), followed by a 2 weeks' recovery phase at 20–22°C.

Silicon was supplied as silicic acid (H_4SiO_4) prepared by passing K_2SiO_3 through a column filled with a cation–exchange resin (Amberlite IR−120, H^+ form, Sigma Aldrich, Germany) according to Maksimovic et al. (2007) and Pavlovic et al. (2013). Silicon fertigation was performed at a dosage of 40 mg H_4SiO_4 kg^{-1} soil DM applied with a pipette close to the plant, directly on top of the soil substrate in four weekly intervals, starting at the sowing date. Seed dressing with Zn and Mn was performed with commercial formulations: Lebosol® Mn500 SC and Lebosol® Zn700 SC (Lebosol® Dünger GmbH, Ermstein, Germany) according to the manufacturer instructions. Lebosol® Zn700 SC: 2 ml 4,000 $seeds^{-1}$, Lebosol® Mn500 SC: 4 ml 4,000 $seeds^{-1}$.

Soil–Free Culture Experiment

Germination of maize seeds (*Z. mays* cv. Colisee), surface–sterilized by 1 min soaking in ethanol (99% v/v), was performed in pre-sterilized Petri dishes (9 cm diameter) on moist filter paper (10 seeds per petri dish). The seeds were soaked with 3 mL deionized water (–Si control) or 3 mL freshly prepared H_4SiO_4 [1.0 mM Si] (Maksimovic et al., 2007; Pavlovic et al., 2013), respectively with four replicates per treatment. The optimum level of Si seed application was determined in a pilot experiment with different levels of Si supply (0–3.0 mM Si, Supplementary Figure 1). Covered Petri dishes were placed into a laboratory incubator (AtmoCONTROL, ICP, 750 Memmert GmbH, Schwabach, Germany) for 3 days in the dark at 18°C in thin unsealed plastic bags to minimize evaporation. For further seedling development, the germinated seeds were placed on the upper edge of rolled filter papers (10*60 cm; 2 seeds per roll), moistened with 100 ml distilled water or H_4SiO_4 solution [1 mM Si] at 3 and 5 days after sowing (DAS). The filter rolls were transferred into the laboratory incubator and incubated for 7 days at 12°C (16/8 h light/dark period and relative humidity of 60%, with a light intensity of 200 $\mu mol \cdot m^{-2} \cdot s^{-1}$ or at 18°C outside the incubator.

Field Experiment

In 2016, a field experiment was established for silo maize production (*Z. mays* cv. *Rolandinio*) at the experimental station "Ihinger Hof" University of Hohenheim, Renningen, Germany (soil properties are specified in Supplementary Table 1). To increase the probability of low-temperature stress in spring, sowing was conducted on April 22nd. Accordingly, a mean air temperature of 13.6°C during April and May was recorded associated with heavy rainfall (469 mm) leading to cold and wet soil conditions during germination and emergence. Fertilization was conducted prior to sowing by broadcast application with subsequent soil incorporation of stabilized ammonium sulfate NovaTec® solub 21: 161 kg N ha^{-1} (Compo–Expert, Münster, Germany) and by underfoot placement of di-ammonium phosphate (29 kg N, 32 kg P ha^{-1}). Seed treatments were performed as seed dressings with Zn and Mn (Lebosol ® Mn500 SC and Lebosol® Zn700 SC (Lebosol® Dünger GmbH, Ermstein, Germany) as described in experiment (1), and as seed priming with 1 mM potassium silicate (KSi, PottaSol, BioFa, Münsingen Germany) with a 24 h seed soaking period and re-drying during 24 h at 28 ± 2°C. A seed water priming treatment without Si was included as a control. Sowing was performed on April 22nd with a sowing density of 9 seeds m^{-2}, a row distance of 75 cm and a sowing depth of 6–7 cm. Foliar Si application (Vitanica® Si, Compo, Münster, Germany 16 L ha^{-1} + 100 ml ha^{-1} Greemax® Stallen Bio Agro AG, Basel, Switzerland) was conducted with a backpack sprayer (Solo®, Sindelfingen–Maichingen, Germany) at 69, and 75 DAS. Due to the extremely cold and wet soil conditions by the end of April, seedling emergence was severely biased, particularly in the untreated control variants. Therefore, after recording of emergence rates at 41 days after sowing (DAS), re–sowing was performed in the heavily affected plots to maintain a comparable level of inter-plant competition for light, water, and nutrients within the rows during the rest of the culture period. Final harvest was conducted at 214 DAS.

Plant Analysis

Visual scorings of leaf chlorosis, necrosis, and anthocyanin formation and determination of shoot height was performed for all experiments. Reflectometric leaf chlorophyll measurements were performed with a SPAD meter (Konica Minolta INC, Osaka, Japan). Estimates of damaged leaf area were obtained by the equation, leaf area (cm^2) = x/y, where x is the weight (g) of the area covered by leaf drawings on a transparent millimeter graph paper, and y is the weight of 1 cm^2 of the same graph paper (Pandey and Singh, 2011). Based on these data, the percentage of the necrotic area was calculated. After final harvest, root and shoot dry matter was determined after 60°C oven-drying. Root length measurements were performed by digital image analysis using the WinRHIZO root analysis software package (Regent Instruments Inc., Quebec, Canada).

Analysis of Mineral Nutrients

One hundred milligrams of dried, milled shoot material were ashed for 5 h in a muffle furnace at 500°C. After cooling, the samples were digested twice with 1 mL of 3.4 M HNO_3 and evaporated until dryness to precipitate SiO2. The ash was dissolved in 1 mL of 4 M HCl, subsequently diluted 10 times with hot deionized water, and boiled for 2 min to convert meta-, and pyro-phosphates to orthophosphate. After addition of 0.1 mL Cs/La buffer to 4.9 mL ash solution, Mg, Fe, Mn, and Zn concentrations were measured by atomic absorption spectrometry (ATI Unicam Solaar 939, Thermo Electron, Waltham, USA). Spectrophotometrical determination (Hitachi U−3300 spectrophotometer, Hitachi LtD. Corporation Japan) of orthophosphate was conducted after addition of molybdate-vanadate color reagent according to the method of Gericke and Kurmis (1952). K and Ca were measured by flame emission photometry (ELEX 6361, Eppendorf, Hamburg, Germany). Silicon was analyzed by ICP–OES (Vista–PRO, Varian Inc., Palo Alto, USA). For the digestion, 0.250 g of sample DM was suspended in 1 mL of H_2O and 2.5 mL of conc. HNO_3. The digestion is carried out by means of microwave–heated pressure digestion with HNO_3 and HF at 220°C in a digestion system Ultra clave II (MLS GmbH, Leutkirch, Germany). The digestion took place over 20 min, the entire digestion program with heating and cooling phases comprised 2 h. After digestion, 0.5 ml HF solution (1% v/v) was added to dissolve sparingly soluble silicates. The solutions were adjusted to 10 mL with distilled H_2O (VDLUFA Method book VII, 2011) and used for ICP–OES analysis.

Superoxide Dismutase Assay

The superoxide dismutase (SOD, EC 1.15.1.1) assay was optimized for root and shoot tissues of maize according to the method described by Beauchamp and Fridovich (1971) and modifications suggested by Giannopolitis and Ries (1977) and Hajiboland and Hasani (2007). One hundred milligrams of fresh plant material, frozen in liquid nitrogen and stored at −80°C, were ground with a pre-cooled mortar and pestle, and homogenized in 1.5 ml extraction buffer containing 25 mM HEPES pH 7.8 and 0.1 mM EDTA. After centrifugation at 10,000 × g (4°C for 10 min), aliquots of supernatant were transferred into 2 ml reaction tubes and kept on ice. For preparation of the reaction mixture, 1 ml cuvettes covered with aluminum foil for light protection, were filled with 300 µl 62.5 mM HEPES, 75 µl 1.0 mM EDTA, 75 µl 120 mM Na_2CO_3, 75 µl 120 mM L-methionine, 150 µl 750 µM nitro-blue tetrazolium (NBT), and 100 µl of plant extract. Finally, 225 µl of 10 µM riboflavin was added. The light reaction was started by removing the aluminum foil, exposing the samples to a light source (8000 Lux) for 25 min. During the light phase, NBT is reduced to a dark blue formazan, measured spectrophotometrically (Spectrophotometer U−3300, Hitachi, Tokyo, Japan) at a wavelength of 650 nm. The final SOD activity, which inhibits the NBT reduction, was calculated as the difference between the absorbance of the sample and a control without plant extract, divided by 50% absorbance of the control. The specific SOD activity was expressed as SOD units per mg total protein. Total, protein content was determined according to Bradford (1976).

Peroxidase Assay

Peroxidase (POD, EC1.11.1.7) activity was determined using the guaiacol test (Chance and Maehly, 1955; Hajiboland and Hasani, 2007). The tetra-guaiacol formed during the reaction is measured photometrically at 470 nm. The enzyme was extracted from fresh leaf material (100 mg) by 10 mM phosphate buffer (pH 7.0) and centrifuged 1,000 g for 10 min. The test mixture (1 mL) contained 10 mM phosphate buffer (300 µL, pH 7.0), 5 mM H_2O_2 (300 µL), and 4 mM guaiacol (300 µL). The reaction was started by addition of the enzyme extract (100 µL) at 25°C. The formation of tetraguaiacol was recorded over a reaction period of 5 min and the specific enzyme activity was expressed in µmoles tetraguiacol formation mg^{-1} total protein.

Determination of H_2O_2

Hydrogen peroxide levels were determined as described by Harinasut et al. (2003). Leaf tissues (100 mg fresh weight) were homogenized in an ice bath with 5 ml 0.1% (w/v) trichloroacetic acid. The homogenate was centrifuged at 12,000 g for 15 min. 0.5 ml of the supernatant was added to 0.5 ml of 10 mM potassium phosphate buffer (pH 7.0) and 1 ml of 1 M KI. The absorbance of the supernatant was recorded at 390 nm. The concentration of hydrogen peroxide was determined using a standard curve ranging from 0 to 120 µM of H_2O_2.

Determination of Total Soluble Sugars, Phenolics, and Proline

For determination of soluble sugars, leaf and root samples were homogenized in 100 mM phosphate buffer (pH 7.5) at 4°C. After centrifugation at 12,000 g for 15 min, the supernatant was used for determination of total soluble sugars (Yemm and Willis, 1954). An aliquot of the supernatant was mixed with anthrone-sulfuric acid reagent (Yemm and Willis, 1954) and incubated for 10 min at 100°C. After cooling, the absorbance was recorded at 625 nm. A calibration curve was created using glucose as external standard (Merck, Darmstadt, Germany). Total phenolics concentration was determined spectrophotometrically at 750 nm, using the Folin method (Hajiboland et al., 2017). For determination of proline, samples were homogenized with 3 % (v/v) sulfosalicylic acid and the homogenate was centrifuged at 3,000 g for 20 min. The supernatant was treated with acetic acid and acid ninhydrin, boiled for 1 h, and then the absorbance was determined at 520 nm. Proline (Sigma-Aldrich, Munich, Germany) was used for the production of a standard curve (Bates et al., 1973).

Determination of Total Soluble Anthocyanins and Flavonoids

Determination of anthocyanins was conducted spectrophotometrically at 510 nm according to Plessi et al. (2007). One hundred milligrams of fresh shoot material was extracted with 2 ml methanol/HCl conc. (98:2 v/v). After centrifugation at 12,000 × g for 10 min, each 0.5 mL of the supernatant was used for spectrophotometric determination by using a pH differential method at pH 1 and pH 4.5 adjusted with 4.5 ml of MES buffer After 5 h incubation at 4°C the absorbance was read at 510 nm from each group. The results were calculated as cyanidine-3-glycoside equivalents, using the

FIGURE 1 | (A) Shoot and **(B)** root development and biomass of maize plants including untreated control (–Si), and different levels (L) of Si (silicic acid) fertigation (L1: 25, L2: 85, L3:1,000 and L4: 10,000 mg Kg^{-1} soil DM). Culture period: 8 weeks under greenhouse conditions with 7 days minimum temperature of 12–14°C. Biomass data represent mean values ± SE of four replicates. Significant differences ($P < 0.05$) are indicated by different letters.

formula ΔA*MW*DF*V*100/ε*Wt, where ΔA is Abs (pH 1) – Abs (pH 4.5), MW = molecular weight of cyanidine-3-glycoside (484.83 g mol^{-1}), DF = dilution factor, V = final volume of the supernatant (0.5 ml), ε = molar absorbance factor of cyanidine-3-glycoside (26,900 Mm^{-1} cm^{-1}), L = diameter of the light path [cm], and Wt = sample fresh weight (0.1 g). Total leaf flavonoids were determined in methanolic extracts according to Hajiboland et al. (2014). One hundred milligrams of fresh leaf material was extracted in $AlCl_3$-methanol (2%, w/v) and after centrifugation at 12,000 × g for 10 min, the supernatant was used for determination at 415 nm with quercetin (Sigma, Munich, Germany) as an external standard.

Determination of Total Antioxidants

The 1,1-diphenyl-2-picrylhydrazyl radical (DPPH •) has been used to evaluate the free radical scavenging activity of antioxidants (Panico et al., 2009). The DPPH solution was prepared by adding 2.37 mg DPPH (Sigma-Aldrich, Munich, Germany) in 2 ml 99% ethanol. One hundred milligrams of fresh leaf samples were grinded in 1 ml of extraction solution (1:1 Ethanol:Water). After centrifugation at 12,000 g for 10 min at 4°C, 50 µl supernatant was used in a reaction cell which contained 50 µl freshly prepared 3 mM DPPH solution and 900 µl ethanol (99%). After incubation for 10 min in a dark room at 25°C, the absorbance was determined at 515 nm. A reference solution contained 50 µl DPPH solution and 950 µl of ethanol (99%). The decline in absorbance at 515 nm was recorded for each sample and the quenching percentage of the DPPH radical was calculated based on the observed decrease in absorbance using the formula:

% Inhibition = $[(A_0\text{-}A_1)/A_0] \times 100$, where A_0 is the absorbance value of the DPPH • blank solution and A_1 is the absorbance value of the sample solution.

Determination of Phytohormones by UHPLC-MS Analysis

Frozen maize tissue samples (shoot, roots) of 1 g of were ground to a fine powder with liquid nitrogen and extracted twice with 2.5 ml of 80% methanol in falcon tubes. Thereafter, the samples were further homogenized by ultrasonication (Micra D-9 homogenizer, Art, Müllheim Germany) for 1 min and 15 s at 10,000 rpm. Two milliliters of the methanol extracts were transferred to microtubes and centrifuged at 5,645 × g for 5 min. Thereafter, 350 µl of the supernatant was mixed with 700 µl ultra-pure water and centrifuged at 5,645 × g for 5 min. The supernatant was cleaned by membrane filtration (Chromafil® O-20/15 MS) and transferred to HPLC vials. UHPLC-MS analysis was carried out on a Velos LTQ System (Thermo Fisher Scientific, Waltham, Massachusetts, USA) fitted with a Synergi Polar column, 4 µ, 150 * 3.0 mm, (Phenomenex, Torrance, California, USA).The injection volume was 3 µL and the flow rate was adjusted to 0.5 ml min^{-1} for gradient elution with mobile phase (A): water and 5% acetonitrile; mobile phase (B): acetonitrile and a gradient profile of: 0–1 min, 95% A, 5% B, 11–13 min, 10% A, 90% B, 13.1 min, 95% A, 5% B, 16 min 95% A, 5% B). All standards were purchased from Sigma Aldrich, (Sigma Aldrich, St. Louis, Missouri, USA) including (+/–)-jasmonic acid; 3-indoleacetic-acid, gibberellic acid, (+/–)-abscisic acid; trans-zeatin; salicylic acid.

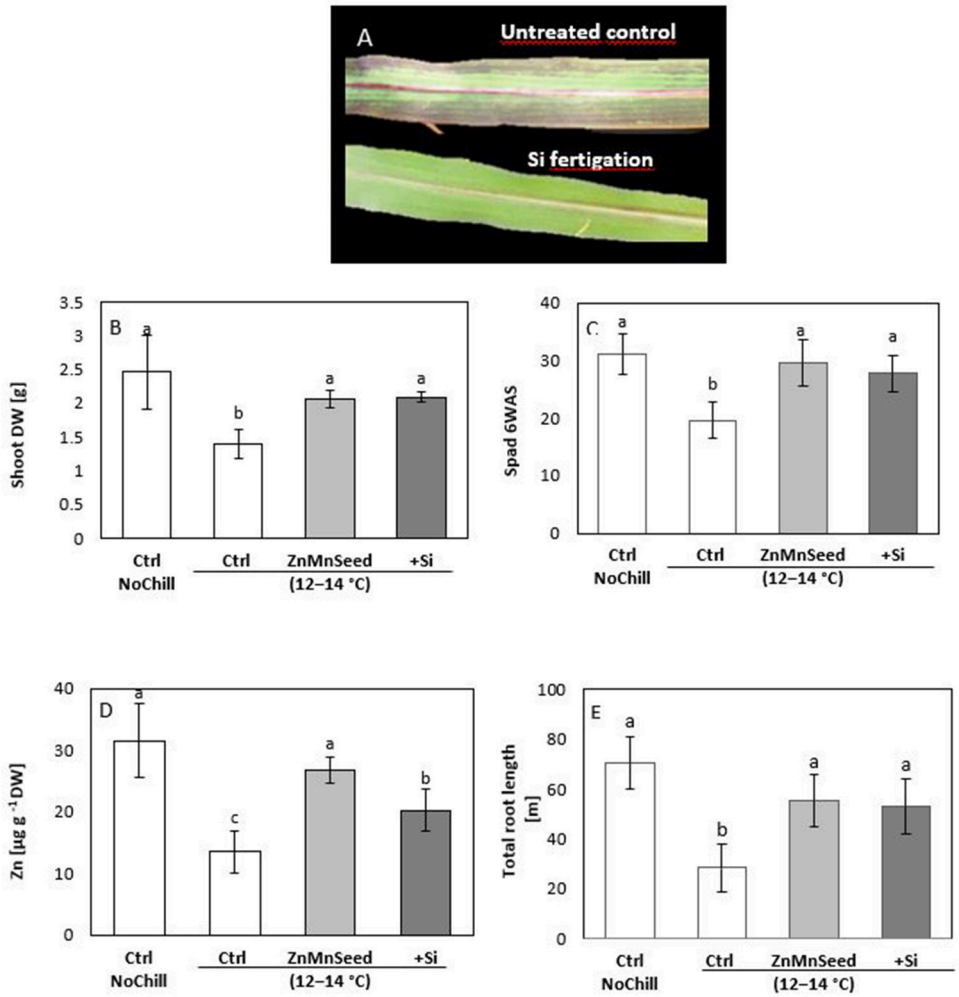

FIGURE 2 | (A) Leaf chlorosis, necrosis, and anthocyanin formation, **(B)** shoot dry weight (DW), **(C)** SPAD values, **(D)** shoot Zn concentration and **(E)** total root length of maize plants exposed to a 2-weeks period of reduced root zone temperature (RZT, 12–14°C) on a silty loam soil, pH 6.9. Un-cooled control: (Ctrl NoCill) and low RZT variants including untreated control (Ctrl); Zn Mn seed dressing (ZnMnSeed), and silicon (H_4SiO_4) fertigation (+Si). Means of three replicates. Significant differences ($P < 0.05$) are indicated by different characters.

Statistical Analyses

The study was carried out in a completely randomized design for pot experiments and a randomized block design for the field experiment. Data are presented as means ± SE. For statistical analysis of significant differences between treatment groups, a one-way ANOVA followed by a Tukey–test ($p < 0.05$ significance level) were performed using the Sigma-Plot software 10.0 (Systat Software GmbH, Erkrath, Germany). For the statical evaluation of yield data from the field experiment, t-grouping instead of the Tukey test was applied as recommended by Mudra (1958).

RESULTS

Soil Culture Experiment

In the first experiment, soil-grown maize seedlings were exposed to 14 days reduced root zone temperature of 12–14°C in a root cooling system. Cooling of the roots started at 2 weeks after sowing, followed by a 14-d recovery period. Seed treatments were performed with a commercial Zn/Mn seed dressing formulation. Silicon was applied as silicic acid (40 mg kg^{-1} dry soil) by fertigation in four weekly intervals. The optimal dosage for silicic acid application has been determined in a pilot experiment (**Figure 1**).

Plant Growth and Development

Confirming the results of our earlier studies (Bradáčová et al., 2016), 2 weeks exposure of maize plants to low RZT of 12–14°C was associated with induction of leaf chlorosis (**Figures 2A,C**) necrosis, formation of stress anthocyanins (**Figure 2A**) limited shoot and root growth (**Figures 2B,E**) and an impaired micronutrient status (particularly Zn and Mn) below the deficiency thresholds (**Figures 2D**, **3A**; Bergmann, 1988). The stress responses and micronutrient deficiencies were mitigated

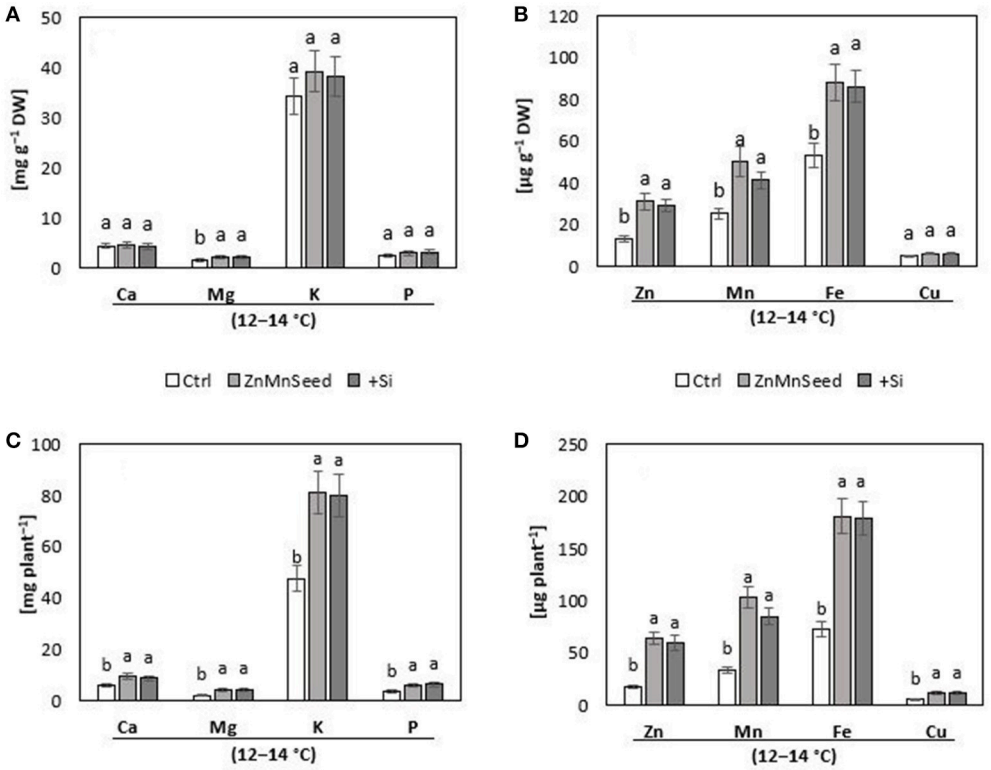

FIGURE 3 | (A,B) Concentrations and **(C,D)** contents of macro-, and micro-nutrients in shoots of maize plants (cv Colisee) exposed to a 2-weeks period at reduced root zone temperature (12–14°C) on a silty loam soil, pH 6.9. Untreated control: (Ctrl); Zn Mn seed dressing: (ZnMnseed), and silicon (H_4SiO_4) fertigation (Si). Means of three replicates. Significant differences ($P < 0.05$) are indicated by different characters.

TABLE 1 | Superoxide dismutase activity (SOD), peroxidase activity (POD), and H_2O_2 concentrations in root tissue and SOD, total protein, total antioxidant capacity, total soluble phenolics, total soluble flavonoids, proline, anthocyanin, total soluble sugars, and Si concentrations in the shoot tissue of maize plants (cv Colisee) exposed to a 2-weeks period at reduced root zone temperature (12–14°C) on a silty loam soil, pH 6.9.

Tissue	Determination	Ctrl	ZnMnSeed	+Si
Root	SOD [U mg^{-1} protein]	85.94 ± 8.68b	124.52 ± 12.44a	125.29 ± 12.62a
	POD [µmol tetra guaicol mg^{-1} protein]	54.19 ± 5.51b	99.76 ± 10.07a	92.51 ± 9.34a
	H_2O_2 [µmol g^{-1} FW]	85.70 ± 8.66a	39.81 ± 4.07b	32.50 ± 3.34b
Shoot	SOD [U mg^{-1} protein]	10.06 ± 1.10b	26.51 ± 2.74a	28.02 ± 2.89a
	Total protein [mgg^{-1} FW]	6.58 ± 0.75b	8.39 ± 0.93a	8.19 ± 0.91a
	Total antioxidants [%]	69.11 ± 7.00b	91.20 ± 9.21a	88.13 ± 8.90a
	Phenolics [mg gallic acid equivalents g^{-1} FW]	50.31 ± 5.12*b*	79.15 ± 8.01a	78.19 ± 7.91a
	Flavonoids [mg g^{-1} FW]	2.25 ± 0.32b	3.41 ± 0.43a	3.35 ± 0.43a
	Proline [µmol g^{-1} FW]	0.92 ± 0.18b	1.68 ± 0.26a	1.89 ± 0.28a
	Anthocyanin [µmol cyanidine-3-glucoside equivalents g^{-1} FW]	9.88 ± 1.08a	6.40 ± 0.73b	6.16 ± 0.71*b*
	Sugar [mg g^{-1} FW]	19.23 ± 2.01b	21.18 ± 2.21ab	24.15 ± 2.51a
	Si [mg g^{-1} DW]	2.70 ± 0.36b	2.88 ± 0.38b	4.15 ± 0.51a

Untreated control: (Ctrl); Zn Mn seed dressing: (ZnMnSeed), and silicon (H_4SiO_4) fertigation: (+Si). Means of three replicates. Significant differences ($P < 0.05$) are indicated by different characters.

by seed treatments with the respective micronutrients, but surprisingly, also by Si application (**Figure 2**). Shoot biomass and chlorophyll contents determined by SPAD measurements were increased by ∼50% (**Figures 2B,C**) and total root length even by 90% (**Figure 2E**).

Mineral Nutritional Status

Macronutrient analysis of the shoot tissue revealed no significant differences for the P, Ca, and K concentrations (**Figure 3A**). While the Ca and K status was in the sufficiency range, low concentrations were recorded for P and Mg. Seed

dressing with Zn/Mn or Si fertigation significantly increased particularly the Mg status of the plants (Bergmann, 1988). The shoot micronutrient concentrations of the untreated control were 0.013 mg g^{-1} DM for Zn and 0.025 mg g^{-1} DM for Mn (**Figure 3B**) which is below the reported deficiency thresholds (Bergmann, 1988). The concentrations increased to the sufficiency range in response to the Zn/Mn seed dressing treatment, but interestingly also after Si fertigation (**Figure 3A**). The Fe and Cu status was low but not critical, without significant differences between the treatments (**Figure 3A**). Shoot Si was significantly increased only by Si fertigation (**Table 1**). In contrast to the nutrient concentrations, as indicators for the plant nutritional status, total shoot contents of all investigated nutrients were significantly increased by the treatments with the chilling stress protectants Si and Zn/Mn (**Figures 3C,D**). This demonstrates that the Si and Zn/Mn applications generally improved nutrient acquisition and any surplus of mineral nutrients was readily transformed into biomass production (**Figure 2B**).

Oxidative Stress Indicators

In the root tissue directly exposed to low-temperature stress, Zn/Mn and Si applications increased the activities of superoxide dismutase (SOD, **Table 1**) and peroxidase (POD, **Table 1**) by 45–46 and 71–84%, respectively. These enzymes are involved in oxidative stress defense and accordingly, H_2O_2 concentrations declined by 54–63% (**Table 1**). In the shoot, SOD activities even increased by 179–183% (**Table 1**). Shoot concentrations of total proteins, antioxidants, total phenolics, total flavonoids, and proline concentrations were also strongly increased (**Table 1**) by both the Zn/Mn and Si treatments, while leaf anthocyanins, significantly declined (**Table 1**). In addition, the concentration of total soluble sugars of shoot tissue was significantly enhanced by Si treatment (**Table 1**).

Soil–Free Culture Experiment

Although Si induced a recovery of maize seedling growth after exposure to low RZT, which was associated with improved root development and mitigation of Zn and Mn deficiency (**Figure 3**, **Table 1**) we hypothesized that Si may exert also effects on improvement of the micronutrient status independent of root uptake. Thus, a second experiment was conducted to separate the root–mediated nutrient acquisition from internal redistribution of Zn and Mn from the seed to the establishing seedling. This was achieved by exposing maize seedlings to low temperature stress (7 d, 12°C) in a soil–free culture system with and without Si application via seed soaking (3 d during germination at 18°C), where the seedlings were exclusively dependent on their nutrient seed reserves and root uptake was excluded.

During the first 3 days of cultivation at 18°C, no significant treatment differences were recorded for germination rates (**Figure 4**). However, the subsequent 7 d–cold stress periods at 12°C induced a retardation in seedling growth, associated with a reduction in shoot and root biomass production by 53 and 60%, respectively, and intense necrotic and chlorotic leaf damage (**Table 2**) similar to the symptoms observed in soil culture (**Figures 2A** and **5**). Silicon treatments reduced the necrotic leaf area by more than 90%. This was associated with increased levels of total antioxidants (+27%) and soluble sugars (+117%) in the leaf tissue. The nutritional status of Zn and Mn was significantly increased by the Si treatment and a trend for increased root and shoot biomass production was detectable after the cold period of 7 d (**Table 2**).

During the 7-days cold stress period, shoot and root concentrations of all important hormonal growth regulators (indole acetic acid—IAA, zeatin, gibberellic acid—GA), as well as stress–related hormones, such as abscisic (ABA), jasmonic

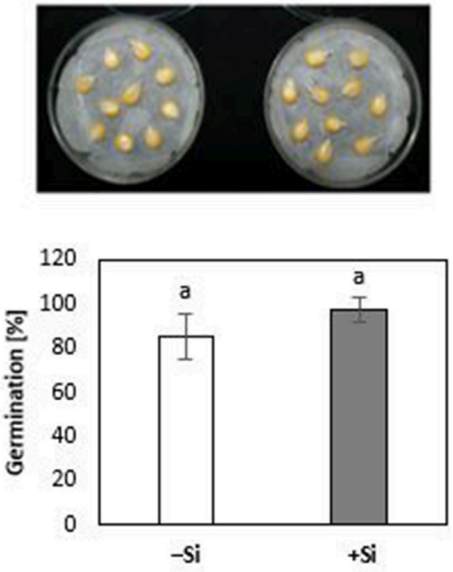

FIGURE 4 | Germination rate [% radicle emergence at 3 DAS; 18°C) of maize seedlings (cv Colisee) on moist filter paper with (+Si) or without (–Si) 3-days seed soaking treatments with 0.1 mM Si (H_4SiO4).

TABLE 2 | Effect of Si seed soaking on biomass production, oxidative leaf damage [% necrotic leaf area], tissue concentrations of Zn, Mn, Si, soluble sugars, and total antioxidants in maize seedlings (cv Colisee) exposed to 7 days chilling stress at 12°C in a soil-free filter roll culture system.

	–Si (18°C)	–Si (12°C)	+Si (12°C)
Dry weight (Shoot) [g]	0.98 ± 0.11a	0.46 ± 0.06b	0.63 ± 0.27ab
Dry weight (Root) [g]	0.85 ± 0.10a	0.34 ± 0.04b	0.41 ± 0.05b
Zn (Shoot) [μg g^{-1} DW]	16.25 ± 1.63a	11.42 ± 1.15*c*	13.73 ± 1.38b
Zn (Root) [μg g^{-1} DW]	11.85 ± 1.20a	9.08 ± 0.92b	10.80 ± 1.09a
Mn (Shoot) [μg g^{-1}DW]	3.23 ± 0.33a	1.56 ± 0.17b	2.63 ± 0.27a
Mn (Root) [μg g^{-1} DW]	2.12 ± 0.22a	0.99 ± 0.11b	1.43 ± 0.69ab
Total Antioxidants (Shoot) [%]	62.25 ± 6.24b	67.30 ± 6.74b	85.21 ± 8.53a
Necrotic leaf area [%]	0.50 ± 0.06*c*	25.25 ± 2.54a	2.35 ± 0.25b
Soluble Sugars (Shoot) [mg g^{-1} FW]	28.15 ± 2.83a	12.12 ± 1.22b	26.23 ± 2.63a
Si (Shoot) [mg g^{-1} DW]	0.86 ± 0.20b	0.63 ± 0.07*c*	1.32 ± 0.14a

Means of five replicates. Significant differences ($P < 0.05$) are indicated by different characters.

and salicylic acids, declined significantly. However, after Si seed soaking, hormonal concentrations were restored comparable to those of unstressed plants or even further increased (shoot concentrations of IAA, gibberellic acid, and ABA, **Table 3**).

Since plant cultivation in this experiment was conducted in a nutrient–free culture system, lacking any additional Zn or Mn (Si treatment solution pre-purified by cation exchange chromatography) (Maksimovic et al., 2007; Pavlovic et al., 2013), it was possible to monitor the redistribution of seed–stored Zn and Mn during seedling development. Thus, any additional nutrient uptake via the roots was excluded. During the 10 days culture period, 50% of the seed Zn contents and 42% of seed Mn were translocated to the developing control seedlings. Interestingly, the translocation of micronutrient seed reserves was stimulated by the Si treatments, resulting in significantly higher total Zn (+67%) and Mn (+62%) contents at the end of the cold stress period, as compared with the untreated controls (**Figure 6**). By comparison with the remaining nutrient contents in the seeds, it was also possible to calculate the nutrient leaching losses. In the untreated control plants exposed to chilling stress, leaching accounted for 29% of the original seed Zn contents and for 41% of Mn. However, silicon treatment significantly reduced the large leaching losses of Zn and Mn by 70 and 48%, respectively (**Figure 6**).

Apart from the micronutrients, also the re-distribution of K was investigated, because of its well-established role as an indicator for nutrient leaching in response to impairment of tissue and membrane integrity (Cakmak and Marschner, 1987) and its function in cold stress protection (Wang et al., 2013). At the end of the cold stress period, untreated control seedlings had lost 72% of their K seed reserves by leaching and only 22% had been translocated to the developing seedling. Silicon treatments reduced these large leaching losses by 17% and increased the K contents of the seedling by 38% (**Figure 6**). For other tested macronutrients, such as P, Mg, and Ca, no significant treatment effects were recorded (data not shown). However, Si not only reduced the leaching losses and improved the translocation of seed reserves of mineral nutrients to growing tissues. Additional selective effects were detectable for the mineral nutrient ratio between shoots and roots. While Si pre-treatments increased the Mn and K contents in shoots and roots to a similar extent (Mn: +68–77%; K: +38–46%), Si preferentially increased the Zn shoot contents by 64%, but less, only by 34%, in the root tissue (**Figure 6**).

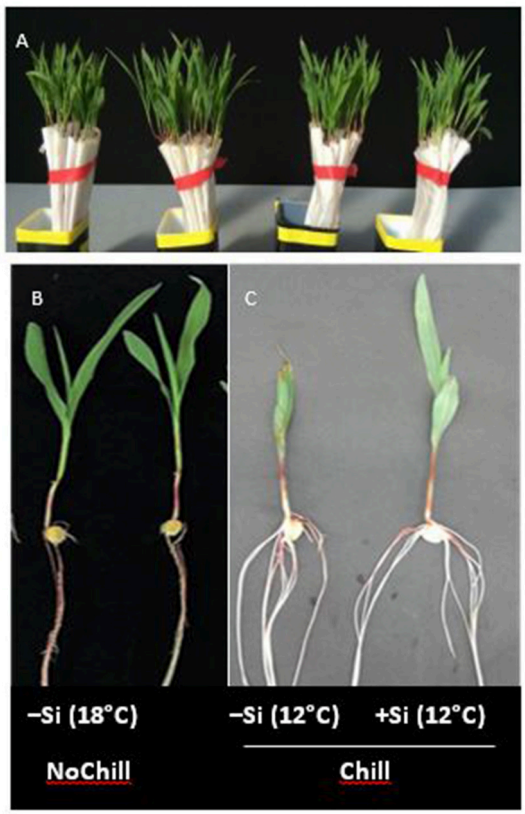

FIGURE 5 | (A–C) Maize seedlings germinated in filter rolls for 7 d at 18°C (NoChill) or at 12°C (Chill) without (–Si) or with (+Si) after 3 d seed soaking in 0.1 mM Si (H_4SiO_4).

TABLE 3 | Endogenous concentrations of phytohormones in maize seedlings (cv Colisee) grown for 7 days at 18 or 12°C, in a soil-free filter roll culture system with (+Si) or without (–Si) silicic acid seed-soaking (–Si) during a 3-day pre-germination period at 18°C.

Tissue	**Shoot**			**Root**		
Temperature	18°C	12°C	12°C	18°C	12°C	12°C
Treatment	–Si	–Si	+Si	–Si	–Si	+Si
Phytohormones	**[ng g^{-1} fresh weight]**					
IAA	76.77 ± 9.90a	28.14 ± 4.65b	102.12 ± 16.54a	31.45 ± 8.81a	12.76 ± 0.37b	40.10 ± 13.43a
Zeatin	3.24 ± 0.84a	1.10 ± 0.22b	3.62 ± 0.65a	1.29 ± 0.49a	0.40 ± 0.04b	1.21 ± 0.31a
ABA	50.63 ± 4.13b	31.02 ± 4.04c	109.56 ± 13.69a	46.56 ± 8.65a	14.97 ± 0.91b	48.78 ± 14.19a
GA	55.60 ± 10.29b	18.26 ± 3.14c	67.20 ± 9.77a	25.07 ± 6.27a	9.51 ± 0.70b	30.12 ± 10.49a
JA	0.44 ± 0.07a	0.28 ± 0.03b	0.42 ± 0.09a	ND	ND	ND
SA	44.89 ± 6.79a	16.78 ± 3.17b	56.27 ± 15.26a	21.96 ± 4.71a	9.53 ± 0.79b	28.94 ± 12.00a

IAA, indole acetic acid; ABA, abcsisic acid; GA, gibberellic acid; JA, jasmonic acid; SA, salicylic acid. Means of three replicates. Significant differences ($P < 0.05$) are indicated by different characters. ND, Not Detectable.

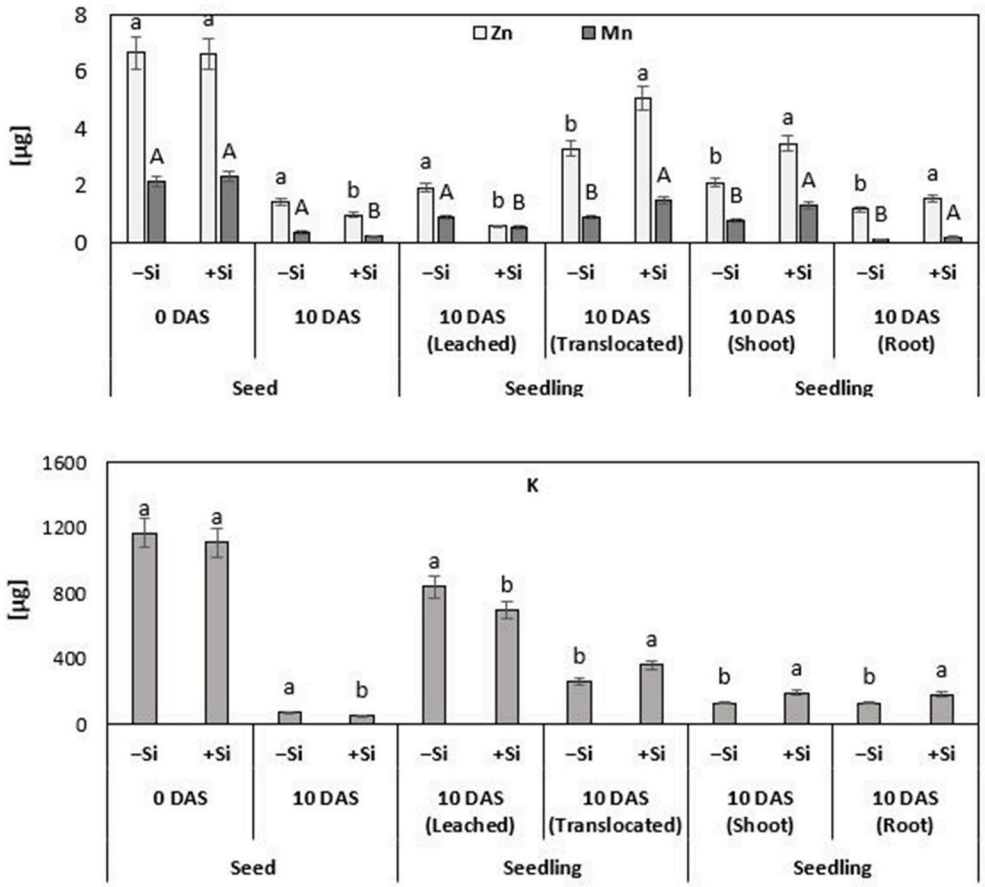

FIGURE 6 | Fate and distribution of Zn, Mn, and K [µg seed^{-1} or µg seedling^{-1}] during germination and seedling growth of maize (cv Colisee) exposed to chilling stress (12°C; 3–10 DAS) in a soil-free filter roll culture system with (+Si) or without (–Si) silicic acid seed soaking (–Si) during a 3-day pre-germination period at 18°C. Means of five replicates. Significant differences ($P < 0.05$) are indicated by different characters.

Field Experiment

To investigate the benefit of Zn/Mn and Si starter treatments on maize performance under on-farm conditions, a field experiment was established. Early sowing on April 22nd resulted in cold stress during germination and early growth. Due to low temperatures (13.6°C) and high precipitation (469 mm) during April and May, emergence and seedling growth were heavily affected by cold stress, but also by oxygen limitation and *Aspergillus niger* infections on the cold and wet silty-loam soil. By the mid of May, at 41 DAS (BBCH 15, stage 1), an emergence rate of only 44% was recorded in the untreated control variant (**Table 1**). However, emergence was significantly increased by the Zn/Mn seed dressing (+12%) and particularly by seed soaking with KSi (+28%). To account for a potential water priming effect of the seed soaking treatment (Lutts et al., 2016), also a water-soaked control was included, which increased emergence by 8% (**Table 4**).

At 49 DAS (BBCH 17, stage 1), a mineral nutrient analysis was conducted for the youngest fully developed leaves. In the control variant, the Zn–nutritional status was low (**Table 4**) as expected, and K and P were even below the deficiency thresholds. Mg, Cu, and Mn supply, by contrast, was sufficient (Supplementary Table 2). Similar to the pot experiment, both, Zn/Mn and Si treatments significantly increased the Zn concentrations to a sufficient level of 65 and 59 µg g^{-1} dry matter (Bergmann, 1988). A trend for an improved status was recorded also for the remaining nutrients (Supplementary Table 2). The protective effects of Zn/Mn and Si starter treatments were finally reflected in substantially higher biomass yield of the heavily cold-affected plots by 56 and 82%, respectively, when calculated according to the plant density determined at 41 DAS. In the Si treatments, 25% of the yield increase could be attributed to a water priming effect. Foliar Si application had no significant impact on final biomass yield (**Table 4**). However, due to the extremely low emergence (44%), particularly in the untreated plots, re-sowing was performed in the most heavily affected parts, by the mid of May after the end of the stress period, to provide comparable inter-plant competition for light, water, and nutrients within the rows during the rest of the culture period. But even including the non-stressed plants after re-sowing into the yield calculation, a

TABLE 4 | Emergence, Zn/Mn status (DAS), and final biomass yield of field-grown silo maize (Rolandinio) on a silty loam soil pH 6.9 at the experimental station "Ihinger Hof" University of Hohenheim with underfoot placement of di-ammonium phosphate (29 kg N, 32 kg P ha^{-1}) and stabilized ammonium sulfate fertilization (161 kg N ha^{-1}) with or without Zn/Mn seed dressing (Lebosol Mn500 SC, Zn700 SC), potassium silicate [1 mM] seed priming, water priming of foliar Si application of Si as (16 L Si [1 mM] + 100 ml Greemax® ha^{-1}).

Seed treatment	Application ode	Emergence 41 DAS [%]	Yield [t DM ha^{-1}]	Zn status (45DAS) [μg g DW^{-1}]	Mn status (45 DAS) [μg g DW^{-1}]
Untreated	–	44.00 ± 6.00d	7.14 ± 0.46d (16.10 ± 1.0b)	32.00 ± 2.60b	48.00 ± 4.00a
Zn/Mn	Seed–dressing	56.00 ± 7.00b	11.07 ± 0.79b (16.40 ± 1.2b)	65.00 ± 5.40a	56.00 ± 4.50a
Water	Priming	52.00 ± 9.00c	8.10 ± 0.81c (17.2 ± 1.60ab)	49.00 ± 4.08a	57.00 ± 4.75a
K_2SiO_4	Priming	72.00 ± 15.00a	12.89 ± 0.74a (17.8 ± 1.0a)	59.00 ± 4.90a	61.00 ± 5.08a
untreated	Si foliar	46.00 ± 7.00d	7.60 ± 0.37d (16.6 ± 3.40ab)	36.00 ± 3.00b	51.00 ± 4.25a

Yield determinations with (in brackets) and without re-sowing by the end of May 2016. Means of five replicates per treatment. Significant differences ($P < 0.05$) are indicated by different characters.

significant yield increase (+10.6%) was measured only for the Si seed priming variant (**Table 4**).

DISCUSSION

Si Mimics Cold Stress-Protective Effects of Zn/Mn Starter Applications

Similar to earlier reports (Imran et al., 2013; Bradáčová et al., 2016), starter treatments by seed dressing or seed priming with Zn and Mn significantly increased cold tolerance of maize in the pot experiment with controlled root-zone temperature (**Figure 2**). The 14-d chilling treatments with 12°C root zone temperature induced Zn and Mn deficiencies in the soil-grown maize seedlings (**Figure 3**). This seems to be not primarily related to Zn/Mn availability in the soil, since Imran et al. (2013) demonstrated that Zn and Mn accumulation in the shoot tissue was suppressed during the cold stress period, even with freely available nutrient supply in a hydroponic culture system. Only Zn and Mn uptake before the onset of the stress period via seed priming, seed dressing or fertigation, could increase shoot micronutrient accumulation above the deficiency thresholds, detectable even after the end of the 2-weeks cold stress period (**Figure 3**). This is in line with findings of Engels and Marschner (1992, 1996), demonstrating that limited Zn and Mn shoot accumulation in maize exposed to low root zone temperatures was particularly dependent on cold-stress effects affecting nutrient uptake and root activity.

In accordance with the low Zn/Mn status, the cold-stressed control plants exhibited various symptoms characteristic for Zn and Mn limitation (Cakmak, 2000), such as chlorosis and oxidative leaf damage, stunted shoot, and root growth (**Figure 2**) reduced activity of enzymes involved in ROS detoxification with micronutrients as co-factors (SODs, PODs), and impaired biosynthesis of phenolic antioxidants (**Table 1**) which depends on Cu and Mn cofactors (Datnoff et al., 2007). Consequently, excessive accumulation of ROS (**Table 1**) resulted in oxidative damage of plant tissues (**Figure 2**) considered as one of the major constraints for cold-stressed plants (Baek and Skinner, 2012; Saeidnejad et al., 2012). Supplementation of Zn and Mn via seed priming (Imran et al., 2013) or seed dressing were able to overcome Zn/Mn deficiency (**Figure 3**) and largely mitigated the related stress symptoms described above. Surprisingly, also starter fertigation or seed soaking with Si completely mimicked all cold-stress-protective effects of Zn/Mn starter applications (**Figures 2**, **Table 1**). Silicon increased the Zn/Mn status, activities of ROS detoxification enzymes, and accumulation of antioxidants to a comparable level as the Zn/Mn treatments (**Figures 3**, **Table 1**) although Si was applied as free silicic acid (H_4SiO_4), pre-purified via cation exchange chromatography, and no Zn or Mn was detectable in the application solution.

Also in the field experiment, seed treatments with Si and Zn Mn improved emergence and the micronutrient status (particularly Zn) of maize seedlings, exposed to sub-optimal germination temperatures and cold and wet soil conditions by early sowing at the mid of April (**Table 4**). A certain protective effect was recorded also for the control treatment with water-primed seeds but less expressed as compared with Si seed priming. This is in line with the well-documented beneficial effects of water priming on seed germination by metabolic pre-activation (Lutts et al., 2016). In accordance with earlier observations (Imran et al., 2013; Bradáčová et al., 2016), application of cold stress protectants was ineffective after the onset of the stress period, i.e., when Si was supplied by the foliar application (**Table 4**). By contrast, silicon seed priming was the most effective treatment and increased emergence by 64% as compared with the untreated control, which translated into a significant increase in final yield in both scenarios of yield determination (with and without re-sowing after the end of the cold stress period; **Table 4**). Similar effects have been reported also in two additional field experiments conducted under comparable climatic conditions when the micronutrient status of the maize seedlings was increased by direct supplementation of Zn, Mn, and Fe via seed priming. In these field trials, marketable grain yields increased by 13–15% (Imran et al., 2013).

The surprisingly long-lasting effects of the starter treatments with cold stress protectants may be related to the intense stimulation of root growth (**Figure 2D**) which has an advantage for plant performance not only during the stress period but also during the recovery phase and under more favorable growth conditions.

Silicon Reduces Leaching Losses and Promotes Utilization of Zn/Mn Seed Reserves

The striking similarity of Zn/Mn and Si effects on cold-stressed maize seedlings raises the question whether Si exerts its protective effects via improvement of the plant micronutrient (Zn/Mn) status. Restoration of cold stress-induced root growth inhibition was among the most apparent effects of Si or Zn/Mn applications (**Figure 2E**). Of course, root growth stimulation can contribute to improved nutrient acquisition in general, as demonstrated for increased shoot accumulation of P, K, Mg, Ca, Fe, Zn, Mn, and Cu recorded after the cold stress period in Si-treated maize plants (**Figure 3**). However, Si was able to improve selectively the Zn/Mn status of maize seedlings, already during the first week of the cold stress period, before a marked stimulation of root growth was detectable (**Table 2**). Moreover, this effect was observed in a soil–free culture system excluding the option for further Zn/Mn root uptake from the external medium (**Figure 5**). This implicates that the improved micronutrient status of the Si-treated maize seedlings exposed to low-temperature stress cannot be exclusively attributed to Si-induced root growth stimulation but involves also Si effects counteracting nutrient leaching and promoting internal distribution of Zn and Mn. Imran et al. (2015) demonstrated that seed reserves can cover the Zn and Mn demand of maize seedlings for about 2–3 weeks. However, cold stress is a well-documented stress factor leading to electrolyte leakage via oxidative membrane damage (Bewley and Black, 1994), which can limit the seed reserves of mineral nutrients. Accordingly, our study revealed large leaching losses of 30–40% for the Zn/Mn seed reserves and even 70% for K, as another mineral nutrient with cold-protective functions (Wang et al., 2013), during the first 10 days of seedling development after a 12°C cold stress period of 7 days (**Figure 6**). Seed soaking with Si dramatically reduced the leaching losses by 70% (Zn), 50% (Mn), and 15% (K), leading to an improved nutrient supply to the developing seedling. This effect may be attributed to the well-documented protective functions of Si against oxidative membrane damage (He et al., 2010). However, Si seed soaking increased the root and shoot contents of Mn by 77 and 68%, respectively, while the root contents of Zn were increased only by 34%, but by 64% in the shoot tissue (**Figure 6**). This indicates a selective effect of Si on the root/shoot distribution of Zn. A similar improved Zn status by Si treatment has been reported for Zn-deficient soybean plants (Pascual et al., 2016).

Different mechanisms have been proposed for effects of Si, improving internal Zn availability in Zn-deficient plants. Increased production of phenolics with metal chelating properties induced by Si treatments (Pavlovic et al., 2013), as observed also in the present study (**Table 1**) may increase internal mobility and transport of Zn within the plant. This may be related to the improved Mn status of Si treated plants (**Figure 3**) as an important enzymatic cofactor for the biosynthesis of phenolics (Datnoff et al., 2007). In later stages of plant development, the same mechanism may be responsible also for the remobilization of Zn sequestered in the apoplast together with iron plaques (Chen et al., 1980), as similarly demonstrated for apoplastic Fe remobilization in cucumber (Pavlovic et al., 2013). Bityutskii et al. (2014) could not confirm this interaction, but in that study, plants were grown in nutrient solution without Zn supply, which may have prevented the accumulation of apoplastic Zn pools. Other studies suggest direct Si-metal interactions counteracting apoplastic metal immobilization and supporting metal transport in plants (Pavlovic et al., 2013; Hernandez–Apaolaza, 2014; Stevic et al., 2016). Effects of Si on the expression of metal acquisition and transport genes have been reported by Pavlovic et al. (2013, 2016), but the underlying mechanisms are unknown.

Si Restores the Levels of Hormonal Growth Regulators in Cold-Stress-Affected Maize Seedlings

Due to the impairment of Zn/Mn-dependent ROS detoxification systems, induced by limited Zn/Mn availability in cold-stressed plants (**Figures 2**, **3**) excessive ROS accumulation causes oxidative damage, leading to leaf chlorosis and necrosis (**Figure 2**). This is associated with an impairment of photosynthesis, resulting in a reduced root allocation of assimilates required for root development, as previously reported also by Sowinski et al. (1998). Moreover, excessive production of ROS can promote oxidative degradation of indole acetic acid and result in a 50% reduction of IAA contents in Zn-deficient *Phaseolus vulgaris*, which could be restored by Zn fertilization. Therefore, auxin deficiency was considered as another important factor for growth limitation in Zn deficient plants (Cakmak et al., 1989). Similarly, in our study cold stress induced, both, Zn/Mn limitation (**Table 1**) and a 60% reduction of IAA accumulation in the shoot and root tissue (**Table 3**) associated with inhibition of shoot and root growth and all symptoms were reverted by exogenous Si application (**Figure 2**). More recent studies suggest that cold stress additionally affects root growth via inhibition of PIN2 and PIN3-mediated basipetal auxin transport within the roots (Shibasaki et al., 2009).

Shoot growth in cold-stressed plants seems to be also affected by a reduction of bioactive growth-promoting gibberellic acid (GA) levels, leading to an increased abundance of nuclear DELLA-protein growth repressors via a signaling pathway involving CBF/DREB1 transcription factors (Miura and Furumoto, 2013; Eremina et al., 2016). Accordingly, in our study GA levels in shoot and roots of cold-stressed maize seedlings declined by ∼60–70%. This effect was completely reverted by Si seed soaking (**Table 3**). In line with this observation, in *Arabidopsis thaliana* it was demonstrated that cold stress stimulates GA degradation by upregulation of the GA 2-oxidase gene and simultaneously impairs GA-biosynthesis by repressing

the GA 20-oxidase gene (Eremina et al., 2016). For Zn-deficient plants, reduced GA concentrations have been recorded (Suge et al., 1986; Sekimoto et al., 1997) similar to the reduction in IAA levels reported by Cakmak et al. (1989). More recently, it was shown that various steps of GA biosynthesis depend on the presence of IAA (Ross et al., 2001). Therefore, the observed reduction of GA levels in cold-stressed maize seedlings (may be a consequence of auxin deficiency, resulting from the limited Zn supply caused by low temperature stress. Interestingly, it was shown that exogenous application of IAA and GA could increase the accumulation of flavonoids and other phenolics in buckwheat (*Fagopyrum esculentum*) seedlings (Park et al., 2017). This observation is in line with the increased production of phenolics and antioxidants, induced by Si application in cold-stressed maize seedlings (**Table 1**) that may be triggered by the increased IAA and GA levels in the respective plants (**Table 3**).

Similar to auxin and GA, also the levels of the metabolically active cytokinin form "zeatin," with functions in stimulation of cell division and cell expansion, declined in cold-stressed maize seedlings (**Table 3**). A similar decline had been previously reported for *Arabidopsis,* rice and, wheat (Eremina et al., 2016). In rice, this was associated with a significant downregulation of gene expression related to cytokinin biosynthesis (Maruyama et al., 2014). Accordingly, external application of cytokinins increased cold tolerance in *Arabidopsis* (Jeon et al., 2010; Shi et al., 2012). In our study, cold-stress protection by Si application was also associated with increased zeatin concentrations in the root and shoot tissue (**Table 3**).

Taken together, the results demonstrated that cold stress significantly reduced the internal concentrations of the most important hormonal regulators of plant growth. Furthermore, the cold-protective effect of Si application was related to a restoration of hormonal levels comparable to those of unstressed plants (**Table 3**).

Si Increases the Levels of Hormonal Stress Regulators in Cold Stress-Affected Maize Seedlings

The Si treatments influenced also the levels of abscisic (ABA) salicylic (SA) and jasmonic acids (JA), known as hormones more directly involved in the regulation of abiotic and biotic stress responses (**Table 3**). These hormones have been also implicated in cold stress signaling (Miura and Furumoto, 2013; Eremina et al., 2016). Improved cold acclimation and increased cold tolerance by exogenous applications of ABA, SA, and JA have been reported for various plant species (Horváth et al., 2007; Kumar et al., 2008; Eremina et al., 2016; Hu et al., 2017). Mutants affected in ABA, SA, and JA metabolism show altered responsiveness to cold stress (Eremina et al., 2016). Accordingly, in our study, exposure of maize, as cold-sensitive plant species to a 7-days cold period, significantly decreased the levels of ABA, SA, and JA. The cold-protective effect of Si starter treatments was associated with an increase of ABA and to a smaller extent also of SA and JA, particularly in the shoot (**Table 3**). Abscisic acid is considered as a central regulator of cold stress responses in plants and seems to regulate the adaptive expression of cold-related genes with cold-protective functions via CBF-dependent and independent pathways, in cross-talks involving also SA and JA (Szalai et al., 2011; Eremina et al., 2016). Direct links between ABA and induction of oxidative stress defense enzymes, such as SOD in cold-stressed plants similar to our study (**Figure 3**) have been reported by Kumar et al. (2008), Szalai et al. (2011), and Li and Zhang (2012). Moreover, the cold stress-induced accumulation of cryo-protectants, such as proline (**Figure 3**) has been linked with a reduction of leaching losses via ABA-induced protection against oxidative membrane damage (Chen and Li, 2002). Proline biosynthesis at least partially depends on ABA signaling (Szabados and Savouré, 2010). Increased ABA levels in the Si-treated plants may be also related to the improved Zn-nutritional status induced by the Si starter treatments (**Figure 3**). Accordingly, Cakmak et al. (1989) and more recently Wang et al. (2012) reported that Zn deficiency reduced the ABA levels in *Phaseolus vulgaris* and in apple rootstocks.

The surprisingly distinct effects of the Si treatments on the hormonal balances (**Table 3**) and the timing of hormonal changes just at the beginning of detectable growth responses (**Table 2**) are clear indicators for the proposed interactions of the Si amendments with hormonal cold stress signaling. Nevertheless, the obvious interactions of Si with hormonal balances require further investigations considering quantitative changes during plant development and a higher spatial resolution, since it is known that local changes in hormone concentrations at the cellular level control adaptive growth and development (Eremina et al., 2016). A conceptual model of the proposed interactions between Si, micronutrients, and hormones mediating chilling tolerance in maize seedlings and its relation to plant growth is presented in **Figure 7** and summarizes our findings.

CONCLUDING REMARKS

The findings of the present study suggest that induced deficiency of Zn and Mn as a consequence of leaching during early development and limited root growth and activity is a major factor determining the sensitivity of young maize plants to chilling stress, with options for mitigation by supplementing germinating seeds with Zn, Mn, or Si. In this context, the protective effect of Si treatments is related to an improved Zn and Mn status, starting already during germination with a protective effect of Si against leaching losses of micronutrient seed reserves and improved translocation to the developing seedling. The improved micronutrient status can at least partially explain the ability of the plants to maintain a balanced hormonal (IAA, GA, cytokinin) status that restores plant growth and particularly root development, which allows further nutrient uptake. The improved micronutrient status also helps to increase the expression of enzymatic (SOD, POD) and non-enzymatic (phenolic antioxidants) defense systems against cold-induced oxidative stress. Finally, it stimulates the accumulation of stress hormones (ABA, SA, JA), potentially priming various physiological adaptations to chilling stress via expression of

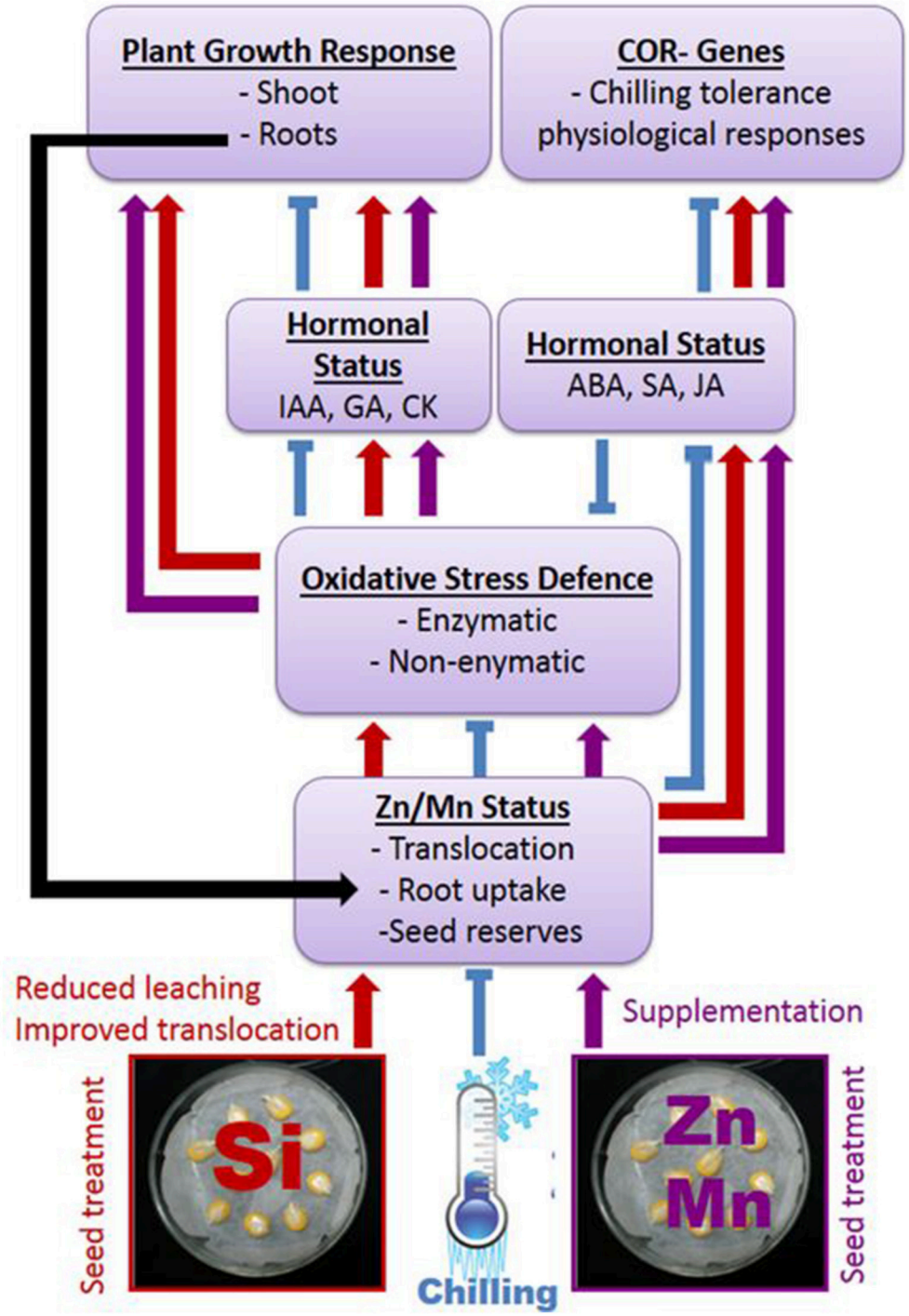

FIGURE 7 | Proposed interactions between Si or Zn/Mn seed treatments and expression of chilling tolerance in maize. Arrows indicate stimulation, t–shaped lines inhibition of the respective processes.

cold response genes. It remains to be established whether this applies also to protective effects of Si against other abiotic stresses, such as drought or salinity, which are also associated with oxidative stress. Remarkably, the improved micronutrient status by Si treatment under low temperature stress is not only restricted to controlled lab conditions. The preliminary field experiment demonstrated that the observed protective effects of Si starter treatments on seedling performance can translate

into improved yields in agricultural practice and requires further investigation considering different soil types and maize varieties.

AUTHOR CONTRIBUTIONS

NM, GN, and MW: conceived and designed the experiments; NM: conducted the experiments, collected the data, and wrote the manuscript with GN and UL; FW, BH, and NM: developed and performed the UHPLC-MS analysis of phytohormones. All authors approved the final manuscript.

ACKNOWLEDGMENTS

This work was supported by the European's Seventh Framework Programme (FP/2007–2013) under Grant Agreement no. 312117.

SUPPLEMENTARY MATERIAL

The Supplementary Material for this article can be found online at: https://www.frontiersin.org/articles/10.3389/fpls.2018.00420/full#supplementary-material

REFERENCES

Al-aghabary, K., Zhu, Z., and Shi, Q. (2005). Influence of silicon supply on chlorophyll content, chlorophyll fluorescence, and antioxidative enzyme activities in tomato plants under salt stress *J. Plant Nutr.* 27, 2101–2115. doi: 10.1081/PLN-200034641

Baek, K. H., and Skinner, D. Z. (2012). Production of reactive oxygen species by freezing stress, and the protective roles of antioxidant enzymes in plants. *J. Agric. Chem. Environ*. 1, 34–40. doi: 10.4236/jacen.2012.11006

Beauchamp, C., and Fridovich, I. (1971). Superoxide dismutase: improved assays and an assay applicable to acrylamide gels. *Anal. Biochem*. 44, 276–287. doi: 10.1016/0003-2697(71)90370-8

Bergmann, W. (1988). *Ernährungsstörungen bei Kulturplanzen: Entstehung, Visuelle und Analytische Diagnose. 2.* Aufl. Gustav Fischer Verlag, Jena.

Bates, L. S., Waldren, R. P., and Teare, I. D. (1973). Rapid determination of free proline for water-stress studies. *Plant Soil.* 39, 205–207. doi: 10.1007/BF00018060

Bewley, J. D., and Black, M. (1994). *Seeds: Physiology of Development and Germination, 2nd Edn.* London: Plenum Press.

Bityutskii, N., Pavlovic, J., Yakkonen, K., Maksimović, V., and Nikolic, M. (2014). Contrasting effect of silicon on iron, zinc and manganese status and accumulation of metal–mobilizing compounds in micronutrient–deficient cucumber. *Plant Physiol. Biochem*. 74, 205–211. doi: 10.1016/j.plaphy.2013.11.015

Bradáčová, K., Weber, N. F., Moradtalab, N., Asim, M., Imran, M., Weinmann, M., et al. (2016). Micronutrients (Zn/Mn), seaweed extracts, and plant growth–promoting bacteria as cold–stress protectants in maize. *Chem. Biol. Technol. Agric*. 3:19. doi: 10.1186/s40538-016-0069-1

Bradford, M. M. (1976). A rapid and sensitive method for the quantitation of microgram quantities of protein utilizing the principle of protein-dye binding. *Anal. Biochem*. 72, 248–254. doi: 10.1016/0003-2697(76)90527-3

Cakmak, I. (2000). Possible role of zinc in protecting plant cells from damage by reactive oxygen species. *New Phytol*. 146, 185–205 doi: 10.1046/j.1469-8137.2000.00630.x

Cakmak, I., and Marschner, H. (1987). Increase in membrane permeability and exudation in roots of zinc deficient plants. *J. Plant. Physiol*. 132, 356–361. doi: 10.1016/S0176-1617(88)80120-2

Cakmak, I., Marschner, H., and Bangerth, F. (1989). Effect of zinc nutritional status on growth, protein metabolism and levels of indole−3–acetic acid and other phytohormones in bean (*Phaseolus vulgaris* L). *J. Exp. Bot*. 40, 405–412.

Chance, B., and Maehly, A. S. (1955). Assay of catalases and peroxidases. *Methods Enzymol*. 2, 764–775. doi: 10.1016/S0076-6879(55)02300-8

Chen, C. C., Dixon, J. B., and Turner, F. T. (1980). Iron coatings on rice roots: morphology and models of development. *Soil Sci. Soc. Am. J*. 44, 1113–1119. doi: 10.2136/sssaj1980.03615995004400050046x

Chen, W. P., and Li, P. H. (2002). Membrane stabilization by abscisic acid under cold aids proline in alleviating chilling injury in maize (*Zea mays* L.) cultured cells. *Plant Cell Environ*. 25, 955–962. doi: 10.1046/j.1365-3040.2002.00874.x

Cutforth, H. W., Shaykewich, C. F., and Cho, C. M. (1986). Effect of soil water and temperature on corn (*Zea mays* L) root growth during emergence. *Can. J. Soil Sci.* 66, 51–58. doi: 10.4141/cjss86-006

Datnoff, L. E., Elmer, W. H., and Huber, D.G. (2007). *Mineral Nutrition and Plant Disease.* St. Paul, MN: The American Phytopathological Society.

Duncan, W. G., and Hesketh, J. D. (1968). Net photosynthetic rates, relative leaf growth rates and leaf numbers of 22 races of maize grown at eight temperatures. *Crop Sci*. 8, 670–674. doi: 10.2135/cropsci1968.0011183X000800060009x

Engels, C., and Marschner, H. (1992). Root to shoot translocation of macronutrients in relation to shoot demand in maize (*Zea mays* L.) grown at different root zone temperatures. *J. Plant Nutr. Soil Sci*. 155, 121–128. doi: 10.1002/jpln.19921550209

Engels, C., and Marschner, H. (1996). Effects of suboptimal root zone temperatures and shoot demand on net translocation of micronutrients from the roots to the shoot of maize. *Plant Soil* 186, 311–320. doi: 10.1007/BF02415526

Eremina, M., Rozhon, W., and Poppenberger, B. (2016). Hormonal control of cold stress responses in plants. *Cell. Mol. Life Sci*. 73, 797–810. doi: 10.1007/s00018-015-2089-6

Farooq, M., Wahid, A., and Siddique, K. H. M. (2012). Micronutrient application through seed treatments - a review. *J. Soil Sci. Plant Nutr*. 12, 125–142. doi: 10.4067/S0718-95162012000100011

Gericke, S., and Kurmis, B. (1952). Die kolorimetrische phophorsäurebestimmung mit ammonium–vanadat–molybdat und ihre anwendung in der pflanzenanalyse. *Z. Pflanzenernaehr. Bodenkd* 59, 235–247.

Giannopolitis, C. N., and Ries, S. K. (1977). Superoxide dismutases – occurrence in higher plants. *Plant Physiol*. 59, 309–314. doi: 10.1104/pp.59.2.309

Gong, H. J., Chen, K. M., Zhao, Z. G., Chen, G. C., and Zhou, W. J. (2008). Effects of silicon on defense of wheat against oxidative stress under drought at different developmental stages. *Biol. Plant*. 52, 592–596. doi: 10.1007/s10535-008-0118-0

Gong, H., Zhu, X., Chen, K., Wang, S., and Zhang, C. (2005). Silicon alleviates oxidative damage of wheat plants in pots under drought. *Plant Sci*. 169, 313–321. doi: 10.1016/j.plantsci.2005.02.023

Gossett, D. R., Millhollon, E. P., and Science, L. M. (1994). Antioxidant response to NaCl stress in salt-tolerant and salt-sensitive cultivars of cotton. *Crop Sci*. 34, 706–714. doi: 10.2135/cropsci1994.0011183X003400030020x

Gunes, A., Inal, A., Bagci, E. G., and Soil, P. D. J. (2007). Silicon-mediated changes of some physiological and enzymatic parameters symptomatic for oxidative stress in spinach and tomato grown in sodic-B toxic soil. *J. Plant Physiol*. 164, 807–811. doi: 10.1016/j.jplph.2006.07.011

Hajiboland, R., and Hasani, B. D. (2007). Responses of antioxidant defense capacity and photosynthesis of bean (*Phaseolus vulgaris* L.) plants to copper and manganese toxicity under different light intensities. *Acta Biol. Szegedien*. 51, 93–106.

Hajiboland, R., Moradtalab, N., Eshaghi, Z., and Feizy, J. (2017). Effect of silicon supplementation on growth and metabolism of strawberry plants at three developmental stages. *N.Z. J. Crop Horticult. Sci.* 46, 144–161. doi: 10.1080/01140671.2017.1373680

Hajiboland, R., Sadeghzadeh, N., and Sadeghzadeh, B. (2014). Effect of Se application on photosynthesis, osmolytes and water relations in two durum wheat (*Triticum durum* L.) genotypes under drought stress. *Acta Agric. Slov*. 103, 167–179. doi: 10.14720/aas.2014.103.2.2

Harinasut, P., Poonsopa, D., Roengmongkol, K., and Charoensataporn, R. (2003). Salinity effects on antioxidant enzymes in mulberry cultivar. *Sci. Asia* 29, 109–113. doi: 10.2306/scienceasia1513-1874.2003.29.109

He, Y., Xiao, H., Wang, H., Chen, Y., and Yu, M. (2010). Effect of silicon on chilling–induced changes of solutes, antioxidants, and membrane stability in seashore paspalum turfgrass. *Acta Physiol. Plant*. 32, 487–494. doi: 10.1007/s11738-009-0425-x

Hernandez–Apaolaza, L. (2014). Can silicon partially alleviate micronutrient deficiency in plants? a review. *Planta* 240, 447–458. doi: 10.1007/s00425-014-2119-x

Horváth, E., Szalai, G., and Janda, T. (2007). Induction of abiotic stress tolerance by salicylic acid signaling. *J. Plant Growth Regul.* 26, 290–300. doi: 10.1007/s00344-007-9017-4

Hu, Y., Jiang, Y., Han, X., Wang, H., Pan, J., and Yu, D. (2017). Jasmonate regulates leaf senescence and tolerance to cold stress: crosstalk with other phytohormones. *J. Exp. Bot.* 68, 1361–1369. doi: 10.1093/jxb/erx004

Hund, A., Fracheboud, Y., Soldati, A., Frascaroli, E., Salvi, S., and Stamp, P. (2004). QTL controlling root and shoot traits of maize seedlings under cold stress. *Theor. Appl. Genet.* 109, 618–629. doi: 10.1007/s00122-004-1665-1

Imran, M., Kolla, M., Römheld, V., and Neumann, G. (2015). Impact of nutrient seed priming on germination, seedling development, nutritional status and grain yield of maize. *J. Plant Nutr.* 38, 1803–1821. doi: 10.1080/01904167.2014.990094

Imran, M., Mahmood, A., Römheld, V., and Neumann, G. (2013). Nutrient seed priming improves seedling development of maize exposed to low root zone temperatures during early growth. *Eur. J. Agron.* 49, 141–148. doi: 10.1016/j.eja.2013.04.001

Inal, A., Pilbeam, D. J., and Gunes, A. (2009). Silicon increases tolerance to boron toxicity and reduces oxidative damage in Barley. *J. Plant Nutr.* 32, 112–128. doi: 10.1080/01904160802533767

Jeon, J., Kim, N. Y., Kim, S., Kang, N. Y., Novák, O., Ku, S. J., et al. (2010). A subset of cytokinin two component signaling system plays a role in cold temperature stress response in Arabidopsis. *J. Biol. Chem.* 285, 23371–23386. doi: 10.1074/jbc.M109.096644

Kasper, T. C., and Bland, W. L. (1992). Soil temperature and root growth. *Soil Sci.* 154, 290–299. doi: 10.1097/00010694-199210000-00005

Kramer, P. J., and Boyer, J. S. (1995). *Water Relations of Plants and Soils*. San Diego, CA: Academic Press.

Kumar, S., Kaur, G., and Nayyar, H. (2008). Exogenous application of abscisic acid improves cold tolerance in chickpea (*Cicer arietinum* L.). *J. Agron. Crop Sci.* 194, 449–456. doi: 10.1111/j.1439-037X.2008.00335.x

Li, H., and Zhang, W. (2012). Abscisic acid–induced chilling tolerance in maize seedlings is mediated by nitric oxide and associated with antioxidant system. *Adv. Mater. Res.* 2011, 423–427. doi: 10.4028/www.scientific.net/AMR.378-379.423

Liang, Y., Chen, Q. I. N., Liu, Q., Zhang, W., and Ding, R. (2003). Exogenous silicon (Si) increases antioxidant enzyme activity and reduces lipid peroxidation in roots of salt-stressed barley (*Hordeum vulgare* L.). *J. Plant Physiol.* 160, 1157–1164. doi: 10.1078/0176-1617-01065

Liang, Y., Nikolic, M., Bélanger, R., Gong, H., and Song, A. (2015). *Silicon–Mediated Tolerance to Drought and Low–Temperature Stress, Silicon in agriculture.* Dordrecht: Springer Science+Business media.

Liang, Y., Zhu, J., Li, Z., Chu, G., Ding, Y., and Botany, Z. J. (2008). Role of silicon in enhancing resistance to freezing stress in two contrasting winter wheat cultivars. *Environ. Exp. Bot.* 64, 286–294. doi: 10.1016/j.envexpbot.2008.06.005

Liu, J. J., Lin, S. H., Xu, P. L., Wang, X. J., and in China, B. J. G. (2009). Effects of exogenous silicon on the activities of antioxidant enzymes and lipid peroxidation in chilling-stressed cucumber leaves. *Agric. Sci. Chin.* 8, 1075–1086. doi: 10.1016/S1671-2927(08)60315-6

Lutts, S., Benincasa, P., LWojtyla, L., Kubala, S., Pace, R., Lechowska, K., et al. (2016). "Seed priming: new comprehensive approaches for an old empirical technique," in *New Challenges in Seed Biology–Basic and Translational Research Driving Seed Technology*, eds S. Araujo and A. Balestrazzi (InTechOpen), 1–40.

Maksimovic, J. D., Bogdanovic, J., Maksimovic, V., and Nikolic, M. (2007). Silicon modulates the metabolism and utilization of phenolic compounds in cucumber (*Cucumis sativus* L.) grown at excess manganese. *J. Plant Nutr. Soil Sci.* 170, 739–744. doi: 10.1002/jpln.200700101

Maruyama, K., Urano, K., Yoshiwara, K., Morishita, Y., Sakurai, N., Suzuki, H., et al. (2014). Integrated analysis of the effects of cold and dehydration on rice metabolites, phytohormones, and gene transcripts. *Plant Physiol.* 164, 1759–1771. doi: 10.1104/pp.113.231720

Miura, K., and Furumoto, T. (2013). Cold signaling and cold response in plants. *Int. J. Mol. Sci.* 14, 5312–5337. doi: 10.3390/ijms14035312

Mudra, A. (1958). *Statistische Methoden für landwirtschaftliche Versuche*. Berlin: Paul Parey Verlag.

Muldoon, D. K., Wheeler, J. L., and Pearson, C. J. (1984). Growth mineral composition and digestibility of maize sorghum and barnyard millets at different temperatures. *Aust. J. Agric. Res.* 35, 367–368. doi: 10.1071/AR9840367

Nkebiwe, P. M., Weinmann, M., Bar-Tal, A., and Müller, T. (2016). Fertilizer placement to improve crop nutrient acquisition and yield: a review and meta-analysis. *Field Crops Res.* 196, 389–401. doi: 10.1016/j.fcr.2016.07.018

Pandey, S. K., and Singh, H. (2011). A simple, cost–effective method for leaf area estimation. *J. Bot.* 2011:658240. doi: 10.1155/2011/658240

Panico, A. M., Garufi, F., Nitto, S., Di Mauro, R., Longhitano, R. C., Magrì, G., et al. (2009). Antioxidant activity and phenolic content of strawberry genotypes from *Fragaria x ananassa*. *Pharm. Biol.* 47, 203–208. doi: 10.1080/13880200802462337

Park, C. H., Yeo, H. J., Park, Y. J., Morgan, A. M., Valan Arasu, M., Al–Dhabi, N. A., et al. (2017). Influence of indole−3–acetic acid and gibberellic acid on phenylpropanoid accumulation in common buckwheat (*Fagopyrum esculentum* Moench) sprouts. *Molecule* 22:E374. doi: 10.3390/molecules22030374

Pascual, M. B., Echevarria, V., Gonzalo, M. J., and Hernández–Apaolaza, L. (2016). Silicon addition to soybean (*Glycine max* L.) plants alleviate zinc deficiency. *Plant Physiol. Biochem.* 108, 132–138. doi: 10.1016/j.plaphy.2016.07.008

Pavlovic, J., Samardzic, J., Kostic, L., Laursen, K. H., Natic, M., Timotijevic, G., et al. (2016). Silicon enhances leaf remobilization of iron in cucumber under limited iron conditions. *Ann. Bot.* 118, 271–280. doi: 10.1093/aob/mcw105

Pavlovic, J., Samardzic, J., Maksimović, V., Timotijevic, G., Stevic, N., Laursen, K. H., et al. (2013). Silicon alleviates iron deficiency in cucumber by promoting mobilization of iron in the root apoplast. *New Phytol.* 198, 1096–1107. doi: 10.1111/nph.12213

Pei, Z. F., Ming, D. F., Liu, D., Wan, G. L., Geng, X. X., Gong, H. J., et al. (2010). Silicon Improves the tolerance to water-deficit stress induced by polyethylene glycol in wheat (*Triticum aestivum* L.) seedlings. *J. Plant Growth Regul.* 29, 106–115. doi: 10.1007/s00344-009-9120-9

Plessi, M., Bertelli, D., and Albasini, A. (2007). Distribution of metals and phenolic compounds as a criterion to evaluate variety of berries and related jams. *Food Chem.* 100, 419–427. doi: 10.1016/j.foodchem.2005.09.018

Ross, J. J., O'Neill, D. P., Wolbang, C. M., Symons, G. M., and Reid, J. B. (2001). Auxin–Gibberellin interactions and their role in plant growth. *J. Plant Growth Regul.* 20, 336–353. doi: 10.1007/s003440010034

Saeidnejad, A. H., Pouramir, F., and Naghizedek, M. (2012). Improving chilling tolerance of maize seedlings under cold conditions by spermine application. *Not. Sci. Biol.* 4, 110–117. doi: 10.15835/nsb437554

Sekimoto, H., Hoshi, M., Nomura, T., and Yokota, T. (1997). Zinc deficiency affects the levels of endogenous gibberellins in *Zea mays*. *Plant Cell Physiol.* 38, 1087–1090. doi: 10.1093/oxfordjournals.pcp.a029276

Shi, Y., Tian, S., Hou, L., Huang, X., Zhang, X., Guo, H., et al. (2012). Ethylene signaling negatively regulates freezing tolerance by repressing expression of CBF and type–A ARR genes in Arabidopsis. *Plant Cell* 24, 2578–2595. doi: 10.1105/tpc.112.098640

Shibasaki, K., Uemura, M., Tsurumi, S., and Rahman, A. (2009). Auxin response in Arabidopsis under cold stress: underlying molecular mechanisms. *Plant Cell* 21, 3823–3838. doi: 10.1105/tpc.109.069906

Sowinski, P., Richner, W., Soldati, A., and Stamp, P. (1998). Assimilate transport in maize (*Zea mays* L.) seedlings at vertical low temperature gradients in the root zone. *J. Exp. Bot.* 49, 747–752. doi: 10.1093/jxb/49.321.747

Stevic, N., Korac, J., Pavlovic, J., and Nikolic, M. (2016). Binding of transition metals to monosilicic acid in aqueous and xylem (*Cucumis sativus* L.) solutions: a low–T electron paramagnetic resonance study. *Biometals* 29, 945–951. doi: 10.1007/s10534-016-9966-9

Suge, H., Takahashi, S., Arita, S., and Takaki, H. (1986). Gibberellin relationships in zinc–deficient plants. *Plant Cell Physiol.* 27, 1005–1012. doi: 10.1093/oxfordjournals.pcp.a077183

Szabados, L., and Savouré, A. (2010). Proline: a multifunctional amino acid. *Trends Plant Sci.* 15, 89–97. doi: 10.1016/j.tplants.2009.11.009

Szalai, G., Pál, M., and Janda, T. (2011). Abscisic acid may alter the salicylic acid–related abiotic stress response in maize. *Acta Biol. Szeg.* 55, 155–157.

Wan, X., Zwiazek, J. J., Lieffers, V. J., and Landhäusser, M. (2001). Hydraulic conductance in aspen (*Populus tremuloides*) seedlings exposed to low root temperatures. *Tree Physiol.* 21, 691–696. doi: 10.1093/treephys/21.10.691

Wang, J., Tan, X., Liu, F., Zhang, H., Fu, C., and Wang, Y. (2012). Effects of zinc deficiency stress on the antioxidative capability and plant hormone level of the different apple rootstocks. *Acta Hortic. Sin.* 39, 1429–1436.

Wang, M., Zheng, Q., Shen, Q., and Guo, S. (2013). The critical role of potassium in plant stress response. *Int. J. Mol. Sci.* 14, 7370–7390. doi: 10.3390/ijms14047370

Yemm, E. W., and Willis, A. J. (1954). The estimation of carbohydrates extracts by anthrone. *Biochem. J.* 57, 508–514. doi: 10.1042/bj0570508

Conflict of Interest Statement: The authors declare that the research was conducted in the absence of any commercial or financial relationships that could be construed as a potential conflict of interest.

frontiers in Plant Science

ORIGINAL RESEARCH
published: 03 July 2018
doi: 10.3389/fpls.2018.00910

Expression of the Intracellular COPT3-Mediated Cu Transport Is Temporally Regulated by the TCP16 Transcription Factor

Nuria Andrés-Colás[1†], Angela Carrió-Seguí[1], Salah E. Abdel-Ghany[2], Marinus Pilon[2] and Lola Peñarrubia[1]*

[1] Departament de Bioquímica i Biologia Molecular, Estructura de Recerca Interdisciplinar en Biotecnologia i Biomedicina, Universitat de València, Valencia, Spain, [2] Department of Biology, Colorado State University, Fort Collins, CO, United States

Copper is an essential element in plants. When scarce, copper is acquired from extracellular environment or remobilized from intracellular sites, through members of the high affinity copper transporters family COPT located at the plasma membrane and internal membrane, respectively. Here, we show that COPT3 is an intracellular copper transporter, located at a compartment of the secretory pathway, that is mainly expressed in pollen grains and vascular bundles. Contrary to the COPT1 plasma membrane member, the expression of the internal *COPT3* membrane transporter was higher at 12 h than at 0 h of a neutral photoperiod day under copper deficiency. The screening of a library of conditionally overexpressed transcription factors implicated members of the TCP family in the COPT3 differential temporal expression pattern. Particularly, *in vitro*, TCP16 was found to bind to the *COPT3* promoter and down-regulated its expression. Accordingly, *TCP16* was mainly expressed at 0 h under copper deficiency and induced at 12 h by copper excess. Moreover, *TCP16* overexpression resulted in increased sensitivity to copper deficiency, whereas the *tcp16* mutant was sensitive to copper excess. Both copper content and the expression of particular copper status markers were altered in plants with modified levels of *TCP16.* Consistent with TCP16 affecting pollen development, the lack of COPT3 function led to altered pollen morphology. Furthermore, analysis of *copt3* and *COPT3* overexpressing plants revealed that COPT3 function exerted a negative effect on *TCP16* expression. Taken together, these results suggest a differential daily regulation of copper uptake depending on the external and internal copper pools, in which TCP16 inhibits copper remobilization at dawn through repression of intracellular transporters.

Keywords: copper transport, COPT3, heavy metals, TCP16, transcriptional regulation

OPEN ACCESS

Edited by:
Manuel González-Guerrero, Universidad Politécnica de Madrid (UPM), Spain

Reviewed by:
Crysten Elizabeth Blaby-Haas, Brookhaven National Laboratory (DOE), United States
Marc Hanikenne, University of Liège, Belgium

****Correspondence:***
Lola Peñarrubia
penarrub@uv.es

†Present address:
Nuria Andrés-Colás, Departamento de Biotecnología, Universitat Politècnica de València, Valencia, Spain

Specialty section:
This article was submitted to Plant Nutrition, a section of the journal Frontiers in Plant Science

Received: *28 March 2018*
Accepted: *08 June 2018*
Published: *03 July 2018*

Citation:
Andrés-Colás N, Carrió-Seguí A, Abdel-Ghany SE, Pilon M and Peñarrubia L (2018) Expression of the Intracellular COPT3-Mediated Cu Transport Is Temporally Regulated by the TCP16 Transcription Factor. Front. Plant Sci. 9:910. doi: 10.3389/fpls.2018.00910

INTRODUCTION

Copper (Cu) is an essential micronutrient for the growth and development of aerobic organisms. Under metal deficiency, Cu^+ is incorporated through high affinity COPper Transporters, denoted COPTs in plants (Kampfenkel et al., 1995; Sancenón et al., 2003; Puig, 2014; Peñarrubia et al., 2015) and referred to as CTR (SLC31) in other organisms (Kim et al., 2013). In *Arabidopsis thaliana*, the COPT family can be divided into two subfamilies: the plasma membrane members

COPT1, COPT2, and COPT6 (pmCOPT), which are transcriptionally induced under Cu deficiency (Sancenón et al., 2004; Garcia-Molina et al., 2013; Perea-García et al., 2013), and the members located in internal membranes COPT3 and COPT5 (imCOPT), which are not clearly induced by Cu deficiency (Sancenón et al., 2003; Garcia-Molina et al., 2011; Klaumann et al., 2011). This subdivision might distinguish at least two Cu^+ sources in the cells (external and internal), differentially mobilized based on the type of COPT activated.

The transcriptional response to Cu deficiency is mainly orchestrated by the transcription factor (TF) SQUAMOSA PROMOTER BINDING PROTEIN-LIKE7 (SPL7) through binding to GTAC motifs in the promoters of target genes, such as *pmCOPT* (Yamasaki et al., 2009; Bernal et al., 2012). Thus, pmCOPT-mediated cytosolic Cu^+ uptake from the extracellular environment is highly increased by SPL7 under Cu deficiency. It has been suggested that the SPL7-mediated auto-regulatory effect of Cu on *pmCOPT* expression could establish a feedback loop responsible for cyclic expression, peaking at dawn (Andrés-Colás et al., 2010; Peñarrubia et al., 2010). Deregulated Cu^+ uptake in COPT-overexpressing plants causes abnormal development in the absence of environmental cycles (Andrés-Colás et al., 2010; Perea-García et al., 2016a,b). Furthermore, the observed interaction between SPL7 and ELONGATED HYPOCOTYL5 (HY5) underscores a connection between Cu homeostasis and light (Zhang et al., 2014).

In yeast, it has been shown that, due to the Cu^+ toxicity, practically no free Cu^+ is found in the cytosolic compartment (Rae et al., 1999). Therefore, pmCOPT-mediated Cu^+ uptake is probably coupled to cupro-chaperone-mediated delivery to different protein targets, among them the P-type ATPase RESPONSIVE-TO-ANTAGONIST1 (RAN1) located at the endoplasmic reticulum (ER) where it pumps Cu^+ into the lumen (Hirayama et al., 1999). SPL7 presents an operative transmembrane domain that allow his localization at the endomembrane system, most likely the ER. During ER stress, as a result of Cu deficiency, SPL7 localizes in the nucleus to modulate the Cu deficiency responses, after activation by proteolytic cleavage. In this sense, SPL7 could function as a double Cu sensor in both the nucleo-cytoplasm and the ER lumen (Garcia-Molina et al., 2014).

With regard to the imCOPT-mediated Cu^+ transport from internal sources, COPT5 plays an important role in the plant response to severe environmental Cu scarcity (Garcia-Molina et al., 2011; Klaumann et al., 2011). COPT5 functions in remobilizing Cu from prevacuolar vesicles, which could act as internal stores or recycling vesicles to provide the metal to key Cu-dependent processes such as photosynthesis (Garcia-Molina et al., 2011; Klaumann et al., 2011; Carrió-Seguí et al., 2015). Little is known about the function of COPT3. COPT3 has been classified as a member of the imCOPT subfamily based on its partial complementation of the respiratory and Cu transport defect exhibited by a *ctr1*Δ*ctr3*Δ yeast mutant (Sancenón et al., 2003; Garcia-Molina et al., 2013). Apparently, *imCOPT* expression is not affected by Cu and temporal factors modulating *imCOPT* expression remain unexplored.

The TCP (named after TEOSINTE BRANCHED 1, CYCLOIDEA and PROLIFERATING CELL FACTOR 1) protein family precisely orchestrates spatial and temporal plant responses to both environmental and endogenous factors (Martín-Trillo and Cubas, 2010; Kieffer et al., 2011; Li, 2015; Danisman, 2016; Dhaka et al., 2017). The TCP family is constituted by plant-specific TFs that share a conserved non-canonical basic helix–loop–helix (bHLH) DNA binding domain, termed TCP domain (Cubas et al., 1999). The TCP members, are grouped into two subfamilies, based on the TCP domain structure and their roles (Cubas et al., 1999). These subfamilies are denoted as class I or PROLIFERATING CELL FACTOR (PCF) and class II, which is divided in CINCINNATA (CIN) and CYCLOIDEA (CYC)/(TEOSINTE BRANCHED 1) TB1 proteins. TCPs bind *cis*-acting regulatory elements (CAREs) known as site II, in the promoter regions of various genes. CAREs come in two classes: class I (GTGGGNCC) and class II (GTGGNCCC), which have different but similar binding preferences (Kosugi and Ohashi, 2002; Viola et al., 2012). The peculiar class I member TCP16 is an exception with preference for class II binding site since it contains Asp instead of Gly at a key discriminatory position (Uberti-Manassero et al., 2016).

A key mechanism underlying temporal control is the circadian clock. Among the central Arabidopsis clock components are the TFs CIRCADIAN CLOCK-ASSOCIATED 1 (CCA1) and LATE ELONGATED HYPOCOTYL (LHY) (for a review, see Nohales and Kay, 2016). Some TCP members interact with different components of the core circadian clock as shown in both yeast two-hybrid and protein–protein interaction assays (Giraud et al., 2010), which indicates that the TCP family is intricately linked to circadian regulation of gene expression in Arabidopsis. TCP21, termed CHE (for CCA1 Hiking Expedition), binds TOC1 (timing of CAB expression 1), which provides an explanation of how TOC1 can regulate expression of *CCA1*, as TOC1 lacks a DNA binding domain (Pruneda-Paz et al., 2009). Moreover, the concomitant binding of TCP20/TCP22 and LWD1 (LIGHT-REGULATED WD1) to the *CCA1* promoter activates its expression at dawn (Wu et al., 2016). Furthermore, TCPs appear to link the diurnal changes in mitochondrial function, particularly in genes encoding components of the oxidative phosphorylation machinery, with transcriptional changes that are regulated and integrated with the central clock function. This provides a molecular link between cellular and organelle metabolic activity and the circadian clock in plants (Palatnik et al., 2003; Welchen and Gonzalez, 2006; Giraud et al., 2010; Danisman, 2016).

Other developmental plant process that requires a TCP-mediated precise spatial and temporal control is the regulation of floral organ development, including secondary cell wall thickening necessary to release pollen grains. This developmental program is under the precise control of TCP24, which functions as a negative regulator (Wang et al., 2015). Moreover, the inhibition of the TCP16 function results in abortion of early pollen development (Takeda et al., 2006). In rice, class I TCP genes have been mainly implicated in stress adaptation, such as salinity tolerance (Almeida et al., 2017) or cold stress (Wang et al., 2014). OsTCP19 facilitates abiotic stress

tolerance by manipulating the abscisic acid (ABA) signaling network (Mukhopadhyay and Tyagi, 2015). The wide crosstalk between TCP and hormones has been recently summarized (Nicolas and Cubas, 2016).

Environmental signals, such as nutrient availability, also lead to TCP-mediated regulation. In this sense, TCP20 and NIN-like proteins (NLP6 and NPL7) are involved in nitrate availability responses (Guan et al., 2014, 2017). This is only an example of the high range of TCPs interactions with other TFs (Bemer et al., 2017). These multiple interactions highlight the central role of TCPs in plant molecular networks that integrate environmental and endogenous processes in plants (Danisman, 2016; Dhaka et al., 2017). Metal availability is a key environmental factor under precise temporal control intricately linked with the circadian clock (Andrés-Colás et al., 2010; Hermans et al., 2010; Chen et al., 2013; Hong et al., 2013; Salomé et al., 2013). In this regard, it has been shown that TCP20 transcriptionally repress the expression of the subgroup Ib of bHLH TFs, previously implicated in iron homeostasis (Wang et al., 2007). Moreover, these TFs are up-regulated in the transition from cell proliferation to cell expansion during sink-source transitions (Andriankaja et al., 2014).

Although the activation of Cu^+ uptake through the pmCOPT transporters under Cu deficiency by SLP7 is a well-established process (Yamasaki et al., 2009; Bernal et al., 2012), their temporal control, as well as the transcriptional regulation of imCOPTs, *COPT3* and *COPT5*, remain unsolved. In this work, we have identified TCP16 as a TF that, besides SPL7, could participate in Cu homeostasis via temporal modulation of gene expression in Arabidopsis.

MATERIALS AND METHODS

Plant Growth Conditions and Treatments

A. thaliana plants, ecotype Col 0, and the transgenic lines indicated in Supplementary Table SI were grown as previously described (Andrés-Colás et al., 2010). The half-strength Murashige and Skoog (½ MS) medium was either commercial (Sigma) or prepared in the laboratory as follows: macronutrients 12.5 ml (NH_4NO_3 825 mg/l, KNO_3 950 mg/l, $MgSO_4{\cdot}7H_2O$ 90.35 mg/l, KH_2PO_4 85 mg/l, and $CaCl_2$ 166.25 mg/l), micronutrients 0.5 ml (H_3BO_3 3.1 mg/l, $MnSO_4{\cdot}H_2O$ 8.45 mg/l, $ZnSO_4{\cdot}7H_2O$ 4.3 mg/l, $NaMoO_4{\cdot}2H_2O$ 0.125 mg/l, and $CoCl_2{\cdot}6H_2O$ 0.0125 mg/l), Fe-EDTA 2.5 ml ($FeSO_4{\cdot}7H_2O$ 13.9 mg/l and $Na_2EDTA{\cdot}2H_2O$ 18.63 mg/l), KI 1.1 ml (0.41 mg/l), in both cases supplemented with MES 0.5 g/l, sucrose 10 g/l, agar 8 g/l, pH 5.7 with KOH. Variable $CuSO_4$ concentrations were added when indicated. Media were supplemented with 100 μM BCS for the Cu-deprived media.

A *COPT3* promoter (*COPT3p*), covering 1,248 bp upstream from the start codon, was fused to the *uidA* (*GUS*) reporter gene (*COPT3p:GUS*) by substitution of the *CaMV35S* promoter in the pBI121 vector. At least two independent transgenic *Arabidopsis* stable homozygous lines harboring the *COPT3p:GUS* chimeric construct were obtained and analyzed.

The phenotype of two independent TRANSPLANTA (TPT) TPT TCP16 lines (Coego et al., 2014) was analyzed on ½ MS medium with 100 μM BCS, with or without 2 μM β-estradiol after germinating on ½ MS medium 2 days or for the indicated period, and under long (16 h light-23°C/8 h dark-16°C) or neutral (12 h light-23°C/12 h dark-16°C) photoperiod conditions, as indicated. For the gene expression analysis by RT-qPCR of TPT TCP16 lines, plants were grown directly with 2 μM β-estradiol. For this expression analysis, one TPT TCP16 line was used and compared to the wild-type. Samples were collected at 0, 12, or 24 h from plants grown under neutral conditions (0 or 24 h, start of light; 12 h, end of light), as indicated.

For the genotyping of the T-DNA insertion lines, plants were self-pollinated and homozygous lines were obtained. PCR (Supplementary Table SIV) or RT-qPCR (Supplementary Table SV) were performed with specific oligonucleotides to genotype or check the loss of expression in the lines, respectively. For the *tcp16* mutant, one line was analyzed and compared to the previously obtained TCP16 RNAi line. For the *copt3* mutant, one line was analyzed and compared to the COPT3-HA overexpressing line. For the *copt5* mutant, one of the previously characterized lines was used as a control for sensitivity to Cu deficiency.

Electrophoretic Mobility Shift Assay (EMSA)

Biotin-labeled and unlabeled oligonucleotides (Supplementary Table SII), including the putative TCP binding motifs of *COPT3* and *COPT5* promoters, and a fragment of the *COPT2* promoter (without TCP binding motifs), were synthetized (VWR) and annealed in TEN buffer (10 mM Tris Base pH 7.8, 1 mM EDTA, 0.1 M NaCl) to generate the probes. The purified TCP16 and TCP23 proteins were obtained from the TRANSPLANTA consortium (Coego et al., 2014). Briefly, full-length *TCP16* and *TCP23* expression constructs were cloned in the destination vector pER8 and mobilized into pDONR201 using BP clonase reaction. cDNAs were transferred to destination vector pDEST-TH1 using LR clonase, yielding Maltose Binding Proteins (MBP) N-terminal fusions and constructs checked by sequencing. MBP-TCP16 and MBP-TCP23 constructs were transformed into BL-21 strain for expression. Induction of bacterial cultures was routinely at 25°C for 6 h with 1 mM Isopropyl β-D-1-thiogalactopyranoside. Expression of recombinant proteins was assessed by Western blot with an anti MBP antibody (BioLab) (Franco-Zorrilla et al., 2014). MBP-TCP16 and MBP-TCP23 proteins were bound to an amylose resin and eluted using maltose. EMSA was carried out with 960–1320 ng of purified protein, 0.01 pmol labeled probe and 225x unlabeled probe, as indicated, in binding buffer in 10 μl of total reaction volume. Protein buffer (2x TEN, 1 mM DTT, 1 mM protease inhibitor). Binding buffer (20 mM HEPES-KOH pH 7.8, 100 mM KCl, 1 mM EDTA, 0.1% BSA, 10 ng salmon sperm DNA, 10% glycerol). Binding reaction was performed at room temperature for 30 min. Electrophoresis was performed at 32 V on ice in a pre-run 5% native polyacrylamide gel in TBE buffer. Transfer was performed onto a nylon membrane at 40 V for 2 h on ice. Membrane crosslinking was at 120

mJ/cm^2 45–60 s at 254 nm in Stratalinker. Streptavidin-HRP conjugate antibody (Pr.Nr.21126, Pierce) was used for detection of the labeled probe. Relative bound DNA was quantified using ImageJ 1.42q software[1]. The experiment was repeated at least two independent times.

Biochemical Fractionation

Plants overexpressing the COPT3-HA fusion protein (Andrés-Colás et al., 2010) were grown on soil. Chloroplasts were isolated and fractionated into stroma and thylakoids from leaves of 3- to 4-week-old plants as described (Pilon-Smits et al., 2002). Samples were normalized based on the number of chloroplasts and chlorophyll content, as determined by the method of Bruinsma (1961) as described (Pilon-Smits et al., 2002). Proteins were quantified by Bradford (1976) assay and separated by native 15% PAGE and then blotted on a nitrocellulose membrane. Immunodetection of SEC12, CpNifS, and PC was used as control of ER, stroma and thylakoids proteins with specific antiserum (Bar-Peled and Raikhel, 1997; Pilon-Smits et al., 2002; Abdel-Ghany et al., 2005). COPT3-HA was detected with anti-HA 3F10 specific antibody (Roche).

For sucrose density gradient fractionation the leaves of 4-week-old plants were ground with mortar and pestle in membrane isolation buffer [20 mM HEPES-KOH, pH 7; 50 mM $C_2H_3KO_2$; 5 mM EDTA; 250 mM sorbitol, 1 mM DTT plus Complete^{TM} protease inhibitor cocktail (Roche)] and centrifuged at 2,000 × *g* for 10 min at 4°C. 3 ml of the supernatant were applied to the top of continuous 10 ml 20–60% (w/v) sucrose gradients, either with or without 5 mM $MgCl_2$ added and centrifuged at 150,000 × *g* for 3 h at 4°C. Fractions of 0.5 ml were taken from the top and concentrated with TCA. The proteins in the fractions were electrophoresed in 12.5% SDS-PAGE, blotted and immunodetected using antibodies against the HA epitope (3F10, Roche), the ER SEC12, the plasma membrane α-AHA and the mitochondrial PMO35 markers, as described above.

Subcellular Localization in *Arabidopsis* Protoplasts

The complete *COPT3* coding sequence was obtained from *Arabidopsis* genomic DNA by PCR using the following specific primers, which introduce the adequate restriction sites for cloning: C3-SalI F, 5′ CCACGCGTCG ACATGAACGGCATGAGTGGATC; C3-NcoI R, 5′ CCATG CCATGGAACAATGTGATTGAACCTCGG. The C-terminus was fused with the GFP reporter and its expression was controlled by the constitutive CaMV35S promoter through its insertion into the transient expression vector pGFPau with the SpeI and SalI restriction enzymes.

The *COPT3-GFP* construct was used to transform *Arabidopsis* protoplasts obtained from the fresh leaf tissue of 3-week-old plants grown on soil, as previously described (Abdel-Ghany et al., 2005). After 16 h under continuous light at 23°C in the wash solution, confocal images were obtained using a fluorescence confocal microscope TCS SP vertical (DM-R) (Leica) equipped with an argon ion (458 and 488 nm), He-Ne I (543 nm) and He-Ne II (633 nm) excitation laser systems and a 60× objective lens. The fluorescence signals were detected at 500–530 nm for GFP and at 650–750 nm for chlorophyll, after exciting at 488 and 633 nm, respectively.

GUS Staining and Pollen Preparations for Scanning Electron Microscopy

Assays were performed as described (Jefferson et al., 1987). Briefly, the organs were embedded with the substrate solution [100 mM $NaPO_4$ pH 7.2, 0.5 mM $K_3Fe(CN)_6$, 0.5 mM $K_4Fe(CN)_6$, 0.1% (v/v) Triton X-100, 0.5 mM 5-bromo-4-chloro-3-indolyl-β-D-glucuronide (X-Gluc, AppliChem) and 10 mM EDTA pH 7.2]. Reactions took place at 37°C.

Pollen was mounted on standard stubs and coated with gold-palladium in a Bio-Rad E5600 ion sputter for 3 min prior to observation on a Hitachi S4100 FE scanning electron microscope. Digital images were acquired with the application EMIP.

Cu Content Measurements

Cu content was determined by atomic absorption as described (Andrés-Colás et al., 2006; Carrió-Seguí et al., 2015) at the "*Servei Central de Suport a la Investigació Experimental SCSIE*" (Universitat de València) and the "*Servicios Centrales de Investigación*" (Universidad de Almería).

Gene Expression by RT-PCR

Total RNA was isolated from *A. thaliana* seedlings with trizol reagent (Ambion). RNA was quantified by UV spectrophotometry and its integrity was visually assessed on ethidium bromide-stained agarose gels. Total RNA (1.5 μg) was first converted into cDNA by reverse transcription (RT) using SuperScript II reverse transcriptase (Invitrogen) and anchored oligo$(dT)_{15}$ (Roche) and 18S reverse primer. PCR was performed under the following conditions to maintain a linear response in the range of the cDNA concentrations used (see Supplementary Table SIV for the primer-specific sequences): 30 cycles, except 20 cycles for *18S*, of three temperature segments of 30 s (Td 94°C/Th 55°C/Te 72°C). The PCR products were visualized in 2% agarose gels. Real-time PCRs (qPCR) were carried out with *SYBR-Green qPCR Super-Mix-UDG* with *ROX* (Invitrogen) and specific oligonucleotides (Supplementary Table SV) in a *StepOnePlus Real-Time PCR System* (Applied Biosystems) under 1 cycle of 95°C for 2 min and 40 cycles consisting in 95°C for 30 s and 60°C for 30 s. The results correspond to the comparative Ct (cycle threshold) method (ΔΔCt). The *UBQ10* gene was used as a loading control. Values are relative expression with respect to the first sample in each graph, in arbitrary units.

Computer-Assisted Sequence

The theoretical promoter sequences analysis was performed by Patmatch from TAIR[2].

[1] https://imagej.nih.gov/ij/

[2] www.arabidopsis.org

RESULTS

COPT3 Protein Was Intracellular Localized

The *COPT3* gene (At5g59040) is located on chromosome V of the *A. thaliana* genome, adjacent to *COPT1*. The two genes are organized head-to-head in opposite orientations separated by 2,266 bp (Supplementary Figure S1A). The *COPT3* gene encodes a 151 amino acid protein that displays features, which are conserved in COPT/CTR-type transport proteins. These conserved features include three transmembrane domains (TMDs) with an external amino terminus, containing a conserved Met residue and a cytosolic carboxy terminus, as well as the Mx_3M and the Gx_3G motifs within TMD2 and TMD3, respectively (Peñarrubia et al., 2010; Puig, 2014).

The 1.4 kb promoter region of the *COPT3* gene contains a number of potential *cis* regulatory elements (Supplementary Figure S1B). One of these is a putative plastid expression box at position −388. Sequence analysis of the coding region suggested that a putative transit sequence for targeting to the chloroplast may be present in COPT3 (*PSORT*[3]) (Supplementary Figure S1C). In order to analyze its subcellular localization, chloroplasts were isolated from an *Arabidopsis* transgenic line expressing the *COPT3* coding sequence tagged with the human influenza hemagglutinin (HA) epitope under the control of the *35S* cauliflower mosaic virus (*CaMV35S*) promoter (*COPT3-HA*) (Andrés-Colás et al., 2010). The analysis of isolated chloroplast fractions clearly indicated that COPT3 was not present in plastids (Supplementary Figures S2A,C).

Next, COPT3 subcellular localization was analyzed by transient expression in *Arabidopsis* protoplasts of the *COPT3* coding region tagged with the green fluorescence protein (GFP) under the control of the *CaMV35S* promoter (*COPT3-GFP*) (Supplementary Table SI). The signal obtained confirmed an intracellular localization of COPT3 excluding the plasma membrane and chloroplasts (**Figure 1A**). Moreover, sucrose density gradient fractionation of membranes from leaves of plants expressing the *COPT3-HA* construct indicated that the COPT3 distribution pattern is more similar to the ER protein marker SEC12 than to the other markers, such as the mitochondrial PMO35 protein or the plasma membrane α-AHA protein (Supplementary Figures S2B,D). These results point to a putative COPT3 localization in the endomembrane system, maybe in the ER.

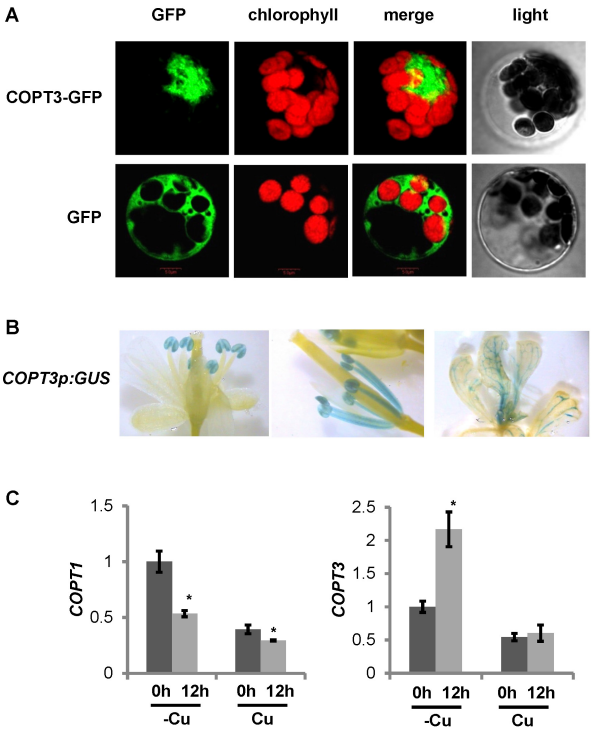

FIGURE 1 | COPT3 expression pattern and regulation by Cu. **(A)** COPT3 subcellular localization. *Arabidopsis* protoplasts isolated from 30-day-old leaves and transiently transformed with the *35S:COPT3-GFP* construct or the *35S:GFP* as a control, were analyzed by confocal microscopy at 16 h post transformation. Green and red fluorescence are indicative of the localization of the GFP protein and the chlorophyll, respectively. Representative protoplasts from at least two independent experiments are shown on the same scale, including their merged and light fields. **(B)** Histochemical β-glucuronidase staining of the *Arabidopsis* lines transformed with the *COPT3p:GUS* construct. A representative flower (left), mature anthers and filaments (middle) and seedling shoot (right) from at least two independent lines are shown. **(C)** *COPT1* and *COPT3* temporal expression pattern and regulation by Cu. Seven-day-old wild-type seedlings grown under Cu deficiency (1/2 MS with 100 μM BCS; –Cu) and Cu sufficiency conditions (1/2 MS with 1 μM $CuSO_4$; Cu). Samples were taken at 0 h (dark bars) and 12 h (light bars) of the 12 h light/12 h dark cycle. Total RNA was extracted and analyzed by RT-qPCR with specific oligonucleotides for *COPT1* and *COPT3*. The relative expression in arbitrary units is represented. Values correspond to arithmetic means ($2^{-\Delta\Delta Ct}$) ± standard deviation from three biological replicates with three technical replicates for each ($n = 3$). Asterisks indicate significant differences for the same group of samples with respect to the 0 h sample ($P < 0.05$) according to *T*-test.

COPT3 Was Mainly Expressed in Pollen and Vascular Bundles

The analysis of the *COPT3* promoter (Supplementary Figure S1B) indicated the presence of several GTGA boxes (7), described in the late pollen *g10* gene promoter (Rogers et al., 2001). Additionally, one of the two co-dependent elements responsible for the pollen-specific activation of tomato *LAT52* gene (Bate and Twell, 1998), the AGAAA element, were present at multiple positions (12). There were also several boxes for expression in embryo (3), endosperm (4) and aleurone (2) (Supplementary Figure S1B).

In order to determine the tissue expression pattern of *COPT3* throughout the plant, we first performed RT-PCR analysis from various organs of adult plants. The result indicated that *COPT3* expression was detected in flowers and dried seeds, but also in stems and leaves, whereas it was hardly detectable in roots (Supplementary Figure S3A). These results were consistent with the Genevestigator database[4], which also indicated that overall

[3]https://psort.hgc.jp/

[4]https://genevestigator.com/gv/doc/intro_plant.jsp

levels of *COPT3* expression were low throughout the plant life cycle compared to other COPT family members.

To further study the *COPT3* spatial expression pattern, stable transgenic *Arabidopsis* lines harboring the *GUS* reporter gene driven by the *COPT3* promoter (*COPT3p:GUS*) were obtained (Supplementary Table SI). During the development of reproductive organs, GUS staining was observed in anthers with a strong signal in pollen (**Figure 1B**, left). Accordingly, GUS staining was detected in the stamen filaments only when the styles were elongating (**Figure 1B**, middle). Moreover, GUS staining was also detected in the leaf vascular bundles (**Figure 1B**, right).

COPT3 Expression Was Up-Regulated at Dusk and Down-Regulated by Cu

The *COPT3* promoter also displayed regulatory elements conserved in light regulated genes, denoted as I-box (GATAA), as well as an element (CAANNNNATC) required for the tomato *LHC* circadian expression and an Evening Element (AAAATATCT) involved in circadian regulation (Terzaghi and Cashmore, 1995; Harmer et al., 2000; Rawat et al., 2005) (Supplementary Figure S1B). Moreover, based on the DIURNAL DataBase[5] (Mockler et al., 2007), *COPT3* expression oscillated with a phase of around 24 h under different circadian and diurnal conditions and peaked at 12 h (end of light period) of the 12 h light/12 h dark neutral photoperiod cycle (Supplementary Figure S3B). Furthermore, it was previously shown that altered Cu transport, through *COPT1* and *COPT3* overexpression, affected circadian rhythms regulation (Andrés-Colás et al., 2010). Taken together, these data may indicate a *COPT3* temporal regulation. As a first approach to address its study, *COPT3* expression was tested at 0 and 12 h in 7-day-old seedlings grown on neutral photoperiod conditions. The result confirmed the higher *COPT3* expression at 12 h (end of the light period), opposite to *COPT1* expression that was higher at 0 h (start of the light period), under Cu deficiency (**Figure 1C**). This result confirmed our previous data on the temporal expression of other *pmCOPT* members, such as *COPT2* and *COPT6,* both peaking at dawn (Perea-García et al., 2016a), whereas the other *imCOPT*, *COPT5,* peaked at dusk (not shown). These data are also in agreement with data in the DIURNAL DataBase for the *pmCOPT* and *imCOPT* expression, where both subfamily member types oppositely oscillated during the diurnal cycle.

Moreover, the *COPT3* promoter displayed three putative Cu deficiency response elements (GTAC) (Supplementary Figure S1B), previously described in the promoters of Cu-deficiency regulated genes that may be target sites for SPL7 (Yamasaki et al., 2009; Bernal et al., 2012). Although *COPT3* expression was previously reported to be independent of the Cu levels (Sancenón et al., 2003), the presence of these elements suggested a possible up-regulation of *COPT3* under Cu deficiency. In order to check if *COPT3* was differentially regulated by Cu over day and night, samples of seedlings grown under Cu deficiency and excess were checked by RT-qPCR at 0 and 12 h (**Figure 1C**). *COPT3* expression was significantly increased under Cu deficiency, specifically at 12 h (end of the light period). Furthermore, a wide range of Cu concentrations were tested and, in general, higher *COPT3* expression levels were observed in Cu deficiency media when compared to Cu sufficiency or Cu excess (Supplementary Figure S3C). However, the temporal specific increase of *COPT3* expression under Cu deficiency at 12 h, did not correlate to the expression peak of SPL7 at 0 h (Perea-García et al., 2016a).

[5]http://diurnal.mocklerlab.org/

Two Independent TPT TCP16 Lines Were Sensitive to Cu Deficiency

In order to find regulatory factors involved in the temporal pattern of *COPT3* expression, a screen of a conditional overexpression TF library, denoted TRANSPLANTA (TPT) (Coego et al., 2014), was performed under Cu deficiency conditions. The TRANSPLANTA collection contains 634 *Arabidopsis* TFs transferred into a vector (pER8) that conferred a β-estradiol-inducible gene overexpression (Zuo et al., 2000). At least, two independent single insertion and homozygous transgenic lines were generated for each TF (Coego et al., 2014). Reporter lines under the same promoter (*pER8G:GUS-GFP*) were used to optimize the expression conditions in our experimental set up (Supplementary Figure S4A). The treatment with 2 μM β-estradiol induced reporter expression after 12 h and treatment with 100 μM BCS did not modify *GUS* expression (Supplementary Figure S4B). Based on these results, a screen was performed in 7-day-old seedlings germinated on ½ MS medium and then grown on 100 μM BCS with 2 μM β-estradiol. Afterward, seedlings were transferred to fresh plates containing 10 μM Cu and 2 μM β-estradiol for checking the recovery of root growth with the aim to discard lines with phenotypes unrelated to Cu deficiency. The *copt5* mutant line, which exhibited a defect in root elongation under Cu deficiency (Garcia-Molina et al., 2011) and WT seedlings were used as controls (Supplementary Figure S4C).

One of the TF families in the TPT lines with a higher percentage of the members showing a short root phenotype in the screen under Cu deficiency, which was reverted under high Cu, was the TCP family (not shown). The TRANSPLANTA collection contains TPT lines for 17 TCPs out of a total of 24 members present in the *Arabidopsis* genome. TPT lines from six of them (TCP14, TCP16, TCP19, TCP20, TCP22, and TCP24) displayed a short root phenotype under Cu deficiency, which reverted under high Cu (**Table 1**). All of them belong to the TCP class I PCF, except TCP24. It is noteworthy that most TCP factors display putative Cu deficiency responsive GTAC boxes in their proximal promoters (500 bp), except TCP4 and TCP17 (**Table 1**). Thus, TPT lines positive in the screening corresponded to TCPs that all contain GTAC boxes. Among them, TCP16 (At3g45150) was chosen for further study since the similar curly leaves phenotype found in plants where TCP16 was fused to a repressor domain (Uberti-Manassero et al., 2016) and in plants overexpressing *COPT1* and *COPT3* (Andrés-Colás et al., 2010; Garcia-Molina et al., 2013).

Two independent TPT TCP16 lines, TPT 3.45150.1B (TPT TCP16-B) and TPT 3.45150.1I (TPT TCP16-I) (Supplementary Table SI), were sensitive to Cu deficiency, as shown by a reduced root elongation (**Figure 2A**). The reduced root length

TABLE 1 | TCPs characteristics and screening results.

TCP	MIPS code	Class	Type	Transplanta	Screening	Class I CAREs GGNCCCAC TGGGCC GCCCR GG(A/T)CCC	Class II CAREs G(T/C)GGNCCC GGACCA	Other CARE versions	CuRE
TCP1	At1g67260	II	CYC/TB1	+	–			ATGGATCCAA	4*
TCP2	At4g18390	II	CIN	+	–	+		0	1
TCP3	At1g53230	II	CIN	–	N.D.			0	1
TCP4	At3g15030	II	CIN	–	N.D.	+		0	0
TCP5	At5g60970	II	CIN	+	–			0	3
TCP6	At5g41030	I	PCF	+	–			0	3
TCP7	At5g23280	I	PCF	–	N.D.	+	+	GTGAGCTCCA	2
TCP8	At1g58100	I	PCF	+	N.D.			0	1
TCP9	At2g45680	I	PCF	+	–	+		ATGGTCCCAT	5*
TCP10	At2g31070	II	CIN	–	N.D.			GTGGGCAACA	1
TCP11	At2g37000	I	PCF	+	–	+		0	5
TCP12	At1g68800	II	CYC/TB1	–	N.D.			0	4
TCP13	At3g02150	II	CIN	–	N.D.			0	3*
TCP14	At3g47620	I	PCF	+	+			0	1
TCP15	At1g69690	I	PCF	+	–	+		0	4
TCP16	At3g45150	I	PCF	+	+			GTGGACCTAT TCAGGTCCAC	2
TCP17	At5g08070	II	CIN	+	–			0	0
TCP18	At3g18550	II	CYC/TB1	+	–			0	3
TCP19	At5g51910	I	PCF	+	+	+		GTGGTCGAGG	2
TCP20	At3g27010	I	PCF	+	+			0	1
TCP21	At5g08330	I	PCF	–	N.D.	+	+	GTGGTCCAAC	2
TCP22	At1g72010	I	PCF	+	+			0	3
TCP23	At1g35560	I	PCF	+	–			GTTAGACCAA TTCGGCGCAT GTGGAAACAG GTGGGACTAC	2
TCP24	At1g30210	II	CIN	+	+			0	3

TRANSPLANTA, available TPT lines (+) or not (–). Screening, germinated in ½ MS medium, grown in 100 μM BCS and recovered with 10 μM Cu after 100 μM BCS. Class I/II CAREs, presence (+) of class I/II TCP CAREs as indicated. Other CARE versions, presence of different versions of the TCP motifs as indicated. CuRE, number of GTAC motifs in the first 500 bp upstream (, 3 GTAC motifs along 65 bp). Motifs were considered in the first 500 bp upstream and in both strains.*

was specifically linked to the Cu deficiency since the root length defect was not observed in the presence of excess Cu (**Figure 2**). Moreover, this phenotype was indeed due to the induced overexpression of *TCP16* since it was not observed in the TPT TCP16 lines in the absence of β-estradiol (Supplementary Figure S4C).

The TCP16 Transcription Factor Bound the *COPT3* Promoter

The promoters of genes participating in Cu homeostasis were analyzed for the presence of putative *cis* CARE elements recognized by TCPs. This indicated that *COPT3* and *COPT5* were the only members of the COPT family that displayed putative CAREs (Supplementary Table SII). These CARE elements in the *COPT3* (TTGAGCCCAT) and *COPT5* (GTGAGCCCAC) promoters where identified as a specific version of the previously described TCP16 CARE (Martín-Trillo and Cubas, 2010).

In order to check if TCP16 had a direct effect on *imCOPTs* regulation, binding to the promoter regions containing the putative CARE elements in *COPT3* and *COPT5* promoters (Supplementary Table SIII) was analyzed by Electrophoretic Mobility Shift Assay (EMSA) with the purified TCP16 protein (provided by the TRANSPLANTA consortium) (Coego et al., 2014). TCP16 interacted with the *COPT3* promoter, as shown by a retarded *COPT3* probe band in the presence of the TCP16 protein (**Figure 3**). An excess of *COPT3* unlabeled probe reduced the TCP16 binding, as shown by a lower intensity of the retarded *COPT3* probe band in the presence of the TCP16 protein. However, with the same amount of the *COPT2* unlabeled probe (the *COPT2* promoter has no CARE; Supplementary Table SIII), a minor reduction was observed, pointing to the specificity of the TCP16 interaction with the *COPT3* promoter. As well as *COPT3*, TCP16 also bound the *COPT5* promoter and specifically compete with an excess of the *COPT5* but not of the *COPT2* unlabeled probe (**Figure 3**). TCP23 is a class I TCP member involved in plant development (Balsemão-Pires et al., 2013) that resulted negative in the TPT screening (**Table 1**). Under the same experimental conditions, no interactions of TCP23 with the *COPT3* (Supplementary Figure S5A) and the *COPT5*

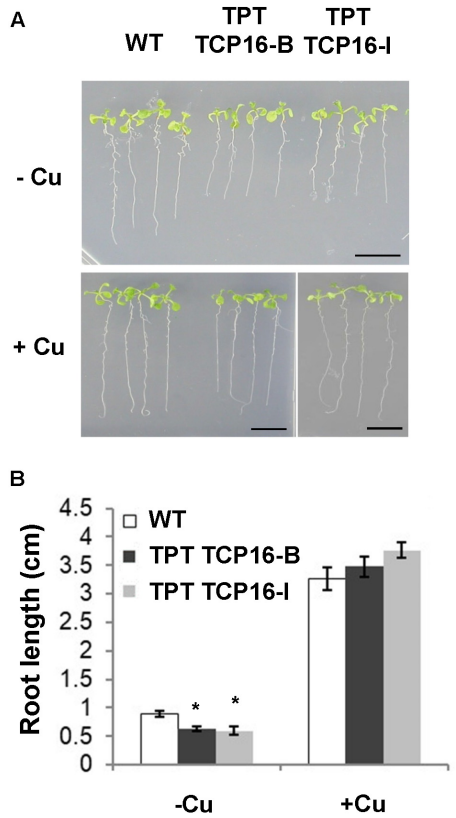

FIGURE 2 | Effect of Cu on root length in the TCP16 TPT lines. **(A)** Photograph of representative 8-day-old wild-type (WT), TCP16-B and TCP16-I TPT seedlings grown in ½ MS medium supplemented with 100 μM BCS (–Cu) or 10 μM $CuSO_4$ (+Cu), in the presence of 2 μM β-estradiol, under 12 h light/12 h dark cycles. A representative image of at least three independent experiments is shown. Scale bars, 1 cm. **(B)** Root length of 7-day-old WT and TCP16-B and TCP16-I TPT seedlings grown under the same conditions as indicated in **(A)**. Bars correspond to means ± standard deviation of three biological replicates of at least 15 plants each. Asterisks indicate statistical differences ($P < 0.05$) with respect to the WT value, according to Tukey test.

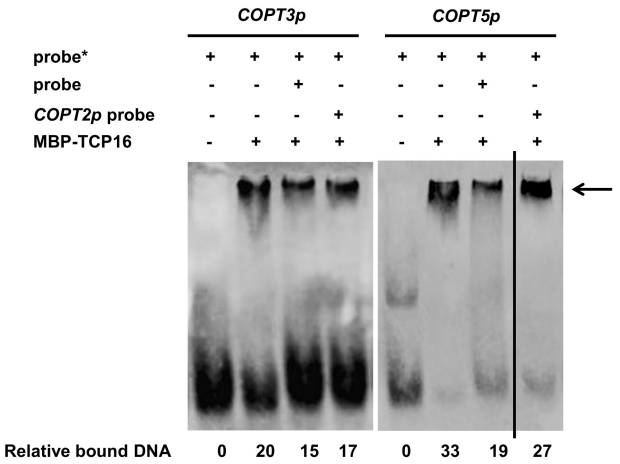

FIGURE 3 | EMSA binding assays between TCP16 protein and *COPTs* promoters. Immunoblot of purified TCP16 protein incubated with biotin-labeled (*) DNA probe from *COPT3* and *COPT5* promoters, containing TCP box. Unlabeled probes were added as a competitor as indicated. The arrow indicates the bound DNA. Relative intensity of the bands corresponding to bound DNA is shown. Representative images of at least two independent experiments are shown.

promoters (Supplementary Figure S5B) were detected. Taken together, the TCP16 TF specifically bound to the *COPT3* and *COPT5* promoters *in vitro*.

TCP16 Was Involved in Repression of *COPT3* Expression

To check the effect of TCP16 on *COPT3* expression, *TCP16* and *COPT3* mRNA levels were determined in 7-day-old TPT TCP16 seedlings at different times after β-estradiol induction. Short-term kinetics indicated that *TCP16* expression levels increased 4–5 times after 24 h induction in both lines (**Figure 4A**). In parallel to the increase in *TCP16* expression at 24 h after induction, *COPT3* expression levels were reduced to 25–15% (**Figure 4B**). Besides, long-term *TCP16* overexpression by β-estradiol was dependent on the diurnal time, being higher at 12 h of the neutral photoperiod cycle (**Figure 4C**) and provoked a repression of *COPT3* expression, specifically at this time of the day, under Cu deficiency (**Figure 4D**). As a control, the *GFP-GUS* line showed similar levels of *GUS* overexpression at 0 and 12 h of the neutral photoperiod cycle (Supplementary Figure S4A) and other TPT lines showed a robust β-estradiol-dependent induction of the TF transgene although to a different extent depending on the line (Coego et al., 2014). These data pointed to a repressive TCP16 role on *COPT3* expression.

TCP16 Expression Was Up-Regulated at Dawn and by Cu

Since the *TCP16* promoter contains a putative SPL7-responsive GTAC box (**Table 1**), we checked its expression in WT seedlings in the same samples that were used for *COPT3* expression analysis (**Figure 1C**). The results indicated that *TCP16* expression was higher at 0 h than at 12 h of the 12 h light/12 h dark cycle, under Cu deficiency (**Figure 5A**). These results may point to a diurnal oscillation of *TCP16* expression opposite to the one shown by *COPT3*. Unfortunately, the *TCP16* expression pattern is unavailable in the DIURNAL DataBase to be compared with the results shown here. Moreover, *TCP16* expression was significantly higher under Cu excess at 12 h with respect to Cu deficiency, thus high transcript levels remained along day and night under Cu excess (**Figure 5A**), coinciding with the reduction in *COPT3* expression (**Figure 1C**). Taken together, these data pointed to a role for TCP16 as a temporal transcriptional repressor of *COPT3*, specially at dawn under Cu deficiency and along day and night under Cu excess.

Cu levels were determined in the conditionally overexpressing TPT TCP16-B and TPT TCP16-I lines (**Figure 5B**). TPT TCP16 lines had lower Cu content than WT under Cu deficiency. This result pointed to affected Cu uptake. To test this possibility, the expression of *pmCOPTs* (*COPT1* and *COPT2*) was analyzed. Both

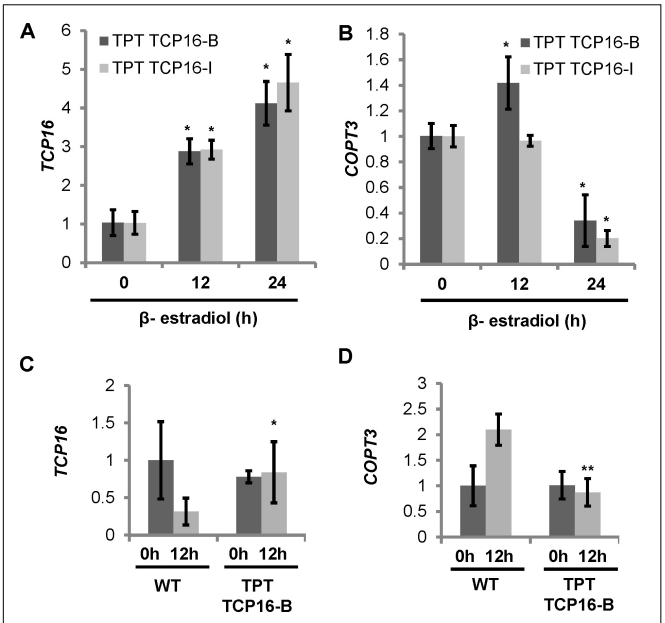

FIGURE 4 | Expression of *TCP16* and *COPT3* under different conditions in the TCP16 TPT lines. **(A,B)** Kinetics of *TCP16* and *COPT3* expression in TCP16 TPT lines by β-estradiol. Seven-day-old TCP16-B (dark bars) and TCP16-I (light bars) TPT seedlings grown in ½ MS medium supplemented with 100 μM BCS. Samples were taken at indicated times, after treatment with 2 μM β-estradiol at 0 h of the 12 h light/12 h dark cycle in day 7. Total RNA was extracted and analyzed by RT-qPCR with specific oligonucleotides for *TCP16* **(A)** and *COPT3* **(B)**. The relative expression in arbitrary units is represented. Values correspond to arithmetic means ($2^{-\Delta\Delta Ct}$) ± standard deviation from three biological replicates with three technical replicates for each ($n = 3$). Asterisks indicate significant differences ($P \leq 0.05$) according to *T*-test. **(C,D)** *TCP16* and *COPT3* temporal expression. Six-day-old wild-type (WT) and TPT TCP16-B seedlings grown in ½ MS medium supplemented with 100 μM BCS and 2 μM β-estradiol. Samples were taken at 0 h (dark bars) and 12 h (light bars) of the 12 h light/12 h dark cycle. Total RNA was extracted and analyzed by RT-qPCR with specific oligonucleotides for *TCP16* **(C)** and *COPT3* **(D)**. The relative expression in arbitrary units is represented. Values correspond to arithmetic means ($2^{-\Delta\Delta Ct}$) ± standard deviation from at least three biological replicates ($n \geq 3$). Asterisks indicate significant differences for the same group of samples respect to the WT line (*$P \leq 0.1$; **$P \leq 0.04$) according to *T*-test.

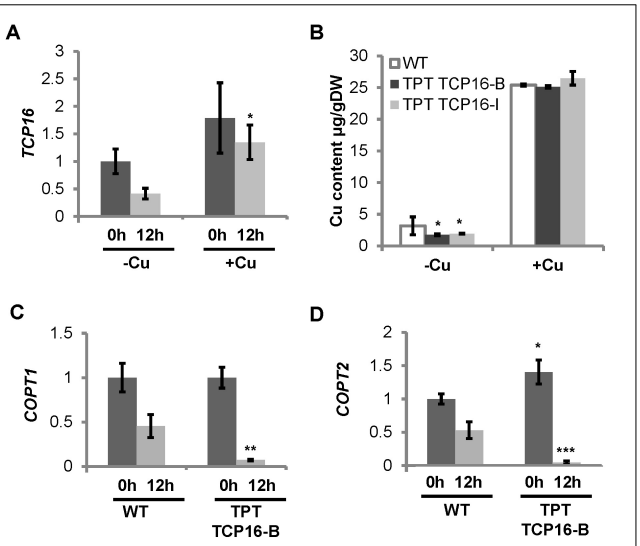

FIGURE 5 | *TCP16* temporal expression pattern, regulation by Cu, and Cu status in the TCP16 TPT lines. **(A)** *TCP16* expression. Six-day-old wild-type seedlings grown in ½ MS medium (MS) and the same medium supplemented with 100 μM BCS (–Cu) or 10 μM $CuSO_4$ (+Cu). Samples were taken at 0 h (dark bars) and 12 h (light bars) of the 12 h light/12 h dark cycle. Total RNA was extracted and analyzed by RT-qPCR with specific oligonucleotides for *TCP16*. The relative expression in arbitrary units is represented. Values correspond to arithmetic means ($2^{-\Delta\Delta Ct}$) ± standard deviation from at least three biological replicates ($n \geq 3$). Asterisk indicates significant differences for the same group of samples with respect to the other conditions ($P \leq 0.002$) according to *T*-test. **(B)** Cu content in TPT TCP16 plants. Seven-day-old wild-type (white bars), TCP16-B (dark gray bars) and TCP16-I (light gray bars) TPT seedlings grown in ½ MS medium supplemented with 100 μM BCS (–Cu) or with 10 μM $CuSO_4$ (+Cu), in the presence of 2 μM β-estradiol, under 12 h light/12 h dark cycles. Values correspond to arithmetic means ± standard deviation from three biological replicates of 120 mg of DW. Asterisks indicate significant differences between WT and mutant lines in the same condition ($P \leq 0.05$) according to *T*-test. **(C,D)** Cu-status marker expression in TPT TCP16 line. Six-day-old wild-type (WT) and TPT TCP16-B seedlings grown in ½ MS medium supplemented with 100 μM BCS and 2 μM β-estradiol. Samples were taken at 0 h (dark bars) and 12 h (light bars) of the 12 h light/12 h dark cycle. Total RNA was extracted and analyzed by RT-qPCR with specific oligonucleotides for *COPT1* **(C)** and *COPT2* **(D)**. The relative expression in arbitrary units is represented. Values correspond to arithmetic means ($2^{-\Delta\Delta Ct}$) ± standard deviation from four biological replicates ($n = 4$). Asterisks indicate significant differences for the same group of samples with respect to the WT line (*$P \leq 0.02$; **$P \leq 0.005$; ***$P \leq 0.0005$) according to *T*-test.

pmCOPT were selectively reduced at 12 h in TPT TCP16-B under Cu deficiency conditions (**Figures 5C,D**), despite the absence of TCP16 binding boxes in their promoters (Supplementary Table SII).

The Loss-of-Function of TCP16 Exhibited Copper-Related Phenotypes

In order to have a better understanding of the role of TCP16 in regulating Cu homeostasis, we used both a RNA interference line TCP16RNAi (Takeda et al., 2006) and a T-DNA insertion mutant *tcp16* (N462818) (Supplementary Table SI). The *tcp16* mutant contains the T-DNA insert at +110 bp of the *TCP16* coding sequence (Supplementary Figures S6A,B). A homozygous *tcp16* line was selected (Supplementary Figure S6C) and the loss of the *TCP16* expression at 0 h corroborated by RT-qPCR (Supplementary Figure S6D). The growth of *tcp16* was checked under Cu deficiency and excess in the medium. The *tcp16* seedlings showed defects in root elongation and fresh weight mostly under Cu excess (**Figures 6A,B**), coincident with the conditions where *TCP16* was mainly expressed (**Figure 5A**). Moreover, Cu content was also determined by atomic absorbance and, whereas conditionally overexpressing TPT TCP16 lines had lower Cu content than WT under Cu deficiency (**Figure 5B**), a decreased level of Cu content was observed in the loss-of-function *TCP16RNAi* and *tcp16* lines under Cu excess (**Figure 6C**).

To check the effect of the TCP16 loss-of-function on *COPT3* expression, *COPT3* mRNA levels were determined in 7-day-old seedlings of the *TCP16RNAi* and *tcp16* lines under Cu excess. An increase in *COPT3* expression levels was observed specifically at

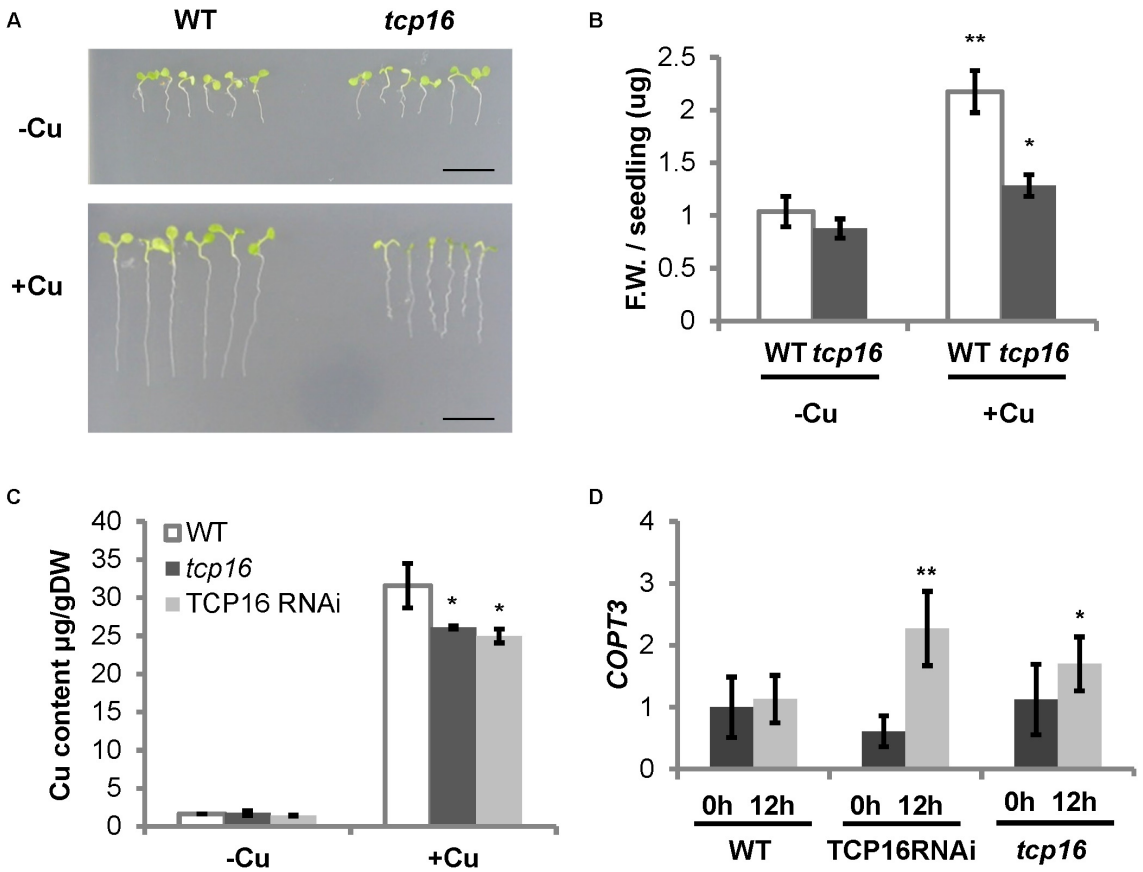

FIGURE 6 | Phenotype of *tcp16* seedlings under different Cu status and *COPT3* expression in TCP16 RNAi and knockout lines. **(A)** Photographs of representative 6-day-old wild-type (WT) and *tcp16* seedlings grown in ½ MS medium supplemented with 100 μM BCS (–Cu) or 10 μM $CuSO_4$ (+Cu) under 12 h light/12 h dark cycles. A representative image of at least three independent experiments is shown. Scale bars, 1 cm. **(B)** Fresh weight of wild-type (white bars) and *tcp16* (dark gray bars) 7-day-old seedlings grown in the same conditions shown in **(A)**. Bars correspond to means ± standard deviation of six biological replicates of five seedlings each. Asterisks indicate significant differences (*$P < 0.05$; **$P < 0.01$) according to Duncan test. **(C)** Cu content in WT (white bars), TCP16 RNAi (dark gray bars) and *tcp16* (light gray bars) 7-day-old seedlings grown in the same conditions shown in **(A)**. Bars correspond to means ± standard deviation of three biological replicates of 120 mg of DW. Asterisks indicate statistical differences between WT and mutant lines in the same condition ($P < 0.05$) according to *T*-test. **(D)** *COPT3* expression. Six-day-old wild-type (WT), TCP16 RNAi and *tcp16* seedlings grown in ½ MS medium supplemented with 10 μM $CuSO_4$. Samples were taken at 0 h (dark bars) and 12 h (light bars) of the 12 h light/12 h dark cycle. Total RNA was extracted and analyzed by RT-qPCR with specific oligonucleotides for *COPT3*. The relative expression in arbitrary units is represented. Values correspond to arithmetic means ($2^{-\Delta\Delta Ct}$) ± standard deviation from at least three biological replicates ($n \geq 3$). Asterisks indicate significant differences for the same group of samples with respect to the WT line (*$P \leq 0.06$; **$P \leq 0.009$) according to *T*-test.

the end of the light period (12 h) (**Figure 6D**). This effect was the opposite to the one observed in the conditionally overexpressing TPT TCP16-B line (**Figure 4D**), further pointing to the function of TCP16 as a repressor of *COPT3*.

COPT3 Function Was Required for Proper Repression of *TCP16*

The possibility that COPT3 function could reciprocally affect *TCP16* expression was also checked. For that purpose, we analyzed the *TCP16* expression in transgenic lines with altered *COPT3* expression levels and used the *COPT3-HA* line (Andrés-Colás et al., 2010) and loss-of-function *copt3* mutant (GK633G06) (Supplementary Table SI). The *copt3* mutant contains a T-DNA insertion at +109 bp of the *COPT3* coding sequence (Supplementary Figure S7A). A homozygous *copt3* line was selected (Supplementary Figure S7B) and the loss of the *COPT3* expression in flowers corroborated by RT-qPCR (Supplementary Figure S7C). The COPT3-HA line was sensitive to Cu excess, as shown by a reduction in root elongation and alteration of the flower morphology and flowering time (Andrés-Colás et al., 2010). On the contrary, the *copt3* mutant was more sensitive to Cu deficiency than WT and accordingly accumulated less Cu than controls (not shown). The levels of the Cu deficiency marker *COPT2* were higher at 12 h in the *copt3* mutant (**Figure 7A**), whereas *SDH1-2*, a mitochondrial marker of Cu excess (Andrés-Colás et al., 2013), was significantly reduced at this time in flowers (**Figure 7B**) further pointing to decreased Cu levels in the *copt3* mutant.

The expression analysis showed that *TCP16* levels were higher at 12 h in the *copt3* mutant line, in contrast with a lower expression at 0 h in the *COPT3-HA* transgenic line (**Figure 7C**).

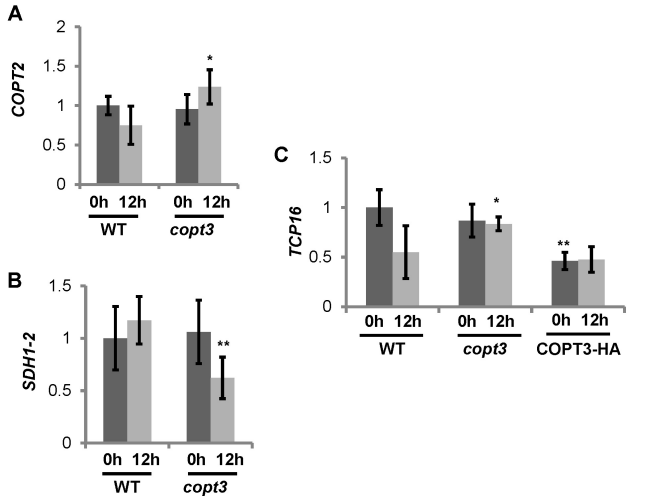

FIGURE 7 | Phenotype of *copt3* knockout seedlings under different Cu status. **(A,B)** Cu-status marker expression in *copt3* lines. Flowers from wild type (WT) and *copt3* knockout plants grown in soil. Samples were taken at 0 h (dark bars) and 12 h (light bars) of the 12 h light/12 h dark cycle. Total RNA was extracted and analyzed by RT-qPCR with specific oligonucleotides for *COPT2* (A) and *SDH1-2* **(B)**. The relative expression in arbitrary units is represented. Values correspond to arithmetic means ($2^{-\Delta\Delta Ct}$) ± standard deviation from at least three biological replicates ($n \geq 3$). Asterisk indicates significant differences for the same group of samples with respect to the WT line (*$P \leq 0.04$; **$P \leq 0.03$) according to *T*-test. **(C)** *TCP16* expression in *copt3* and COPT3^{OE} lines. Six-day-old wild-type (WT), *copt3* and COPT3^{OE} seedlings grown in ½ MS medium supplemented with 100 μM BCS. Samples were taken at 0 h (dark bars) and 12 h (light bars) of the 12 h light/12 h dark cycle. Total RNA was extracted and analyzed by RT-qPCR with specific oligonucleotides for *TCP16*. The relative expression in arbitrary units is represented. Values correspond to arithmetic means ($2^{-\Delta\Delta Ct}$) ± standard deviation from at least two biological replicates ($n \geq 2$). Asterisks indicate significant differences for the same group of samples with respect to the WT line (*$P \leq 0.15$; **$P \leq 0.005$) according to *T*-test.

These data suggested that, in addition to the already mentioned repression of TCP16 over *COPT3*, a reciprocal repressing effect of the COPT3 function on *TCP16* expression was taking also place.

In agreement with the observation that *COPT3* expression was higher in pollen, the *copt3* mutant showed a significantly higher percentage of pollen ornamentation defects than the WT plants, but only under Cu deficient conditions (**Figure 8**). *TCP16* was also highly expressed in pollen and abortion of early pollen development has been shown in the *TCP16RNAi* plants (Takeda et al., 2006). These results reinforced the relevance of Cu homeostasis for pollen viability and the temporal and reciprocal regulation established between TCP16 and COPT3, necessary to fully accomplish this crucial process in plants.

DISCUSSION

COPT1 and COPT3 transporters belong to two subfamilies (pmCOPT and imCOPT, respectively) involved in Cu^+ uptake from different extra- and intra-cellular pools. The *COPT1* and *COPT3* are two flanking genes organized head-to-head in opposite orientations. In general, bidirectional activity was shown to be an inherent feature of most promoters, being especially relevant in divergent promoters (Seila et al., 2008; Wakano et al., 2012). In *Arabidopsis*, 5,763 divergent gene pairs were reported (Krom and Ramakrishna, 2008) and among them, 462 are separated by a small distance (<250 bp) sharing a single bidirectional promoter that may regulate the co-expression of the two genes (Dhadi et al., 2009). The intergenic region between transcriptional start sites of *COPT1* and *COPT3* is 2,266 bp (Supplementary Figure S1A), a similar size to the 2,177 DNA segment between the genes *cab1* and *cab2* which was shown to function as a bidirectional promoter (Mitra et al., 2009). It is thus possible, that *COPT1* and *COPT3* spatial expression is co-regulated via the shared bidirectional promoter. Indeed, both were mostly present in pollen, seeds and vascular bundles (**Figures 1B** and Supplementary Figure S3A) (Sancenón et al., 2004; Bock et al., 2006). However, whereas *COPT3* was expressed early in pollen development, *COPT1* was expressed at later stages (Bock et al., 2006). Indeed, Cu is highly required for pollen development and its regulated delivery through COPT transporters could be an important step. Both SPL7 and a Cu-DEFICIENCY-INDUCED TRANSCRIPTION FACTOR 1 (CITF1) belonging to the bHLH family (bHLH160) were recently shown to participate in the regulation of Cu delivery to the anthers and in jasmonic acid synthesis during Cu deficiency (Yan et al., 2017).

Our data indicated that COPT3 might be located in a compartment of the secretory pathway, which could be the ER, where COPT3 would recover Cu^+ from the ER lumen. Although further experimental approaches are required to localize COPT3 to a precise organelle, it is interesting to note that the ER was also the proposed location of the Cu deficiency sensor SPL7 (Garcia-Molina et al., 2014). SPL7 was proposed to sense both cytosolic and the ER lumen Cu status. Our COPT3 localization data pointed that COPT3 could be interestingly involved in the partitioning of these two differential Cu pools (**Figure 9**).

The fact that the *COPT3* transcriptional expression pattern was initially described as not being affected by Cu status in the medium (Sancenón et al., 2003), could be attributed to the particular temporal dependence of the Cu-regulation of *COPT3* expression. Both *COPT1* and *COPT3* present several GTAC elements nearby the translational start sites that could be involved in SPL7-mediated Cu deficiency responses (Yamasaki et al., 2009; Bernal et al., 2012). In regard to this, the expression in phase of both the activator *SPL7* and the target *COPT1* could drive a robust Cu deficiency response for *COPT1* expression, whereas the antiphase expression between the SPL7 and the target *COPT3* could temporally affect the intensity of the SPL7-mediated regulation, as already modeled (Peñarrubia et al., 2015). This result suggested that, at the temporal level, the promoter region could be alternatively used in each direction for *COPT1* and *COPT3* transcription, instead of co-expression. However, the SPL7-mediated antiphase regulation of *COPT3* expression cannot explain *per se* the anti-correlated expression observed at the temporal level between *COPT1* and *COPT3* driven from a putative bidirectional promoter (**Figure 1C**), but rather

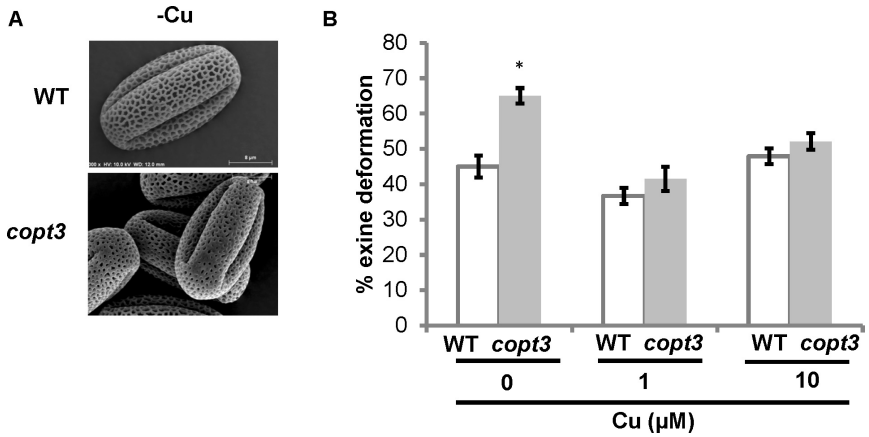

FIGURE 8 | Pollen grains morphology of *copt3* knockout plants. **(A)** Electronic photography of representative wild-type (WT) and *copt3* pollen grains obtained from flowers at the anthesis stage. **(B)** Quantification of exine deformation in pollen grains. The plants were grown in soil under long day conditions and watered with Hoagland' solution with 0 (–Cu), 1 and 10 μM $CuSO_4$. Bars correspond to means ± standard deviation of five biological replicates of 15 flowers. One hundred pollen grains were analyzed for each genotype and condition. Asterisks indicate statistical differences ($P < 0.05$) according to *Z*-test.

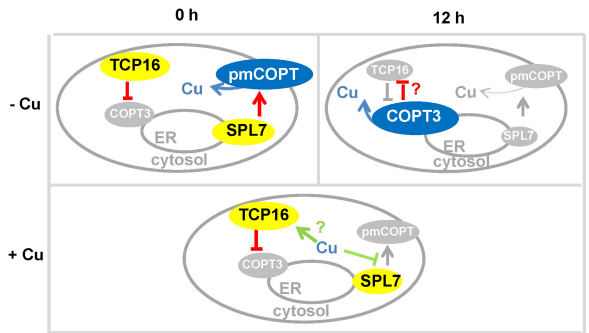

FIGURE 9 | Model for TCP16 function in copper homeostasis. Scheme of the temporal (0 and 12 h) regulation of *pmCOPTs* and *imCOPT3* expression by *TCP16* and *SPL7* in wild-type seedlings under different Cu status (–Cu and +Cu).

suggested the presence of other temporal transcriptional regulators.

Thanks to the TRANSPLANTA consortium, we could screen for conditionally inducible TFs that might participate in the response to Cu availability (Coego et al., 2014). The TCP family was one of the most overrepresented with regard to the number of positive members in the screen. Moreover, the presence of putative elements denoted CAREs in the *COPT3* and *COPT5* promoters, as well as in other Cu homeostasis components (Supplementary Table SII), is compatible with a regulatory role of TCPs in Cu homeostasis. We selected the TCP family for further study, because pollen morphology was also affected in plants with altered levels of *COPT1*, *COPT3*, and *TCP16* (Sancenón et al., 2004; Takeda et al., 2006; this study). Moreover, CHE is a TCP factor that was involved in *CCA1* repression by interacting with TOC1, both components of the circadian clock (Pruneda-Paz et al., 2009), which expression was altered in *COPT1* overexpressing plants (Andrés-Colás et al., 2010). *COPT1* and *COPT3* overexpression displayed similar phenotypes that were attributed to the temporal deregulation of the Cu entrance that could affect the circadian rhythms (Andrés-Colás et al., 2010). This fact could explain the phenotype observed for the *COPT3* overexpressing and *copt3* seedlings under Cu deficiency in this work. Finally, in microarrays analysis performed in transgenic plants with modified levels of *COPT2*, differential expression of several TCP members was observed (Perea-García et al., 2013).

There are several lines of evidence to support the model that TCP16 represses *COPT3* expression. First, TCP16 specifically bound to the *COPT3* and *COPT5* promoters *in vitro* as shown by EMSA (**Figure 3**). And second, *COPT3* was repressed as *TCP16* expression increased (**Figure 4**) and conversely, *COPT3* was upregulated in a *tcp16* mutant (**Figure 6**). The presence of a putative TCP16 binding site nearby the translational start site of *COPT3*, but not of *COPT1*, could account for the particular temporal repression of *COPT3*. The relative short distance (109 bp) between the GTAC boxes and the putative TCP16 binding site in the *COPT3* promoter (Supplementary Figure S1) brings to discussion if there is a competence between SPL7 and TCP16 for binding. Any kind of interaction between the activation and the repression function of SPL7 and TCP16, respectively, is also plausible since TCPs interact with a wide variety of other TF families, including other SPL member in the described TCP4-SPL9 temporal interaction taking place during flower development (Rubio-Somoza et al., 2014; Bemer et al., 2017). Furthermore, as a conclusion of the *COPT3* expression analysis, TCP16 could act as a repressor of COPT3-mediated Cu transport in a time specific manner.

Under Cu deficient conditions, we hypothesized that COPT3-mediated Cu recovery from the secretory pathway was repressed by TCP16 at 0 h, while the pmCOPT would participate in the uptake extracellular Cu at this time being activated by SPL7 (**Figure 9**). Under Cu excess, *pmCOPTs* were not activated by SPL7 and TCP16 will further repressed *COPT3* and *COPT5* along day and night (**Figure 9**). On the

other hand, the expression of the *pmCOPT* transporters at 12 h could be subjected to a feedback autoregulatory loop that was proposed to act as a biochemical oscillator (Peñarrubia et al., 2010). Moreover, COPT3 and TCP16 were mutually repressing each other's expression. TCP16 may directly act as a *COPT3* repressor, whereas COPT3 probably indirectly affected *TCP16* expression. Subsequently, Cu entrance from extracellular pools was prioritized at dawn and Cu mobilization from internal pools was favored at dusk. Whether this affected cytosolic Cu or the destiny of Cu coming from the different pools was being used for separate purposes still deserves further investigation. In addition, *HMA5* and *RAN1* also display putative CARE elements in their promoters (Supplementary Table SII) that could indicate that Cu transport in both directions (entrance and exit) through internal membranes was under control of TCPs.

The fine regulation exerted by TCP16 as a repressor of Cu entrance from internal stores specifically at dawn suggested a temporal division requirement for incompatible processes. Among the possibilities, the avoidance of a putative excessive increase in oxidative stress in this period that could not be properly counteracted. In this sense, Cu^{+} uptake through COPT transporters imposed an increased oxidative stress (Rodrigo-Moreno et al., 2013) that could interfere at multiple cellular processes and damage biological structures (Ravet and Pilon, 2013). The redox state of the cell was shown to influence the DNA binding ability of class I TCP proteins (Viola et al., 2013). The oxidation of a conserved cysteine residue (C-20) leaded to the formation of intermolecular disulfide bonds that cannot bound target promoters (Viola et al., 2016). Although the C-20 residue is not conserved, a single cysteine (C-107) residue is present in TCP16 (Supplementary Figure S6A).

On the other hand, *TCP16* repression could be aimed to protect a Cu sensitive process operating at dawn. In this sense, a specially Cu sensitive process that takes place in the mitochondria is the Fe-S cluster assembly, required for multiple processes including the respiratory electron transfer chain (Brancaccio et al., 2017). Since the mitochondrial matrix contains a labile Cu^{+} pool and is also the place where the Fe-S cluster assembly machinery resides, a strict temporal regulated Cu uptake might prevent a blocking of mitochondrial Fe-S protein maturation (Brancaccio et al., 2017). This process is in agreement with the regulatory function of mitochondrial proteins by TCPs (Welchen and Gonzalez, 2006) and is also connecting Fe and Cu homeostasis, as already described for the *copt2* mutant (Perea-García et al., 2013). Accordingly, *tcp16* seedlings were sensitive to Cu excess (**Figure 6**), maybe due to an impaired temporal Cu entrance to the mitochondria. The source of Cu that reaches organelles from an endosymbiotic origin, such as mitochondria and chloroplasts, remains an unsolved question. Under environmental nutrient deprivation, a putative Cu source is the lumen of the endocytic compartments that were recently shown to participate in dynamic intracellular metal homeostasis (Blaby-Haas and Merchant, 2014; Hong-Hermesdorf et al., 2014). Although further work is needed to confirm this hypothesis, the internal membrane COPT3 and COPT5 transporters might participate in Cu delivery from the secretory pathway to organelles under metal deficiency. In agreement, photosynthesis is affected in *copt5* mutants (Garcia-Molina et al., 2011). The mitochondrial *SDH1-2* promoter displayed 3 putative CARE elements (Welchen and Gonzalez, 2006) and it was shown to be regulated by TCPs (Giraud et al., 2010). Moreover, *SDH1-2* was a good marker for mild Cu excess (Andrés-Colás et al., 2013). In accordance, *SDH1-2* expression was down-regulated in the *copt3* mutant (**Figure 7B**). This result suggested that a Cu-TCP interplay may mediate mitochondrial *SDH1-2* expression. This would constitute a new pathway for gene expression regulation under mild Cu excess that might be aimed to protect mitochondria from Cu toxicity.

The fact that *COPT1* and *COPT3* were mostly expressed in vascular tissues points to a role for the temporal differences in metal long distance transport. In this sense, since the higher Cu affinity for common metal chelators (Álvarez-Fernández et al., 2014), competition with other metals, such as Fe, in the xylem transport could involve a metal interference in long distance transport, especially relevant under metal deficiencies. Although further work will be needed to address this hypothesis, a putative solution could be a metal differential temporal arrangement in vascular transport.

Finally, the *in silico* analysis of the hormone-responsive *cis*-elements present in the promoter sequences (1,000 bp upstream of the five prime untranslated region) from the *COPT1* and *COPT3* genes indicated a differential hormonal response (Peñarrubia et al., 2015). Major differences were observed for those *cis*-elements involved in ABA and gibberellic acid (GA) signaling. Whereas the total elements for ABA were 11 and 3, those for GA were 7 and 20 in the *COPT1* and *COPT3* promoters, respectively (Peñarrubia et al., 2015). Since the antagonism between ABA and GA is well-known (Weiss and Ori, 2007), as well as their interplay with the circadian clock (Atamian and Harmer, 2016) and their wide crosstalk with TCPs (Nicolas and Cubas, 2016), the results shown here underscore the role of phytohormones in the temporal orchestration of metal homeostasis that might control plant development depending on the environmental nutrient conditions.

AUTHOR CONTRIBUTIONS

LP conceived the idea and wrote the manuscript. MP, NA-C, and SA-G conceived and performed the COPT3 localization experiments. NA-C performed the TF screening. NA-C and AC-S performed the physiological and molecular experiments in mutant plants.

FUNDING

This work has been supported by grants BIO2017-87828-C2-1-P (LP) and the TRANSPLANTA Consortium (CSD2007-00057) from the Spanish Ministry of Economy and Competitiveness, and by FEDER funds from the European Union. NA-C and AC-S

were recipients of a predoctoral FPI fellowship from the Spanish Ministry of Economy and Competitiveness.

ACKNOWLEDGMENTS

We acknowledge the SCSIE (Universitat de València) for the sequencing and greenhouse services, Dr. Sergi Puig for critical reading of the manuscript and Drs. Pablo Vera and José Luis Carrasco (IBMCP-UPV València) for providing the TCP16 and TCP23 proteins for EMSA analysis. TCP16 RNAi line was kindly provided by Chiharu Ueguchi (Takeda et al., 2006).

SUPPLEMENTARY MATERIAL

The Supplementary Material for this article can be found online at: https://www.frontiersin.org/articles/10.3389/fpls.2018.00910/full#supplementary-material

REFERENCES

Abdel-Ghany, S. E., Müller-Moulé, P., Niyogi, K. K., Pilon, M., and Shikanai, T. (2005). Two P-type ATPases are required for copper delivery in *Arabidopsis thaliana* chloroplasts. *Plant Cell* 17, 1233–1251. doi: 10.1105/tpc.104.030452

Almeida, D. M., Gregorio, G. B., Oliveira, M. M., and Saibo, N. J. (2017). Five novel transcription factors as potential regulators of *OsNHX1* gene expression in a salt tolerant rice genotype. *Plant Mol. Biol.* 93, 61–77. doi: 10.1007/s11103-016-0547-7

Álvarez-Fernández, A., Díaz-Benito, P., Abadía, A., López-Millán, A. F., and Abadía, J. (2014). Metal species involved in long distance metal transport in plants. *Front. Plant Sci.* 5:105. doi: 10.3389/fpls.2014.00105

Andrés-Colás, N., Perea-García, A., Mayo de Andrés, S., Garcia-Molina, A., Dorcey, E., Rodríguez-Navarro, S., et al. (2013). Comparison of global responses to mild deficiency and excess copper levels in *Arabidopsis* seedlings. *Metallomics* 5, 1234–1246. doi: 10.1039/c3mt00025g

Andrés-Colás, N., Perea-García, A., Puig, S., and Peñarrubia, L. (2010). Deregulated copper transport affects Arabidopsis development especially in the absence of environmental cycles. *Plant Physiol.* 153, 170–184. doi: 10.1104/pp.110.153676

Andrés-Colás, N., Sancenón, V., Rodríguez-Navarro, S., Mayo, S., Thiele, D. J., Ecker, J. R., et al. (2006). The Arabidopsis heavy metal P-type ATPase HMA5 interacts with metallochaperones and functions in copper detoxification of roots. *Plant J.* 45, 225–236. doi: 10.1111/j.1365-313X.2005.02601.x

Andriankaja, M. E., Danisman, S., Mignolet-Spruyt, L. F., Claeys, H., Kochanke, I., Vermeersch, M., et al. (2014). Transcriptional coordination between leaf cell differentiation and chloroplast development established by TCP20 and the subgroup Ib bHLH transcription factors. *Plant Mol. Biol.* 85, 233–245. doi: 10.1007/s11103-014-0180-2

Atamian, H. S., and Harmer, S. L. (2016). Circadian regulation of hormone signaling and plant physiology. *Plant Mol. Biol.* 91, 691–702. doi: 10.1007/s11103-016-0477-4

Balsemão-Pires, E., Andrade, L. R., and Sachetto-Martins, G. (2013). Functional study of TCP23 in *Arabidopsis thaliana* during plant development. *Plant Physiol. Biochem.* 67, 120–125. doi: 10.1016/j.plaphy.2013.03.009

Bar-Peled, M., and Raikhel, N. V. (1997). Characterization of AtSEC12 and AtSAR1. Proteins likely involved in endoplasmic reticulum and Golgi transport. *Plant Physiol.* 114, 315–324. doi: 10.1104/pp.114.1.315

Bate, N., and Twell, D. (1998). Functional architecture of a late pollen promoter: pollen-specific transcription is developmentally regulated by multiple stage-specific and co-dependent activator elements. *Plant Mol. Biol.* 37, 859–869. doi: 10.1023/A:1006095023050

Bemer, M., van Dijk, A. D., Immink, R. G., and Angene, G. C. (2017). Cross-family transcription factor interactions: an additional layer of gene regulation. *Trends Plant Sci.* 22, 66–80. doi: 10.1016/j.tplants.2016.10.007

Bernal, M., Casero, D., Singh, V., Wilson, G. T., Grande, A., Yang, H., et al. (2012). Transcriptome sequencing identifies *SPL7*-regulated copper acquisition genes *FRO4/FRO5* and the copper dependence of iron homeostasis in *Arabidopsis*. *Plant Cell* 24, 738–761. doi: 10.1105/tpc.111.090431

Blaby-Haas, C. E., and Merchant, S. S. (2014). Lysosome-related organelles as mediators of metal homeostasis. *J. Biol. Chem.* 289, 28129–28136. doi: 10.1074/jbc.R114.592618

Bock, K. W., Honys, D., Ward, J. M., Padmanaban, S., Nawrocki, E. P., Hirschi, K. D., et al. (2006). Integrating membrane transport with male gametophyte development and function through transcriptomics. *Plant Physiol.* 140, 1151–1168. doi: 10.1104/pp.105.074708

Bradford, M. M. (1976). A rapid and sensitive method for the quantitation of microgram quantities of protein utilizing the principle of protein-dye binding. *Anal. Biochem.* 72, 248–254. doi: 10.1016/0003-2697(76)90527-3

Brancaccio, D., Gallo, A., Piccioli, M., Novellino, E., Ciofi-Baffoni, S., and Banci, L. (2017). [4Fe-4S] Cluster assembly in mitochondria and its impairment by copper. *J. Am. Chem. Soc.* 139, 719–730. doi: 10.1021/jacs.6b09567

Bruinsma, J. (1961). A comment on the spectrophotometric determination of chlorophyll. *Biochim. Biophys. Acta* 52, 576–578. doi: 10.1016/0006-3002(61)90418-8

Carrió-Seguí, A., Garcia-Molina, A., Sanz, A., and Peñarrubia, L. (2015). Defective copper transport in the *copt5* mutant affects cadmium tolerance. *Plant Cell Physiol.* 56, 442–454. doi: 10.1093/pcp/pcu180

Chen, Y.-Y., Wang, Y., Shin, L.-J., Wu, J.-F., Shanmugam, V., Tsednee, M., et al. (2013). Iron is involved in maintenance of circadian period length in Arabidopsis. *Plant Physiol.* 161, 1409–1420. doi: 10.1104/pp.112.212068

Coego, A., Brizuela, E., Castillejo, P., Ruíz, S., Koncz, C., del Pozo, J. C., et al. (2014). The TRANSPLANTA collection of Arabidopsis lines: a resource for functional analysis of transcription factors based on their conditional overexpression. *Plant J.* 77, 944–953. doi: 10.1111/tpj.12443

Cubas, P., Lauter, N., Doebley, J., and Coen, E. (1999). The TCP domain: a motif found in proteins regulating plant growth and development. *Plant J.* 18, 215–222. doi: 10.1046/j.1365-313X.1999.00444.x

Danisman, S. (2016). TCP transcription factors at the interface between environmental challenges and the plant's growth responses. *Front. Plant Sci.* 7:1930. doi: 10.3389/fpls.2016.01930

Dhadi, S. R., Krom, N., and Ramakrishna, W. (2009). Genome-wide comparative analysis of putative bidirectional promoters from rice, *Arabidopsis* and *Populus*. *Gene* 429, 65–73. doi: 10.1016/j.gene.2008.09.034

Dhaka, N., Bhardwaj, V., Sharma, M. K., and Sharma, R. (2017). Evolving tale of TCPs: new paradigms and old lacunae. *Front. Plant Sci.* 8:479. doi: 10.3389/fpls.2017.00479

Franco-Zorrilla, J. M., López-Vidriero, I., Carrasco, J. L., Godoy, M., Vera, P., and Solano, R. (2014). DNA-binding specificities of plant transcription factors, and their potential to define target genes. *Proc. Natl. Acad. Sci. U.S.A.* 111, 2367–2372. doi: 10.1073/pnas.1316278111

Garcia-Molina, A., Andrés-Colás, N., Perea-García, A., Del Valle-Tascón, S., Peñarrubia, L., and Puig, S. (2011). The intracellular Arabidopsis COPT5 transport protein is required for photosynthetic electron transport under severe copper deficiency. *Plant J.* 65, 848–860. doi: 10.1111/j.1365-313X.2010.04472.x

Garcia-Molina, A., Andrés-Colás, N., Perea-García, A., Neumann, U., Dodani, S. C., Huijser, P., et al. (2013). The Arabidopsis COPT6 transport protein functions in copper distribution under copper-deficient conditions. *Plant Cell Physiol.* 54, 1378–1390. doi: 10.1093/pcp/pct088

Garcia-Molina, A., Xing, S., and Huijser, P. (2014). Functional characterisation of Arabidopsis SPL7 conserved protein domains suggests novel regulatory mechanisms in the Cu deficiency response. *BMC Plant Biol.* 14:231. doi: 10.1186/s12870-014-0231-5

Giraud, E., Ng, S., Carrie, C., Duncan, O., Low, J., Lee, C. P., et al. (2010). TCP transcription factors link the regulation of genes encoding mitochondrial

proteins with the circadian clock in *Arabidopsis thaliana*. *Plant Cell* 22, 3921–3934. doi: 10.1105/tpc.110.074518

Guan, P., Ripoll, J., Wang, R., Vuong, L., Bailey-Steinitz, L. J., Ye, D., et al. (2017). Interacting TCP and NLP transcription factors control plant responses to nitrate availability. *Proc. Natl. Acad. Sci. U.S.A.* 114, 2419–2424. doi: 10.1073/pnas.1615676114

Guan, P., Wang, R., Nacry, P., Breton, G., Kay, S. A., Pruneda-Paz, J. L., et al. (2014). Nitrate foraging by *Arabidopsis* roots is mediated by the transcription factor TCP20 through the systemic signaling pathway. *Proc. Natl. Acad. Sci. U.S.A.* 111, 15267–15272. doi: 10.1073/pnas.1411375111

Harmer, S. L., Hogenesch, J. B., Straume, M., Chang, H. S., Han, B., Zhu, T., et al. (2000). Orchestrated transcription of key pathways in *Arabidopsis* by the circadian clock. *Science* 290, 2110–2113. doi: 10.1126/science.290.5499.2110

Hermans, C., Vuylsteke, M., Coppens, F., Craciun, A., Inzé, D., and Verbruggen, N. (2010). Early transcriptomic changes induced by magnesium deficiency in *Arabidopsis thaliana* reveal the alteration of circadian clock gene expression in roots and the triggering of abscisic acid-responsive genes. *New Phytol.* 187, 119–131. doi: 10.1111/j.1469-8137.2010.03258.x

Hirayama, T., Kieber, J. J., Hirayama, N., Kogan, M., Guzman, P., Nourizadeh, S., et al. (1999). RESPONSIVE-TO-ANTAGONIST1, a Menkes/Wilson disease-related copper transporter, is required for ethylene signaling in *Arabidopsis*. *Cell* 97, 383–393. doi: 10.1016/S0092-8674(00)80747-3

Hong, S., Kim, S. A., Guerinot, M. L., and McClung, C. R. (2013). Reciprocal interaction of the circadian clock with the iron homeostasis network in Arabidopsis. *Plant Physiol.* 161, 893–903. doi: 10.1104/pp.112.208603

Hong-Hermesdorf, A., Miethke, M., Gallaher, S. D., Kropat, J., Dodani, S. C., Chan, J., et al. (2014). Subcellular metal imaging identifies dynamic sites of Cu accumulation in *Chlamydomonas*. *Nat. Chem. Biol.* 10, 1034–1042. doi: 10.1038/nchembio.1662

Jefferson, R. A., Kavanagh, T. A., and Bevan, M. W. (1987). GUS fusions: beta-glucuronidase as a sensitive and versatile gene fusion marker in higher plants. *EMBO J.* 6, 3901–3907.

Kampfenkel, K., Kushnir, S., Babiychuk, E., Inzé, D., and Van Montagu, M. (1995). Molecular characterization of a putative *Arabidopsis thaliana* copper transporter and its yeast homologue. *J. Biol. Chem.* 270, 28479–28486. doi: 10.1074/jbc.270.47.28479

Kieffer, M., Master, V., Waites, R., and Davies, B. (2011). TCP14 and TCP15 affect internode length and leaf shape in Arabidopsis. *Plant J.* 68, 147–158. doi: 10.1111/j.1365-313X.2011.04674.x

Kim, H., Wu, X., and Lee, J. (2013). SLC31 (CTR) family of copper transporters in health and disease. *Mol. Aspects Med.* 34, 561–570. doi: 10.1016/j.mam.2012.07.011

Klaumann, S., Nickolaus, S. D., Fürst, S. H., Starck, S., Schneider, S., Ekkehard Neuhaus, H., et al. (2011). The tonoplast copper transporter COPT5 acts as an exporter and is required for interorgan allocation of copper in *Arabidopsis thaliana*. *New Phytol.* 192, 393–404. doi: 10.1111/j.1469-8137.2011.03798.x

Kosugi, S., and Ohashi, Y. (2002). DNA binding and dimerization specificity and potential targets for the TCP protein family. *Plant J.* 30, 337–348. doi: 10.1046/j.1365-313X.2002.01294.x

Krom, N., and Ramakrishna, W. (2008). Comparative analysis of divergent and convergent gene pairs and their expression patterns in rice, Arabidopsis, and *Populus*. *Plant Physiol.* 147, 1763–1773. doi: 10.1104/pp.108.122416

Li, S. (2015). The *Arabidopsis thaliana* TCP transcription factors: a broadening horizon beyond development. *Plant Signal. Behav.* 10:e1044192. doi: 10.1080/15592324.2015.1044192

Martín-Trillo, M., and Cubas, P. (2010). TCP genes: a family snapshot ten years later. *Trends Plant Sci.* 15, 31–39. doi: 10.1016/j.tplants.2009.11.003

Mitra, A., Han, J., Zhang, Z. J., and Mitra, A. (2009). The intergenic region of *Arabidopsis thaliana* cab1 and cab2 divergent genes functions as a bidirectional promoter. *Planta* 229, 1015–1022. doi: 10.1007/s00425-008-0859-1

Mockler, T. C., Michael, T. P., Priest, H. D., Shen, R., Sullivan, C. M., Givan, S. A., et al. (2007). The DIURNAL project: DIURNAL and circadian expression profiling, model-based pattern matching, and promoter analysis. *Cold Spring Harb. Symp. Quant. Biol.* 72, 353–363. doi: 10.1101/sqb.2007.72.006

Mukhopadhyay, P., and Tyagi, A. K. (2015). *OsTCP19* influences developmental and abiotic stress signaling by modulating ABI4-mediated pathways. *Sci Rep.* 5:9998. doi: 10.1038/srep09998

Nicolas, M., and Cubas, P. (2016). TCP factors: new kids on the signaling block. *Curr. Opin. Plant Biol.* 33, 33–41. doi: 10.1016/j.pbi.2016.05.006

Nohales, M. A., and Kay, S. A. (2016). Molecular mechanisms at the core of the plant circadian oscillator. *Nat. Struct. Mol. Biol.* 23, 1061–1069. doi: 10.1038/nsmb.3327

Palatnik, J. F., Allen, E., Wu, X., Schommer, C., Schwab, R., Carrington, J. C., et al. (2003). Control of leaf morphogenesis by microRNAs. *Nature* 425, 257–263. doi: 10.1038/nature01958

Peñarrubia, L., Andrés-Colás, N., Moreno, J., and Puig, S. (2010). Regulation of copper transport in *Arabidopsis thaliana*: a biochemical oscillator? *J. Biol. Inorg. Chem.* 15, 29–36. doi: 10.1007/s00775-009-0591-8

Peñarrubia, L., Romero, P., Carrió-Seguí, A., Andrés-Bordería, A., Moreno, J., and Sanz, A. (2015). Temporal aspects of copper homeostasis and its crosstalk with hormones. *Front. Plant Sci.* 6:255. doi: 10.3389/fpls.2015.00255

Perea-García, A., Andrés-Bordería, A., Mayo de Andrés, S., Sanz, A., Davis, A. M., Davis, S. J., et al. (2016a). Modulation of copper deficiency responses by diurnal and circadian rhythms in *Arabidopsis thaliana*. *J. Exp. Bot.* 67, 391–403. doi: 10.1093/jxb/erv474

Perea-García, A., Garcia-Molina, A., Andrés-Colás, N., Vera-Sirera, F., Pérez-Amador, M. A., Puig, S., et al. (2013). Arabidopsis copper transport protein COPT2 participates in the cross talk between iron deficiency responses and low-phosphate signaling. *Plant Physiol.* 162, 180–194. doi: 10.1104/pp.112.212407

Perea-García, A., Sanz, A., Moreno, J., Andrés-Bordería, A., Mayo de Andrés, S., Davis, A. M., et al. (2016b). Daily rhythmicity of high affinity copper transport. *Plant Signal. Behav.* 11:e1140291. doi: 10.1080/15592324.2016.1140291

Pilon-Smits, E. A., Garifullina, G. F., Abdel-Ghany, S., Kato, S., Mihara, H., Hale, K. L., et al. (2002). Characterization of a NifS-like chloroplast protein from Arabidopsis. Implications for its role in sulfur and selenium metabolism. *Plant Physiol.* 130, 1309–1318. doi: 10.1104/pp.102.010280

Pruneda-Paz, J. L., Breton, G., Para, A., and Kay, S. A. (2009). A functional genomics approach reveals CHE as a component of the Arabidopsis circadian clock. *Science* 323, 1481–1485. doi: 10.1126/science.1167206

Puig, S. (2014). Function and regulation of the plant COPT family of high-affinity copper transport proteins. *Adv. Bot.* 2014:476917. doi: 10.1155/2014/476917

Rae, T. D., Schmidt, P. J., Pufahl, R. A., Culotta, V. C., and O'Halloran, T. V. (1999). Undetectable intracellular free copper: the requirement of a copper chaperone for superoxide dismutase. *Science* 284, 805–808. doi: 10.1126/science.284.5415.805

Ravet, K., and Pilon, M. (2013). Copper and iron homeostasis in plants: the challenges of oxidative stress. *Antioxid. Redox Signal.* 19, 919–932. doi: 10.1089/ars.2012.5084

Rawat, R., Xu, Z.-F., Yao, K.-M., and Chye, M.-L. (2005). Identification of *cis*-elements for ethylene and circadian regulation of the *Solanum melongena* gene encoding cysteine proteinase. *Plant Mol. Biol.* 57, 629–643. doi: 10.1007/s11103-005-0954-7

Rodrigo-Moreno, A., Andrés-Colás, N., Poschenrieder, C., Gunsé, B., Peñarrubia, L., and Shabala, S. (2013). Calcium- and potassium-permeable plasma membrane transporters are activated by copper in *Arabidopsis* root tips: linking copper transport with cytosolic hydroxyl radical production. *Plant Cell Environ.* 36, 844–855. doi: 10.1111/pce.12020

Rogers, H. J., Bate, N., Combe, J., Sullivan, J., Sweetman, J., Swan, C., et al. (2001). Functional analysis of cis-regulatory elements within the promoter of the tobacco late pollen gene g10. *Plant Mol. Biol.* 45, 577–585. doi: 10.1023/A:1010695226241

Rubio-Somoza, I., Zhou, C. M., Confraria, A., Martinho, C., von Born, P., and Baena-Gonzalez, E. (2014). Temporal control of leaf complexity by miRNA-regulated licensing of protein complexes. *Curr. Biol.* 24, 2714–2719. doi: 10.1016/j.cub.2014.09.058

Salomé, P. A., Oliva, M., Weigel, D., and Kramer, U. (2013). Circadian clock adjustment to plant iron status depends on chloroplast and phytochrome function. *EMBO J.* 32, 511–523. doi: 10.1038/emboj.2012.330

Sancenón, V., Puig, S., Mateu-Andrés, I., Dorcey, E., Thiele, D. J., and Peñarrubia, L. (2004). The *Arabidopsis* copper transporter COPT1 functions in root elongation and pollen development. *J. Biol. Chem.* 279, 15348–15355. doi: 10.1074/jbc.M313321200

Sancenón, V., Puig, S., Mira, H., Thiele, D. J., and Peñarrubia, L. (2003). Identification of a copper transporter family in *Arabidopsis thaliana*. *Plant Mol. Biol.* 51, 577–587. doi: 10.1023/A:1022345507112

Seila, A. C., Calabrese, J. M., Levine, S. S., Yeo, G. W., Rahl, P. B., Flynn, R. A., et al. (2008). Divergent transcription from active promoters. *Science* 322, 1849–1851. doi: 10.1126/science.1162253

Takeda, T., Amano, K., Ohto, M.-a., Nakamura, K., Sato, S., Kato, T., et al. (2006). RNA interference of the *Arabidopsis* putative transcription factor *TCP16* gene results in abortion of early pollen development. *Plant Mol. Biol.* 61, 165–177. doi: 10.1007/s11103-006-6265-9

Terzaghi, W. B., and Cashmore, A. R. (1995). Photomorphenesis: seeing the light in plant development. *Curr. Biol.* 5, 466–468. doi: 10.1016/S0960-9822(95)00092-3

Uberti-Manassero, N. G., Coscueta, E. R., and Gonzalez, D. H. (2016). Expression of a repressor form of the *Arabidopsis thaliana* transcription factor TCP16 induces the formation of ectopic meristems. *Plant Physiol. Biochem.* 108, 57–62. doi: 10.1016/j.plaphy.2016.06.031

Viola, I. L., Camoirano, A., and Gonzalez, D. H. (2016). Redox-dependent modulation of anthocyanin biosynthesis by the TCP transcription factor TCP15 during exposure to high light intensity conditions in Arabidopsis. *Plant Physiol.* 170, 74–85. doi: 10.1104/pp.15.01016

Viola, I. L., Güttlein, L. N., and Gonzalez, D. H. (2013). Redox modulation of plant developmental regulators from the class I TCP transcription factor family. *Plant Physiol.* 162, 1434–1447. doi: 10.1104/pp.113.216416

Viola, I. L., Reinheimer, R., Ripoll, R., Manassero, N. G., and Gonzalez, D. H. (2012). Determinants of the DNA binding specificity of class I and class II TCP transcription factors. *J. Biol. Chem.* 287, 347–356. doi: 10.1074/jbc.M111.256271

Wakano, C., Byun, J. S., Di, L. J., and Gardner, K. (2012). The dual lives of bidirectional promoters. *Biochim. Biophys. Acta* 1819, 688–693. doi: 10.1016/j.bbagrm.2012.02.006

Wang, H., Mao, Y., Yang, J., and He, Y. (2015). *TCP24* modulates secondary cell wall thickening and anther endothecium development. *Front. Plant. Sci.* 6:436. doi: 10.3389/fpls.2015.00436

Wang, H. Y., Klatte, M., Jakoby, M., Bäumlein, H., Weisshaar, B., and Bauer, P. (2007). Iron deficiency-mediated stress regulation of four subgroup Ib BHLH genes in *Arabidopsis thaliana*. *Planta* 226, 897–908. doi: 10.1007/s00425-007-0535-x

Wang, S.-t., Sun, X.-l., Hoshino, Y., Yu, Y., Jia, B., Sun, Z.-w., et al. (2014). *MicroRNA319* positively regulates cold tolerance by targeting *OsPCF6* and *OsTCP21* in rice (*Oryza sativa* L.). *PLoS One* 9:e91357. doi: 10.1371/journal.pone.0091357

Weiss, D., and Ori, N. (2007). Mechanisms of cross talk between gibberellin and other hormones. *Plant Physiol.* 144, 1240–1246. doi: 10.1104/pp.107.100370

Welchen, E., and Gonzalez, D. H. (2006). Overrepresentation of elements recognized by TCP-domain transcription factors in the upstream regions of nuclear genes encoding components of the mitochondrial oxidative phosphorylation machinery. *Plant Physiol.* 141, 540–545. doi: 10.1104/pp.105.075366

Wu, J. F., Tsai, H. L., Joanito, I., Wu, Y. C., Chang, C. W., Li, Y. H., et al. (2016). LWD-TCP complex activates the morning gene CCA1 in *Arabidopsis*. *Nat. Commun.* 7:13181. doi: 10.1038/ncomms13181

Yamasaki, H., Hayashi, M., Fukazawa, M., Kobayashi, Y., and Shikanai, T. (2009). *SQUAMOSA* promoter binding protein-like7 is a central regulator for copper homeostasis in *Arabidopsis*. *Plant Cell* 21, 347–361. doi: 10.1105/tpc.108.060137

Yan, J., Chia, J. C., Sheng, H., Jung, H. I., Zavodna, T. O., Zhang, L., et al. (2017). Arabidopsis pollen fertility requires the transcription factors CITF1 and SPL7 that regulate copper delivery to anthers and jasmonic acid synthesis. *Plant Cell* 29, 3012–3029. doi: 10.1105/tpc.17.00363

Zhang, H., Zhao, X., Li, J., Cai, H., Deng, X. W., and Li, L. (2014). MicroRNA408 is critical for the HY5-SPL7 gene network that mediates the coordinated response to light and copper. *Plant Cell* 26, 4933–4953. doi: 10.1105/tpc.114.127340

Zuo, J., Niu, Q.-W., and Chua, N.-H. (2000). An estrogen receptor-based transactivator XVE mediates highly inducible gene expression in transgenic plants. *Plant J.* 24, 265–273. doi: 10.1046/j.1365-313x.2000.00868.x

Conflict of Interest Statement: The authors declare that the research was conducted in the absence of any commercial or financial relationships that could be construed as a potential conflict of interest.

frontiers in Plant Science

ORIGINAL RESEARCH
published: 10 July 2018
doi: 10.3389/fpls.2018.00990

MtMTP2-Facilitated Zinc Transport Into Intracellular Compartments Is Essential for Nodule Development in *Medicago truncatula*

*Javier León-Mediavilla[1], Marta Senovilla[1], Jesús Montiel[1], Patricia Gil-Díez[1], Ángela Saez[1], Igor S. Kryvoruchko[2†], María Reguera[1], Michael K. Udvardi[2], Juan Imperial[1,3] and Manuel González-Guerrero[1,4]**

[1] Centro de Biotecnología y Genómica de Plantas (UPM-INIA), Universidad Politécnica de Madrid, Madrid, Spain, [2] Noble Research Institute, Ardmore, OK, United States, [3] Instituto de Ciencias Ambientales, Consejo Superior de Investigaciones Científicas, Madrid, Spain, [4] Escuela Técnica Superior de Ingeniería Agronómica, Alimentaría y de Biosistemas, Universidad Politécnica de Madrid (UPM), Madrid, Spain

OPEN ACCESS

Edited by:
Michael A. Grusak, Agricultural Research Service (USDA), United States

Reviewed by:
Ulrike Mathesius, Australian National University, Australia
Erik Limpens, Wageningen University & Research, Netherlands

***Correspondence:**
Manuel González-Guerrero
manuel.gonzalez@upm.es

†Present address:
Igor S. Kryvoruchko, Department of Molecular Biology and Genetics, Bogazici University, Istanbul, Turkey

Specialty section:
This article was submitted to Plant Nutrition, a section of the journal Frontiers in Plant Science

Received: 15 March 2018
Accepted: 19 June 2018
Published: 10 July 2018

Citation:
León-Mediavilla J, Senovilla M, Montiel J, Gil-Díez P, Saez Á, Kryvoruchko IS, Reguera M, Udvardi MK, Imperial J and González-Guerrero M (2018) MtMTP2-Facilitated Zinc Transport Into Intracellular Compartments Is Essential for Nodule Development in Medicago truncatula. Front. Plant Sci. 9:990. doi: 10.3389/fpls.2018.00990

Zinc (Zn) is an essential nutrient for plants that is involved in almost every biological process. This includes symbiotic nitrogen fixation, a process carried out by endosymbiotic bacteria (rhizobia) living within differentiated plant cells of legume root nodules. Zn transport in nodules involves delivery from the root, via the vasculature, release into the apoplast and uptake into nodule cells. Once in the cytosol, Zn can be used directly by cytosolic proteins or delivered into organelles, including symbiosomes of infected cells, by Zn efflux transporters. *Medicago truncatula* MtMTP2 (*Medtr4g064893*) is a nodule-induced Zn-efflux protein that was localized to an intracellular compartment in root epidermal and endodermal cells, as well as in nodule cells. Although the *MtMTP2* gene is expressed in roots, shoots, and nodules, *mtp2* mutants exhibited growth defects only under symbiotic, nitrogen-fixing conditions. Loss of MtMTP2 function resulted in altered nodule development, defects in bacteroid differentiation, and severe reduction of nitrogenase activity. The results presented here support a role of MtMTP2 in intracellular compartmentation of Zn, which is required for effective symbiotic nitrogen fixation in *M. truncatula*.

Keywords: zinc, cation diffusion facilitator, metal transport protein, symbiotic nitrogen fixation, metal nutrition, nodulation

INTRODUCTION

Zinc (Zn) is an essential nutrient for plants as a cofactor of enzymes or as a structural element (Coleman, 1998; Broadley et al., 2007). Consequently, plants grown in soils with low Zn bioavailability, which include some of the main agricultural areas of the world, have severe growth defects (Alloway, 2008; Marschner, 2012). These include interveinal chlorosis, necrotic leaves, and stunted growth, the result of alterations in the plethora of processes mediated by Zn proteins (Coleman, 1998; Broadley et al., 2007). To prevent this and ensure proper Zn allocation, plants have developed a complex network of transcription factors, transporters, and small Zn-chelating molecules that direct this metal to the proper tissue, cell compartments, and apoproteins (Assunção et al., 2010; Sinclair and Krämer, 2012; Olsen and Palmgren, 2014).

Zinc transport is mediated typically by four different transporter families: the Zrt1/Irt1-like (ZIP) and the yellow stripe-like (YSL) families for transport into the cytosol; and the metal tolerance protein (MTP) and Zn^{2+}-ATPase families for efflux out of the cytosol (DiDonato et al., 2004; Eren and Argüello, 2004; Desbrosses-Fonrouge et al., 2005; Ishimaru et al., 2005; Olsen and Palmgren, 2014). Uptake of Zn from soils in dicots is mediated by ZIP proteins (Korshunova et al., 1999), in a process induced by soil acidification (Pedas and Husted, 2009). Zn can move symplastically from cell to cell and is released from endodermal cells into the xylem, via Zn^{2+}-ATPases (Hussain et al., 2004). YSL transporters are likely candidates to mediate Zn loading into the phloem, as a Zn-nicotianamine complex (Waters et al., 2006). Within cells, Zn is transported into organelles by MTP or Zn^{2+}-ATPases, either to be stored when in excess, or to be used to assemble Zn-proteins (Blaudez et al., 2003; Desbrosses-Fonrouge et al., 2005; Morel et al., 2009). Overall, these processes are regulated by a set of transcription factors that orchestrate Zn homeostasis (Assunção et al., 2010).

While leaves are the main Zn sink in most plants during vegetative growth (Broadley et al., 2007), legumes have an additional one: nitrogen-fixing root nodules (González-Guerrero et al., 2014, 2016). Nodules are root- or stem-associated organs that develop as a result of complex chemical exchanges with soil bacteria known as rhizobia (Downie, 2014). After detection of specific nodulation factors synthesized by the colonizing rhizobia (Oldroyd, 2013), cells of the root pericycle and cortex proliferate to originate the nodule primordia (Xiao et al., 2014). As the nodule develops, a root hair curls to surround the rhizobia in the root rhizoplane. The plasma membrane of this hair cell retracts into the cytosol, forming an infection thread that guides the rhizobia from the epidermis into the nodule core (Gage, 2002). There, in an endocytic-like process, rhizobia are released into the cytosol of cortical cells (Limpens et al., 2009). Under the proper physico-chemical conditions, rhizobia differentiate into bacteroids (Kereszt et al., 2011). Surrounded by a specialized plant-derived membrane, the symbiosome membrane, and protected from oxygen, bacteroids are able to synthesize nitrogenase, the iron-molybdenum enzyme complex responsible for converting atmospheric N_2 into NH_4^+ (Rubio and Ludden, 2005). Fixed nitrogen is transferred to the host plant, in exchange for photosynthate and mineral nutrients from the plant (Udvardi and Poole, 2013). Two morphological types of nodules are known as follows: determinate and indeterminate (Brewin, 1991). Indeterminate nodules, such as those present in the genera *Medicago* or *Pisum*, are characterized by the presence of a persistent apical meristem(s) that produce cylindrical or coralloid-shaped organs (Vasse et al., 1990). As a consequence, different developmental zones can be distinguished in such nodules: the meristem or Zone I, the region where rhizobia colonize the nodule and differentiate into bacteroids or Zone II, the nitrogen fixation zone or Zone III, and, in old nodules, the senescent zone or Zone IV (Vasse et al., 1990). To this, some authors add an Interzone between Zones II and III, were oxygen levels transition from atmospheric levels (20%) to microaerobiosis (<1%); and a Zone V, where the rhizobia grow saprophytically (Timmers et al., 2000; Roux et al., 2014). In addition to the zonation pattern, determinate and indeterminate nodules differ in the process of bacteroid differentiation, that is irreversible for the majority of indeterminate nodules, to the extent that they cannot proliferate if released from the nodules. These bacteroids also have a higher ploidy level and larger size, as a consequence of cysteine-rich peptides released by the host cell that participate in bacteroid development (Van de Velde et al., 2010; Kereszt et al., 2011; Kondorosi et al., 2013; Stonoha-Arther and Wang, 2018).

The specific role(s) of Zn in symbiotic nitrogen fixation is not clear. Given the multitude of Zn-proteins in a cell, Zn could act at several different levels. It has been reported that plants growing under Zn deficiency suffer reduced growth and reduced nitrogenase activity (Ibrikci and Moraghan, 1993; O'Hara, 2001). Similar effects result from silencing the expression of *MtZIP6*, a *Medicago truncatula* Zn transporter located in the plasma membrane of nitrogen-fixing nodule cells (Abreu et al., 2017). Nodule development in these silenced plants was also affected, resulting in smaller nodules compared to wild-type controls. Understanding how reduced uptake of Zn into cells affects nodule development and symbiotic nitrogen fixation is complicated by the fact that Zn plays a role in numerous intracellular processes. Knowledge of the intracellular fate of Zn would help in this regard. To this end, we are characterizing Zn transporters likely to be involved in organelle loading, especially be members of the MTP and Zn^{2+}-ATPase families.

Exploration of publicly available transcriptome databases (Benedito et al., 2008; Roux et al., 2014) revealed no Zn^{2+}-ATPase to be upregulated during nodule development. In contrast, *M. truncatula MtMTP2* (*Medtr4g064893*) was found to be expressed at higher levels in nodules than in any other organ. Here, we show that MtMTP2 is a Zn efflux protein located in an intracellular compartment, with an important role in nodule development and bacteroid differentiation.

MATERIALS AND METHODS

Biological Materials and Growth Conditions

Medicago truncatula R108 ecotype, the *Tnt1*-insertion mutants *mtp2-1* (NF11171) and *mtp2-2* (NF18305) were used in this study. Seeds were scarified in concentrated H_2SO_4 for 7 min and washed in dH_2O. Later, seeds were surface sterilized using 50% bleach for 90 s, washed in sterile dH_2O, and left overnight in sterile water to facilitate imbibition. After 48 h at 4°C, seeds were germinated in water-agar plates at 22°C for 48 h. Seedlings were then transplanted to sterilized perlite pots and inoculated with *Sinorhizobium meliloti* 2011, *S. meliloti* 2011 transformed with the GFP expressing pHC60 vector (Cheng and Walker, 1998), or *S. meliloti* 1021 expressing pCMB13 DsRED (Gage, 2002), as indicated. Plants were cultivated in a greenhouse in 16 h of light and 22°C conditions, and watered every 2 days with Jenner's solution or water, alternatively (Brito et al., 1994). This nutrient solution contained 5 mM $CaSO_4$, 1 mM KCl, 1 mM K_2HPO_4, 1 mM $MgSO_4$, 11.5 μM H_3BO_3, 7.3 μM Fe-citrate, 3.6 μM $MnSO_4$, 0.38 μM $ZnSO_4$, 0.16 mM

$CuSO_4$, and 4 nM $(NH_4)_6Mo_2O_{24}$. Nodules were collected 28 dpi. Non-nodulated plants were watered every 2 weeks with solutions supplemented with 20 mM NH_4NO_3. For hairy-root transformations, *M. truncatula* seedlings were transformed with *Agrobacterium rhizogenes* ARqua1 carrying the appropriate binary vector as described (Boisson-Dernier et al., 2001).

Complementation assays were performed using the yeast (*Saccharomyces cerevisiae*) strains DY1457 (MATa *ade6 can1 his3 leu2 trp1 ura3*), the yeast double mutant *zrc1cot1* (MATa *ade6 can1 his3 leu2 trp1 ura3 zrc1::his3 cot1::ura3*) (MacDiarmid et al., 2000), DY150 (MATa *ade2-1 his3-11 leu2-3,112 trp1-1 ura3-52 can1-100*(*oc*)), the mutant *ccc1* (MATa *ade2-1 his3-11 leu2-3,112 trp1-1 ura3-52 can1-100*(*oc*) *ccc1::his3*; Li et al., 2001), BY4741 (*his3 leu2 met1 ura3*), and the strain Δ*smf1* (*his3 leu2 met1 ura3* Δ*smf1*; ThermoFisher). All strains were grown in synthetic dextrose (SD) medium (Sherman et al., 1981) supplemented with necessary auxotrophic requirements, with 2% (w/v) glucose as the carbon source, and supplemented with Zn, iron, or manganese, when required.

Sequence Analysis and Protein Structure Prediction

To identify *M. truncatula* MTP family members, BLASTN and BLASTX searches were carried out in the *M. truncatula* Genome Project site[1] and include 13 members: MtMTP1, *Medtr8g024240*; MtMTP2, *Medtr4g064893*; MtMTP3, *Medtr2g036390*; MtMTP4, *Medtr3g080090*; MtMTP5, *Medtr7g093290*; MtMTP6, *Medtr1g088870*; MtMTP7, *Medtr4g008150*; MtMTP8, *Medtr3g062610*; MtMTP9, *Medtr2g064405*; MtMTP10, *Medtr8g046550*; MtMTP11, *Medtr7g022890*; MtMTP12, *Medtr6g463330*, MtMTP13, *Medtr5g075680*. Sequences from model MTP genes were obtained from the Transporter Classification Database[2] (Saier et al., 2014), NCBI[3] and Phytozome[4], and include *A. thaliana MTPs* (AtMTP1, *At2g46800*; AtMTP2, *At3g61940*, AtMTP3, *At3g58810*; AtMTP4, *At2g29410*; AtMTP5, *At3g12100*; AtMTP6, *At2g4783*; AtMTP7, *At1g51610*; AtMTP8, *At3g58060*; AtMTP9, *At1g79520*; AtMTP10, *At1g16310*; AtMTP11, *At2g39450*; AtMTP12, *At2g04620*), *Oryza sativa* MTPs (OsMTP1, *LOC_Os05g03780*; OsMTP8, *LOC_Os05g03780*) *Cucumis sativus* MTPs (CsMTP1, *Cucsa.362220*; CsMTP4, *Cucsa.146570*; CsMTP8, *Medtr3g062610*; CsMTP9, *Cucsa.118550*), *Anemone halleri* MTPs (AhMTP1-*A*, *FN428855*; AhMTP1-*B*, *Fn386317*; AhMTP1-*C*, *Fn386316*; AhMTP1-*D*, *Fn386315*), *Hordeum vulgare* MTPs (HvMTP1, *HORVU1Hr1G015500*; HvMTP8.*1*, *HORVU4Hr1G065110.1*), and *Populus trichocarpa* MTPs (PtdMTP1, *Potri.014G106200*; PtMTP11, *POPTR_0010s21810*). All these protein sequences were processed with MEGA7[5]. First, protein sequences were aligned using the Clustal Omega algorithm[6] (Sievers et al., 2011), and the alignment was visually examined to exclude alignment artifacts. Then, phylogenetic reconstruction was performed using the Neighbor-joining method, the Jones–Taylor–Thornton (JTT) substitution model, and assuming uniform rates (Saitou and Nei, 1987; Jones et al., 1992). Deletion sites were excluded from the alignment following the partial deletion method (95% site coverage cutoff). Unrooted tree visualization was carried out using FigTree[7].

MtMTP2 protein sequence from R108 was obtained from the Medicago Hapmap website[8]. The automated protein homology-modeling server SWISS-model[9] (Biasini et al., 2014) was used to predict the MtMTP2 protein structure based on the template 3h90 from the *Escherichia coli* Zn transporter YiiP (Lu et al., 2009). Protein structure was visualized using PyMOL (Schörindeger LLC, United States).

RNA Extraction and RT-qPCR

RNA was isolated from leaves, roots, or nodules from three-pooled plants (from independent experiments each) following the protocol previously described by Abreu et al. (2017). Briefly, RNA was extracted using Tri-Reagent® (Life Technologies, Carlsbad, CA) followed by a DNase treatment and later cleaned with RNeasy Minikit (Qiagen, Valencia, CA). Denaturing agarose gel was used to verify RNA quality. One microgram of DNA-free RNA was employed to generate cDNA by using PrimeScript RT Reagent Kit (Takara). Gene expression was determined by quantitative Real time RT-PCR (9700, Applied Biosystems, Carlsbad, CA, United States) using primers listed in Supplementary Table S1. The *M. truncatula ubiquitin carboxyl-terminal hydrolase* gene was used to normalize the results. Real-time cycler conditions have been previously described (González-Guerrero et al., 2010). The threshold cycle (Ct) was determined in triplicate. The relative levels of transcription were calculated using the $2^{-\Delta\Delta Ct}$ method (Livak and Schmittgen, 2001). As control, a non-RT sample was used to detect any possible DNA contamination.

Yeast Complementation Assays

Yeast complementation was performed by cloning the *MtMTP2* cDNA between the XbaI and BamHI sites of the yeast expression vector pAMBV or pDR196. Cloning in pAMBV was carried out by homologous recombination of *MtMT2* cDNA using primers 5 MtMTP2 XbaI pMBV and 3 MtMTP2 BamHI pAMBV (Supplementary Table S1). Cloning in pDR196 was carried out by restriction digestion and T4 ligation of the DNA fragment resulting from the XbaI and BamHI digestion of the amplicon resulting from amplifying by PCR *MtMTP2* cDNA with primers 5MtMTP2-XbaI and 3MtMTP2-BamHI (Supplementary Table S1). Yeast transformations were performed using a lithium acetate-based method (Schiestl and Gietz, 1989). Cells transformed with *pAMBV* or *pAMBV::MtMTP2* (in Zn phenotypic assays) or pDR196 or pDR196 (in the case of iron or manganese phenotypic assays) were selected in SD medium by leucine or uracil autotrophy, respectively.

[1] http://www.jcvi.org/medicago/index.php
[2] http://www.tcdb.org/
[3] http://www.ncbi.nlm.nih.gov/
[4] https://phytozome.jgi.doe.gov/pz/portal.html
[5] http://www.megasoftware.net
[6] https://www.ebi.ac.uk/Tools/msa/clustalo/
[7] http://tree.bio.ed.ac.uk/software/figtree/
[8] www.medicagohapmap.org
[9] https://swissmodel.expasy.org

For phenotypic tests, DY1457 and *zrc1cot1* transformants were plated in SD with or without supplementation of 500 μM $ZnSO_4$, DY150, and *ccc1* transformants were plated in SD with or without supplementation with 4 mM $FeSO_4$ and BY4741 and Δ*smf1* transformants were plated in SD with or without supplementation with 10 mM $MnCl_2$.

GUS Staining

A transcriptional fusion was constructed by amplifying 889 bases upstream of *MtMTP2* start codon using primers indicated on Supplementary Table S1, cloned in pDONR207 (Invitrogen), and transferred to pGWB3 (Nakagawa et al., 2007) using Gateway technology® (Invitrogen). This led to the fusion of the promoter region of *MtMTP2* with the β-*glucoronidase* (*gus*) gene in pGWB3. pGWB3::*MtMTP2* was transformed in *A. rhizogenes* ARqua1 and used to obtain *M. truncatula* composite root plants as indicated (Boisson-Dernier et al., 2001). GUS activity was determined in 28 dpi plants as described (Vernoud et al., 1999). The process was carried out from biological material originated from three independent assays carried out at different times of the year to select a representative image.

Immunolocalization of MtMTP2-HA

By using Gateway Technology® (Invitrogen), a DNA fragment of the full length *MtMTP2* genomic region and the 1,961 bases upstream of its start codon, was cloned into the plasmid pGWB13 (Nakagawa et al., 2007). Hairy-root transformation was performed as previously described (Boisson-Dernier et al., 2001). For confocal microscopy, transformed plants were inoculated with *S. meliloti* 2011 containing the pHC60 plasmid that constitutively expresses GFP (Cheng and Walker, 1998) or DsRED (Gage, 2002). Roots and nodules collected from 28 dpi plants were fixed by overnight incubation in 4% paraformaldehyde, 2.5% sucrose in phosphate buffer saline (PBS) at 4°C. After washing in PBS, nodules were cut in 100 μm sections with a Vibratome 1000 plus (Vibratome, St. Louis, MO, United States). Sections were dehydrated in a methanol series (30, 50, 70, 100% in PBS) for 5 min and then rehydrated. Cell walls were treated with 4% cellulase in PBS for 1 h at room temperature and with 0.1% Tween 20 in PBS for an additional 15 min. Sections were blocked with 5% bovine serum albumin (BSA) in PBS before their incubation with an anti-HA mouse monoclonal antibody (Sigma, St. Louis, MO) for 2 h at room temperature. After washing, an Alexa 594-conjugated anti-mouse rabbit monoclonal antibody (Sigma) was added to the sections for 1 h at room temperature. DNA was stained with DAPI after washing. Images were acquired with a confocal laser-scanning microscope (Leica SP8, Wetzlar, Germany). The process was carried out from biological material originated from three independent assays carried out at different times of the year to select a representative image.

Immunolocalization of MtMTP2-HA in an electron-microscope was carried out with *M. truncatula* plants transformed with *A. rhizogenes* ARqua1 pGWB13 carrying *MtMTP2* full gene and the 1,961 bases upstream the start codon. Transformed plants were inoculated with *S. meliloti* 2011 and 28 dpi nodules were collected and fixed in 1% formaldehyde and 0.5% glutaraldehyde in 50 mM potassium phosphate (pH 7.4) for 2 h. After that, the fixation solution was renewed for 1.5 h. Samples were washed in 50 mM potassium phosphate (pH 7.4) 3 × 30 min and 3 × 10 min. Nodules were dehydrated by incubation with ethanol dilution series of 30, 50, 70, 90 (10 min each), 96 (30 min), and 100% (1 h). Nodules were included in a series of ethanol and LR–white resin (London Resin Company Ltd., United Kingdom) dilutions: 1:3 (3 h), 1:1 (overnight), and 3:1 (3 h). Samples were included in resin during 48 h. All the process was performed at 4°C. Nodules were placed in gelatine capsules and filled with resin and polymerized at 60°C for 24 h. One-micron thin sections were prepared at *Centro Nacional de Microscopía Electrónica* (Madrid, Spain) with a Reichert Ultracut S-ultramicrotome fitted with a diamond knife. Thin sections were blocked in 2% bovine serum albumin in PBS for 30 min. Anti-HA rabbit monoclonal antibody (Sigma) was used as primary antibody, a 1:20 dilution in PBS. Samples were washed 10 times in PBS for 2 min. Anti-rabbit goat conjugated to a 15-nm gold particle (BBI solutions) was used as secondary antibody diluted 1:150 in PBS. Incubation was performed for 1 h followed by 10 washes in PBS for 2 min and 15 times in water for 2 min. Sections were stained with 2% uranyl acetate and imaged in a JEM 1400 electron microscope at 80 kV.

Acetylene Reduction Assay

Nitrogenase activity was measured by the acetylene reduction assay (Hardy et al., 1968). Nitrogen fixation was assayed in 28 dpi wild-type and mutant plants in 30 ml tubes fitted with rubber stoppers. Each tube contained roots from five independently transformed plants. Three milliliters of air inside were replaced with 3 ml of acetylene. Tubes were incubated at room temperature for 30 min. Gas samples (0.5 ml) were analyzed in a Shimadzu GC-8A gas chromatograph fitted with a Porapak N column. The amount of ethylene produced was determined by measuring the height of the ethylene peak relative to background. Each point consists of three tubes each with five pooled plants measured in triplicate.

Metal Content Determination

Inductively coupled plasma mass spectrometry (ICP-MS) was carried out at the Metal Analysis Unit of the Scientific and Technology Centre, Universidad de Barcelona (Barcelona, Spain). These samples were digested with HNO_3, H_2O_2, HF in a Teflon reactor at 90°C. The sample was diluted with deionized water. The final volume of the solution was calculated by weight difference with the original sample, and with the measured density of the solution, obtained from weighting a small aliquot of known volume. Samples were digested with three blanks in parallel. Metal determination was carried out in Agilent 7500ce instrument under standard conditions (RF power 1550 W, Nebulizer Burgener AriMist HP, Nebulizer Ar flow 0.75 l/min, sample pump 0.1 rps, QP resolution 0.7 amu at 10% height (^{7}Li, ^{89}Y, ^{205}Tl), integration time 0.9 s, reading replicates 3, calibration linear through zero, internal standard online addition ^{103}Rh, gas cell mode He collision). Calibration was carried out with five measurements using commercial certified solutions analyzed and compared with reference NIST solutions.

Confocal Imaging of Bacteroids and Colony-Forming-Units Assays

Confocal microscopy images of bacteroids were obtained from 28 dpi nodules. Nodules were ground with a micropestle in TY medium to release the bacteroids. The nodule homogenate was filtered using CellTrics® 30 μm columns and stained using propidium iodide (50 μg/ml) to visualize the bacteroids by using confocal microscopy at a 535 nm Ex/617 nm Em. Colony-forming-units (CFU) were obtained from fresh nodules harvested at 28 dpi. Nodules were weighed and surface-sterilized in 70% ethanol for 10 min followed by five washes with distillated water. The tissue was later ground with a micropestle in 200 μl TY medium. Serial dilutions of the homogenate were plated on TY solid media. Plates were incubated 48 h at 30°C, and the number of colonies was recorded (Montiel et al., 2016).

Statistical Tests

Results are presented as mean value ± standard deviation. Multiple comparisons were performed by one-way analysis of variance (ANOVA) followed by Tukey HSD *post hoc* at a probability level of 5% ($P < 0.05$). Pairwise comparisons were done by using Student's *t*-test at a probability level of 5% ($P < 0.05$). The JMP® (ver.11.0) statistical package (SAS Institute) was used for statistical analyses.

RESULTS

MtMTP2 Is Up-Regulated During Nodule Development

Out of the thirteen MTP genes in the *M. truncatula* genome, MtMTP2 was the one with the highest expression levels in nodules, as reported in the Medicago Gene Expression Atlas (Benedito et al., 2008) and in the Symbimics database (Roux et al., 2014; Supplementary Figure S1). *MtMTP2* expression analysis was performed to identify organs in which the gene/protein operates. Relatively high levels of *MtMTP2* transcripts were found in nodules compared to shoots and roots of inoculated plants (**Figure 1**). Shoots of nitrogen-fertilized, non-nodulated plants exhibited higher transcript levels than those of nodulated plants, although levels were still much lower than in nodules (**Figure 1**).

MTP proteins fall into seven groups, based on sequence similarity, which roughly correspond to putative metal substrates and subcellular localizations (Ricachenevsky et al., 2013). To gain insight into the possible metal substrates of MtMTP2, phylogenetic analysis was performed on 13 *M. truncatula* MTPs and homologous proteins in *Arabidopsis thaliana*, *Oryza sativa*, *Crocus sativus*, *Arabidopsis halleri*, *Populus trichocarpa*, *and Hordeum vulgare*. MtMTP2 showed strong similarity to CsMTP4 (54% similarity) described as a protein involved in Zn homeostasis in cucumber (Migocka et al., 2015) and AtMTP4 (48% similarity), a predicted Zn transporter of *A. thaliana* (Waters and Grusak, 2008; **Figure 1B**). To explore further Zn as a candidate substrate, a predicted tertiary structure of MtMTP2 was obtained by homology modeling based on the known crystal structure of the *E. coli* Zn transporter YiiP (Lu et al., 2009). The generated model revealed a Zn-binding domain made of residues H88, D92, H271, and D275 that corresponded to the YiiP site Z1 (D45, D49, H153, and D157; **Figure 1C**). The substitution of YiiP D45 residue by a histidine, H88, observed in MtMTP2 is also conserved in other plant MTP proteins (**Figure 1D**).

MtMTP2 Complements a Zinc Detoxification-Deficient Yeast Mutant

In *S. cerevisiae*, ZRC1 and COT1 are tonoplast transporters responsible for the storage of Zn in vacuoles (MacDiarmid et al., 2000). Yeast *zrc1/cot1* double mutants are hyper-sensitive to Zn in the growth medium. Genetic complementation assays using a yeast *zrc1/cot1* double mutant showed that expression of *MtMTP2* enabled the mutant strain to grow on otherwise toxic levels of Zn (500 μM $ZnSO_4$), consistent with a role of MtMTP2 in Zn efflux out of the cytosol (**Figure 2A**). In contrast, complementation assays using a yeast *ccc1* mutant affected in the transport of iron into the vacuole (Li et al., 2001), and an *smf1* mutant strain, which is unable to store manganese in the vacuole (Portnoy et al., 2000), showed no recovery of growth on media supplemented with 4 mM $FeSO_4$ or 10 mM $MnCl_2$, respectively (**Figures 2B,C**), indicating that MtMTP2 does not transport Fe or Mn in yeast.

MtMTP2 Is Located in an Endomembrane Compartment in Cells of Nodule Zones II to III

To determine *MtMTP2* expression distribution in nodules and roots, a segment of 889 bp upstream of the *MtMTP2* start codon was fused to the *gus* reporter gene and subsequently expressed in roots of *M. truncatula* inoculated with rhizobia. *MtMTP2* promoter activity was detected in roots and nodules (**Figure 3A**) and was most active in the segment from late Zone II to early Zone III, while lower GUS signal was detected at the meristematic zone and late zone III (**Figure 3B**). *In silico* analysis of *MtMTP2* expression in nodules using data obtained from the Symbimics database[10] (Roux et al., 2014) was consistent with GUS assays showing an increased expression pattern in the late differentiation zone (proximal Zone II) and in Zone III (Supplementary Figure S2). In roots, *MtMTP2*-regulated GUS activity was faintly detected at the epidermis, pericycle, and vascular tissue (**Figure 3C**).

Subcellular localization of *MtMTP2* was performed by fusing the DNA segment from 1,961 bp upstream of the *MtMTP2* start codon to the last codon before the stop codon to either GFP or to 3 hemagglutinin (HA) epitopes, resulting in *pMtMTP2::MtMTP2-GFP* and *pMtMTP2:: MtMTP2-HA*, respectively. Plants were transformed with these constructs and inoculated with *S. meliloti* strains constitutively expressing DsRED or GFP, followed by DAPI staining (**Figure 4**). Subcellular localization using both constructs was consistent with the results obtained with the GUS reporter assays. *pMtMTP2::MtMTP2-GFP* was localized intracellularly from the infection and

[10]https://iant.toulouse.inra.fr/symbimics/

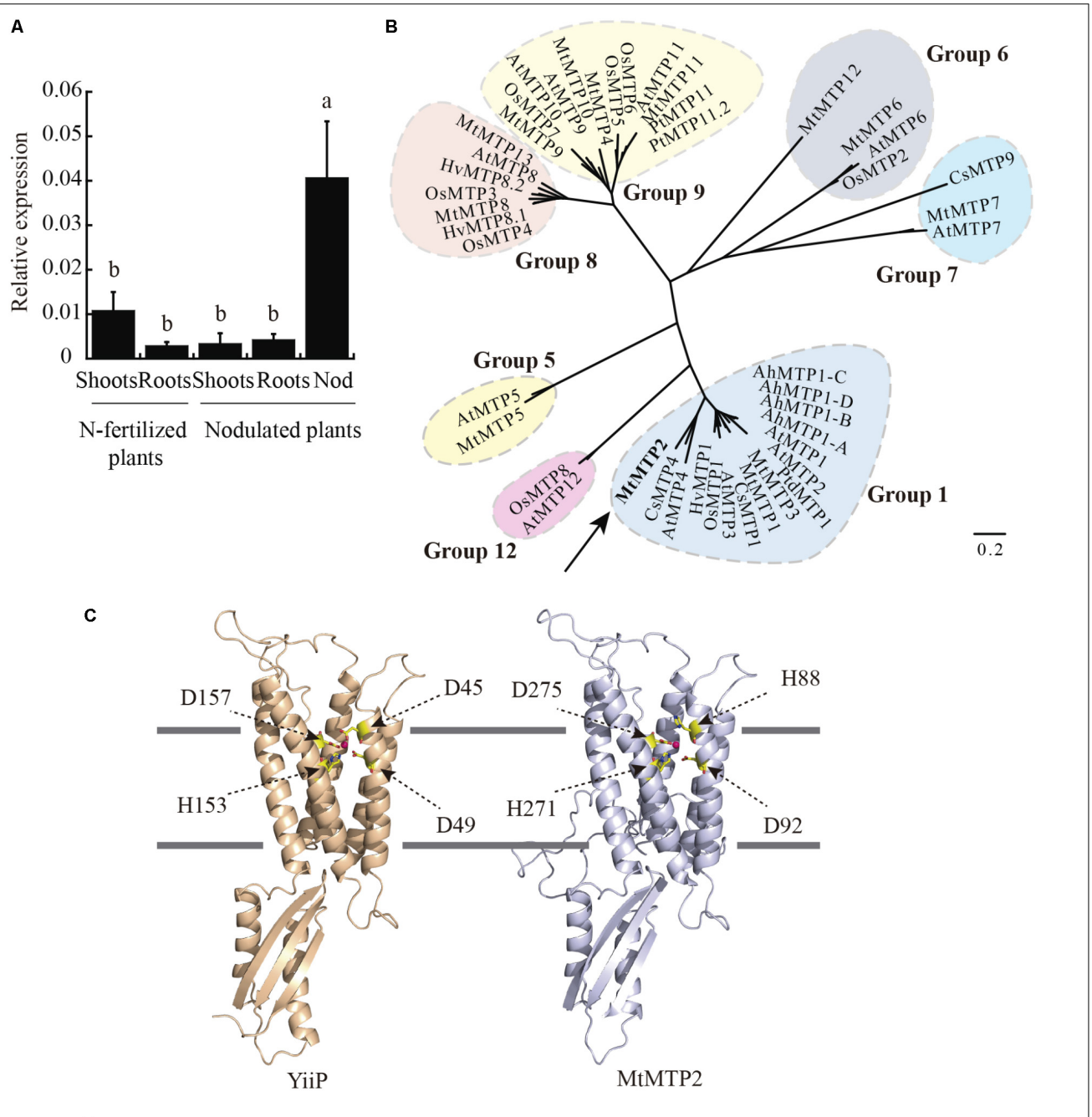

FIGURE 1 | *Medicago truncatula* metal tolerance protein 2 (MtMTP2), a member of the MTP protein family, is highly expressed in the nodule. **(A)** *MtMTP2* expression in nitrogen-fertilized and 28 dpi nodulated *M. truncatula* plants relative to the internal standard gene *Ubiquitin carboxyl-terminal hydrolase*. Values with different letters are significantly different (Tukey's HSD $p < 0.05$; $n = 4$). **(B)** Unrooted phylogenetic tree of the plant metal tolerance protein family. **(C)** Tertiary structure model of MtMTP2 and its template YiiP (3h90). Positions of metal coordinating amino acids and Zn(II) elements are indicated. **(D)** Alignment of the conserved amino acids in MTP members. The amino acid sequences were aligned using the ClustalW method.

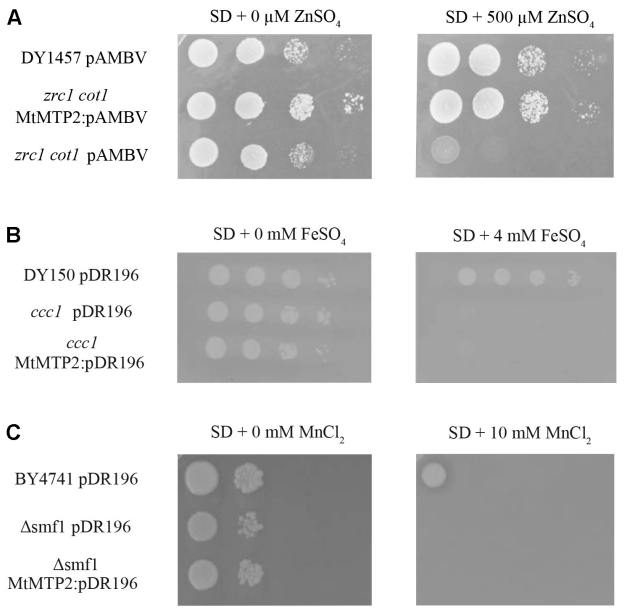

FIGURE 2 | MtMTP2 yeast complementation assays. **(A)** Yeast strain DY1457 was transformed with the pYPGE15 empty vector, while the double mutant *zrt1/cot1* was transformed with the empty pYPGE15 or with pYPEG15 containing *MtMTP2* coding DNA sequence. Serial dilutions (10×) of each transformant were grown for 3 days at 28°C on SD media with all the required amino acids and 500 μM $ZnSO_4$. Positive control was obtained without supplementing the media with $ZnSO_4$. **(B)** Yeast strain DY150 was transformed with the pDR196 empty vector, while *ccc1* mutant was transformed either with the empty pDR196 or with pDR196 containing *MtMTP2* coding DNA sequence. Serial dilutions (10×) of each transformant were grown for 3 days at 28°C on SD media with all the required amino acids and 4 mM $FeSO_4$. Positive control was obtained without supplementing the media with $FeSO_4$. **(C)** Yeast strain BY4741 was transformed with the pDR196 empty vector, while a deletion strain in *smf1* was transformed either with empty pDR196 or with pDR196 containing *MtMTP2* coding DNA sequence. Serial dilutions (10×) of each transformant were grown for 3 days at 28°C on SD media with all the required amino acids and 10 μM $MnCl_2$. Positive control was obtained without $MnCl_2$ supplementation.

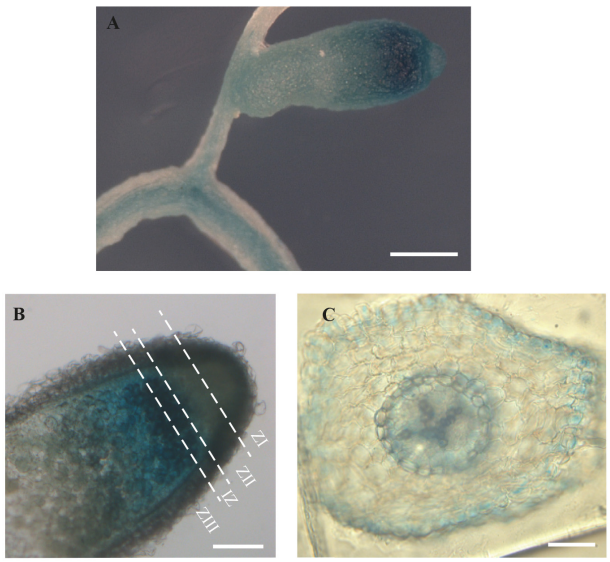

FIGURE 3 | Organ and tissue expression localization of *MtMTP2*. **(A)** GUS expression assay in roots and nodules of plants transformed with pGWB3 containing the *pMtMTP2::GUS* construct. Bar: 1 μm. **(B)** GUS expression assay in a longitudinal section of a nodule transformed with pGWB3 containing *pMtMTP2::GUS* construct. Bar: 100 mm. **(C)** Cross section of a *M. truncatula* root transformed with the plasmid pGWB3 containing the *pMtMTP2::GUS* construct. Bar: 50 μm.

differentiation zones and into the fixation zone in 28 dpi nodules, while no signal was found at the meristematic zone (**Figure 4A**). Localization using the *pMtMTP2::MtMTP2-HA* construct by immunostaining with Alexa594-conjugated antibody (Supplementary Figure S3), showed an identical pattern of distribution to that observed with *pMtMTP2::MtMTP2-GFP*. High magnification imaging of nodules 28 dpi allowed the visualization of *MtMTP2* intracellularly in infected cells (**Figures 4B,C**). No autofluorescence signal was detected under the experimental conditions used, as shown when primary anti-HA antibody for MtMTP2-HA detection was removed (Supplementary Figure S4), or when no MtMTP2-GFP protein was present (Supplementary Figure S5). In roots, MtMTP2-HA was detected in the epidermis and around the vasculature (**Figure 4D**), consistent with the promoter-GUS assays.

To further clarify the subcellular localization of MtMTP2, immunolocalization of MtMTP2-HA with a gold-conjugated antibody and transmission electron microscopy was used (**Figure 4E**). Gold particles were found concentrated in electron dense structures corresponding to intracellular compartments resembling endoplasmic reticulum (or associated domains) of infected cells and non-infected cells. No gold particles were detected associated with symbiosomes. When no primary antibody was used, no gold particles were found to be concentrated in any cell sections (Supplementary Figure S6).

MtMTP2 Mutants Exhibit Abnormal Accumulation of Zinc in Nodules and Impaired Nitrogen Fixation and Growth

To determine the physiological role of MtMTP2, two homozygous mutant lines of *MtMTP2*, *mtpt2-1* (NF11171), and *mtp2-2* (NF18305) were evaluated. Mutant line *mtpt2-1* harbors the *tnt1* insertion at the promoter region (−69 upstream of the start codon) while *mtp2-2* contains a *tnt1* insertion at the unique exon of the gene (+623 downstream the start codon; **Figure 5A**). These insertions resulted in a reduced level of *MtMTP2* expression in nodules, 80% reduction in the case of *mtpt2-1* and more than 99% in *mtpt2-2* (**Figure 5B**). Accordingly, they were designated as a knock-down and a knock-out *MtMTP2* mutants, respectively. Plant phenotypes were analyzed when nitrogen was provided in the nutrient solution as ammonium nitrate. Under these non-symbiotic conditions, no changes in the plant phenotype were detected in the *mtp2* mutants compared to wild-type plants (**Figure 5C**). Plant biomass (determined by the dry weight of shoots and roots) did not show significant differences among the genotypes analyzed (**Figure 5D**). Similarly,

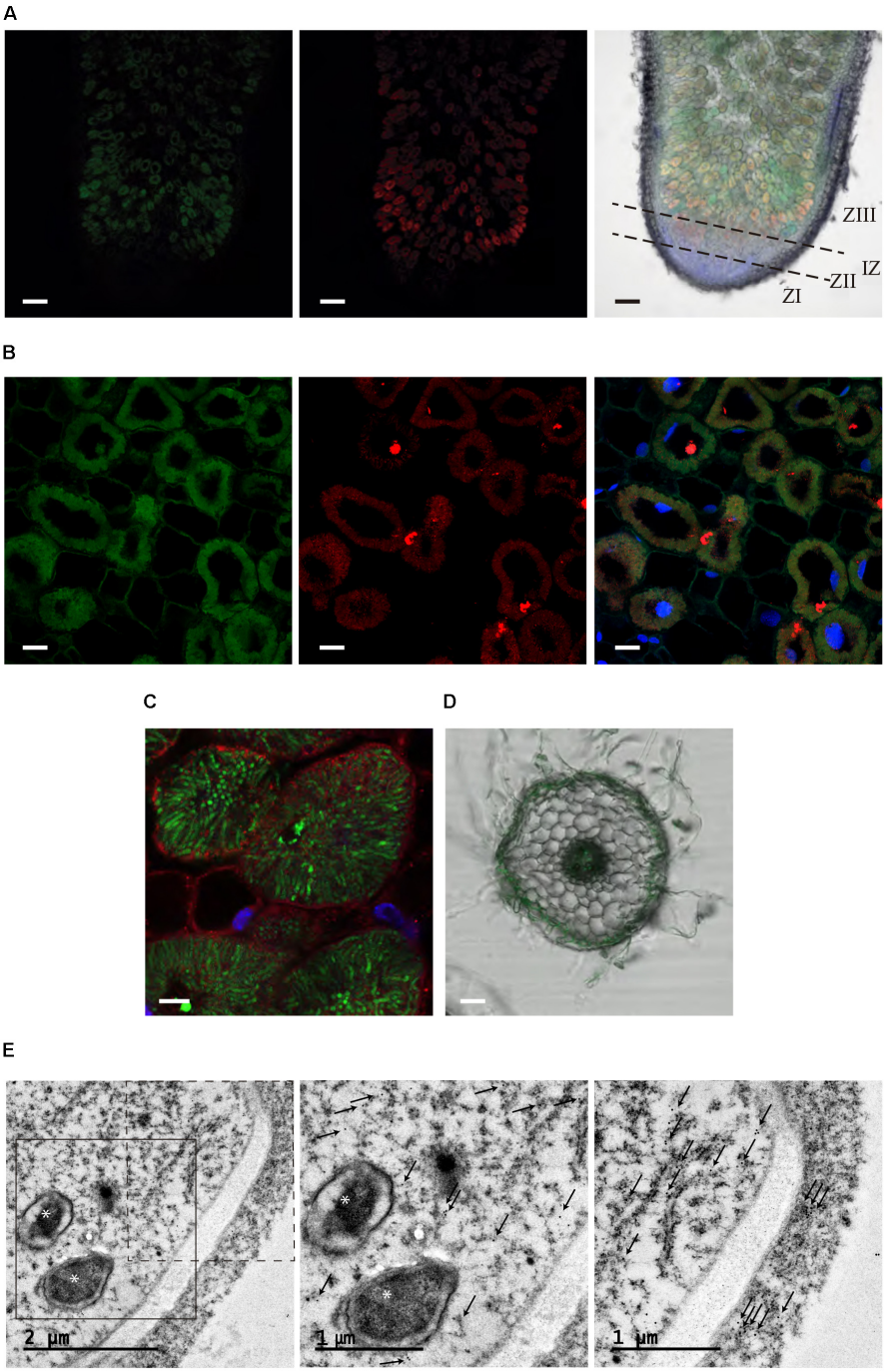

FIGURE 4 | Subcellular localization of *MtMTP2* in *Medicago truncatula*. **(A)** Cross section of a 28-dpi *M. truncatula* nodule expressing *pMtMTP2::MtMTP2-GFP* (green) **(A)** inoculated with a *Sinorhizobium meliloti* 1021 strain constitutively expressing DsRed (red). DNA was stained using 4′-6-diamino-phenylindole (DAPI) (blue). Left panel, GFP channel; central panel, DsRed channel; right panel, overlay of the previous two panels with DAPI channel and transillumination image. Bars: 100 µm. **(B)** Closer view of infection zone of a 28-dpi *M. truncatula* nodule expressing *pMtMTP2::MtMTP2-GFP* (green) inoculated with a *Sinorhizobium meliloti* 1021 strain constitutively expressing DsRed (red). DNA was stained using 4′-6-diamino-phenylindole (DAPI) (blue). Left panel, GFP channel; central panel, DsRed channel; right panel, overlay of the previous two panels with DAPI channel image. Bars: 25 µm. **(C)** Detail of an infected area of *M. truncatula* nodules transformed with *pMtMTP2::MtMTP2-HA*. Sections were immunostained with the antibody Alexa 594 (red). Transformed plants were inoculated with *S. meliloti* 2011 pHC60 strain constitutively expressing GFP (green). Bars: 10 µm. **(D)** Cross section of a 28-dpi *M. truncatula* root transiently expressing *pMtMTP2::MtMTP2-GFP* (green) overlaid with transillumination image. Bar: 50 µm. **(E)** Transmission electron microscopy (TEM) image of an infected cell of a 28 dpi *M. truncatula* nodule expressing the *pMtMTP2::MtMTP2-HA* construct, inoculated with *S. meliloti* 2011. Gold particles are indicated by arrows; bacteroids are indicated by asterisks. Left panel, general overview of an infected (left) and un-infected (right) cells; central panel, closer view of the region boxed with continuous line from the previous panel; right panel, closer view of the region boxed with discontinuous line in the left panel.

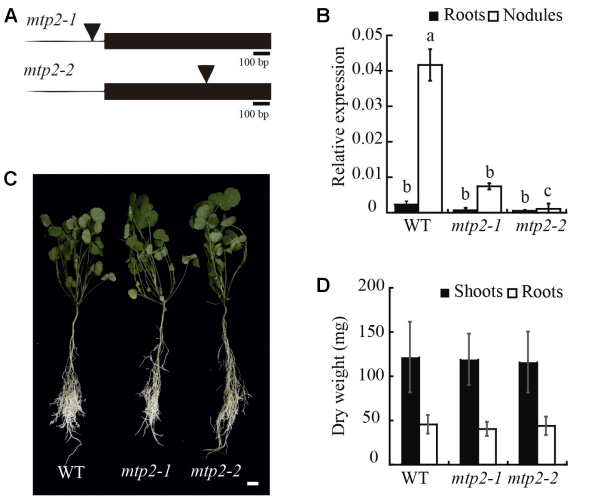

FIGURE 5 | *MtMTP2* mutants grown under non-symbiotic conditions did not show an altered phenotype. **(A)** Position of the transposable element of tobacco (*Nicotiana tabacum*) cell type 1 (*Tnt1*) in the *MtMTP2* genomic region in *mtp2-1* and *mtp2-2* mutants. **(B)** *MtMTP2* expression in roots (black) and nodules (white) of WT, *mtp2-1*, and *mtp2-2* plants relative to the internal gene *Ubiquitin carboxyl-terminal hydrolase 1*. Data are the mean ± SD of two independent experiments with four pooled plants. **(C)** From the left to the right, representative plants of *M. truncatula* WT, *mtp2-1*, and *mtp2-2* N-fertilized plants. Bars: 1 cm. **(D)** Dry weight of shoots (black) and roots (white). Data represent the mean ± SD of three experiments pooling, at least, ten independent plants (n = 10).

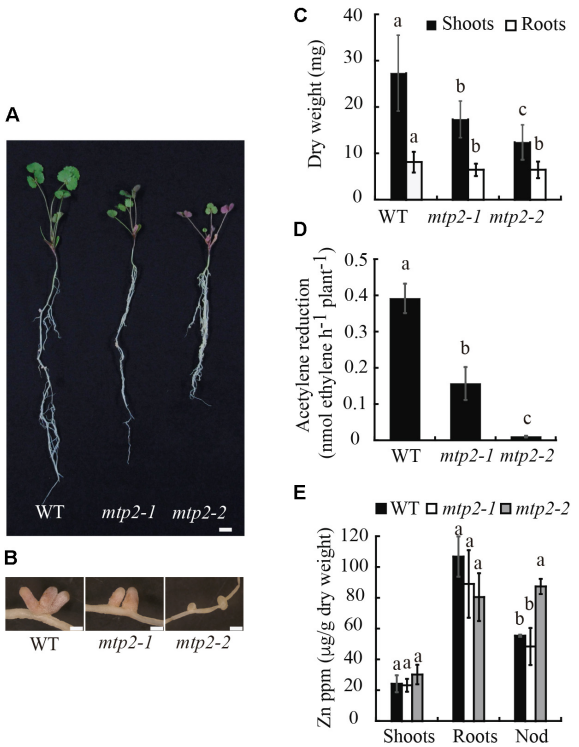

FIGURE 6 | *Medicago truncatula MTP2* mutation impairs nitrogen fixation. **(A)** Representative WT, *mtp2-1*, and *mtp2-2* plants. Bars: 1 cm. **(B)** Representative nodules of WT, *mtp2-1*, and *mtp2-2* plants. Bars: 500 µm. **(C)** Dry weight of shoots (black) and roots (white). Data are the mean ± SD of, at least, 10 plants. Comparisons have been made among the shoots and among the roots. **(D)** Nitrogenase activity of 28-dpi nodules. Acetylene reduction was measured in duplicate from three sets of four pooled plants. Data are the mean ± SD. **(E)** Zn content in shoots, roots and nodules of WT (black), *mtp2-1* (white), and *mtp2-2* (gray). Data are the mean ± SD of three sets of at least ten pooled plants. Values with different letters are significantly different (Tukey's HSD, $p < 0.05$).

no significant differences between wild type and mutant lines were observed when either no Zn or excess Zn (100×) were added to the nutrient solution (Supplementary Figure S7).

In contrast, under symbiotic conditions without mineral-N, mutant plants exhibited reduced growth and an altered nodule development (**Figure 6**). Nodules of the *mtp2-2* mutant were small, round, and white, in contrast to the long, cylindrical, pink nodules of the wild-type (**Figures 6A,B**). A time-course analysis of nodule growth was performed, which showed a progressive delay in nodule growth, but no delay in the start of nodulation of the mutants (Supplementary Figure S8). Consistent with the plant phenotypes observed, plant biomass (determined as dry weight) was reduced in both mutants (**Figure 6C**). Shoot biomass suffered a more drastic decrease linked to the mutation than did root biomass (a 36% reduction in the case of *mtpt2-1* and 55% for *mtpt2-2* shoots). However, root biomass was still significantly diminished in both mutants, and to a similar extent (20%). In order to determine if the phenotypic alterations observed were a consequence of a decline in nitrogenase activity, acetylene reduction assays were performed (Hardy et al., 1968). The knock-down mutant, *mtpt2-1* exhibited a reduction of 60% in nitrogenase activity while the knock-out mutant, *mtpt2-2* barely showed detectable enzyme activity (**Figure 6D**). Similar activity profile was observed when data were normalized to nodule number per root (Supplementary Figure S9). Zn content in shoots, roots, and nodules were determined in order to evaluate changes in the putative metal substrate of MtMTP2. While no significant changes in Zn content were detected in roots, and a slight increase was detected in the shoots of *mtpt2-2*, nodules of knock-out plants showed a substantial accumulation of Zn (∼40% increase; **Figure 6E**). This phenotype was not the result of additional insertions in the *tnt1* lines. Both mutant lines only share insertions in *MtMTP2*. Moreover, segregants containing the two wild-type copies of *MtMTP2* did not show any significant differences with wild-type plants (Supplementary Figure S10). A Zn gradient including suboptimal (0 µM added $ZnSO_4$), control (0.38 µM $ZnSO_4$) and supra-optimal Zn conditions (38 µM $ZnSO_4$) was applied in an attempt to complement the *mtp2* mutants' defective symbiotic phenotype (Supplementary Figure S11). None of the Zn conditions tested enabled recovery in growth (including biomass; Supplementary Figure S11A,B) nor in nitrogenase activity (Supplementary Figure S11C).

Absence of MTP2 Alters Nodule and Bacteroid Development

The smaller size of *mtp2* mutant nodules indicated altered nodule development. To explore this further, nodules were

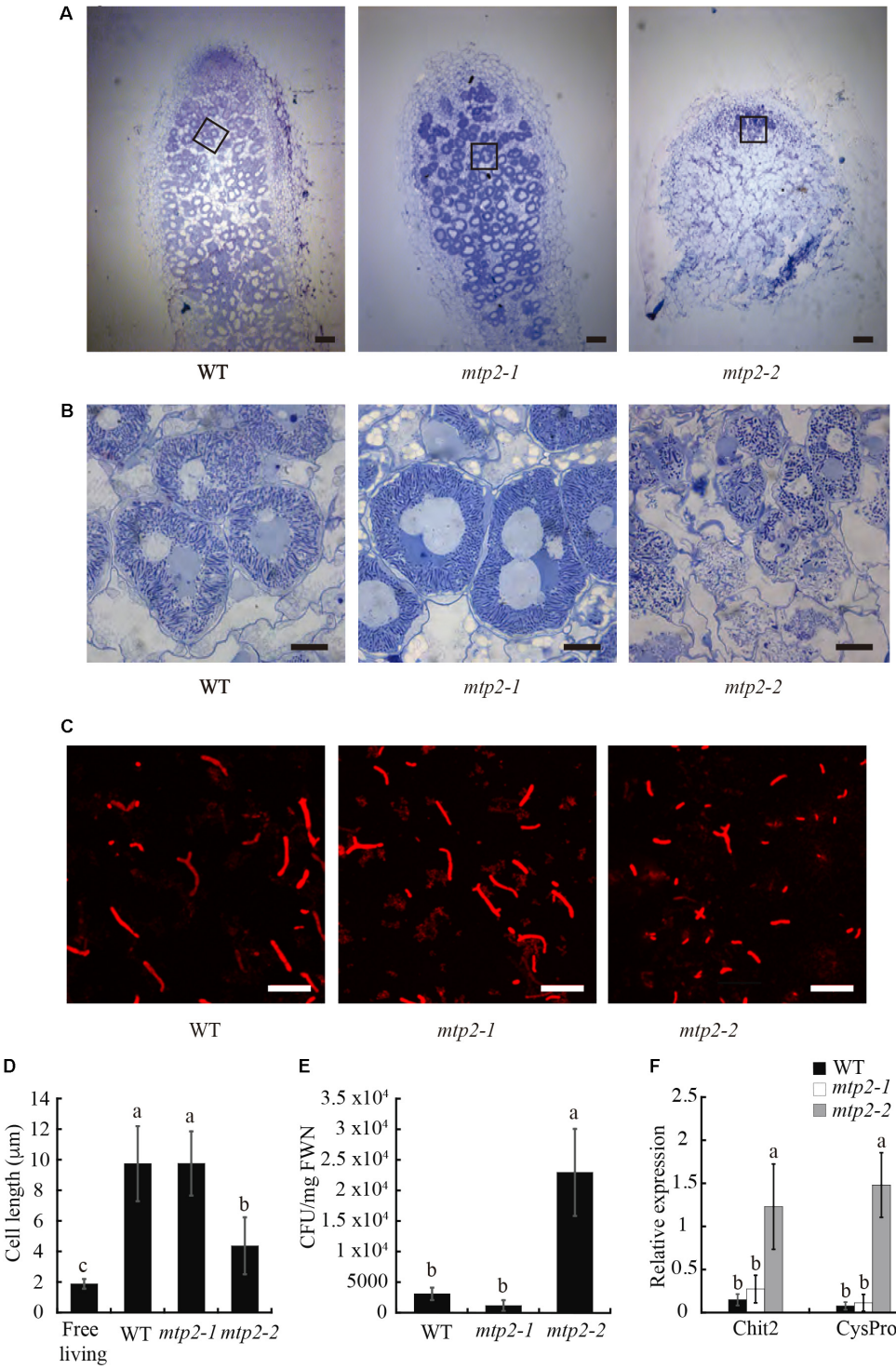

FIGURE 7 | Nodule and bacteroid development in *MtMTP2* mutants. **(A)** Longitudinal sections of *M. truncatula* WT, *mtp2-1*, and *mtp2-2* nodules stained with toluidine blue and visualized by light microscopy. Bars: 100 μm. **(B)** Detail of infected nodule cells of *M. truncatula* WT, *mtp2-1*, and *mtp2-2* nodules stained with toluidine blue and visualized by light microscopy. Bars: 10 μm. **(C)** Confocal image of *S. meliloti* stained with propidium iodide from 28-dpi *M. truncatula* WT, *mtp2-1*, and *mtp2-2* nodules. **(D)** Cell length of *S. meliloti* bacteroids isolated from WT, *mtp2-1*, and *mtp2-2* nodules. Data are the mean ± SD of at least 100 cells. **(E)** *S. meliloti* CFU per mg fresh weight of 28-dpi nodules from WT, *mtp2-1*, and *mtp2-2* plants. Data are the mean of three independent experiments ± SE. Values with different letters are significantly different (Tukey's HSD, $p < 0.05$). **(F)** Expression of the senescence marker genes Chit2 (chitinase *Medtr5g022560*) and CysProt (cysteine protease *Medtr6g079630*) in 28 dpi *M. truncatula* nodules of WT, *mtp2-1*, and *mtp2-2* plants relative to the internal standard gene *Ubiquitin carboxyl-terminal hydrolase*. Data are the mean of three independent experiments ± SE. Values with different letters are significantly different (Tukey's HSD, $p < 0.05$).

sectioned, stained with toluidine blue, and observed by light microscopy. Nodules of *mtpt2-2* a reduced infection zone and the disappearance of the fixation zone compared to WT nodules (**Figures 7A,B**).

The lack of a fixation zone in *mtp2-2* suggested that rhizobia may not have differentiated fully into bacteroids in these nodules. To test this idea, bacteroids were isolated from WT and *mtp2* mutant nodules and characterized (**Figures 7C,D**). Bacteroids from *mtp2-2* nodules were shorter in length than those of wild-type nodules, longer than free-living rhizobia (**Figure 7D**) and formed more colonies on solid growth medium (**Figure 7E**). These results are consistent with lack of full differentiation of rhizobia into nitrogen-fixing bacteroids within *mtp2-2* mutant nodules, or with early senescence that would hamper further nodule development. To test the later, gene expression of a chitinase (*Medtr5g022560*) and cystine protease (*Medtr6g079630*), two genes induced in senescence (Xi et al., 2013), was determined in 28 dpi nodules from wild-type and *mtp2-1* and *mtp2-2* plants (**Figure 7F**). The result showed an induction of senescent genes in *mtpt2-2* nodules.

DISCUSSION

MTP proteins are members of the Cation Diffusion Facilitator (CDF) family and known in plants (Ricachenevsky et al., 2013).These proteins are typically involved in Zn^{2+}, Mn^{2+}, or Fe^{2+} efflux from the cytosol, either out of the cell or into organelles (Desbrosses-Fonrouge et al., 2005; Eroglu et al., 2015). From a physiological point of view, their functions can be diverse, including metal detoxification (Desbrosses-Fonrouge et al., 2005), metal storage and allocation to sink organs (Eroglu et al., 2017), and metalation of apo-metalloproteins (Ellis et al., 2004). From a structural point of view, they seem to function as homodimers (Wei et al., 2004; Lu and Fu, 2007; Lu et al., 2009), in which each of the monomers is able to independently pump cations. This is made possible by transmembrane metal binding sites that, by being arranged in a specific geometry, confer specificity to the transporter (Argüello et al., 2012).

The genome of *M. truncatula* encodes 13 MTP proteins of which only one, MtMTP1, was previously characterized (Chen et al., 2009). MtMTP1 is a Zn transporter also involved in Zn efflux from the cytosol. It is expressed in roots and shoots. Zn modulates *MtMTP1* transcription: in roots, it is down-regulated, while it is up-regulated in shoots in response to Zn supply. Although there is no published information on its expression in nodules, its overall expression decreases with *S. meliloti* inoculation, and the ˆMedicago Gene Expression Atlas and the Symbimics databases indicate that it is downregulated in nodules. In this manuscript, we characterized MtMTP2 as an additional Zn^{2+}-transporting MTP family member that is involved in nodule development. Homology modeling of the structure of MtMTP2 shows that its metal substrate would likely be tetrahedrally coordinated by two histidine and two glutamate residues, since they occupy a similar location to the transmembrane metal binding site of template *E. coli* YiiP (Lu and Fu, 2007; Lu et al., 2009). Three of the four amino acid residues are conserved between both proteins, and the fourth, a change from glutamate to histidine, is consistent with Zn binding, both by its occurrence in many Zn-coordinating sites, and by its being conserved in other plant Zn-transporting MTPs (Ricachenevsky et al., 2013). Further supporting this ability to transport Zn are two related observations: the capability of MtMTP2 to functionally complement the Zn transport defect of the yeast *zrc1/cot1* double mutant (MacDiarmid et al., 2000); as well as the changes in Zn concentration in nodules of the *mtp2-2* mutant line. Although MTP proteins have been shown to be able to transport more than one substrate, MtMTP2 did not complement defects in Fe or Mn transport of specific yeast mutants (Podar et al., 2012; Migocka et al., 2015; Eroglu et al., 2017).

MtMTP2 is expressed in different plant organs. In roots, it is located in the epidermal and in vascular and endodermal cells; in nodules, in cells in Zones II and III, as indicated by promoter::*gus* fusions, fluorescence of a GFP-labeled MtMTP2, and immunolocalization of a HA-tagged protein. The latter two approaches also provide insight into the subcellular localization of MtMTP2, which is associated with an endomembrane compartment. Given the importance of Zn in symbiotic nitrogen fixation (Ibrikci and Moraghan, 1993; O'Hara, 2001), and the direction of transport of MTPs in general and MtMTP2 in particular (Wei and Fu, 2006), it was tempting to speculate that MtMTP2 might deliver Zn across the symbiosome membrane. However, electron microscopy analyses of the localization of HA-tagged MtMTP2 indicated that this is not the case, since no protein was associated with symbiosomes. Instead, signal was located in electron-dense bodies in the cell cytosol, that are distributed all over the cells. This allows us to discard plastids or mitochondria as putative locations based on their unique morphology, as well as the nucleus (based on its uniqueness), Golgi cisternae (very few in a cell), or late endosomal compartment (with a close distribution to the plasma membrane). Putative localization would be the endoplasmic reticulum. Considering that transport into the vacuole would mean a role in Zn storage, rather than a more active role in the cell functioning, and the severe phenotype observed by *MtMTP2* mutation, it can be speculated that the intracellular compartment would correspond to the endoplasmic reticulum. Previously, other MTP/CDF proteins have been associated to the endoplasmic reticulum, where they would play a role in metallating metalloproteins. Mutation of yeast *Msc2* gene results in the induction of the unfolded protein response, as a consequence of the Zn cofactor not being inserted in the proteins (Ellis et al., 2004, 2005). Similar roles of CDF proteins being involved in metallation of proteins have been attributed to *Schizosaccharomyces pombe* Zhf1 (Choi et al., 2018), or to mammalian ZnT5 and ZnT6 (Suzuki et al., 2005). However, co-localization with ER-specific markers would be needed to conclusively demonstrate MtMTP2 subcellular localization.

In spite of being expressed in many plant organs, MtMTP2 is primarily involved in nodule development. No aberrant

phenotype was observed for *mtp2* mutants under non-symbiotic conditions, indicating that either MtMTP2 is not required for key physiological processes in plants in the vegetative stage of growth when watered with NH_4NO_3, or that another, yet-to-be-determined protein can serve as a substitute for MTP2. However, when nitrogen is provided by endosymbiotic rhizobia in root nodules, mutating MtMTP2 has a dramatic effect. As was the case with silencing the Zn transporter *MtZIP6* (Abreu et al., 2017), altering Zn homeostasis in the nodule resulted in reduced nodule development and a substantial decrease in nitrogenase activity. However, the effect of mutating *MtMTP2* was more severe because its loss lead to alterations in nodule development, in bacteroid maturation, and nodule senescence. Phenotypic differences between *MtZIP6* silenced plants and the *MtMTP2* knock-out mutant seem to result from the inability to completely silence gene expression, since an activity of just 40% in the knock-down *mtp2-1* line is enough to allow for bacteroid development, a situation similar to what was reported for *MtZIP6* RNAi plants. This result is striking since it indicates the existence of one or several Zn proteins that receive Zn in an endomembrane compartment (likely the endoplasmic reticulum) that have an effect on bacteroid differentiation and/or nodule development, leading to early senescence. Alternatively, it could be argued that MtMTP2 might be protecting the nodule against Zn toxicity by sequestering the metal, as has been proposed for other MTP transporters (Blaudez et al., 2003; Desbrosses-Fonrouge et al., 2005). However, when no Zn was provided in the nutrient solution, no improvement of the mutant phenotype was observed, suggesting that no toxicity effect was at play. Moreover, altered nodule development has also been reported when mutating iron transporter SEN1 in *Lotus japonicus* (Hakoyama et al., 2012). Lowering Zn levels in the nutrient solution did not have any effect on plant growth or nitrogen fixation. This could be due to not being able to diminish enough the Zn levels (traces in perlite) or to already having achieved the bare minimum nitrogenase activity in *mtp2-2* plants. Future work will be directed toward characterizing the nodulation Zn-proteome to identify the Zn-proteins that might be governing nodule development and bacteroid differentiation.

AUTHOR CONTRIBUTIONS

JL-M and MS carried out most of the experimental work with assistance from ÁS (yeast complementation), PG-D (nodule development time course and effect of added metals on mtp2-2 phenotype), and JM (bacteroid development). IK and MU obtained the mtp2-1 and mtp2-2 mutants. MR, JI, and MG-G were responsible for experimental design, data analyses, and wrote the manuscript with contributions from all authors.

FUNDING

This work was supported by the Spanish Ministry of Economy and Competitiveness (grant AGL-2012-32974), a Marie Curie International Reintegration grant (IRG-2010-276771), and a European Research Council Starting grant (ERC-2013-StG-335284) to MG-G.

ACKNOWLEDGMENTS

The authors would like to thank Dr. David Eide (University of Wisconsin-Madison) for providing the DY1457 and *zrc1cot1* yeast strains, Dr. Jack Kaplan (University of Utah) for the DY150 and the *ccc1* yeast strains, Dr. Stephan Pollmann for the gift of the pAMBV vector, and members of CBGP laboratory 281 for critical discussions of the manuscript.

SUPPLEMENTARY MATERIAL

The Supplementary Material for this article can be found online at: https://www.frontiersin.org/articles/10.3389/fpls.2018.00990/full#supplementary-material

REFERENCES

Abreu, I., Saez, A., Castro-Rodríguez, R., Escudero, V., Rodríguez-Haas, B., Senovilla, M., et al. (2017). *Medicago truncatula* Zinc-Iron Permease6 provides zinc to rhizobia-infected nodule cells. *Plant Cell Environ.* 40, 2706–2719. doi: 10.1111/pce.13035

Alloway, B. J. (2008). *Zinc in Soils and Crop Nutrition*, 2nd Edn. Brussels: International Zinc Association and International Fertilizer Industry Association.

Argüello, J. M., Raimunda, D., and González-Guerrero, M. (2012). Metal transport across biomembranes: emerging models for a distinct chemistry. *J. Biol. Chem.* 287, 13510–13517. doi: 10.1074/jbc.R111.319343

Assunção, A. G. L., Herrero, E., Lin, Y.-F., Huettel, B., Talukdar, S., Smaczniak, C., et al. (2010). *Arabidopsis thaliana* transcription factors bZIP19 and bZIP23 regulate the adaptation to zinc deficiency. *Proc. Natl. Acad. Sci. U.S.A.* 107, 10296–10301. doi: 10.1073/pnas.1004788107

Benedito, V. A., Torres-Jerez, I., Murray, J. D., Andriankaja, A., Allen, S., Kakar, K., et al. (2008). A gene expression atlas of the model legume *Medicago truncatula*. *Plant J.* 55, 504–513. doi: 10.1111/j.1365-313X.2008.03519.x

Biasini, M., Bienert, S., Waterhouse, A., Arnold, K., Studer, G., Schmidt, T., et al. (2014). SWISS-MODEL: modelling protein tertiary and quaternary structure using evolutionary information. *Nucleic Acid. Res.* 42, W252–W258. doi: 10.1093/nar/gku340

Blaudez, D., Kohler, A., Martin, F., Sanders, D., and Chalot, M. (2003). Poplar metal tolerance protein 1 confers zinc tolerance and is an oligomeric vacuolar zinc transporter with an essential leucine zipper motif. *Plant Cell* 15, 2911–2928. doi: 10.1105/tpc.017541

Boisson-Dernier, A., Chabaud, M., Garcia, F., Bécard, G., Rosenberg, C., and Barker, D. G. (2001). Agrobacterium rhizogenes-transformed roots of *Medicago truncatula* for the study of nitrogen-fixing and endomycorrhizal symbiotic associations. *Mol. Plant Microbe Interact.* 14, 695–700. doi: 10.1094/MPMI.2001.14.6.695

Brewin, N. J. (1991). Development of the legume root nodule. *Annu. Rev. Cell Biol.* 7, 191–226. doi: 10.1146/annurev.cb.07.110191.001203

Brito, B., Palacios, J. M., Hidalgo, E., Imperial, J., and Ruíz-Argüeso, T. (1994). Nickel availability to pea (*Pisum sativum* L.) plants limits hydrogenase activity of *Rhizobium leguminosarum* bv. viciae bacteroids by affecting the processing of

the hydrogenase structural subunits. *J. Bacteriol.* 176, 5297–5303. doi: 10.1128/jb.176.17.5297-5303.1994

Broadley, M. R., White, P. J., Hammond, J. P., Zelko, I., and Lux, A. (2007). Zinc in plants. *New Phytol.* 173, 677–702. doi: 10.1111/j.1469-8137.2007.01996.x

Chen, M., Shen, X., Li, D., Ma, L., Dong, J., and Wang, T. (2009). Identification and characterization of MtMTP1, a Zn transporter of CDF family, in the *Medicago truncatula*. *Plant Physiol. Biochem.* 47, 1089–1094. doi: 10.1016/j.plaphy.2009.08.006

Cheng, H. P., and Walker, G. C. (1998). Succinoglycan is required for initiation and elongation of infection threads during nodulation of alfalfa by Rhizobium meliloti. *J. Bacteriol.* 180, 5183–5191.

Choi, S., Hu, Y.-M., Corkins, M. E., Palmer, A. E., and Bird, A. J. (2018). Zinc transporters belonging to the Cation Diffusion Facilitator (CDF) family have complementary roles in transporting zinc out of the cytosol. *PLoS Genet.* 14:e1007262. doi: 10.1371/journal.pgen.1007262

Coleman, J. E. (1998). Zinc enzymes. *Curr. Opin. Chem. Biol.* 2, 222–234. doi: 10.1016/S1367-5931(98)80064-1

Desbrosses-Fonrouge, A. G., Voigt, K., Schroder, A., Arrivault, S., Thomine, S., and Kramer, U. (2005). *Arabidopsis thaliana* MTP1 is a Zn transporter in the vacuolar membrane which mediates Zn detoxification and drives leaf Zn accumulation. *FEBS Lett.* 579, 4165–4174. doi: 10.1016/j.febslet.2005.06.046

DiDonato, R. J., Roberts, L. A., Sanderson, T., Eisley, R. B., and Walker, E. L. (2004). Arabidopsis Yellow Stripe-Like2 (YSL2) a metal-regulated gene encoding a plasma membrane transporter of nicotianamine-metal complexes. *Plant J.* 39, 403–414. doi: 10.1111/j.1365-313X.2004.02128.x

Downie, J. A. (2014). Legume nodulation. *Curr. Biol.* 24, R184–R190. doi: 10.1016/j.cub.2014.01.028

Ellis, C. D., MacDiarmid, C. W., and Eide, D. J. (2005). Heteromeric protein complexes mediate zinc transport into the secretory pathway of eukaryotic cells. *J. Biol. Chem.* 280, 28811–28818. doi: 10.1074/jbc.M505500200

Ellis, C. D., Wang, F., MacDiarmid, C. W., Clark, S., Lyons, T., and Eide, D. J. (2004). Zinc and the Msc2 zinc transporter protein are required for endoplasmic reticulum function. *J. Cell Biol.* 166, 325–335. doi: 10.1083/jcb.200401157

Eren, E., and Argüello, J. M. (2004). Arabidopsis HMA2, a divalent heavy metal-transporting PIB-type ATPase, is involved in cytoplasmic Zn2 + homeostasis. *Plant Physiol.* 136, 3712–3723. doi: 10.1104/pp.104.046292

Eroglu, S., Giehl, R. F. H., Meier, B., Takahashi, M., Terada, Y., Ignatyev, K., et al. (2017). Metal tolerance protein 8 mediates manganese homeostasis and iron reallocation during seeddevelopment and germination. *Plant Physiol.* 174, 1633–1647. doi: 10.1104/pp.16.01646

Eroglu, S., Meier, B., von Wiren, N., and Peiter, E. (2015). The vacuolar manganese transporter MTP8 determines tolerance to Fe deficiency-induced chlorosis in Arabidopsis. *Plant Physiol.* 170, 1030–1045. doi: 10.1104/pp.15.01194

Gage, D. J. (2002). Analysis of infection thread development using Gfp- and DsRed-expressing *Sinorhizobium meliloti*. *J. Bacteriol.* 184, 7042–7046. doi: 10.1128/JB.184.24.7042-7046.2002

González-Guerrero, M., Matthiadis, A., Sáez, Á, and Long, T. A. (2014). Fixating on metals: new insights into the role of metals in nodulation and symbiotic nitrogen fixation. *Front. Plant Sci* 5:45. doi: 10.3389/fpls.2014.00045

González-Guerrero, M., Raimunda, D., Cheng, X., and Argüello, J. M. (2010). Distinct functional roles of homologous Cu + efflux ATPases in *Pseudomonas aeruginosa*. *Mol. Microbiol.* 78, 1246–1258. doi: 10.1111/j.1365-2958.2010.07402.x

González-Guerrero, M. V. E., Sáez, Á, and Tejada-Jiménez, M. (2016). Transition metal transport in plants and associated endosymbionts. Arbuscular mycorrhizal fungi and rhizobia. *Front. Plant Sci.* 7:1088. doi: 10.3389/fpls.2016.01088

Hakoyama, T., Niimi, K., Yamamoto, T., Isobe, S., Sato, S., Nakamura, Y., et al. (2012). The integral membrane protein SEN1 is required for symbiotic nitrogen fixation in *Lotus japonicus* nodules. *Plant Cell Physiol.* 53, 225–236. doi: 10.1093/pcp/pcr167

Hardy, R. W., Holsten, R. D., Jackson, E. K., and Burns, R. C. (1968). The acetylene-ethylene assay for n(2) fixation: laboratory and field evaluation. *Plant Physiol.* 43, 1185–1207. doi: 10.1104/pp.43.8.1185

Hussain, D., Haydon, M. J., Wang, Y., Wong, E., Sherson, S. M., Young, J., et al. (2004). P-Type ATPase heavy metal transporters with roles in essential zinc homeostasis in Arabidopsis. *Plant Cell* 16, 1327–1339. doi: 10.1105/tpc.020487

Ibrikci, H., and Moraghan, J. T. (1993). Differential responses of soybean and dry bean to zinc deficiency. *J. Plant Nutr.* 16, 1791–1805. doi: 10.1080/01904169309364650

Ishimaru, Y., Suzuki, M., Kobayashi, T., Takahashi, M., Nakanishi, H., Mori, S., et al. (2005). OsZIP4, a novel zinc-regulated zinc transporter in rice. *J. Exp. Bot.* 56, 3207–3214. doi: 10.1093/jxb/eri317

Jones, D., Taylo, W., and Thronton, J. (1992). The rapid generation of mutation data matrices from protein sequences. *Comput. Appl. Biosci.* 8, 275–282. doi: 10.1093/bioinformatics/8.3.275

Kereszt, A., Mergaert, P., and Kondorosi, E. (2011). Bacteroid development in legume nodules: evolution of mutual benefit or of sacrificial victims? *Mol. Plant Microbe Interact.* 24, 1300–1309. doi: 10.1094/MPMI-06-11-0152

Kondorosi, E., Mergaert, P., and Kereszt, A. (2013). A Paradigm for endosymbiotic life: cell differentiation of Rhizobium bacteria provoked by host plant factors. *Annu. Rev. Microbiol.* 67, 611–628. doi: 10.1146/annurev-micro-092412-155630

Korshunova, Y. O., Eide, D., Clark, W. G., Guerinot, M. L., and Pakrasi, H. B. (1999). The IRT1 protein from *Arabidopsis thaliana* is a metal transporter with a broad substrate range. *Plant Mol. Biol.* 40, 37–44. doi: 10.1023/A:1026438615520

Li, L., Chen, O. S., Ward, D. M., and Kaplan, J. (2001). CCC1 is a transporter that mediates vacuolar iron storage in yeast. *J. Biol. Chem.* 276, 29515–29519. doi: 10.1074/jbc.M103944200

Limpens, E., Ivanov, S., van Esse, W., Voets, G., Fedorova, E., and Bisseling, T. (2009). Medicago N2-fixing symbiosomes acquire the endocytic identity marker Rab7 but delay the acquisition of vacuolar identity. *Plant Cell* 21, 2811–2828. doi: 10.1105/tpc.108.064410

Livak, K. J., and Schmittgen, T. D. (2001). Analysis of relative gene expression data using Real-Time Quantitative PCR and the 2-ΔΔCT method. *Methods* 25, 402–408. doi: 10.1006/meth.2001.1262

Lu, M., Chai, J., and Fu, D. (2009). Structural basis for autoregulation of the zinc transporter YiiP. *Nat. Struct. Mol. Biol.* 16, 1063–1067. doi: 10.1038/nsmb.1662

Lu, M., and Fu, D. (2007). Structure of the zinc transporter YiiP. *Science* 317, 1746–1748. doi: 10.1126/science.1143748

MacDiarmid, C. W., Gaither, L., and Eide, D. (2000). Zinc transporters that regulate vacuolar zinc storage in *Saccharomyces cerevisiae*. *EMBO J.* 19, 2845–2855. doi: 10.1093/emboj/19.12.2845

Marschner, P. (2012). *Mineral Nutrition of Higher Plants*, 3rd Edn. Cambridge, MA: Academic Press.

Migocka, M., Kosieradzka, A., Papierniak, A., Maciaszczyk-Dziubinska, E., Posyniak, E., Garbiec, A., et al. (2015). Two metal-tolerance proteins, MTP1 and MTP4, are involved in Zn homeostasis and Cd sequestration in cucumber cells. *J. Exp. Bot.* 66, 1001–1015. doi: 10.1093/jxb/eru459

Montiel, J., Szücs, A., Boboescu, I. Z., Gherman, V. D., Kondorosi, É, and Kereszt, A. (2016). Terminal bacteroid differentiation is associated with variable morphological changes in legume species belonging to the inverted repeat-lacking clade. *Mol. Plant Microbe Interact.* 29, 210–219. doi: 10.1094/MPMI-09-15-0213-R

Morel, M., Crouzet, J., Gravot, A., Auroy, P., Leonhardt, N., Vavasseur, A., et al. (2009). AtHMA3, a P1B-ATPase allowing Cd/Zn/Co/Pb vacuolar storage in Arabidopsis. *Plant Physiol.* 149, 894–904. doi: 10.1104/pp.108.130294

Nakagawa, T., Kurose, T., Hino, T., Tanaka, K., Kawamukai, M., Niwa, Y., et al. (2007). Development of series of gateway binary vectors, pGWBs, for realizing efficient construction of fusion genes for plant transformation. *J. Biosci. Bioeng.* 104, 34–41. doi: 10.1263/jbb.104.34

O'Hara, G. W. (2001). Nutritional constraints on root nodule bacteria affecting symbiotic nitrogen fixation: a review. *Aust. J. Exp. Agric.* 41, 417–433. doi: 10.1071/EA00087

Oldroyd, G. E. D. (2013). Speak, friend, and enter: signalling systems that promote beneficial symbiotic associations in plants. *Nat. Rev. Microbiol.* 11, 252–263. doi: 10.1038/nrmicro2990

Olsen, L. I., and Palmgren, M. G. (2014). Many rivers to cross: the journey of zinc from soil to seed. *Front. Plant Sci.* 5:30. doi: 10.3389/fpls.2014.00030

Pedas, P., and Husted, S. (2009). Zinc transport mediated by barley ZIP proteins are induced by low pH. *Plant Signal. Behav.* 4, 842–845. doi: 10.4161/psb.4.9.9375

Podar, D., Scherer, J., Noordally, Z., Herzyk, P., Nies, D., and Sanders, D. (2012). Metal selectivity determinants in a family of transition metal transporters. *J. Biol. Chem.* 287, 3185–3196. doi: 10.1074/jbc.M111.305649

Portnoy, M. E., Liu, X. F., and Culotta, V. C. (2000). *Saccharomyces cerevisiae* expresses three functionally distinct homologues of the nramp family of metal transporters. *Mol. Cell Biol.* 20, 7893–7902. doi: 10.1128/MCB.20.21.7893-7902.2000

Ricachenevsky, F., Menguer, P., Sperotto, R., Williams, L., and Fett, J. (2013). Roles of plant metal tolerance proteins (MTP) in metal storage and potential use in biofortification strategies. *Front. Plant Sci.* 4:144. doi: 10.3389/fpls.2013.00144

Roux, B., Rodde, N., Jardinaud, M.-F., Timmers, T., Sauviac, L., Cottret, L., et al. (2014). An integrated analysis of plant and bacterial gene expression in symbiotic root nodules using laser-capture microdissection coupled to RNA sequencing. *Plant J.* 77, 817–837. doi: 10.1111/tpj.12442

Rubio, L. M., and Ludden, P. W. (2005). Maturation of nitrogenase: a biochemical puzzle. *J. Bacteriol.* 187, 405–414. doi: 10.1128/JB.187.2.405-414.2005

Saier, M. H., Reddy, V. S., Tamang, D. G., and Västermark, Å. (2014). The transporter classification database. *Nucleic Acids Res* 42, D251–D258. doi: 10.1093/nar/gkt1097

Saitou, N., and Nei, M. (1987). The neighbor-joining method: a new method for reconstructing phylogenetic trees. *Mol. Biol. Evol.* 4, 406–425.

Schiestl, R. H., and Gietz, R. D. (1989). High efficiency transformation of intact yeast cells using single stranded nucleic acids as a carrier. *Curr. Genet*. 16, 339–346. doi: 10.1007/BF00340712

Sherman, F., Fink, G. R., and Hicks J. B. (1981). *Methods in Yeast Genetics: Laboratory Manual*. New York, NY: Cold Spring Harbor Laboratory.

Sievers, F., Wilm, A., Dineen, D., Gibson, T. J., Karplus, K., Li, W., et al. (2011). Fast, scalable generation of high-quality protein multiple sequence alignments using Clustal Omega. *Int Mol. Syst. Biol.* 7:539. doi: 10.1038/msb.2011.75

Sinclair, S. A., and Krämer, U. (2012). The zinc homeostasis network of land plants. *Biochim. Biophys. Acta* 1823, 1553–1567. doi: 10.1016/j.bbamcr.2012.05.016

Stonoha-Arther, C., and Wang, D. (2018). Tough love: accomodating intracellular bacteria through directed secretion of antimicrobial peptides during the nitrogen-fixing symbiosis. *Curr. Opin. Plant Biol.* 44, 155–163. doi: 10.1016/j.pbi.2018.04.017

Suzuki, T., Ishihara, K., Migaki, H., Ishihara, K., Nagao, M., Yamaguchi-Iwai, Y., et al. (2005). Two different zinc transport complexes of Cation Diffusion Facilitator proteins localized in the secretory pathway operate to activate alkaline phosphatases in vertebrate cells. *J. Biol. Chem.* 280, 30956–30962. doi: 10.1074/jbc.M506902200

Timmers, A. C. J., Soupène, E., Auriac, M. C., de Billy, F., Vasse, J., Boistard, P., et al. (2000). Saprophytic intracellular rhizobia in alfalfa nodules. *Mol. Plant Microbe Interact.* 13, 1204–1213. doi: 10.1094/MPMI.2000.13.11.1204

Udvardi, M., and Poole, P. S. (2013). Transport and metabolism in legume-rhizobia symbioses. *Annu. Rev. Plant Biol.* 64, 781–805. doi: 10.1146/annurev-arplant-050312-120235

Van de Velde, W., Zehirov, G., Szatmari, A., Debreczeny, M., Ishihara, H., Kevei, Z., et al. (2010). Plant peptides govern terminal differentiation of bacteria in symbiosis. *Science* 327, 1122–1126. doi: 10.1126/science.1184057

Vasse, J., de Billy, F., Camut, S., and Truchet, G. (1990). Correlation between ultrastructural differentiation of bacteroids and nitrogen fixation in alfalfa nodules. *J. Bacteriol.* 172, 4295–4306. doi: 10.1128/jb.172.8.4295-4306.1990

Vernoud, V., Journet, E. P., and Barker, D. G. (1999). MtENOD20, a Nod factor-inducible molecular marker for root cortical cell activation. *Mol. Plant Microbe Interact.* 12, 604–614. doi: 10.1094/MPMI.1999.12.7.604

Waters, B. M., Chu, H.-H., DiDonato, R. J., Roberts, L. A., Eisley, R. B., Lahner, B., et al. (2006). Mutations in Arabidopsis Yellow Stripe-Like1 and Yellow Stripe-Like3 reveal their roles in metal ion homeostasis and loading of metal ions in seeds. *Plant Physiol.* 141, 1446–1458. doi: 10.1104/pp.106.082586

Waters, B. M., and Grusak, M. A. (2008). Quantitative trait locus mapping for seed mineral concentrations in two *Arabidopsis thaliana* recombinant inbred populations. *New Phytol.* 179, 1033–1047. doi: 10.1111/j.1469-8137.2008.02544.x

Wei, Y., and Fu, D. (2006). Binding and transport of metal ions at the dimer interface of the *Escherichia coli* metal transporter YiiP. *J. Biol. Chem.* 281, 23492–23502. doi: 10.1074/jbc.M602254200

Wei, Y., Li, H., and Fu, D. (2004). Oligomeric state of the *Escherichia coli* metal transporter YiiP. *J. Biol. Chem.* 279, 39251–39259. doi: 10.1074/jbc.M407044200

Xi, J. L., Chen, Y., Nakashima, J., Wang, S. M., and Chen, R. (2013). *Medicago truncatula* esn1 defines a genetic locus involved in nodule senescence and symbiotic nitrogen fixation. *Mol. Plant Microbe Interact.* 26, 893–902. doi: 10.1094/MPMI-02-13-0043-R

Xiao, T. T., Schilderink, S., Moling, S., Deinum, E. E., Kondorosi, E., Franssen, H., et al. (2014). Fate map of *Medicago truncatula* root nodules. *Development* 141, 3517–3528. doi: 10.1242/dev.110775

Conflict of Interest Statement: The authors declare that the research was conducted in the absence of any commercial or financial relationships that could be construed as a potential conflict of interest.

frontiers in Plant Science

ORIGINAL RESEARCH
published: 16 July 2018
doi: 10.3389/fpls.2018.00872

Copper Nanoparticles Induced Genotoxicty, Oxidative Stress, and Changes in Superoxide Dismutase (SOD) Gene Expression in Cucumber (*Cucumis sativus*) Plants

Kareem A. Mosa[1,2], Mohamed El-Naggar[3], Kalidoss Ramamoorthy[4], Hussain Alawadhi[5], Attiat Elnaggar[4], Sylvie Wartanian[1], Emy Ibrahim[1] and Hala Hani[1]*

[1] Department of Applied Biology, College of Sciences, University of Sharjah, Sharjah, United Arab Emirates, [2] Department of Biotechnology, Faculty of Agriculture, Al-Azhar University, Cairo, Egypt, [3] Department of Chemistry, College of Sciences, University of Sharjah, Sharjah, United Arab Emirates, [4] Environmental and Chemical Biology Research Group, Research Institute of Science and Engineering, University of Sharjah, Sharjah, United Arab Emirates, [5] Center of Advanced Materials Research, Research Institute of Sciences and Engineering, University of Sharjah, Sharjah, United Arab Emirates

OPEN ACCESS

Edited by:
Hannetz Roschzttardtz, Pontificia Universidad Católica de Chile, Chile

Reviewed by:
Julio Paez Valencia, University of Wisconsin-Madison, United States
Anjana Jajoo, Devi Ahilya University, India

***Correspondence:**
Kareem A. Mosa
kmosa@sharjah.ac.ae

Specialty section:
This article was submitted to Plant Nutrition, a section of the journal Frontiers in Plant Science

Received: *17 February 2018*
Accepted: *04 June 2018*
Published: *16 July 2018*

Citation:
Mosa KA, El-Naggar M, Ramamoorthy K, Alawadhi H, Elnaggar A, Wartanian S, Ibrahim E and Hani H (2018) Copper Nanoparticles Induced Genotoxicty, Oxidative Stress, and Changes in Superoxide Dismutase (SOD) Gene Expression in Cucumber (Cucumis sativus) Plants. Front. Plant Sci. 9:872. doi: 10.3389/fpls.2018.00872

With the increased use of metal nanoparticles (NPs), their access to the food chain has become a main concern to scientists and holds controversial social implications. This research particularly sheds light on copper nanoparticles (CuNP), as they have been commonly used in several industries nowadays. In this study, we investigated the phytotoxicity of CuNP on cucumber (*Cucumis sativus*) plants grown hydroponically. Atomic Absorption Spectroscopy (AAS), X-Ray Fluorescence (XRF), and Scanning Electron Microscopy (SEM) analysis confirmed that *C. sativus* treated with CuNP accumulated CuNP in the plant tissues, with higher levels in roots, with amounts that were concentration dependent. Furthermore, genotoxicity was assessed using Random amplified polymorphic DNA (RAPD) technique, and our results showed that CuNP caused genomic alterations in *C. sativus*. Phenotypical, physiological, and biochemical changes were assessed by determining the CuNP treated plant's total biomass, chlorophyll, H_2O_2 and MDA contents, and electrolyte leakage percentage. The results revealed notable adverse phenotypical changes along with decreased biomass and decreased levels of the photosynthetic pigments (Chlorophyll a and b) in a concentration-dependent manner. Moreover, CuNP induced damage to the root plasma membrane as determined by the increased electrolyte leakage. A significant increase in H_2O_2 and MDA contents were detected in *C. sativus* CuNP treated plants. Additionally, copper-zinc superoxide dismutase (Cu-Zn SOD) gene expression was induced under CuNP treatment. Overall, our results demonstrated that CuNP of 10–30 nm size were toxic to *C. sativus* plants. This finding will encourage the safe production and disposal NPs. Thus, reducing nano-metallic bioaccumulation into our food chain through crop plants; that possesses a threat to the ecological system.

Keywords: phytotoxicity, copper nanoparticles, hydrophonic system, XRF analysis, genotoxicity, *Cucumis sativus*

INTRODUCTION

Nanotechnology, being a revolutionary science, has been a top trend field in the scientific community because of the enormous uses and utilization of nanoparticles (NPs) in many industrial sectors and research fields. NPs have been used in various domains including medicine, electronics, and cosmetics (Roco, 2003; Biswas and Wu, 2005; Nowack and Bucheli, 2007). Despite the obvious benefits that NPs offer, there are open questions as to how the NPs used for everyday life may affect the environment. The extensive utilization of these NPs allows them to be unintentionally released into the environment either during production, use or disposal (Gottschalk and Nowack, 2011; Peralta-Videa et al., 2011; Rico et al., 2011). Increased production of NPs leads to toxic effects on living organisms including plants (Bhatt and Tripathi, 2011). Eventually, phytotoxicity in crop plants leads to threats to human health through the food chain (Servin et al., 2013). Although several reports representing phytotoxicity of NPs in plants have been demonstrated (Dreher, 2004; Yang and Watts, 2005; Wiesner et al., 2006; Handy et al., 2008; Wang et al., 2012; Yang et al., 2015), comprehensive knowledge is still lacking.

According to the United States Environmental Protection Agency (USEPA), engineered NPs are divided into four categories; carbon-based materials, metal-based materials, dendrimers, and composites (USEPA, 2007). NPs that have both positive and negative impacts on higher plants have been reported. For example, SiO_2 and TiO_2 enhanced the absorbance of water and fertilizers in soybean (*Glycine max*) by increasing the level of nitrate reductase enzyme to stimulate antioxidant system (Lu et al., 2002). *Pisum sativum* plants (green peas) treated with ZnO NP showed induced root growth compared to control plants (Mukherjee et al., 2014). A particular concentration of TiO_2 NP has been shown to increase the growth of spinach by increasing photosynthesis and nitrogen metabolism (Hong et al., 2005a,b; Zheng et al., 2005; Yang et al., 2006). On the other hand, inhibition of root elongation of corn, cucumber, soybean, cabbage, and carrot was demonstrated when plants were treated with nanoscale alumina (nano-Al_2O_3) powders (Yang and Watts, 2005). To the best of our knowledge, this study by Yang and Watts, 2005 was the first study which highlighted the negative impact of metal NPs in plants and initiated the focus on studying the phytotoxic effect of metal NPs on plants. Later, several reports investigated the phytotoxic impact of several NPs in different plant species. For example, maize seedlings, treated with TiO_2 NP showed reduced leaf growth and transpiration (Asli and Neumann, 2009).

Copper nanoparticles (CuNP) received great interest in the textile industry due to their immediate antimicrobial effects when introduced into synthetic and natural fibers. Also, it is now being used in the microelectronics industry for its highly conductive properties where it is being implied to conductive pastes and heaters (Ravishankar Rai and Jamuna Bai, 2011). Copper oxide nanoparticles (CuONP) have been used as catalysts for a typical C-N cross-coupling reactions (Pan et al., 2011; Poreddy et al., 2015). Copper oxide is a semiconductor with special optical, electrical, and magnetic properties; it has been used in developing super capacitors and sensors (Dagher et al., 2014; Devi et al., 2014; Zhang et al., 2014). Due to its antimicrobial and biocidal activities, CuONP attracted more researchers than other metal NP for medical applications (Perreault et al., 2012; Nations et al., 2015). In the medical field, CuONP are used to detect viruses in the human body (Ahamed et al., 2014). Sankar et al. (2014) highlighted the anticancer activity of CuONP on human lung cancer cells and showed apoptosis due to reactive oxygen species (ROS) dependent disruption of mitochondrial membranes.

Despite their many useful applications, CuNP might also have a negative impact on the environment. Generally, the toxicity of the NPs depends on size, surface charge, and pH of the environment (Chang et al., 2012). CuNP on algae showed higher toxic effect than its bulk material and the existence of the toxicity remains after 72 h of the treatment (Aruoja et al., 2009). Mussels *Mytilus galloprovincialis* treated with CuONP exhibited higher production of ROS which leads to genotoxicity and cancer (Ruiz et al., 2015). Additionally, potential toxic effects of CuONP have been reported in different tissues in rainbow trout (*Oncorhynchus mykiss*). (Baek and An, 2011; Isani et al., 2013; Ostaszewska et al., 2016).

Phytotoxicity of CuNP has been studied on wheat and mung bean plants grown on agar media and was found to reduce seedling and shoot growth (Lee et al., 2008). Additionally, Kim et al., 2012 reported the phytotoxic effect of CuONP with a size of 50 nm on cucumber plants grown hydroponically which exhibited a significant increase in ROS enzymes; catalase (CAT), peroxidase (POD), and superoxide dismutase (SOD) (Kim et al., 2012). In another report, CuONP significantly reduced the growth of cucumber plants cultivated on soil microcosm system (Kim et al., 2013). Although, the previous reports suggested the phytotoxic effects of CuNP on plants, the underlying physiological, cellular, and molecular mechanisms need further investigation.

In this study, a comprehensive analysis on cucumber (*Cucumis sativus*) plants treated with CuNP with an average size of 10–30 nm in a hydroponic system has been performed. The hydroponic system was used to maintain the uniform concentration of NPs in each different treatment compared to soil system grown plants. The phytotoxicity and genotoxicity of CuNP and its accumulation in *C. sativus* plant tissues were investigated in details.

MATERIALS AND METHODS

Characterization of CuNP

Copper nanoparticles with an average particle size of 20 nm were purchased from Hengqiu Graphene Technology (Suzhou) Co., Ltd., Shanghai, China with a purity of 99.9%. To find out the exact size and nature of the NPs, they were analyzed using SEM. The analysis was carried out using a TESCAN VEGA4 XM SEM (SE Detector, 30 kV, high vacuum). Conductive carbon tape was used to attach the sample to the measurement stub.

Seed Germination and Seedling Development

Soil mixture was prepared by mixing autoclaved Peat Moss with Perlite in a 3:1 ratio and was then made moist by adding distilled water. The mixture was then added to sterile plastic pots. The overnight soaked seeds of *C. sativus* were placed randomly onto the surface of the pots and a pinch of soil was added on top to fully cover the seeds. The pots were placed in the growth chamber and were watered at regular intervals for 3 weeks.

Development of Hydroponic System

Cucumis sativus plants of 3 weeks old were carefully removed from the soil, washed with distilled water, transferred to glass jars containing 20% Hoagland solution prepared from Hoagland's No. 2 Basal Salt Mixture (Sigma-Aldrich), and placed in the growth chamber maintained at 25°C (12 h with light) and 15°C (12 h dark) for 3 weeks. After 7 days of growth in the hydroponic system, well-developed lateral root system was observed. The jars were replaced every 3 days with fresh Hoagland solutions to maintain stable health.

Nanoparticles Treatment and Plant Tissues Harvesting

Various concentrations (50, 100, and 200 mg/L) of CuNP powders were dispersed in distilled water and sonicated for 30 min, and the required Hoagland powder was mixed with it prior treatment. The 6 weeks old plants were treated by replacing the Hoagland solution with fresh Hoagland solution containing CuNP and placed back in the growth chamber for 4 days. There were 8 replicate plants per treatment. After the 4 days treatment, plants were washed to remove excess particles and dried on a tissue paper for 30 min. Fresh biomass was determined for each plant before and after treatment. Shoot and root of four replicates were separated, and kept in a 50 ml polystyrene falcon tube and then stored at −80°C until further use. The remaining four replicates were kept in a paper bags and dried in the oven (65°C) till complete dryness for metal analysis.

Metal Analysis

Oven dried tissues of shoots and roots were weighed, crushed to powder, and digested with Nitric acid (HNO_3) at 95°C water bath till brown fumes ceased. After cooling; distilled water and 30% H_2O_2 were added and samples were heated till no effervescence was observed. HCl was added to the mixture and heated. The samples were allowed to cool and filtered, and then metal accumulation was measured using Atomic Absorption Spectroscopy.

XRF and SEM Analysis of CuNP in Plant Tissues

The XRF analysis was performed using a Horiba XGT 7200 X-ray analytical microscope. The microscope is equipped with a 50-W Rhodium X-ray source (operating at up to 50 kV) and a silicon drift detector. Two beam sizes of diameter 50 μm and 1.2 mm are available for spot and mapping analysis. XRF microscopy was used for elemental analysis of *C. sativus* roots treated with 200 mg/L CuNP. Oven dried root samples treated with CuNP were ground using mortar and pestles. The powdered samples were coated with a thin layer of gold for further analysis with SEM. The SEM analysis was carried out similar to the analysis of CuNP powders described previously.

DNA Extraction and RAPD Analysis

Root samples stored at −80°C were powdered in liquid nitrogen, and DNA extraction was performed using NORGEN BIOTEK DNA extraction kit for plant/fungi according to the manufacturer instructions. The quality of the extracted DNA was checked by gel electrophoresis on 1% agarose gel and was quantified using NanoDrop. PCR reactions were prepared using NORGEN BIOTEK CROP master mix kit according to the manufacturer's instruction. The PCR tubes were inserted into the PCR machine, and the random amplified polymorphic DNA (RAPD) program was set (5 min initial denaturation at 94°C, 35 cycles at 95°C for 3 min, annealing for 1 min at 40°C, extension at 72°C for 2 min, and final extension set at 72°C for 7 min). The PCR products were then run at 2% agarose gel observed under UV to check for the presence or absence of bands. RAPD primers used in this experiment were OPA-07 (GAAACGGGTG), OPA-08 (GTGACGTAGG), and OPA-09 (GGGTAACGCC).

Chlorophyll Analysis

Shoot samples were ground in liquid nitrogen. Chlorophyll a and b contents were quantified by adding 5 ml of 80% acetone to 300 mg of powder tissue samples and placed in a shaker in the dark for 15 min, then centrifuged at 4°C for 15 min at a speed of 3,000 RPM. The supernatant was transferred to a new centrifuge tube and diluted with 80% acetone (1:5 ratio). The absorbance was measured using a spectrophotometer at two wavelengths: 663 nm (chlorophyll a) and 645 nm (chlorophyll b), and chlorophyll contents were calculated.

Electrolyte Leakage Estimation

After CuNP treatment, 0.1 g of control and treated root tips were excised and placed in falcon tubes containing 10 ml deionized water. The initial electrical conductivity (C_I) was measured at time zero. After 48 h, C_N was measured. The samples were then autoclaved at 121°C, allowed to cool and the final electrical conductivity (C_F) was measured. Three readings of the three replicates were measured. Degree of electrical leakage was calculated using the following formula: $E_T = ((C_N - C_I)/C_F) \times 100$. The experiments were performed in triplicate.

DAB Staining

After the CuNP treatment, the plant roots were washed well with tap and distilled water to get rid of the surface attached NPs. A small portions of the roots were excised and stained with 3, 3′-diaminobenzidine (DAB) (Daudi and O'Brien, 2012). Two ml of the DAB staining solution (1 mg/ml with 10 mM Na_2HPO_4) were added into the portion of the root samples and kept in desiccator for 5 min to allow the DAB into the tissues. Hence the DAB is light sensitive the samples were covered with

aluminum foil. The samples were kept in a shaker for 4–5 h for incubation. After the incubation, DAB solution was removed and washing solution (ethanol:acetic acid:glycerol = 3:1:1) were added and kept for 15 min at 90°C for chlorophyll removal. Then the wash solutions were changed and observed under light microscope.

Lipid Peroxidation and H_2O_2 Content

Lipid peroxidation was analyzed by measuring malondialdehyde (MDA) content according to Zhou and Leul (1998). 100 mg of control and treated plant tissues were homogenized with 1 ml of 0.1% (w/v) trichloroacetic acid (TCA) then centrifuged at 10,000 rpm for 15 min. In another 15 ml Falcon tube, 2 ml of TBA (0.5%) in TCA (20%) were added along with 800 µl of the supernatant. This mixture was incubated at 80°C water bath for 30 min and then immediately cooled into ice for 5 min. Then the mixture was centrifuged for 13,500 rpm, 5 min at 4°C. The supernatant was transferred into cuvettes and measured absorbance at 532 and 600 nm after blanking. The level of MDA was represented as nmol g^{-1} FW using extinction coefficient of 155 $mM^{-1}cm^{-1}$.

For determination of H_2O_2 content, 0.1 g of ground tissues were mixed with 2 ml of 0.1% TCA (w/v) and then the homogenate were centrifuged at 12,000 rpm for 15 min (Velikova et al., 2000). 0.5 ml of the supernatant was mixed with 0.5 ml of potassium phosphate buffer (10 mM, pH 7) and 1 ml of 1 M potassium iodide (KI) was added and checked their absorbance at 390 nm. The H_2O_2 content was determined using extinction coefficient of 0.28 µm cm^{-1} and it was measured as nmol g^{-1} FW.

RNA Extraction and Quantitative Real-Time PCR (qRT-PCR)

0.1 g of the −80°C stored control and CuNP treated plant tissues were ground in liquid nitrogen and were used to extract total RNA using Qiagen RNeasy® Plant Mini kit protocol. RNA concentrations were checked using NanoDrop, and the final concentrations of 1 µg RNA were used for cDNA synthesis using Invitrogen™ SuperScript™ II Reverse Transcriptase according to manufacturer's protocol. Real-time PCR was performed with the following primer pairs; copper-zinc SOD (Cu-Zn SOD)_F (GGTTGCTGGTGATGATGGTACTG), Cu-Zn SOD_R (TGCATGGACAACAATAGACCTTCC), Actin_F (GGAAATACAGTGTCTGGATTGGAG), Actin_R (TGAACTTAGAAGCACTTCCTGTG) with Power SYBR™ Green PCR Master mix (Applied Biosystems™) using BioRad CFX96 Touch™ Real-Time PCR detection system. The real time data were analyzed using $2^{-\Delta\Delta C_T}$ method (Livak and Schmittgen, 2001).

RESULTS

Characterization of CuNP

SEM analysis confirmed that the purchased CuNP sizes were in the 10–30 nm range (**Figure 1A**). Scanning Electron Microscope-Electron Dispersive X-ray Spectroscopy (SEM-EDS) analysis also showed the presence of oxygen along with copper, indicating that at least part of the CuNP was oxidized by air (**Figure 1B**).

Biomass Analysis of CuNP Treated *C. sativus* Plants

Plants treated with various concentrations of CuNP showed a clear senescence effect (leaf yellowing) at the end of the treatment period (4 days), with brown spots observed compared to control plants (**Figure 2A**). The total biomass of the *C. sativus* plants was measured before and after treatment (**Figure 2B**). Biomass analysis showed significant biomass reduction of *C. sativus* plants treated with 100, and 200 mg/ L CuNP for 4 days compared with the biomass of the same plants before treatment. Although, the biomass of the plants treated with 50 mg/L CuNP showed decreased biomass as well, but it was not significant.

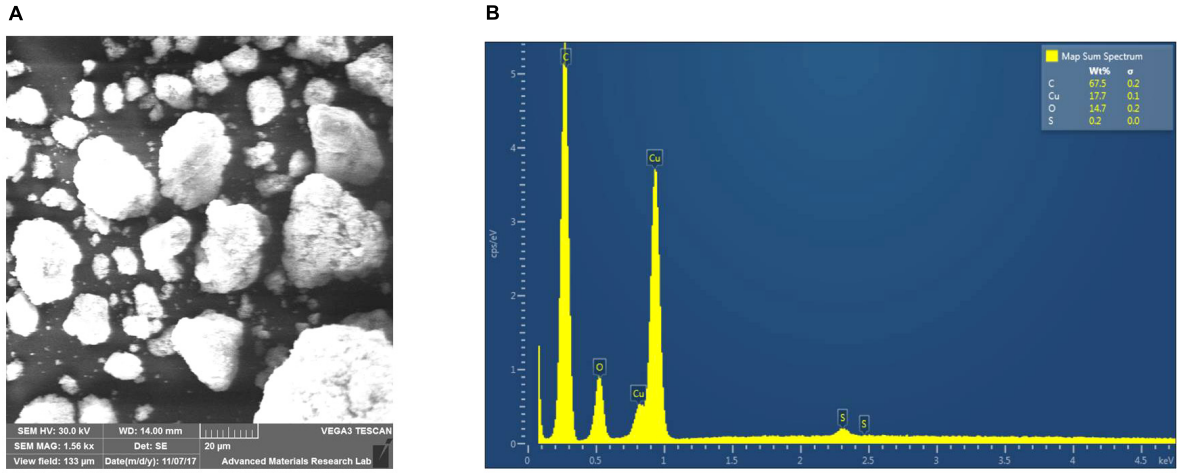

FIGURE 1 | Characterization of the copper nanoparticles (CuNP). **(A)** Scanning Electron Microscope-Electron Dispersive X-ray Spectroscopy (SEM-EDS) analysis of copper (Cu) nanoparticles. **(B)** EDX characteristic spectrum shows the presence of copper, and oxygen in the sample confirms the oxidation of the CuNP by air.

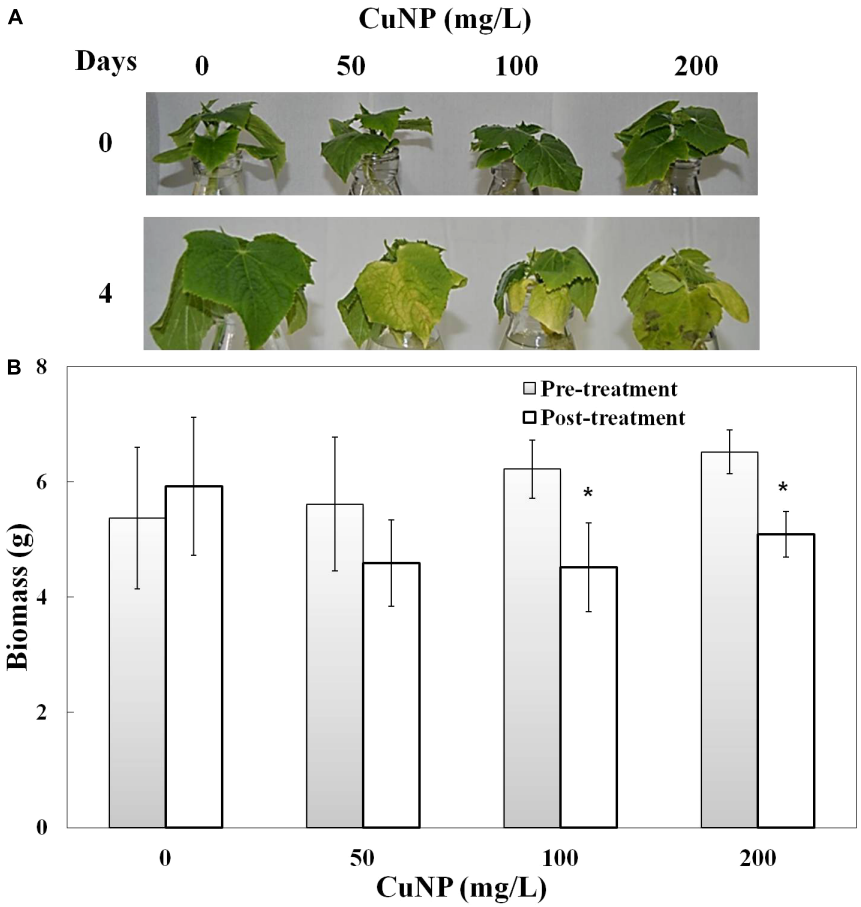

FIGURE 2 | Phenotype **(A)** and biomass measurement **(B)** of *Cucumis sativus* treated with various concentrations of CuNP (50, 100, and 200 mg/L) in pre- and post-treatment. Error bars represent standard errors of mean values of eight replicates. Statistically significant difference was calculated at $*P \leq 0.05$, $**P \leq 0.01$.

Furthermore, as expected, the non-treated control plants (0 mg/L CuNP) showed an enhanced but not significant increase in the biomass after the 4 days.

Copper Detection and Accumulation

To investigate whether *C. sativus* plants treated with CuNP mediate CuNP accumulation, XRF microscopy was utilized to measure the relative elemental composition represented as mass% of *C. sativus* shoot and root tissues treated with CuNP (**Figures 3A,B**). Besides copper, other elements of the Hoagland solution, such as Ca, K, Si, P, S, and Cl were also detected. Interestingly, the XRF analysis of shoots and roots exhibited more copper in roots compared to shoots (**Figures 3A,B**). To confirm and to quantify the Cu levels, the concentrations of Cu in shoots and roots of *C. sativus* plants were measured after 4 days of CuNP treatment using AAS (**Figures 3C,D**). The results showed increased Cu accumulation in these plants in proportion to the CuNP concentrations (100 and 200 mg/L). Again, it was observed that the accumulation of CuNP was more in the roots compared to the shoots. SEM analysis of *C. sativus* root samples confirmed the presence of CuNP in aggregated form and the sizes ranged between 80–140 nm in the treated plant tissues (**Figure 4**). However, no CuNP were observed in the control roots.

Genotoxicity Analysis by RAPD

Random amplified polymorphic DNA was employed to assess the CuNP toxicity effect on the genomic level of *C. sativus*. Genomic DNA was extracted from the root of both control, and CuNP treated samples. Various set of primers were used to amplify all DNA samples. Control sample amplified OPA- 07 primer showed five bands ranging between 300 to 800 bps. For 50 mg/L treatment of CuNP sample DNA amplified same bands as the control DNA sample as well as two additional bands at 200 and much above 1000 bp marker band. Similar band patterns were observed for DNA samples treated with 100 mg/L CuNP. In the case of the 200 mg/L CuNP treated DNA sample amplified same bands of control DNA with the exception of 800 bp and the additional 200 bp band (**Figure 5A**). Control sample DNA for OPA- 08 primer amplified three high intensity bands between 200 to 800 bps. For 50 mg/L treatment of CuNP sample DNA amplified several bands ranging from 300 to above 1000 bps marker band. In case of 100 and 200 mg/L treated with CuNP sample amplified almost similar band patterns of same intensity (**Figure 5B**).

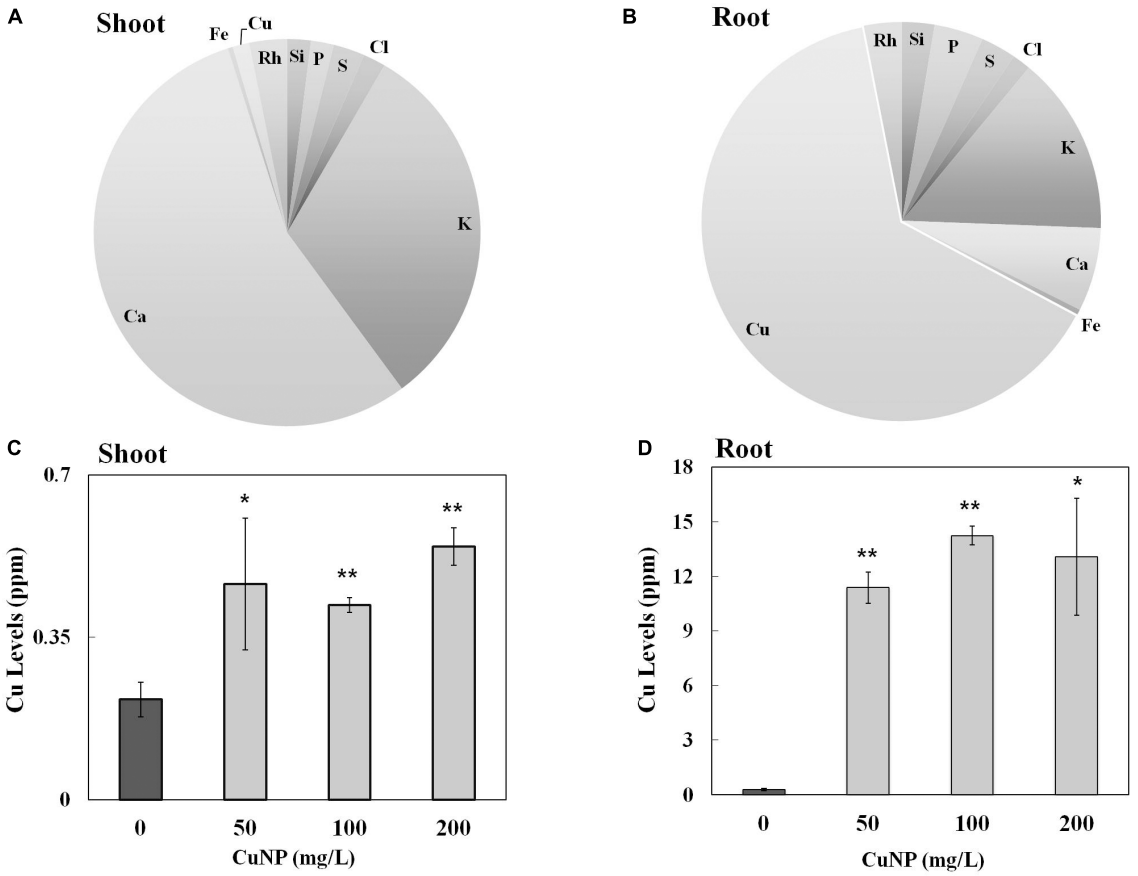

FIGURE 3 | Elemental and metal analysis by XRF and AAS. Relative element concentrations in CuNP treated *C. sativus* plants represented as (mass%) in **(A)** shoot and **(B)** root tissues analyzed by XRF. Metal analysis of control and CuNP treated *C. sativus* plant shoots **(C)** and roots **(D)** analyzed by AAS. Error bars represent standard errors of mean values of three replicates. Statistically significant difference was calculated at $*P \leq 0.05$, $**P \leq 0.01$.

Control sample DNA amplified with OPA- 09 primer exhibited six bands ranging from 100 to 1000 bps. Samples treated with 50 and 100 mg/L CuNP showed two additional bands at 400 and 500 bps. However, 200 mg/L treated sample DNA amplified same band pattern as 50 and 100 mg/L treated sample DNA along with an additional band at 600 bps (**Figure 5C**).

Effect of CuNP on Chlorophyll Content

When the plants were treated with CuNP for 4 days, induced senescence between control and treated plants was observed. To quantify the levels of senescence, the contents of chlorophyll a and b were measured. Compared to the untreated control plants, shoots of CuNP treated plants showed a significant decrease in chlorophyll a and b contents as the concentration of CuNP increased (**Figure 6**).

Electrolyte Leakage Analysis

To measure the plasma membrane integrity of the *C. sativus* plants treated with CuNP, electrolyte leakage analysis was performed. The results showed increased electrolyte leakage in CuNP treated plants compared to control plants (**Figure 7**). Hence, CuNP induced damage to root plasma membrane of *C. sativus* as indicated by the significant increase in electrolyte leakage in 50 and 200 mg/L CuNP treatment.

Effect of CuNP on H_2O_2 and MDA Contents

To examine whether CuNP induced oxidative stress on *C. sativus* plants, H_2O_2 and lipid peroxidation contents were measured (**Figure 8**). H_2O_2 levels in both shoots and roots of all the concentrations we checked were higher compared to control plants. The levels were almost four times higher than control plants of shoots and roots (**Figures 8A,B**).

In terms of lipid peroxidation, we measured MDA levels in both control and CuNP treated *C. sativus* plants. The root and shoot samples of *C. sativus* treated plants showed significant increase in all the concentrations of CuNP as compared to the control plants (**Figures 8C,D**).

H_2O_2 Detection by DAB Staining

To visualize the H_2O_2 accumulation in root tips due to CuNP treatment, we performed the histochemical staining with DAB reagent. The roots observed under the light microscope showed a clear difference between control and treated plants. CuNP

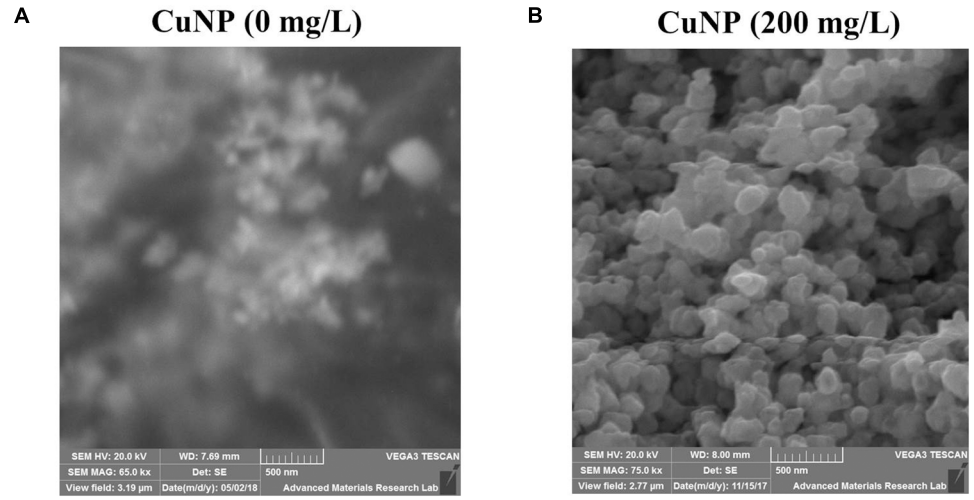

FIGURE 4 | Scanning Electron Microscope (SEM) image showing **(A)** no CuNP were observed in the control roots, and **(B)** CuNP were observed in aggregates in 200 mg/L CuNP treated root samples of *C. sativus*.

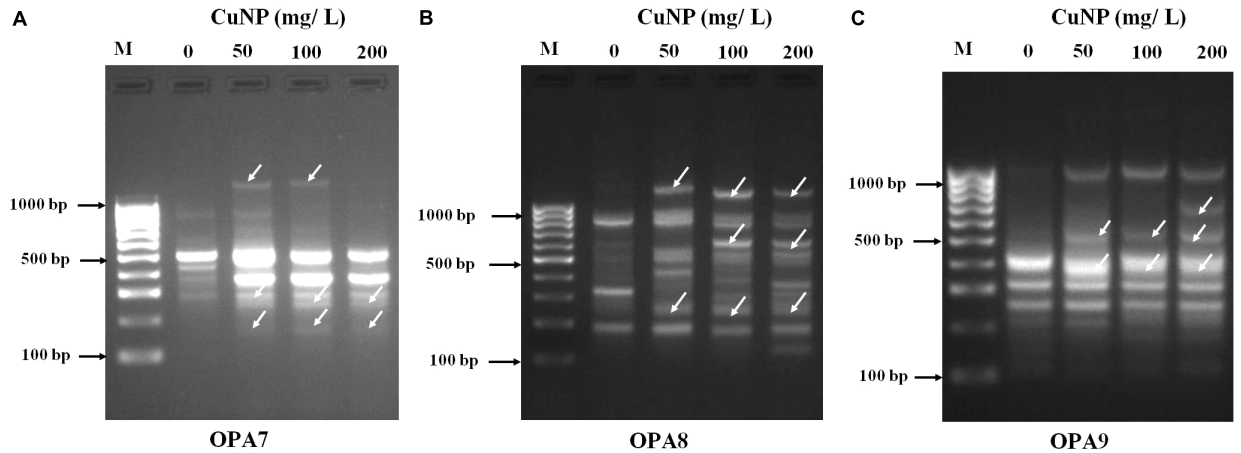

FIGURE 5 | Random amplified polymorphic DNA (RAPD) analysis. Banding patterns generated with different random oligonucleotide primers **(A)** OPA7, **(B)** OPA8, and **(C)** OPA9 to evaluate the genotoxicity effects of CuNP in *C. sativus*. [Lanes M- Molecular marker (100 bp), 1- control 0, 2- 50 mg/L, 3- 100 mg/L, 4- 200 mg/L of CuNP].

treated *C. sativus* roots stained more than control plants in a dose-dependent manner as the CuNP concentration increases it induces higher H_2O_2 accumulation (**Figure 9**).

Impact of CuNP on Superoxide Dismutase (SOD) Gene Expression

Superoxide dismutase is one of the major enzymatic antioxidants. In order to evaluate the regulation of *C. sativus* Cu-Zn SOD gene in response to CuNP treatment, quantitative RT-PCR (qRT-PCR) was performed to analyze the changes in transcripts of Cu-Zn SOD in response to 50, 100, and 200 mg/L of CuNP in *C. sativus* shoots and roots (**Figure 10**). Expression levels of Cu-Zn SOD were induced in shoots under 50, 100, and 200 mg/L of CuNP compared to control untreated plants (0 mg/L of CuNP) (**Figure 10A**). Similarly, in 50 mg/L CuNP treated roots, the expression level of Cu-Zn SOD was increased by six-fold compared to control untreated roots. However, a clear decrease but still significantly higher than control untreated roots was detected in Cu-Zn SOD expression level in response to 100, and 200 mg/L of CuNP (**Figure 10B**).

DISCUSSION

Generally, metal NPs have really strong bonds that allow them to reside within the environment for a long time as they are hardly degraded or destroyed (Svintradze and Pidaparti, 2010). This puts the ecological system in great danger as metal NPs possess highly reactive or catalytic properties compared to their bulk material, and thus can be potentially toxic. The current research

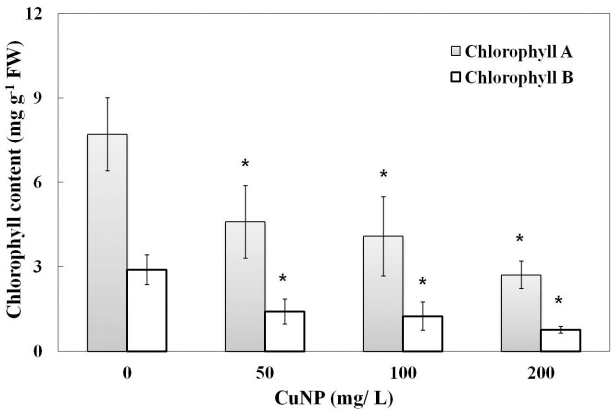

FIGURE 6 | Chlorophyll content of control and CuNP treated *C. sativus* plants. Control plants have higher chlorophyll content, and when the concentration of CuNP increases the chlorophyll content decreases. Error bars represent standard errors of mean values of four replicates. Statistically significant difference was calculated at $^{*}P \leq 0.05$, $^{**}P \leq 0.01$.

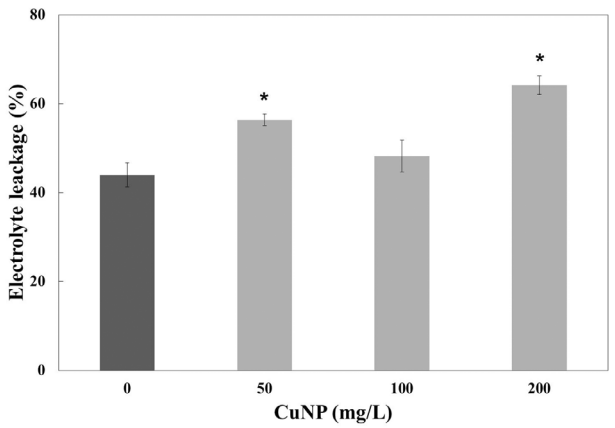

FIGURE 7 | Electrolyte leakage analysis of CuNP on *C. sativus* plants. Error bars represent standard errors of mean values of three replicates. Statistically significant difference was calculated at $^{*}P \leq 0.05$, $^{**}P \leq 0.01$.

highlighted the phytotoxicity effect of CuNP on cucumber (*C. sativus*) plants under hydroponic growth conditions, due to the limited studies available concerning the implications of CuNP and its phytotoxic effect on *C. sativus* plants. We have chosen the hydroponic system for this study to obtain a uniform concentration of NPs compared to soil systems. If we perform such experiments in soil grown plants, it's difficult to attain the uniformity in the concentration of NPs as well as the clear impact of toxicity on plants. Furthermore, for maintaining the uniformity of the NPs by growing plants on agar media, though its well suited for seedlings stage (Taylor and Foy, 1985; Munzuroglu and Geckil, 2002; Lee et al., 2008) rather than mature plants (6–7 week old in our study). *C. sativus* was selected for our study as one of the plant species recommended by McLean and Bledsoe (1996) for phytotoxicity studies. There are high chances of Cu oxidation by air to become copper oxide (Miyagawa et al., 2016). The purchased CuNP got oxidized to form copper oxide by air exposure as indicated by SEM-EDS analysis.

In the present study, we observed that plants exposed to CuNP exhibited higher toxicity based on the concentration of the CuNP with regard to its biomass reduction, which was similar to the reported earlier in hydroponically and soil grown cucumber plants treated with CuONP of 50 nm size (Kim et al., 2013). X-Ray Fluorescence (XRF) is one of the advanced techniques to estimate the relative quantity of elements present in the sample as semi-quantitatively (mass%). Earlier, Attaelmanan and Kawam, 2012 evaluated the elemental composition of *Calotropis procera* using such XRF microscope (Attaelmanan and Kawam, 2012). We used the same technique and the same instrument to show the elemental composition of *C. sativus* shoot and root samples treated with CuNP. There were several reports regarding micro XRF analysis of NPs treated plant tissues. micro XRF analysis of TiO_2 of hydroponically grown cucumber plants showed titanium accumulation in their leaf trichomes (Servin et al., 2012). The translocation of TiO_2 NP and multi-walled carbon nanotubes in red clover and wheat plant tissues were studied using XRF techniques (Gogos et al., 2016). Wang et al. (2017) demonstrated that phytotoxicity of silver sulfide NP in dicot and monocot plants and used XRF analysis to show the NP accumulation. Our elemental analysis of CuNP treated samples revealed 64 and 1.38% of Cu in root and shoot tissues, respectively.

To characterize the CuNP in cucumber treated plant tissues we performed Scanning Electron Microscopy (SEM) analysis. SEM analysis of CuNP treated root samples showed the aggregates of CuNP. Several reports already demonstrated the detection of NPs in aggregated form within the plant tissues regardless the small size of the NPs used for the treatment. González-Melendi et al. (2007) reported that charged NPs can be targeted into specific locations of plant tissues for delivery purposes and found that they tend to form aggregates in their targeted positions. TEM analysis of carbon-coated iron NP into *Cucurbita pepo* L plants showed the aggregates of NPs in various parts of the plants (Corredor et al., 2009). Another study revealed that green synthesized gold NP were found to increase rice germination, where the TEM analysis revealed the aggregated form of gold NP in root tissues of rice (Nji Tsi et al., 2017). Similarly, in our study SEM-EDS analysis showed the aggregation of CuNP in treated *C. sativus.*

Random amplified polymorphic DNA technique was employed in this study to check for any genetic alteration caused by CuNP. Unlike traditional PCR, RAPD technology is rapid, reproducible and does not require specific knowledge of the DNA sequence, which makes it ideal for examining and estimating the genomic variation in genotoxic studies (Atienzar et al., 1999). RAPD has been used to confirm the genotoxic effect of ZnO and CuO NP on buckwheat (*Fagopyrum esculentum*) seedlings (Comrey and Lee, 2013). Additionally, RAPD analysis of zucchini (*C. pepo*) plants treated with TiO_2 NP exhibited DNA changes compared to the control plants (Moreno-Olivas et al., 2014). Genotoxicity of CeO_2 and ZnO NP on soybean seedlings was demonstrated by the appearance of new DNA bands through RAPD analysis by López-Moreno et al. (2010).

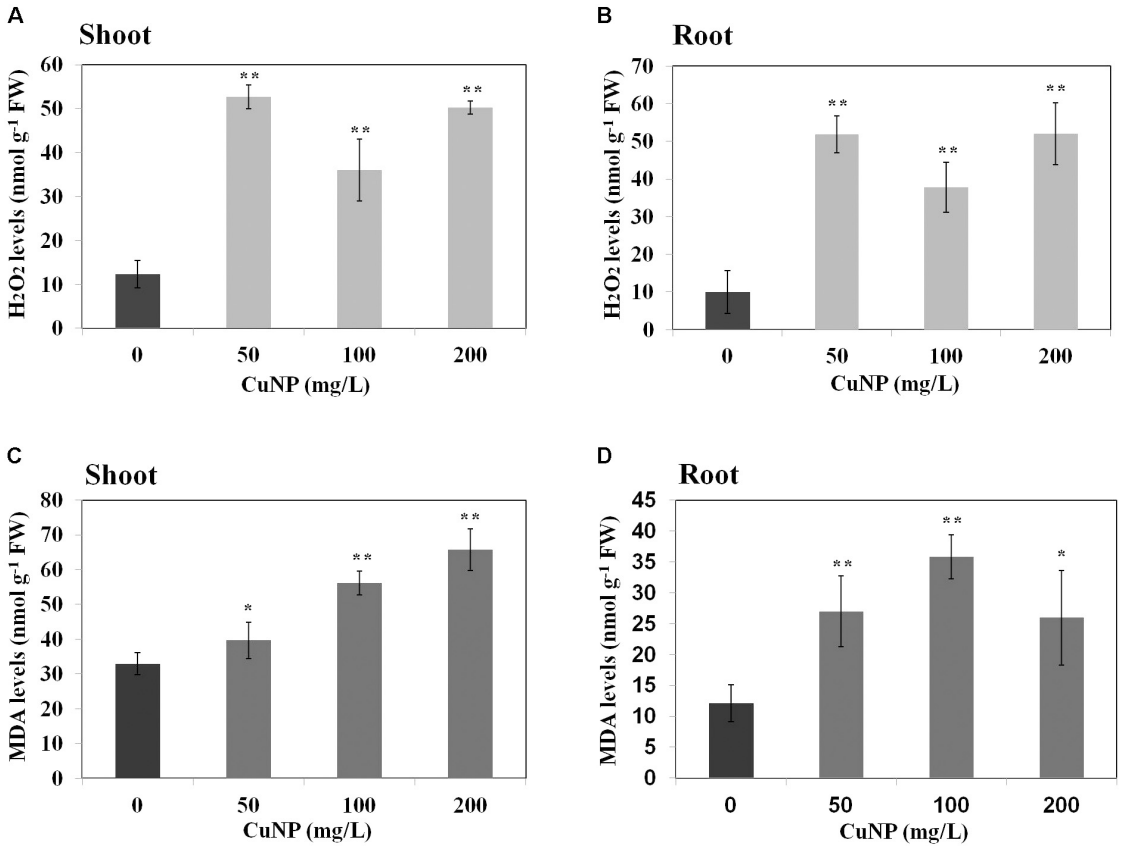

FIGURE 8 | Effect of CuNP on H_2O_2 **(A,B)** and MDA **(C,D)** contents in *C. sativus* shoots and roots, respectively. Error bars represent standard errors of mean values of three replicates. Statistically significant difference was calculated at $^*P \leq 0.05$, $^{**}P \leq 0.01$.

Furthermore, the genotoxicity of $nCeO_2$ and $nTiO_2$ NP were reported in seedlings of *Hordeum vulgare* L. using RAPD approach (Marchiol et al., 2016). In our investigation, three standard primers (OPA7, OPA8, and OPA9) were employed, and different bands appeared/disappeared when comparing the treated plants to the untreated control plants, rendering CuNP toxic to *C. sativus* at high exposure concentrations. The presence of these new bands may exhibit alterations in the priming sites leading to new annealing conditions in addition to homologous recombination which lead to the appearance of new bands (Atienzar and Jha, 2006). Our plants were more sensitive to the effects of CuNP as more band alterations were observed when compared to the control. The only difference between the treated and control plants was the presence or absence of CuNP which support that the changes in the DNA were caused by the effect of the CuNP.

The assessments of chlorophyll content of plants exposed to NPs were included as new parameters for phytotoxicity analysis (Ruttkay-Nedecky et al., 2017). When NPs are adsorbed to the root surface, it interrupts the absorption of macro and micronutrients required for plant's development reducing the nutrient uptake and thus resulting in lower chlorophyll content. Martinez-Fernandez et al. (2016) investigated the uptake of water contaminated with iron oxide NP by the roots of *Helianthus annuus*. They found that macronutrients such as Ca, K, Mg, and S reduced subsequently in the plant's shoot, and accordingly the chlorophyll pigmentation contents were decreased as well (Martinez-Fernandez et al., 2016). Our study has also demonstrated the negative effect of CuNP on chlorophyll a and chlorophyll b contents of *C. sativus*. The decrease in chlorophyll contents was obvious to the eyes after assessing treated and untreated plants.

The plasma membranes permeability was analyzed by testing the electrolyte leakage of the control and CuNP treated root tissues. It has been reported that 500 mg/L cerium oxide ($nCeO_2$) NP increased electrolyte leakage in the roots of rice seedlings (Hernandez-Viezcas et al., 2013). Additionally, a significant increase in electrolyte leakage was reported in asparagus lettuce root cultured in an agar medium treated with cerium oxide NP (Cui et al., 2014). In our study, *C. sativus* was sensitive to CuNP and significantly increased electrolyte leakage which caused the high reactivity of CuNP. CuNP changed the permeability of the plant membrane and as a result, damaged the plant's cell membranes which increased the probability of NPs entering into the cells. *C. sativus* showed increased permeability when plants were treated with CuNP which could be then accumulated into the roots and could also be translocated to the shoots, thus affecting the cell metabolic pathway. It has been already

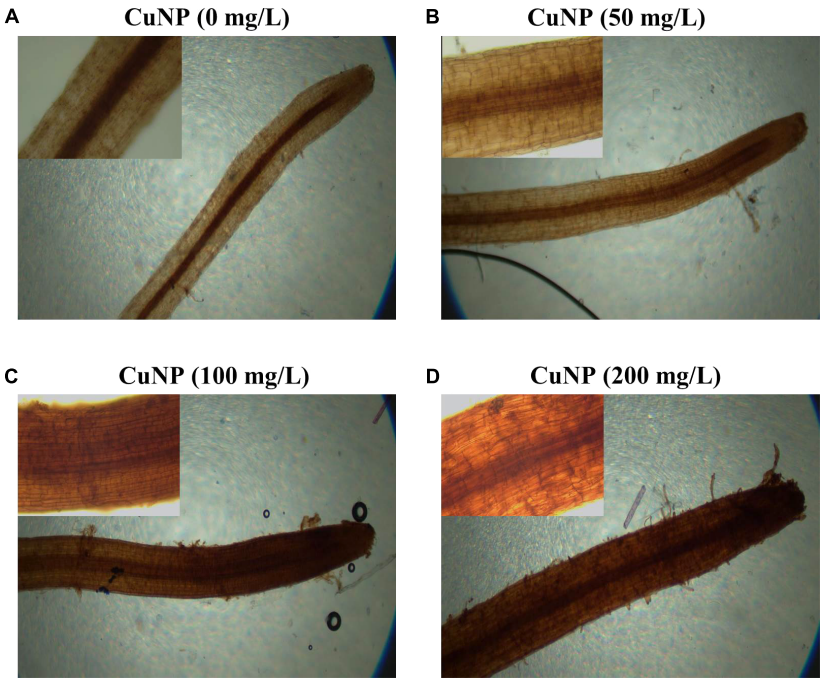

FIGURE 9 | H_2O_2 detection in *C. sativus* root tip by DAB stain. **(A)** control, **(B)** treatment with 50 mg/L, **(C)** treatment with 100 mg/L, and **(D)** treatment with 200 mg/L. For each group of treatment the magnified image (20×) of the root tip were shown inside each panel.

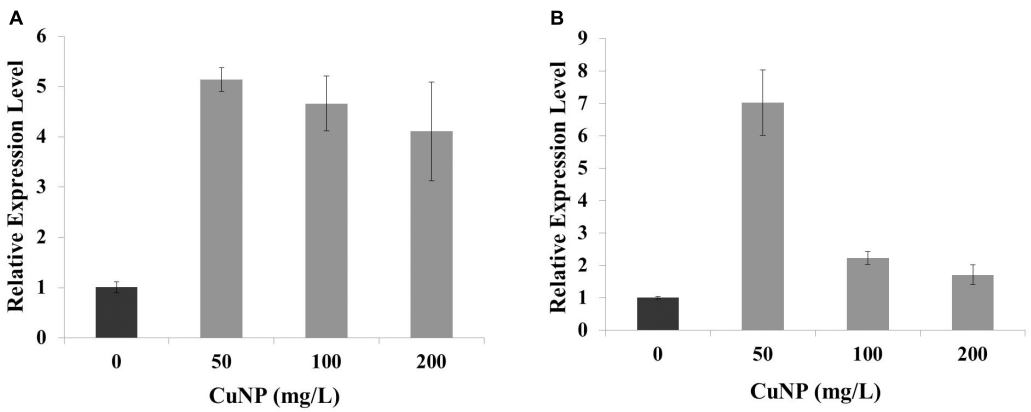

FIGURE 10 | Relative expression of copper-zinc SOD (Cu-Zn SOD) gene under CuNP (50, 100, and 200 mg/L) treatment in **(A)** shoots and **(B)** roots of *C. sativus*.

reported that CuONP is able to be translocated from roots to shoots (Shi et al., 2014). Our results demonstrated that CuNP were highly accumulated in roots with slight accumulations in the shoot system, indicating that only a small quantity of CuNP was translocated to the shoot of *C. sativus* during the treatment time period of our experiment (4 days). Kim et al. (2012) reported the increased accumulation of Cu and Zn ions in roots of *C. sativus* when treated with CuO and ZnO NP. It's already reported that plant systems are tend to absorb CuONP according to their concentration in the nutrient solution (Shi et al., 2014). Plants with more thin roots accumulate more metals than those with less thick roots as the surface area is decreased. It was apparent that our *C. sativus* plants had numerous thin and long root systems resulting in higher root accumulation of Cu.

It has been already highlighted earlier that metal toxicity in plants lead to enhanced production of ROS which is causing oxidative stress by increased electrolyte leakage, protein oxidation, lipid peroxidation, DNA damage and finally cell death (Meriga et al., 2004; Sharma et al., 2012; Wani et al., 2018). Cu is catalyzing the overproduction of ROS, such as H_2O_2 by Haber-Weiss and Fenton reactions leading to lipid peroxidation, damaging nucleic acids, and oxidizing proteins (Gill and Tuteja, 2010; Fidalgo et al., 2013). Hence we measured

the major molecules associated with oxidative stress such as MDA and H_2O_2 in *C. sativus* plants upon CuNP treatment. The highest levels of MDA were observed in *C. sativus* shoots and roots treated with 100 and 200, and 50 and 100 mg/L CuNP, respectively. The increase in MDA levels is directly proportional to the concentration of the CuNP used for the treatment. Similarly, such effect has been already shown in rice seedlings treated with CuONP which induced MDA levels compared to control plants (Wang et al., 2014). Likewise, the major reactive oxygen molecule, H_2O_2, levels were measured in control and CuNP treated plants. Our results demonstrated that all the treatment conditions showed increased H_2O_2 levels in both roots and shoots samples. Such induction of oxidative stress mediated H_2O_2 levels were also confirmed by DAB staining of root tips where dark brown stains were observed in all the treated root tip samples. Similarly, TiO_2NP treated *Hydrilla verticillata* showed increased H_2O_2 which was due to oxidative stress caused by the NPs (Spengler et al., 2017).

In order to reduce the oxidative stress, plants develop a defense mechanism involving the antioxidant enzymes such as SOD to scavenge excessive ROS. SODs are classified into three isoforms; Cu-Zn SOD, manganese SOD (Mn SOD), and iron SOD (Fe SOD) based on their metal cofactors (Alscher et al., 2002). In general, SOD is catalyzing the disproportionating superoxide anion free radicals into hydrogen peroxide and molecular oxygen (Gill and Tuteja, 2010). Our results showed a significant upregulation of Cu-Zn SOD gene expression in roots and shoots of CuNP treated *C. sativus* plants, demonstrating the increased ROS production and the conversion of superoxide anion free radicals into hydrogen peroxide which is displayed in our study by the increased H_2O_2 levels in both root and shoot samples of CuNP treated *C. sativus*. Similarly, a significant increase in SOD gene expression was reported in *P. sativum* L roots treated with 100, 200, 400, and 500 mg dm^{-3} CuONP (Nair and Chung, 2015).

CONCLUSION

This study was performed to assess the phytotoxicity of CuNP on *C. sativus*. We investigated the toxicity on the physiological, phenotypical, biochemical, and genomic levels. It was found that tested CuNP of the size 10–30 nm were toxic to *C. sativus*. CuNP showed a decrease in the total biomass of the *C. sativus* treated plants. XRF, Scanning Electron Microscope (SEM), and Atomic Absorption Spectroscopy (AAS) analysis demonstrated that CuNP were accumulated in the *C. sativus* plant tissues, with higher accumulation level in root tissues. RAPD PCR analysis confirmed the genotoxic effect of CuNP which induced genomic DNA modifications in *C. sativus*. Additionally, CuNP showed a significant decrease in chlorophyll a and b contents, increase in H_2O_2 and MDA contents, as well as an increase in electrolyte leakage which induced damage to cucumber root plasma membrane. Collectively, this demonstrated that CuNP induced oxidative stress in *C. sativus*. Finally, Cu-Zn SOD gene expression was induced under CuNP treatment. The availability of *C. sativus* genome information could enhance our understanding of CuNP phytotoxicity through deep molecular and gene expression analysis studies.

AUTHOR CONTRIBUTIONS

KM conceived and designed the experiments. KM, KR, AE, SW, EI, and HH performed the experiments. KM, ME-N, and KR analyzed the data. ME-N performed the AAS metal analysis. HA performed the XRF and SEM analysis. KM wrote the manuscript. KM, ME-N, KR, and HA edited the manuscript.

FUNDING

This research was financially supported by the Office of VC for Research and Graduate Studies at the University of Sharjah.

ACKNOWLEDGMENTS

We would like to thank Mr. Mohamed Shameer, Ms. Mona Mahfood, and Ms. Fatima Shaheen for their assistance.

REFERENCES

Ahamed, M., Alhadlaq, H. A., Khan, M. A. M., Karuppiah, P., and Al-Dhabi, N. A. (2014). Synthesis, characterization, and antimicrobial activity of copper oxide nanoparticles. *J. Nanomater.* 2014:637858. doi: 10.1155/2014/637858

Alscher, R. G., Erturk, N., and Heath, L. S. (2002). Role of superoxide dismutases (SODs) in controlling oxidative stress in plants. *J. Exp. Bot.* 53, 1331–1341. doi: 10.1093/jexbot/53.372.1331

Aruoja, V., Dubourguier, H. C., Kasemets, K., and Kahru, A. (2009). Toxicity of nanoparticles of CuO, ZnO and TiO2 to microalgae *Pseudokirchneriella subcapitata*. *Sci. Total Environ.* 407, 1461–1468. doi: 10.1016/j.scitotenv.2008.10.053

Asli, S., and Neumann, P. M. (2009). Colloidal suspensions of clay or titanium dioxide nanoparticles can inhibit leaf growth and transpiration via physical effects on root water transport. *Plant Cell Environ.* 32, 577–584. doi: 10.1111/j.1365-3040.2009.01952.x

Atienzar, F. A., Conradi, M., Evenden, A. J., Jha, A. N., and Depledge, M. H. (1999). Qualitative assessment of genotoxicity using random amplified polymorphic DNA: comparison of genomic template stability with key fitness parameters in Daphnia magna exposed to benzo[a]pyrene. *Environ. Toxicol. Chem.* 18, 2275–2282. doi: 10.1002/etc.5620181023

Atienzar, F. A., and Jha, A. N. (2006). The random amplified polymorphic DNA (RAPD) assay and related techniques applied to genotoxicity and carcinogenesis studies: a critical review. *Mutat. Res.* 613, 76–102. doi: 10.1016/j.mrrev.2006.06.001

Attaelmanan, A. G., and Kawam, M. A. (2012). Determining the elemental composition of *Calotropis procera* using X-ray analytical microscopy. *Xray Spectrom.* 41, 284–287. doi: 10.1002/xrs.2393

Baek, Y.-W., and An, Y.-J. (2011). Microbial toxicity of metal oxide nanoparticles (CuO, NiO, ZnO, and Sb2O3) to *Escherichia coli*, *Bacillus subtilis*, and *Streptococcus aureus*. *Sci. Total Environ.* 409, 1603–1608. doi: 10.1016/j.scitotenv.2011.01.014

Bhatt, I., and Tripathi, B. N. (2011). Interaction of engineered nanoparticles with various components of the environment and possible strategies for their risk assessment. *Chemosphere* 82, 308–317. doi: 10.1016/j.chemosphere.2010.10.011

Biswas, P., and Wu, C. Y. (2005). 2005 critical review: Nanoparticles and the environment. *J. Air. Waste. Manag. Assoc.* 55, 708–746. doi: 10.1080/10473289.2005.10464656

Chang, Y.-N., Zhang, M., Xia, L., Zhang, J., and Xing, G. (2012). The toxic effects and mechanisms of CuO and ZnO nanoparticles. *Materials* 5, 2850–2871. doi: 10.3390/ma5122850

Comrey, A. L., and Lee, H. B. (2013). *A First Course in Factor Analysis*. Abingdon: Psychology Press.

Corredor, E., Testillano, P. S., Coronado, M.-J., González-Melendi, P., Fernández-Pacheco, R., Marquina, C., et al. (2009). Nanoparticle penetration and transport in living pumpkin plants: in situ subcellular identification. *BMC Plant Biol.* 9:45. doi: 10.1186/1471-2229-9-45

Cui, D., Zhang, P., Ma, Y., He, X., Li, Y., Zhang, J., et al. (2014). Effect of cerium oxide nanoparticles on asparagus lettuce cultured in an agar medium. *Environ. Sci. Nano* 1, 459–465. doi: 10.1039/C4EN00025K

Dagher, S., Haik, Y., Ayesh, A. I., and Tit, N. (2014). Synthesis and optical properties of colloidal CuO nanoparticles. *J. Luminesci.* 151, 149–154. doi: 10.1016/j.jlumin.2014.02.015

Daudi, A., and O'Brien, J. A. (2012). Detection of hydrogen peroxide by DAB staining in Arabidopsis leaves. *Bio Protoc.* 2:e263. doi: 10.21769/BioProtoc.263

Devi, A. B., Moirangthem, D. S., Talukdar, N. C., Devi, M. D., Singh, N. R., and Luwang, M. N. (2014). Novel synthesis and characterization of CuO nanomaterials: Biological applications. *Chin. Chem. Lett.* 25, 1615–1619. doi: 10.1016/j.cclet.2014.07.014

Dreher, K. L. (2004). Health and environmental impact of nanotechnology: toxicological assessment of manufactured nanoparticles. *Toxicol. Sci.* 77, 3–5. doi: 10.1093/toxsci/kfh041

Fidalgo, F., Azenha, M., Silva, A. F., Sousa, A., Santiago, A., Ferraz, P., et al. (2013). Copper-induced stress in *Solanum nigrum* L. and antioxidant defense system responses. *Food Energy Secur.* 2, 70–80. doi: 10.1016/j.jhazmat.2010.05.080

Gill, S. S., and Tuteja, N. (2010). Reactive oxygen species and antioxidant machinery in abiotic stress tolerance in crop plants. *Plant Physiol. Biochem.* 48, 909–930. doi: 10.1016/j.plaphy.2010.08.016

Gogos, A., Moll, J., Klingenfuss, F., van der Heijden, M., Irin, F., Green, M. J., et al. (2016). Vertical transport and plant uptake of nanoparticles in a soil mesocosm experiment. *J. Nanobiotechnol.* 14:40. doi: 10.1186/s12951-016-0191-z

González-Melendi, P., Fernández-Pacheco, R., Coronado, M., Corredor, E., Testillano, P., Risueno, M., et al. (2007). Nanoparticles as smart treatment-delivery systems in plants: assessment of different techniques of microscopy for their visualization in plant tissues. *Ann. Bot.* 101, 187–195. doi: 10.1093/aob/mcm283

Gottschalk, F., and Nowack, B. (2011). The release of engineered nanomaterials to the environment. *J. Environ. Monit.* 13, 1145–1155. doi: 10.1039/C0EM00547A

Handy, R. D., von der Kammer, F., Lead, J. R., Hassellöv, M., Owen, R., and Crane, M. (2008). The ecotoxicology and chemistry of manufactured nanoparticles. *Ecotoxicology* 17, 287–314. doi: 10.1007/s10646-008-0199-8

Hernandez-Viezcas, J. A., Castillo-Michel, H., Andrews, J. C., Cotte, M., Rico, C., Peralta-Videa, J. R., et al. (2013). *In situ* synchrotron X-ray fluorescence mapping and speciation of CeO_2 and ZnO nanoparticles in soil cultivated soybean (*Glycine max*). *ACS Nano* 7, 1415–1423. doi: 10.1021/nn305196q

Hong, F., Yang, F., Liu, C., Gao, Q., Wan, Z., Gu, F., et al. (2005a). Influences of Nano-TiO2 on the chloroplast aging of spinach under light. *Biol. Trace Elem. Res.* 104, 249–260.

Hong, F., Zhou, J., Liu, C., Yang, F., Wu, C., Zheng, L., et al. (2005b). Effect of nano-TiO2 on photochemical reaction of chloroplasts of spinach. *Biol. Trace Elem. Res.* 105, 269–279.

Isani, G., Falcioni, M. L., Barucca, G., Sekar, D., Andreani, G., Carpenè, E., et al. (2013). Comparative toxicity of CuO nanoparticles and CuSO4 in rainbow trout. *Ecotoxicol. Environ. Saf.* 97(Suppl. C), 40–46. doi: 10.1016/j.ecoenv.2013.07.001

Kim, S., Lee, S., and Lee, I. (2012). Alteration of phytotoxicity and oxidant stress potential by metal oxide nanoparticles in *Cucumis sativus*. *Water Air and Soil Pollut.* 223, 2799–2806. doi: 10.1007/s11270-011-1067-3

Kim, S., Sin, H., Lee, S., and Lee, I. (2013). Influence of metal oxide particles on soil enzyme activity and bioaccumulation of two plants. *J. Microbiol. Biotechnol.* 23, 1279–1286. doi: 10.4014/jmb.1304.04084

Lee, W.-M., An, Y.-J., Yoon, H., and Kweon, H.-S. (2008). Toxicity and bioavailability of copper nanoparticles to the terrestrial plants mung bean (*Phaseolus radiatus*) and wheat (*Triticum aestivum*): Plant agar test for water-insoluble nanoparticles. *Environ. Toxicol. Chem.* 27, 1915–1921. doi: 10.1897/07-481.1

Livak, K. J., and Schmittgen, T. D. (2001). Analysis of relative gene expression data using real-time quantitative PCR and the 2-ΔΔCT method. *Methods* 25, 402–408. doi: 10.1006/meth.2001.1262

López-Moreno, M. L., de la Rosa, G., Hernández-Viezcas, J. Á, Castillo-Michel, H., Botez, C. E., Peralta-Videa, J. R., et al. (2010). Evidence of the differential biotransformation and genotoxicity of ZnO and CeO2 nanoparticles on soybean (*Glycine max*) plants. *Environ. Sci. Technol.* 44, 7315–7320. doi: 10.1021/es903891g

Lu, C., Zhang, C., Wen, J., Wu, G., and Tao, M. (2002). Research of the effect of nanometer materials on germination and growth enhancement of Glycine max and its mechanism. *Soybean Sci.* 21, 168–171.

Marchiol, L., Mattiello, A., Poščic, F., Fellet, G., Zavalloni, C., Carlino, E., and Musetti, R. (2016). Changes in physiological and agronomical parameters of barley (*Hordeum vulgare*) exposed to cerium and titanium dioxide nanoparticles. *Int. J. Environ. Res. Public Health* 13:E332. doi: 10.3390/ijerph13030332

Martinez-Fernandez, C., Weyman, T., Fol, S., Audirac, I., Cunningham-Sabot, E., Wiechmann, T., et al. (2016). Shrinking cities in Australia, Japan, Europe and the USA: from a global process to local policy responses. *Prog. Plann.* 105, 1–48. doi: 10.1016/j.progress.2014.10.001

McLean, J. E., and Bledsoe, B. E. (1996). *Behavior of Metals in Soils*. Washington, DC: EPA Environmental Assessment Sourcebook, 19.

Meriga, B., Krishna Reddy, B., Rajender Rao, K., Ananda Reddy, L., and Kavi Kishor, P. B. (2004). Aluminium-induced production of oxygen radicals, lipid peroxidation and DNA damage in seedlings of rice (*Oryza sativa*). *J. Plant Physiol.* 161, 63–68. doi: 10.1078/0176-1617-01156

Miyagawa, M., Maeda, T., Tokuda, R., Shibusawa, A., Aoki, T., Okumura, K., et al. (2016). Precious metal-like oxide-free copper nanoparticles: high oxidation resistance and geometric structure. *RSC Adv.* 6, 104560–104565. doi: 10.1039/C6RA18076K

Moreno-Olivas, F., Gant, V. U., Johnson, K. L., Peralta-Videa, J. R., and Gardea-Torresdey, J. L. (2014). Random amplified polymorphic DNA reveals that TiO_2 nanoparticles are genotoxic to *Cucurbita pepo*. *J. Zhejiang Univ. Sci. A* 15, 618–623. doi: 10.1631/jzus.A1400159

Mukherjee, A., Peralta-Videa, J. R., Bandyopadhyay, S., Rico, C. M., Zhao, L., and Gardea-Torresdey, J. L. (2014). Physiological effects of nanoparticulate ZnO in green peas (*Pisum sativum* L.) cultivated in soil. *Metallomics* 6, 132–138. doi: 10.1039/C3MT00064H

Munzuroglu, O., and Geckil, H. (2002). Effects of metals on seed germination, root elongation, and coleoptile and hypocotyl growth in *Triticum aestivum* and *Cucumis sativus*. *Arch. Environ. Contam. Toxicol.* 43, 203–213. doi: 10.1007/s00244-002-1116-4

Nair, P. M. G., and Chung, I. M. (2015). The responses of germinating seedlings of green peas to copper oxide nanoparticles. *Biol. Plant.* 59, 591–595. doi: 10.1007/s10535-015-0494-1

Nations, S., Long, M., Wages, M., Maul, J. D., Theodorakis, C. W., and Cobb, G. P. (2015). Subchronic and chronic developmental effects of copper oxide (CuO) nanoparticles on *Xenopus laevis*. *Chemosphere* 135(Suppl. C), 166–174. doi: 10.1016/j.chemosphere.2015.03.078

Nji Tsi, N., Santi, M., and Duangkamol, M. (2017). The effect of green synthesized gold nanoparticles on rice germination and roots. *Adv. Nat. Sci.* 8:035008.

Nowack, B., and Bucheli, T. D. (2007). Occurrence, behavior and effects of nanoparticles in the environment. *Environ. Pollut.* 150, 5–22. doi: 10.1016/j.envpol.2007.06.006

Ostaszewska, T., Chojnacki, M., Kamaszewski, M., and Sawosz-Chwalibóg, E. (2016). Histopathological effects of silver and copper nanoparticles on the epidermis, gills, and liver of Siberian sturgeon. *Environ. Sci. Pollut. Res.* 23, 1621–1633. doi: 10.1007/s11356-015-5391-9

Pan, K., Ming, H., Yu, H., Liu, Y., Kang, Z., Zhang, H., et al. (2011). Different copper oxide nanostructures: synthesis, characterization, and application for

C-N cross-coupling catalysis. *Crystal Res. Technol.* 46, 1167–1174. doi: 10.1002/crat.201100258

Peralta-Videa, J. R., Zhao, L., Lopez-Moreno, M. L., de la Rosa, G., Hong, J., and Gardea-Torresdey, J. L. (2011). Nanomaterials and the environment: a review for the biennium 2008–2010. *J. Hazard. Mater* 186, 1–15. doi: 10.1016/j.jhazmat.2010.11.020

Perreault, F., Melegari, S. P., da Costa, C. H., de Oliveira Franco Rossetto, A. L., Popovic, R., and Matias, W. G. (2012). Genotoxic effects of copper oxide nanoparticles in Neuro 2A cell cultures. *Sci. Total Environ.* 441(Suppl. C), 117–124. doi: 10.1016/j.scitotenv.2012.09.065

Poreddy, R., Engelbrekt, C., and Riisager, A. (2015). Copper oxide as efficient catalyst for oxidative dehydrogenation of alcohols with air. *Catal. Sci. Technol.* 5, 2467–2477. doi: 10.1039/C4CY01622J

Ravishankar Rai, V., and Jamuna Bai, A. (2011). *Nanoparticles and Their Potential Application as Antimicrobials*, ed. A Méndez-Vilas A. Mysore: Formatex.

Rico, C. M., Majumdar, S., Duarte-Gardea, M., Peralta-Videa, J. R., and Gardea-Torresdey, J. L. (2011). Interaction of nanoparticles with edible plants and their possible implications in the food chain. *J. Agric. Food Chem.* 59, 3485–3498. doi: 10.1021/jf104517j

Roco, M. C. (2003). Broader societal issues of nanotechnology. *J. Nanopart. Res.* 5, 181–189. doi: 10.1023/a:1025548512438

Ruiz, P., Katsumiti, A., Nieto, J. A., Bori, J., Jimeno-Romero, A., Reip, P., et al. (2015). Short-term effects on antioxidant enzymes and long-term genotoxic and carcinogenic potential of CuO nanoparticles compared to bulk CuO and ionic copper in mussels *Mytilus galloprovincialis*. *Mar. Environ. Res.* 111(Suppl. C), 107–120. doi: 10.1016/j.marenvres.2015.07.018

Ruttkay-Nedecky, B., Krystofova, O., Nejdl, L., and Adam, V. (2017). Nanoparticles based on essential metals and their phytotoxicity. *J. Nanobiotechnology* 15:33. doi: 10.1186/s12951-017-0268-3

Sankar, R., Maheswari, R., Karthik, S., Shivashangari, K. S., and Ravikumar, V. (2014). Anticancer activity of *Ficus religiosa* engineered copper oxide nanoparticles. *Mat. Sci. Engin.* 44(Suppl. C), 234–239. doi: 10.1016/j.msec.2014.08.030

Servin, A. D., Castillo-Michel, H., Hernandez-Viezcas, J. A., Diaz, B. C., Peralta-Videa, J. R., and Gardea-Torresdey, J. L. (2012). Synchrotron Micro-XRF and Micro-XANES confirmation of the uptake and translocation of TiO2 nanoparticles in Cucumber (*Cucumis sativus*) plants. *Environ. Sci. Technol.* 46, 7637–7643. doi: 10.1021/es300955b

Servin, A. D., Morales, M. I., Castillo-Michel, H., Hernandez-Viezcas, J. A., Munoz, B., Zhao, L., et al. (2013). Synchrotron verification of TiO2 accumulation in cucumber fruit: a possible pathway of TiO2 nanoparticle transfer from soil into the food chain. *Environ. Sci. Technol.* 47, 11592–11598. doi: 10.1021/es403368j

Sharma, P., Jha, A. B., Dubey, R. S., and Pessarakli, M. (2012). Reactive oxygen species, oxidative damage, and antioxidative defense mechanism in plants under stressful conditions. *J. Bot.* 2012:217037. doi: 10.1155/2012/217037

Shi, J., Peng, C., Yang, Y., Yang, J., Zhang, H., Yuan, X., et al. (2014). Phytotoxicity and accumulation of copper oxide nanoparticles to the Cu-tolerant plant Elsholtzia splendens. *Nanotoxicology* 8, 179–188. doi: 10.3109/17435390.2013.766768

Spengler, A., Wanninger, L., and Pflugmacher, S. (2017). Oxidative stress mediated toxicity of TiO2 nanoparticles after a concentration and time dependent exposure of the aquatic macrophyte *Hydrilla verticillata*. *Aquat. Toxicol.* 190, 32–39. doi: 10.1016/j.aquatox.2017.06.006

Svintradze, D. V., and Pidaparti, R. M. (2010). A theoretical model for metal corrosion degradation. *Int. J. Corrosion* 2010:279540. doi: 10.1155/2010/279540

Taylor, G. J., and Foy, C. D. (1985). Differential uptake and toxicity of ionic and chelated copper in *Triticum aestivum*. *Can. J. Bot.* 63, 1271–1275. doi: 10.1139/b85-176

USEPA (2007). *Nanotechnology White Paper. EPA 100/B-07/001*. Washington, DC: Science Policy Council, US Environmental Protection Agency.

Velikova, V., Yordanov, I., and Edreva, A. (2000). Oxidative stress and some antioxidant systems in acid rain-treated bean plants: protective role of exogenous polyamines. *Plant Sci.* 151, 59–66. doi: 10.1016/S0168-9452(99)00197-1

Wang, P., Lombi, E., Sun, S., Scheckel, K. G., Malysheva, A., McKenna, B. A., et al. (2017). Characterizing the uptake, accumulation and toxicity of silver sulfide nanoparticles in plants. *Environ. Sci.* 4, 448–460. doi: 10.1039/C6EN00489J

Wang, S. L., Zhang, Y. X., Liu, H. Z., and Xin, H. (2014). Phytotoxicity of copper oxide nanoparticles to metabolic activity in the roots of rice. *Huan Jing ke Xue*35, 1968–1973.

Wang, Z., Xie, X., Zhao, J., Liu, X., Feng, W., White, J. C., et al. (2012). Xylem- and phloem-based transport of CuO nanoparticles in maize (*Zea mays* L.). *Environ. Sci. Technol.* 46, 4434–4441. doi: 10.1021/es204212z

Wani, W., Masoodi, K. Z., Zaid, A., Wani, S. H., Shah, F., Meena, V. S., et al. (2018). Engineering plants for heavy metal stress tolerance. *Rend. Lincei. Sci. Fis. Nat.* 2018, 1–5. doi: 10.1007/s12210-018-0702-y

Wiesner, M. R., Lowry, G. V., Alvarez, P., Dionysiou, D., and Biswas, P. (2006). Assessing the risks of manufactured nanomaterials. *Environ. Sci. Technol.* 40, 4336–4345. doi: 10.1021/es062726m

Yang, F., Hong, F., You, W., Liu, C., Gao, F., Wu, C., et al. (2006). Influence of nano-anatase TiO2 on the nitrogen metabolism of growing spinach. *Biol. Trace Elem. Res.* 110, 179–190. doi: 10.1385/BTER:110:2:179

Yang, L., and Watts, D. J. (2005). Particle surface characteristics may play an important role in phytotoxicity of alumina nanoparticles. *Toxicol. Lett.* 158, 122–132. doi: 10.1016/j.toxlet.2005.03.003

Yang, Z. Z., Chen, J., Dou, R. Z., Gao, X., Mao, C. B., and Wang, L. (2015). Assessment of the phytotoxicity of metal oxide nanoparticles on two crop plants, maize (*Zea mays* L.) and rice (*Oryza sativa* L.). *Int. J. Environ. Res. Public Health* 12, 15100–15109. doi: 10.3390/ijerph121214963

Zhang, Q., Zhang, K., Xu, D., Yang, G., Huang, H., Nie, F., et al. (2014). CuO nanostructures: Synthesis, characterization, growth mechanisms, fundamental properties, and applications. *Progr. Mat. Sci.* 60(Suppl. C), 208–337. doi: 10.1016/j.pmatsci.2013.09.003

Zheng, L., Hong, F., Lu, S., and Liu, C. (2005). Effect of nano-TiO2 on strength of naturally aged seeds and growth of spinach. *Biol. Trace Elem. Res.* 104, 83–91. doi: 10.1385/BTER:104:1:083

Zhou, W., and Leul, M. (1998). Uniconazole-induced alleviation of freezing injury in relation to changes in hormonal balance, enzyme activities and lipid peroxidation in winter rape. *Plant Growth Regul.* 26, 41–47. doi: 10.1023/a:1006004921265

Conflict of Interest Statement: The authors declare that the research was conducted in the absence of any commercial or financial relationships that could be construed as a potential conflict of interest.

frontiers in Plant Science

ORIGINAL RESEARCH
published: 03 August 2018
doi: 10.3389/fpls.2018.01112

Cellular Fractionation and Nanoscopic X-Ray Fluorescence Imaging Analyses Reveal Changes of Zinc Distribution in Leaf Cells of Iron-Deficient Plants

Gianpiero Vigani[1,2], Sylvain Bohic[3], Franco Faoro[2], Bart Vekemans[4], Lazlo Vincze[4] and Roberto Terzano[5]**

[1] Plant Physiology Unit, Department of Life Sciences and Systems Biology, University of Turin, Turin, Italy, [2] Department of Agricultural and Environmental Sciences, Production, Landscape, Agroenergy, University of Milano, Milan, Italy, [3] European Synchrotron Radiation Facility, NINA Beamline, Grenoble, France, [4] Department of Analytical Chemistry, Ghent University, Ghent, Belgium, [5] Department of Soil, Plant and Food Sciences, University of Bari, Bari, Italy

OPEN ACCESS

Edited by:
Hannetz Roschzttardtz, Pontificia Universidad Católica de Chile, Chile

Reviewed by:
Ferenc Fodor, Eötvös Loránd University, Hungary
Isidro Abreu, Centre for Plant Biotechnology and Genomics, Spain

***Correspondence:**
Gianpiero Vigani
gianpiero.vigani@unito.it
Roberto Terzano
roberto.terzano@uniba.it

Specialty section:
This article was submitted to Plant Nutrition, a section of the journal Frontiers in Plant Science

Received: *26 March 2018*
Accepted: *10 July 2018*
Published: *03 August 2018*

Citation:
Vigani G, Bohic S, Faoro F, Vekemans B, Vincze L and Terzano R (2018) Cellular Fractionation and Nanoscopic X-Ray Fluorescence Imaging Analyses Reveal Changes of Zinc Distribution in Leaf Cells of Iron-Deficient Plants. Front. Plant Sci. 9:1112. doi: 10.3389/fpls.2018.01112

Multilevel interactions among nutrients occur in the soil-plant system. Among them, Fe and Zn homeostasis in plants are of great relevance because of their importance for plant and human nutrition. However, the mechanisms underlying the interplay between Fe and Zn in plants are still poorly understood. In order to elucidate how Zn interacts with Fe homeostasis, it is crucial to assess Zn distribution either in the plant tissues or within the cells. In this study, we investigated the subcellular Zn distribution in Fe-deficient leaf cells of cucumber plants by using two different approaches: cellular fractionation coupled with inductively coupled plasma mass spectrometry (ICP/MS) and nanoscopic synchrotron X-ray fluorescence imaging. Fe-deficient leaves showed a strong accumulation of Zn as well as a strong alteration of the organelles' ultrastructure at the cellular level. The cellular fractionation-ICP/MS approach revealed that Zn accumulates in both chloroplasts and mitochondria of Fe deficient leaves. Nano-XRF imaging revealed Zn accumulation in chloroplast and mitochondrial compartments, with a higher concentration in chloroplasts. Such results show that (i) both approaches are suitable to investigate Zn distribution at the subcellular level and (ii) cellular Fe and Zn interactions take place mainly in the organelles, especially in the chloroplasts.

Keywords: cellular fractionation, iron, nanoscopic X-ray fluorescence imaging, zinc, plant

INTRODUCTION

Among nutrients, iron (Fe) represents an essential element for the life cycle of plants, because it is a key cation to ensure electron flow in photosynthetic and respiratory pathways. For this reason, Fe can be a limiting factor for biomass production as well as for the quality of plant products. On the other hand, Fe is also potentially toxic because of its reactivity with oxygen, which catalyzes the formation of reactive oxygen species (Briat et al., 2015a).

The chlorosis observed in younger leaves represents the most typical visual symptom of Fe deficiency in plants. Indeed, Fe deficiency impairs chlorophyll synthesis, leading to interveinal chlorosis in developing leaves (Rodriguez-Celma et al., 2013) and decreased photosynthesis rates (Terry, 1980). However, the excess of several heavy metals can induce such chlorosis as well (Vert et al., 2002; Leskova et al., 2017), probably because Fe shares a number of similarities (i.e., electronic configuration, availability in the soil, or uptake mechanisms by plant) with other transition metals.

Accordingly, the changes in the Fe nutritional status of a plant are usually associated with changes in a given subset of metals, such as Mn, Zn, Cu, Mo, Co (Baxter et al., 2008a,b; Murgia and Vigani, 2015), pinpointing to the existence of a multi-level interaction among nutrients in plant. For example, a strong interaction between Fe and Mo has been recently characterized in cucumber plants (Vigani et al., 2017). Also, Tomasi et al. (2014) observed that zinc (Zn) accumulates in the leaves of Fe-deficient cucumber plants as compared to Fe-sufficient and Fe-resupplied plants.

Iron deficiency is often determined by the physico-chemical characteristics of the soil. Indeed, in alkaline and calcareous soils Fe is mainly present as insoluble oxi-hydroxide compounds leading to a very low bioavailability of Fe for plant uptake. To survive in these stress conditions, plants have developed adaptive mechanisms to cope with the low bioavailability of Fe in order to increase its acquisition (Tsai and Schmidt, 2017 and references therein). Dicots and non-graminaceous monocots have evolved a reduction-based mechanism known as Strategy I. The main responses induced by Fe deficiency in Strategy I species are the increase in (i) a Fe(III)-chelate reductase activity (FC-R), the function of which is the NAD(P)H-dependent reduction of the ferric to the ferrous form; (ii) the activity of a ferrous iron transporter (IRT1), and (iii) a H^+-ATPase activity whose task is to extrude protons useful both to acidify the rhizosphere and to generate and maintain a transmembrane electrochemical gradient which facilitates the Fe^{2+} uptake (Tsai and Schmidt, 2017 and references therein).

IRT1 has a weak substrate specificity and contributes therefore to the accumulation of a broad range of divalent transition metals, including Zn (Vert et al., 2002; Arrivault et al., 2006; Haydon et al., 2012). Similar to Fe, Zn is still an essential microelement for cell life, being a crucial cofactor for all six classes of enzymes: oxidoreductases, hydrolases, transferases, lyases, isomerases, and ligases (Coleman, 1998). Moreover, Zn plays an important structural role in regulatory proteins (Berga and Shi, 1996). However, high concentrations of Zn can be toxic for the cell causing oxidative stress (Sresty and Madhava Rao, 1999).

Zn is a highly effective cofactor since its coordination geometry is highly flexible (Fraústo da Silva and Williams, 1991). For this reason, Zn is an important structural component of small protein motifs, named Zinc fingers, characterized by the coordination of one or more Zn ions in order to stabilize protein structures. Zinc finger motifs are known to bind several target ligands, for example, DNA.

Thanks to these properties, Zn can play different roles when interacting with proteins: (i) catalytic, where Zn ions directly participate in the reaction (e.g., carbonic anhydrase); (ii) co-catalytic, where Zn plays a catalytic role together with several metal ions that interact with each other in a co-catalytic Zn site (e.g., alkaline phosphatase); (iii) structural, where Zn ions stabilize the tertiary structure of the enzyme in a similar way as the disulphide bonds (e.g., DNA-binding proteins; alcohol dehydrogenase) (Vallee and Auld, 1990; Escudero-Almanza et al., 2012).

Despite plant symptoms under Zn excess resemble symptoms of Fe-deficient plants, the mechanism underlying the interplay between Fe and Zn in plants is poorly understood. Indeed, it is known that Zn excess causes physiological Fe deficiency, probably due to an alteration of Fe transport form soil. The ability to take up iron and zinc by IRT1 is inhibited by the addition of excess zinc and iron, respectively (Rogers et al., 2000).

In order to understand how Zn interacts with Fe homeostasis, it is crucial to know how Zn is distributed in the plant tissues and in the cells of Fe-deficient plants.

The distribution of metals in plants can be studied by various imaging techniques, using histochemical methods or analytical techniques employing electrons, charged particles, or X-ray beams (Terzano et al., 2013). Nevertheless, scanty information is still available concerning the Zn distribution within plant cells (Wu et al., 2005; Li et al., 2006). Some authors stated, indeed, that one hurdle to the study of subcellular zinc homeostasis is the lack of techniques applicable to the study of this spectroscopically silent ion (Blaby-Haas and Merchant, 2013). X-ray fluorescence (XRF) methods are powerful analytical techniques for non-destructive elemental analysis with the capability to detect trace level concentrations of multiple elements. At third-generation synchrotron facilities, submicrometer resolutions and parts-per-million (ppm) to parts-per-billion (ppb) minimum detection limits can be obtained within a feasible experimental time frame.

Micro X-ray florescence (μ-XRF) analyses on cucumber plants showed an amount of Zn more than double in leaf tissues of Fe deficient plants as compared to plants resupplied with natural Fe-sources (Tomasi et al., 2014). Subcellular elemental distributions in plant samples have been imaged by μ-XRF for As in *Ceratophyllum demersum* (Mishra et al., 2016); Cd and Zn in arbuscular mycorrhizas (Nayuki et al., 2014); and As, Fe, Zn, Mn, and macronutrients in *Oryza sativa* (Moore et al., 2014). However, in all these studies, the X-rays were focused to a beam size ranging from about 500 nm to 20 μm, thus not allowing a clear visualization of the cell's internal structures and organelles. A new generation of synchrotron nanoprobes is nowadays available with ever-smaller spot sizes, down to a few tens of nanometers (Laforce et al., 2014). An example of such synchrotron X-ray nanoprobe is the newly developed ID16 NINA (nano imaging nano analysis) beamline at the European Synchrotron Radiation Facility (ESRF) of Grenoble (France) (Laforce et al., 2014).

In this work, we provide evidence about the localization and homeostasis of Zn at sub-cellular level in Fe-deficient cucumber leaves by mapping for the first time a plant cell with XRF at nanometers resolution, and by comparing XRF data with data from cell fractionation coupled to ICP/MS analysis.

MATERIALS AND METHODS

Plant Material and Growth Conditions

Seeds of cucumber (*Cucumis sativus* L. cv. Marketer) were surface-sterilized and sown in Agriperlite, watered with 0.1 mm $CaSO_4$, allowed to germinate in the dark at 26°C for 3 days, and then 70 seedlings were transferred to a box containing 20 L of the following nutrient solution: 2 mM $Ca(NO)_3$, 0.75 mM K_2SO_4, 0.65 mM $MgSO_4$, 0.5 mM KH_2PO_4, 10 μM H_3BO_3, 1 μM $MnSO_4$, 0.5 μM $CuSO_4$, 0.5 μM $ZnSO_4$, 0.05 μM $(NH_4)Mo_7O_{24}$; 0.1 mM Fe(III)-EDTA was added to control (+Fe) plants but omitted in Fe-deficient (–Fe) plants. The pH was adjusted to 6.0–6.2 with NaOH. Aerated hydroponic cultures were maintained in a growth chamber with a day:night regime of 16:8 h and a photosynthetic photon flux density (PPFD) of 200 μmol photons m^{-2} s^{-1}. The temperature was 18°C in the dark and 24°C in the light. Expanded leaves of 10 days-old cucumber plants, grown in the presence (+Fe) and in the absence of Fe (−Fe) in the medium were harvested. As previously described, 10-days-old cucumber leaves of plants grown under Fe deficiency displayed evident chlorosis symptoms and the chlorophyll content decreased by about 80% with respect to +Fe leaves (Vigani et al., 2013a).

Purification of Mitochondria and Chloroplasts

Mitochondria and chloroplasts were purified according to Rödiger et al. (2010) from expanded leaves of 10-days-old cucumber plants grown in the presence (+Fe) and in the absence of Fe (−Fe) in the medium. During purification steps, the following cellular fraction were harvested: total extract (TE, collected after homogenized tissues filtration), soluble fraction (SF, collected after mitochondrial precipitation and representing the cytosolic plus vacuolar lumen compartments), purified chloroplasts (Ch, collected at the interface between 35/80% percoll gradient), and purified mitochondria (Mit, collected at the interface between 23/40% percoll gradient) (**Supplementary Figure S1**). The purity degree was tested by Western blot analysis according to Vigani et al. (2015). Zinc and Fe content was determined on TE, SF, Ch, and Mit fractions.

Ionomics

Sampled tissues were dried and then mineralized in HNO_3 by using a Microwave Digestion System (Multiwave ECO). Chloroplast and mitochondrial fractions were mineralized in HNO_3 at 100–120°C according to Vigani et al. (2017). Metal content was determined by inductively coupled plasma-mass spectrometry (ICP/MS, aurora M90 BRUKER) according to Vigani et al. (2013a, 2017). Data collected are from three independent experiments.

Transmission Electron Microscopy

Samples of +Fe and −Fe expanded leaf tissues were fixed in a mixture of 3% (v/v) glutaraldehyde and 2% (w/v) paraformaldehyde in 0.1 mM phosphate buffer, pH 7, overnight at room temperature. Samples were subsequently post fixed with 1% (w/v) osmium tetroxide in the same buffer for 1 h at 4°C and dehydrated in a graded ethanol series before being embedded in SPURR resin (Electron Microscopy Sciences, Washington, PA, United States) according to Vigani et al. (2009). Ultrathin sections (100 nm thickness) were cut from at least three leaf samples from different plants and contrasted with uranyl acetate and lead citrate and examined with a Jeol JEM-100 SX TEM at 80 kV.

Nano X-Ray Fluorescence Imaging

Ultrathin sections were prepared as described for TEM analyses with a few modifications: osmium post-fixation was omitted and thin sections (around 200 nm thickness) were stained with toluidine blue before mounting them on SiN support meshes for X-ray analysis (DuraSiN, distributed by Electron Microscopy Sciences). Staining was necessary to visualize the portion of the sample to analyze at the synchrotron facility through the use of an optical microscope.

The nano-XRF analyses were performed at the nano-imaging beamline ID 16A of the ESRF in Grenoble (France). The synchrotron X-rays were focused at an energy of 17 keV to a beam size varying from 100 to 20 nm (depending on the sample) by means of an X-ray focusing optics based on a Kirkpatrick–Baez mirror system with a multilayer surface coating. A six elements silicon drift diode detector was used to collect the fluorescence signal.

XRF data were analyzed by using PyMca software (version 5.1.1). Zinc distribution maps are displayed by using the same grayscale for all the samples so that they can be directly visually compared. The relative amount of Zn in chloroplasts and mitochondria was obtained from the XRF sum spectrum of each organelle by dividing the peak area of the Kα line of the element multiplied per 10^3 for the area of the scatter signal, used to normalize the data for synchrotron current variations. The sum spectra were extrapolated from XRF maps by using PyMca and selecting the pixels forming the image of each organelle. All the spectra from each pixel were then summed to have the final sum spectrum. Eight chloroplasts and four mitochondria were considered for each sample. The number of mitochondria was lower because it was more difficult to distinguish them from other organelles (like peroxisomes) due to the low resolution of the XRF images, which did not allow to clearly distinguish the internal structures for all the organelles.

RESULTS

Transmission Electron Microscopy

Ultrathin sections obtained from mesophyll of +Fe and –Fe cucumber leaves were observed by TEM at different magnifications (**Figure 1**). From these observations, it is evident that the most striking morphological alteration in −Fe leaf tissues is related to chloroplast ultrastructure (**Figures 1b,d**). The organelles appeared swollen and some of them almost roundish with a dense stroma and a very low number of thylakoids, usually not organized in grana (**Figure 1d**). In some instance, also mitochondria showed altered organization with reduced number of cristae (**Figure 1d**), while no other apparent cytopathic effect

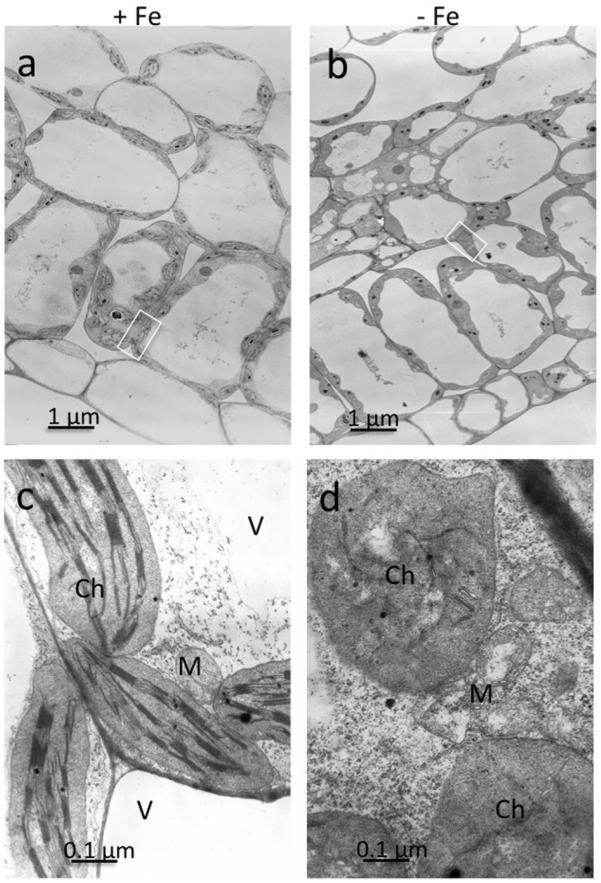

FIGURE 1 | Transmission electron microscopy (TEM) analysis of leaf tissues from cucumber plants grown in control condition (+Fe) or under Fe deficiency (–Fe). Control leaf tissues **(a,c)** and –Fe leaf tissues **(b,d)**. All scale bars = 1 µm **(a,b)** 0.1 µm **(c,d)**. M, mitochondrion; Ch, chloroplast; V, vacuole.

was detectable in cell ultrastructure, in comparisons with +Fe tissue (**Figures 1a,c**).

Leaf Ionome Profile

To evaluate the metabolic consequences of induced Fe deficiency, ionome of +Fe and −Fe plants was profiled by quantifying the content of the macronutrients sodium (Na), magnesium (Mg), potassium (K), calcium (Ca) as well as of the micronutrients manganese (Mn), zinc (Zn), copper (Cu), Fe and Mo in leaves (**Table 1**).

As expected, the growth of –Fe plants modulated Fe concentration, as seen by the reduced Fe content (by about 59%) in −Fe leaves when compared with +Fe ones.

The increased levels of K, Mg, Mn, Zn, and Cu, under Fe deficiency, indicate that these elements are dependent on Fe availability in leaves, while Na and Ca are not affected (**Table 1**). Moreover, Mo levels decreased in −Fe leaves relative to control leaves. The ionome profile of the leaves revealed that under Fe-deficiency Zn was the element which displayed the highest overall increase respect to the +Fe plants.

TABLE 1 | Na, Mg, K, Ca, Mn, Fe, Cu, Zn, and Mo concentration (µg/gDW) in leaves of cucumber plants grown under Fe-sufficient (+Fe) and Fe-deficient (−Fe) conditions.

	+Fe	−Fe	−Fe/+Fe (%)
Na	84.81 ± 31.94	122.96 ± 32.86	–
Mg	5478.54 ± 1176.69	11, 988.53 ± 3150.08*	+119
K	34, 312.26 ± 126.55	61, 947.68 ± 7.59*	+81
Ca	19, 925.31 ± 11, 504.09	17, 731.98 ± 6616.97	–
Mn	30.31 ± 8.72	75.23 ± 27.65*	+148
Fe	166.49 ± 30.88	68.95 ± 24.96*	**−59**
Cu	11.97 ± 2.05	29.01 ± 4.42*	+142
Zn	31.75 ± 8.44	113.64 ± 16.40*	**+258**
Mo	15.26 ± 0.91	7.26 ± 0.21*	−52

Value significantly different ($p < 0.05$) in Student's t-test are indicated with. Percentage changes of Fe and Zn content between +Fe and −Fe treatment are highlighted in bold.*

Cellular Fractionation-ICP/MS Analyses

In order to further investigate the Zn distribution in −Fe cells in relation to Fe, the subcellular distribution of Fe and Zn was assessed by ICP/MS analysis on four different cellular fractions collected from leaf tissues of +Fe and –Fe plants: TE, SF, Ch, and Mit (see Materials and Methods section and **Supplementary Figure S1**). Significant differences in protein yield for each fraction between +Fe and –Fe samples were not observed, as the variability among biological replicates was high. Forty grams of fresh weight of leaf material (regardless of treatments) yielded proteins amount of 0.9–1.8 g TE, 0.8–1.5 g SF, 1–3 mg Ch, and 70–100 µg Mit [i.e., 23–45 mg TE protein per gram of fresh weight (mg/g), 20–38 mg/g of SF proteins, 250–300 µg/g of Ch proteins, and 1.7–2.5 µg/g of Mit proteins]. In the TE fraction, a significant decrease of Fe concentration (expressed as ng/mg of protein) as well as a significant increase of Zn was detected in –Fe samples, while in the SF only a significant increase of Zn concentration was observed (**Figure 2A**). Interestingly, Fe concentration did not change in –Fe respect to +Fe in SF samples. Under Fe deficiency, Zn accumulated in both chloroplast and mitochondrial-enriched fractions (**Figures 2B,C**). However, in –Fe samples, Fe content in the chloroplasts and mitochondria dramatically decreased as compared to +Fe plants, being below the detection limit in chloroplasts, and reduced by 90% in the mitochondria (**Figures 2B,C**). Although possible contamination among fractions might occur under cellular fractionation, such analysis revealed that under Fe deficiency: (i) Fe content was greater (at least detectable) in mitochondria than in chloroplasts; and (ii) Zn accumulated more in chloroplasts than in mitochondria.

Nano XRF Imaging of Leaf Cells and Zn Distribution in Chloroplasts and Mitochondria

Leaf mesophyll cells were imaged by nano-XRF and elemental distribution maps were obtained as reported in **Figure 3** for a Fe-deficient plant. Clear distribution maps were obtained

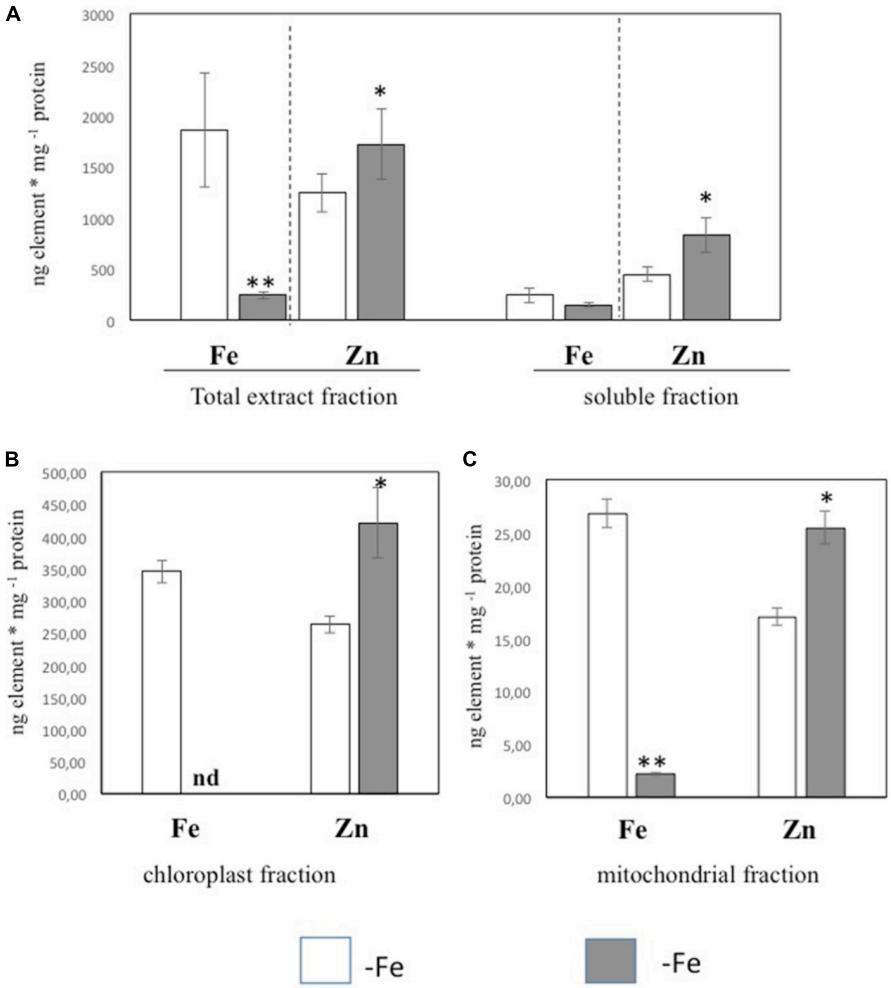

FIGURE 2 | Fe and Zn concentration in total protein extract and soluble protein fractions **(A)** and in chloroplast **(B)** and mitochondrial **(C)** fractions purified from leaf tissues of cucumber plants grown in control condition (+Fe) or under Fe deficiency (–Fe). Values, expressed as ng element * mg –1 protein are the means ± SE of three independent samples. Value significantly different $p < 0.05$ or $p < 0.01$ in Student's *t*-test are indicated with * and **, respectively.

only for few elements: Zn (**Figure 3a**), S (**Figure 3c**), and Ca (**Figure 3d**). An RGB map showing all the three elements together is also reported in **Figure 3b**. For other elements like Fe (**Figure 3e**) and Cu (**Figure 3f**), no subcellular distribution was visible except for contaminating particles (also visible in the Zn, S, and Ca maps), likely deriving from the staining process or atmospheric particulate contamination. Despite this contamination, while for certain elements like Fe and Cu, the concentration within the cell was too low to allow distribution mapping by this technique, Zn distribution appears to be not affected by staining and/or particulate except for the presence of highly concentrated spots, corresponding to the same hotspots of Fe, Cu, S, and Ca (**Figure 3**). Sum spectra of single chloroplasts and mitochondria from −Fe and +Fe plants are presented in **Figure 4**. Beside Zn, S, Ca, Fe, and Cu, other elements were detected: Si, Cl, K, Mn, Ni, and Pb. The Si signal derives from the SiN mesh used as support for the ultrathin sections. Pb signal is due to the staining solution used to allow the visualization of the cell structures within the thin section. Sum spectra showing the elemental composition of cytoplasm as compared to the full investigated areas (also containing organelles and vacuoles) are presented as **Supplementary Figure S2**. **Figure 5** shows Zn distribution maps within leaf organelles for +Fe (**Figures 5a,b**) and −Fe (**Figures 5c,d**) samples. As can be seen, Zn concentration in all the organelles of −Fe plants is higher than that in +Fe plants (darker pixels correspond to higher concentrations). The distribution maps of S, Ca, Fe, and Cu in the same areas are presented as **Supplementary Figure S3**. Chloroplasts are clearly discernible because of their large size and typical internal structures (thylakoid membranes are clearly visible). Peroxisomes appear as small rounded objects while mitochondria show a more elongated shape (**Figure 5**).

On the basis of their characteristic size and shape, various chloroplasts and mitochondria were identified in different cells and the XRF sum spectra of each organelle were used

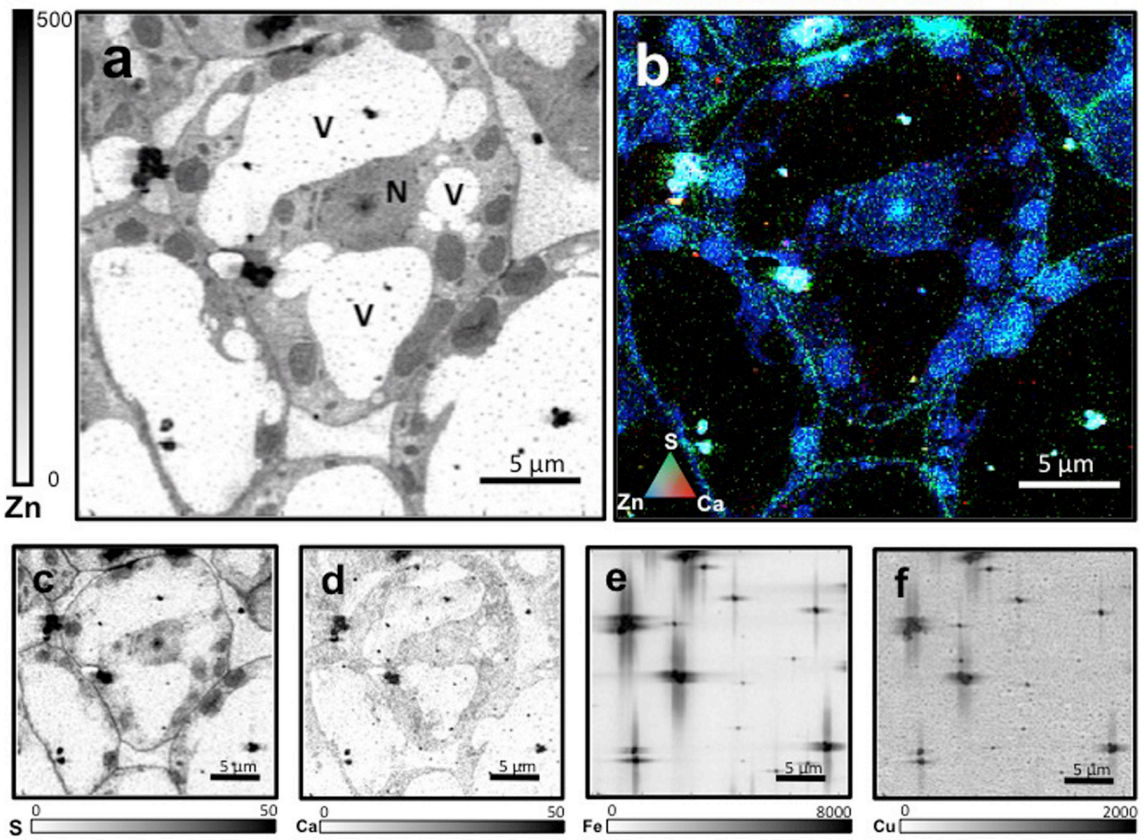

FIGURE 3 | Nano X-ray fluorescence (K_α lines) metal distribution maps of Fe-deficient leaf cells for Zn **(a)**, S **(c)**, Ca **(d)**, Fe **(e)**, and Cu **(f)**. Darker pixels correspond to higher elemental concentrations. Scale bars based on counts are reported for each element. An RGB image of the distribution of Zn (blue), S (green), and Ca (red) is also presented **(b)**. N, nucleus; V, vacuole.

to extrapolate Zn relative concentration. As can be seen from **Figure 6**, both in chloroplasts and mitochondria Zn concentration is higher in −Fe plants compared to +Fe plants. In particular, Zn concentration in −Fe chloroplasts was about 85% higher than in control +Fe chloroplasts and about 55% higher in mitochondria. These data thus confirm what was observed with cell fractionation followed by ICP/MS analyses, i.e., a higher increase of Zn concentration in chloroplasts compared to mitochondria in −Fe plants.

DISCUSSION

In this work, we aimed to provide new evidences about the interplay between Fe and Zn in plants by characterizing the subcellular localization of accumulated Zn in leaf tissues of Fe-deficient cucumber plants. The investigation of subcellular Zn homeostasis in plants is quite difficult as specific techniques applicable for such ion are still lacking (Blaby-Haas and Merchant, 2013).

Therefore, we compared the results from two different analytical approaches in order to assess Zn distribution at sub-cellular level under Fe deficiency: ion determination by ICP/MS technique on different cellular fractions separated by ultracentrifugation, and nanoscopic XRF imaging method.

ICP/MS has been established as the most reliable technique for quantifying metals, metalloids, and some non-metals in a wide range of samples with a wide working range of concentrations, high sensitivity, and low interferences. The use of ICP/MS, by allowing simultaneous measurement of multiple elements in the same sample tissue, has significant advantages for biological applications. However, few reports analyzed the metal content at subcellular level in plants (Tan et al., 2010; Vigani et al., 2017).

According to the data obtained by cellular fractionation and organelles purification followed by ICP/MS analysis, under Fe deficiency the Fe content decreased in TE, Ch, and Mit cellular fractions, while Zn content increased in all the cellular fractions collected. In particular, Fe content in chloroplasts and mitochondria was strongly reduced, with a decrease of 90% in mitochondria and close to 100% in chloroplasts, not being detected anymore by ICP/MS. It is well known that chloroplasts represent the major sink of Fe in leaf cells (Nouet et al., 2011; Vigani et al., 2013b). It has been estimated that 68% of the Fe present in the vegetative shoot of Arabidopsis plant was found to be in the chloroplast (Shikanai et al., 2003). Therefore, our results suggest that Fe deficiency weakens Fe content more in

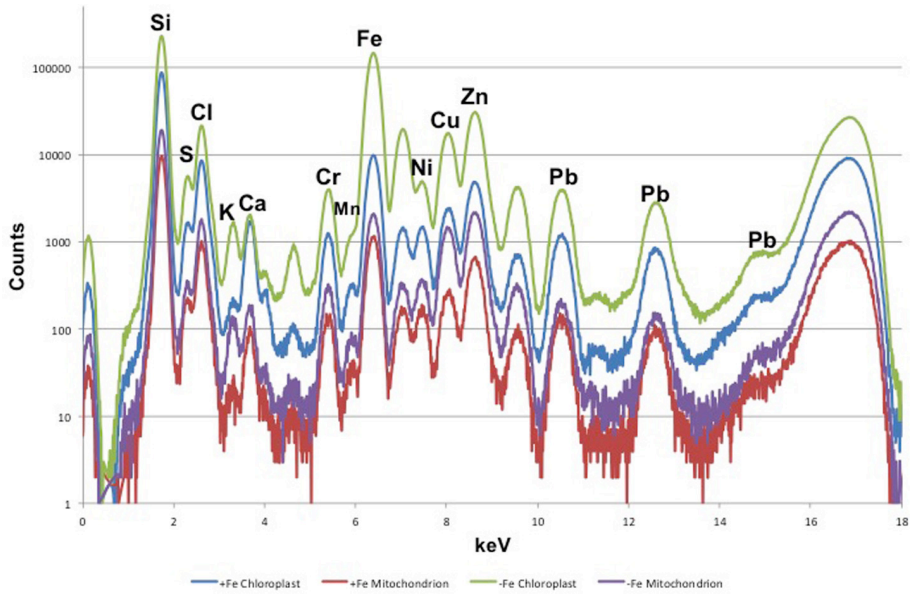

FIGURE 4 | XRF sum spectra of single chloroplasts and mitochondria from Fe-deficient (–Fe) and Fe-sufficient (+Fe) plants.

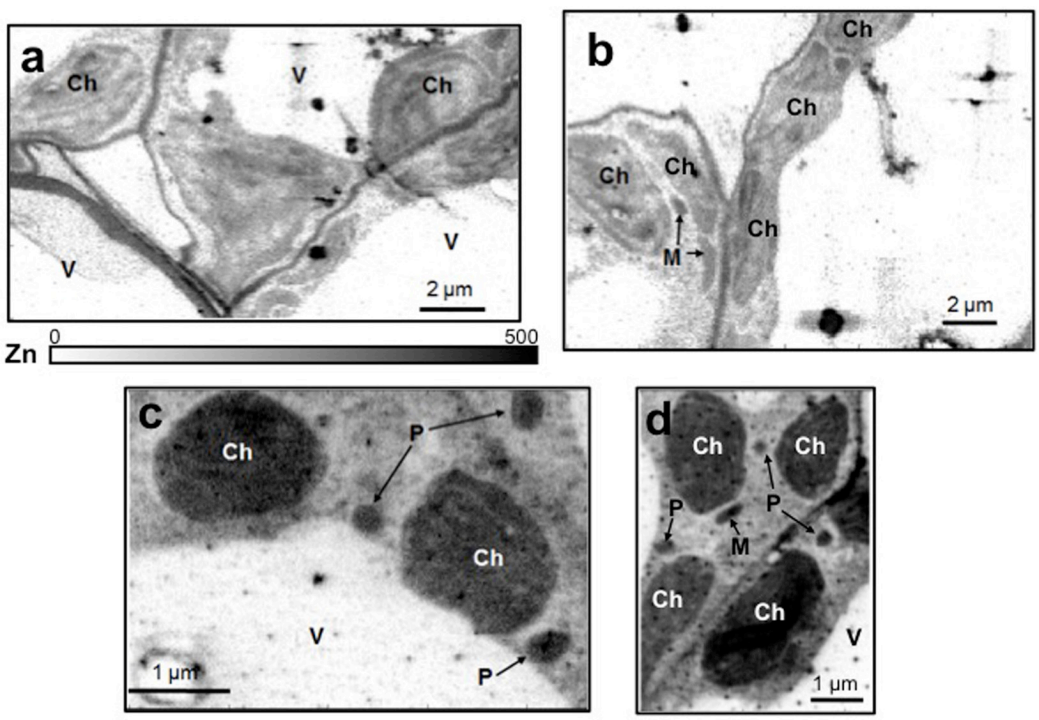

FIGURE 5 | Subcellular Zn distribution maps (XRF K_α lines) within leaf cells for +Fe **(a,b)** and –Fe **(c,d)** samples. Darker pixels correspond to higher elemental concentrations. A scale bar based on counts is also reported. M, mitochondrion; Ch, chloroplast; P, peroxisome; V, vacuole.

chloroplasts than in mitochondria or, alternatively, that under Fe starvation conditions mitochondria might have a priority for Fe allocation with respect to chloroplasts. Accordingly, in the green microalgae, mitochondria seem to be more resistant than chloroplast to Fe deficiency, suggesting a preference for Fe delivery to mitochondria when Fe is low (Nouet et al., 2011). Additionally, it has been stated that chloroplast play a central role in the regulation of Fe economy strategy of the cell under

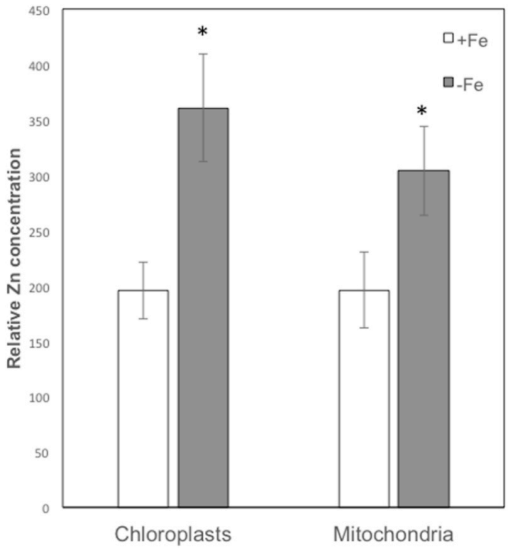

FIGURE 6 | Zn relative concentration (±SD) in chloroplasts and mitochondria of +Fe and –Fe samples, as determined from the XRF sum spectra of each organelle. Value significantly different ($p < 0.05$) in Student's *t*-test are indicated with *.

Fe deficiency in *Chlomydomonas reinhardtii* (Page et al., 2012). Recently, Hantzis et al. (2018) observed that in Arabidopsis Fe deficiency first affect photosynthesis than respiration, suggesting that photosynthesis is more dispensable under Fe deficiency compared to respiration. Accordingly, our results along with those provided by Hantzis et al. (2018) demonstrated that chloroplast is the main target of Fe deficiency highlighting the hypothesis that respiration might be preserved compared to photosynthesis under such nutritional stress.

Additionally, ICP/MS analysis revealed that Zn accumulation under Fe deficiency was significant both in chloroplast and in mitochondrial compartments. Therefore, the opposite behavior between Fe and Zn was observed in both organelles: when the Fe content decreased, the content of Zn increased. Interestingly, this did not occur in the SF, suggesting that both organelles may represent important cellular compartments where Fe and Zn interplay take place.

Nanoscopic XRF Imaging analyses of cucumber leaf confirmed that Zn accumulate mainly in chloroplasts and mitochondria of −Fe plants. Unfortunately, Fe distribution was not detectable because of the low concentration and the lower sensibility of the technique for this element, as compared to Zn. Beside the higher fluorescence yield of Zn (0.435) compared to Fe (0.32), also the energy of the X-rays used in the experiment (17 keV) favored the excitation of Zn atoms (9.657 keV) rather than Fe ones (7.109 keV). Overall, our results showed that Fe deficiency significantly affects the distribution of Zn in leaf cellular compartments: in particular chloroplast might represent a Zn sink under Fe deficiency.

An important issue to consider when dealing with synchrotron XRF analyses is the possible creation of artifacts. In this type of experiments, artifacts may derive mainly from sample preparation and photon damage (Lombi et al., 2011; Zhao et al., 2014; Kopittke et al., 2017). To image subcellular structures, ultrathin sectioning is needed as well as high flux synchrotron X-ray sources (to focus a sufficient number of photons on nm-sized spots). Therefore, we cannot completely exclude that artifacts were created during sample preparation and/or analysis. However, differently from Fe and Cu, it seems that Zn distribution was not biased by these issues, as it can be argued from the clean distribution maps and the relative Zn concentrations in −Fe and +Fe samples, which confirm the ICP/MS data.

The interplay between Fe and Zn has been already observed in different plants, but the specific molecular mechanism underlining such interaction is less investigated (Leskova et al., 2017). Indeed, it is known that at the root level Zn competes with Fe for the uptake via IRT1 (Korshunova et al., 1999). Additionally, it has been observed that foliar Fe supply strongly suppressed the development of chlorosis upon excess Zn and reduced shoot Zn accumulation (Leskova et al., 2017). Such results were not observed when foliar Fe was supplied to *irt1* mutant grown under Zn excess, suggesting a probably shoot-derived interaction between Fe and Zn, which might be relevant for the induction of Fe deficiency symptoms instead of the IRT1-mediated Zn uptake. Recently, it has been stated that the activation of Fe deficiency responses of plants growing under excess Zn were caused by an antagonist interaction between Zn and Fe (Leskova et al., 2017). In plants, Zn-dependent processes are located in all cellular compartments, including mitochondria (Heazlewood et al., 2004), and chloroplasts (Blaby-Haas and Merchant, 2013). To date, the requirement for Zn inside plant mitochondria has been linked to its role in important processes such as the degradation of mitochondrial presequences (Moberg et al., 2003; Tan et al., 2010). In this contest, several Zn-dependent metalloproteases have been identified in plant mitochondria (Moberg et al., 2003). Additionally, Zn is involved in the mitochondrial RNA editing and in in the small TIM (Translocase of the Inner Membrane) folding, and it is also requests by the COX4 subunit of cytochrome *c* oxidase in plant mitochondria (Vigani and Hanikenne, 2018 and references therein).

The role of Zn in chloroplasts has been overlooked because of its inability to perform redox chemistry. However, the interest in understanding Zn homeostasis in plant is gaining prominence (Sinclair and Kramer, 2012). Blaby-Haas and Merchant (2013) summarized the metal-dependent metabolic pathways in chloroplasts by considering different publicly available data. Chloroplast Zn-requiring enzymes are Superoxide dismutase (Cu/Zn), Alkenal/one oxidoreductase, Carboxy-transferase beta subunit of the acetyl-CoA carboxylase, proteases (FtsH proteins, peptidase M50 family protein, stromal processing peptidase), Zinc-finger proteins (involved in chloroplast and palisade cell development, in the ribosomal subunits, in the cyclic electron flow and chloroplast splicing factor). Therefore, several Zn-requiring proteins are localized in chloroplasts. Considering that Fe deficiency negatively impacts on morphology and functions of both chloroplasts and mitochondria, it is plausible to think that an increased requirement of Zn might sustain ROS detoxification

and proteins degradation processes. However, further studies are needed in order to understand the specific role of Zn under Fe deficiency in such cellular compartments.

CONCLUSION

Understanding nutrient interactions is a challenging and relevant issue in the plant nutrition field as it might reveal useful insights to develop new plant genotypes with improved mineral use efficiency and for biofortification programs (Briat et al., 2015b).

Iron and Zn represent important targets for such programs and several evidences reveal a strong interaction among these nutrients in plants. An impaired balance between Fe and Zn is perceived as Fe deficiency by plant. In order to identify the cellular site where such interaction take place we determined the subcellular distribution of Zn in −Fe leaf cells and we observed that Zn strongly accumulates in the cells of the leaves of −Fe cucumber plants. By comparing cellular fractionation-ICP/MS and nanoscopic XRF imaging results, we showed that under Fe-deficiency Zn accumulates both in chloroplasts and in mitochondria, with a higher level in chloroplasts. Our findings highlight the importance of focusing future investigations on Fe and Zn interaction at the subcellular level, especially on chloroplasts and mitochondria.

However, in order to reduce the possibility of artifacts creation during sample preparation and/or analysis, two possible approaches should be considered in future nanoscopic XRF experiments: (i) frozen-hydrated samples can be prepared by a fast-freezing process, cut as thin sections by using a cryomicrotome, and kept at low temperature until the analysis. Cryopreparations are usually less disturbing and limit the redistribution of metals and changes in speciation. However, also beamlines equipped with cryostages or cryochambers are then needed to preserve the frozen-hydrated state during the analysis. (ii) In order to avoid chemical staining, fast preliminary maps of larger areas in the sample can be acquired to locate the areas of interest prior to longer scans of the subcellular structures. For this purpose multi-crystal detector arrays, like the Maia detector (Kirkham et al., 2010), could dramatically reduce the sample exposition time thus reducing the risks of beam damage.

AUTHOR CONTRIBUTIONS

GV and RT conceived and designed the study. GV performed the cellular fraction analysis. FF carried out TEM analysis and revised the manuscript. SB, BV, LV, GV, and RT carried out nano XRF imaging analysis. GV and RT drafted the article. FF, SB, BV, and LV revised it critically. All the authors approved the final version of the article.

FUNDING

This research was supported by a FIRB-Programme Futuro in Ricerca grant from the Italian Ministry of University and Research – MIUR (Grant No. RBFR127WJ9). This work was also supported by the local research funds of Department of Life Science and Systems Biology, University of Turin.

ACKNOWLEDGMENTS

The authors thank Dr. Dario Maffi for the assistance in the ultrathin sections for both TEM and Nano X ray fluorescent imaging analysis and Giorgio Lucchini for assistance in the ICP-MS analysis.

SUPPLEMENTARY MATERIAL

The Supplementary Material for this article can be found online at: https://www.frontiersin.org/articles/10.3389/fpls.2018.01112/full#supplementary-material

FIGURE S1 | Workflow of the isolation of chloroplast and mitochondria from leaf tissues. Tube after percoll gradient for chloroplast (left) and mitochondria (right) purification are reported. Cellular fractions collected and analyzed are highlighted in yellow.

FIGURE S2 | XRF sum spectra of the whole area imaged in **Figure 5b** (+Fe Full) and 5C (−Fe Full) in comparison with sum spectra of the cytosol extracted from pixel analysis of **Figure 5b** (+Fe Cytoplasm) and **Figure 5c** (−Fe Cytoplasm).

FIGURE S3 | Subcellular distribution maps (XRF K_α lines) of S, Ca, Fe, Cu within leaf cells for +Fe **(A,B)** and −Fe **(C,D)** samples, as in **Figure 5** of the main text. Darker pixels correspond to higher elemental concentrations. A scale bar based on counts is also reported.

REFERENCES

Arrivault, S., Senger, T., and Kramer, U. (2006). The Arabidopsis metal tolerance protein AtMTP3 maintains metal homeostasis by mediating Zn exclusion from the shoot under Fe deficiency and Zn oversupply. *Plant J.* 46, 861–879. doi: 10.1111/j.1365-313X.2006.02746.x

Baxter, I., Muthukumar, B., Park, H. C., Buchner, P., Lahner, B., Danku, J., et al. (2008a). Variation in molybdenum content across broadly distributed populations of Arabidopsis thaliana is controlled by a mitochondrial Molybdenum Transporter (MOT1). *PLoS Genet.* 4:e1000004. doi: 10.1371/journal.pgen.1000004

Baxter, I., Vitek, O., Lahner, B., Muthukumar, B., Borghi, M., Morrissey, J., et al. (2008b). The leaf ionome as a multivariable system to detect a plant's physiological status. *Proc. Natl. Acad. Sci. U.S.A.* 105, 12081–12086. doi: 10.1073/pnas.0804175105

Berga, J. M., and Shi, Y. (1996). The galvanization of biology: a growing appreciation for the roles of Zinc. *Science* 271, 1081–1085. doi: 10.1126/science.271.5252.1081

Blaby-Haas, C. E., and Merchant, S. S. (2013). "Sparing and salvaging metals in chloroplast," in *Metal in Cells*, eds V. Culotta and R. A. Scott (Hoboken, NJ: John Wiley & Sons).

Briat, J. F., Dubos, C., and Gaymard, F. (2015a). Iron nutrition, biomass production and plant product quality. *Trends Plant Sci.* 20, 33–40. doi: 10.1016/j.tplants.2014.07.005

Briat, J. F., Rouached, H., Tissot, N., Gaymard, F., and Dubos, C. (2015b). Integration of P, S, Fe and Zn nutrition signals in *Arabidopsis thaliana*: potential

involvement of PHOSPHATE STARVATION RESPONSE 1 (PHR1). *Front. Plant Sci.* 6:290. doi: 10.3389/fpls.2015.00290

Coleman, J. E. (1998). Zinc enzymes. *Curr. Opin. Chem. Biol.* 2, 222–234. doi: 10.1016/S1367-5931(98)80064-1

Escudero-Almanza, D. J., Ojeada-Barrios, D. L., Hernández-Rodríguez, O. A., Sánchez Chávez, E., Ruíz-Anchondo, T., and Sida-Arreola, J. P. (2012). Carbonic Anhydrase and zinc in plant physiology. *Chil. J. Agric. Res.* 72, 140–146. doi: 10.4067/S0718-58392012000100022

Fraústo da Silva, J. J. R., and Williams, R. J. P. (1991). *The Biological Chemistry of the Elements*. Oxford: Clarendon Press.

Hantzis, L. J., Froh, G. E., Jahn, C. E., Cantrell, M., Peers, G., Pilon, M., et al. (2018). A program for iron economy during deficiency targets specific Fe proteins. *Plant Physiol.* 176, 596–610. doi: 10.1104/pp.17.01497

Haydon, M. J., Kawachi, M., Wirts, M., Stefan, H., Hell, R., and Kramer, U. (2012). Vacuolar nicotianamine has critical and distinct roles under iron deficiency and for zinc sequestration in Arabidopsis. *Plant Cell* 24, 724–737. doi: 10.1105/tpc.111.095042

Heazlewood, J. L., Tonti-Filippini, J. S., Gout, A. M., Day, D. A., Whelan, J., and Millar, A. H. (2004). Experimental analysis of the Arabidopsis mitochondrial proteome highlights signaling and regulatory components, provides assessment of targeting prediction programs, and indicates plant-specific mitochondrial proteins. *Plant Cell* 16, 241–256. doi: 10.1105/tpc.016055

Kirkham, R., Dunn, P., Kuczewski, A., Siddons, P., Dodanwela, R., Moorhead, G., et al. (2010). The maia spectroscopy detector system: engineering for integrated pulse capture, low-latency scanning and real-time processing. *AIP Conf. Proc.* 1234, 240–243. doi: 10.1063/1.3463181

Kopittke, P. M., Wang, P., Lombi, E., and Donner, E. (2017). Synchrotron-based X-ray approaches for examining toxic trace metal(loid)s in soil-plant systems. *J. Environ. Qual.* 46, 1175–1189. doi: 10.2134/jeq2016.09.0361

Korshunova, Y. O., Eide, E., Clark, W. G., Guerinot, M. L., and Pakrasi, H. B. (1999). The IRT1 protein from *Arabidopsis thaliana* is a metal transporter with a broad substrate range. *Plant Mol. Biol.* 40, 37–44. doi: 10.1023/A:1026438615520

Laforce, B., Schmitz, S., Vekemans, B., Rudloff, J., Garrevoet, J., Tucoulou, R., et al. (2014). Nanoscopic X-ray fluorescence imaging of meteoritic particles and diamond inclusions. *Anal. Chem.* 86, 12369–12374. doi: 10.1021/ac503764h

Leskova, A., Giehl, R. F. H., Hartmann, A., Fargasovà, A., and von Wiren, N. (2017). Heavy metals induce iron-deficiency responses at different hierarchic and regulatory levels. *Plant Physiol.* 174, 1648–1668. doi: 10.1104/pp.16.01916

Li, T.-G., Yang, X.-E., Yang, J. Y., and He, Z. L. (2006). Zn accumulation and subcellular distribution in the Zn hyperaccumulator *Sedum alfredii* hence. *Pedosphere* 16, 616–623. doi: 10.1016/S1002-0160(06)60095-7

Lombi, E., Scheckel, K. G., and Kempson, I. M. (2011). In situ analysis of metal(loid)s in plants: state of the art and artefacts. *Environ. Exp. Bot.* 72, 3–17. doi: 10.1016/j.envexpbot.2010.04.005

Mishra, S., Alfeld, M., Sobotka, R., Andresen, E., Falkenberg, G., and Kupper, H. (2016). Analysis of sublethal arsenic toxicity to *Cerathophyllum demersum*: subcellular distribution of arsenic and inhibition of chlorophyll biosynthesis. *J. Exp. Bot.* 67, 4639–4646. doi: 10.1093/jxb/erw238

Moberg, P., Ståhl, A., Bhushan, S., Wright, S. J., Eriksson, A., Bruce, B. D., et al. (2003). Characterization of a novel zinc metalloprotease involved in degrading targeting peptides in mitochondria and chloroplasts. *Plant J.* 36, 616–628. doi: 10.1046/j.1365-313X.2003.01904.x

Moore, K. L., Chen, L., van de Meene, A. M., Hughes, L., Lui, W., Geraki, T., et al. (2014). Combined nanoSIMS and synchrotron X-ray fluorescence reveal distinct cellular and subcellular distribution patterns of trace elements in rice tissues. *New Phytol.* 201, 104–115. doi: 10.1111/nph.12497

Murgia, I., and Vigani, G. (2015). Analysis of *Arabidopsis thaliana* atfer4-1, atfh and atfer4-1/atfh mutants uncovers frataxin and ferritin contributions to leaf ionome homeostasis. *Plant Physiol. Biochem.* 94, 65–72. doi: 10.1016/j.plaphy.2015.05.011

Nayuki, K., Chen, B., Ohtomo, R., and Kuga, Y. (2014). Cellular imaging of cadmium in resin sections of arbuscular mycorrhizas using synchrotron micro X-ray fluorescence. *Microbes Environ.* 29, 60–66. doi: 10.1264/jsme2.ME13093

Nouet, C., Motte, P., and Hanikenne, M. (2011). Chloroplast and mitochondria metal homeostasis. *Trends Plant Sci.* 16, 395–404. doi: 10.1016/j.tplants.2011.03.005

Page, M. D., Allen, M. D., Kropat, J., Urzica, E. I., Karpowicz, S. J., Hsieh, S. I., et al. (2012). Fe sparing and Fe recycling contribute to increased superoxide dismutase capacity in iron-starved *Chlamydomonas reinhardtii*. *Plant Cell* 24, 2649–2665. doi: 10.1105/tpc.112.098962

Rödiger, A., Baudisch, B., and Klosgen, R. B. (2010). Simultaneous isolation of intact mitochondria and chloroplasts from a single pulping of plant tissue. *J. Plant Physiol.* 167, 620–624. doi: 10.1016/j.jplph.2009.11.013

Rodriguez-Celma, J., Pan, I. C., Li, W., Lan, P., Buckhout, T. J., and Schmidt, W. (2013). The transcriptional response of Arabidopsis leaves to Fe deficiency. *Front. Plant Sci.* 4:276. doi: 10.3389/fpls.2013.00276

Rogers, E. E., Eide, D. J., and Guerinot, M. L. (2000). Altered selectivity in an Arabidopsis metal transporter. *Proc. Natl. Acad. Sci. U.S.A.* 97, 12356–12360. doi: 10.1073/pnas.210214197

Shikanai, T., Muller-Moulé, P., Munekage, Y., Niyogi, K. K., and Pilon, M. (2003). PAA1, a P-type ATPase of Arabidopsis, functions in copper transport in chloroplast. *Plant Cell* 15, 1333–1346. doi: 10.1105/tpc.011817

Sinclair, S. A., and Kramer, U. (2012). The zinc homeostasis network of land plants. *Biochim. Biophys. Acta* 1823, 1553–1567. doi: 10.1016/j.bbamcr.2012.05.016

Sresty, T. V. S., and Madhava Rao, K. V. (1999). Ultrastructural alterations in response to zinc and nickel stress in the root cells of pigeon pea. *Environ. Exp. Bot.* 41, 3–13. doi: 10.1016/S0098-8472(98)00034-3

Tan, Y. F., O'Toole, N., Taylor, N. L., and Millar, A. H. (2010). Divalent metal ions in plant mitochondria and their role in interactions with proteins and oxidative stress-induced damage to respiratory function. *Plant Physiol.* 152, 747–761. doi: 10.1104/pp.109.147942

Terry, N. (1980). Limiting factors in photosynthesis: I. Use of iron stress to control photochemical capacity in vivo. *Plant Physiol.* 65, 114–120. doi: 10.1104/pp.65.1.114

Terzano, R., Alfeld, M., Janssens, K., Vekemans, B., Schoonjans, T., Vincze, L., et al. (2013). Spatially resolved (semi)quantitative determination of iron (Fe) in plants by means of synchrotron micro X-ray fluorescence. *Anal. Bioanal. Chem.* 405, 3341–3350. doi: 10.1007/s00216-013-6768-6

Tomasi, N., Mimmo, T., Terzano, R., Alfeld, M., Janssens, K., Zanin, L., et al. (2014). Nutrient accumulation in leaves of Fe-deficient cucumber plants treated with natural Fe complexes. *Biol. Fertil. Soil* 50, 973–982. doi: 10.1007/s00374-014-0919-6

Tsai, H. H., and Schmidt, W. (2017). Mobilization of iron by plant born coumarins. *Trends Plant Sci.* 22, 538–548. doi: 10.1016/j.tplants.2017.03.008

Vallee, B. L., and Auld, D. S. (1990). Zinc coordination, function, and structure of zinc enzymes and other proteins. *Biochemistry* 29, 5647–5659. doi: 10.1021/bi00476a001

Vert, G., Grozt, N., Dedaldechamp, F., Gaymard, F., Guerinot, M. L., Briat, J. F., et al. (2002). IRT1, an Arabidopsis transporter essential for iron uptake from the soil and for plant growth. *Plant Cell* 14, 1223–1233. doi: 10.1105/tpc.001388

Vigani, G., Di Silvestre, D., Agresta, A. M., Donnini, S., Mauri, P., Gehl, C., et al. (2017). Molybdenum and iron mutually impact their homeostasis in cucumber (*Cucumis sativus* L) plants. *New Phytol.* 213, 1222–1241. doi: 10.1111/nph.14214

Vigani, G., Faoro, F., Ferretti, A. M., Cantele, F., Maffi, D., Marelli, M., et al. (2015). Three-dimensional reconstruction, by TEM tomography, of the ultrastructural *Cucumis sativus* L. mitochondria under Fe deficiency. *PLoS One* 10:e0129141. doi: 10.1371/journal.pone.0129141

Vigani, G., and Hanikenne, M. (2018). "Metal homeostasis in plant mitochondria," in *Plant Mitochondria*, 2nd Edn, ed. D. Logan (Hoboken, NY: Wiley-Blackwell), 111–142.

Vigani, G., Maffi, D., and Zocchi, G. (2009). Iron availability affects the function of mitochondria in cucumber root. *New Phytol.* 182, 127–136. doi: 10.1111/j.1469-8137.2008.02747.x

Vigani, G., Tarantino, D., and Murgia, I. (2013a). Mitochondrial ferritin is a functional iron-storage protein in cucumber (*Cucumis sativus*) roots. *Front. Plant Sci.* 4:316. doi: 10.3389/fpls.2013.00316

Vigani, G., Zocchi, G., Bashir, K., Philippar, K., and Briat, J. F. (2013b). Signal from chloroplasts and mitochondria for iron homeostasis regulation. *Trends Plant Sci.* 18, 305–311. doi: 10.1016/j.tplants.2013.01.006

Wu, F. B., Dong, J., Qiu Qion, Q., and Zhang, G.-P. (2005). Subcellular distribution and chemical form of Cd and Cd-Zn interaction in different barley genotypes. *Chemosphere* 60, 1437–1446. doi: 10.1016/j.chemosphere.2005.01.071

Zhao, F. J., Moore, K. L., Lombi, E., and Zhu, Y. G. (2014). Imaging element distribution and speciation in plant cells. *Trends Plant Sci.* 19, 183–192. doi: 10.1016/j.tplants.2013.12.001

Conflict of Interest Statement: The authors declare that the research was conducted in the absence of any commercial or financial relationships that could be construed as a potential conflict of interest.

frontiers in Plant Science

ORIGINAL RESEARCH
published: 11 September 2018
doi: 10.3389/fpls.2018.01325

A Shoot Fe Signaling Pathway Requiring the OPT3 Transporter Controls GSNO Reductase and Ethylene in *Arabidopsis thaliana* Roots

*María J. García[1], Francisco J. Corpas[2], Carlos Lucena[3], Esteban Alcántara[3], Rafael Pérez-Vicente[1], Ángel M. Zamarreño[4], Eva Bacaicoa[4], José M. García-Mina[4], Petra Bauer[5] and Francisco J. Romera[3]**

[1] Department of Botany, Ecology and Plant Physiology, Campus de Excelencia Internacional Agroalimentario, Universidad de Córdoba, Córdoba, Spain, [2] Department of Biochemistry, Cell and Molecular Biology of Plants, Estación Experimental del Zaidín, Spanish National Research Council, Granada, Spain, [3] Department of Agronomy, Campus de Excelencia Internacional Agroalimentario, Universidad de Córdoba, Córdoba, Spain, [4] Department of Environmental Biology, Faculty of Sciences, University of Navarra, Pamplona, Spain, [5] Institute of Botany, University of Düsseldorf, Düsseldorf, Germany

OPEN ACCESS

Edited by:
Hannetz Roschzttardtz,
Pontificia Universidad Católica de Chile, Chile

Reviewed by:
Ping Lan,
Institute of Soil Science (CAS), China
Louis Grillet,
Academia Sinica, Taiwan

***Correspondence:**
Francisco J. Romera
ag1roruf@uco.es

Specialty section:
This article was submitted to Plant Nutrition, a section of the journal Frontiers in Plant Science

Received: 19 March 2018
Accepted: 23 August 2018
Published: 11 September 2018

Citation:
García MJ, Corpas FJ, Lucena C, Alcántara E, Pérez-Vicente R, Zamarreño ÁM, Bacaicoa E, García-Mina JM, Bauer P and Romera FJ (2018) A Shoot Fe Signaling Pathway Requiring the OPT3 Transporter Controls GSNO Reductase and Ethylene in Arabidopsis thaliana Roots. Front. Plant Sci. 9:1325. doi: 10.3389/fpls.2018.01325

Ethylene, nitric oxide (NO) and glutathione (GSH) increase in Fe-deficient roots of Strategy I species where they participate in the up-regulation of Fe acquisition genes. However, *S*-nitrosoglutathione (GSNO), derived from NO and GSH, decreases in Fe-deficient roots. GSNO content is regulated by the GSNO-degrading enzyme *S*-nitrosoglutathione reductase (GSNOR). On the other hand, there are several results showing that the regulation of Fe acquisition genes does not solely depend on hormones and signaling molecules (such as ethylene or NO), which would act as activators, but also on the internal Fe content of plants, which would act as a repressor. Moreover, different results suggest that total Fe in roots is not the repressor of Fe acquisition genes, but rather the repressor is a Fe signal that moves from shoots to roots through the phloem [hereafter named LOng Distance Iron Signal (LODIS)]. To look further in the possible interactions between LODIS, ethylene and GSNOR, we compared *Arabidopsis* WT Columbia and LODIS-deficient mutant *opt3-2* plants subjected to different Fe treatments that alter LODIS content. The *opt3-2* mutant is impaired in the loading of shoot Fe into the phloem and presents constitutive expression of Fe acquisition genes. In roots of both Columbia and *opt3-2* plants we determined 1-aminocyclopropane-1-carboxylic acid (ACC, ethylene precursor), expression of ethylene synthesis and signaling genes, and GSNOR expression and activity. The results obtained showed that both 'ethylene' (ACC and the expression of ethylene synthesis and signaling genes) and 'GSNOR' (expression and activity) increased in Fe-deficient WT Columbia roots. Additionally, Fe-sufficient *opt3-2* roots had higher 'ethylene' and 'GSNOR' than Fe-sufficient WT Columbia roots. The increase of both 'ethylene' and 'GSNOR' was not related to the total root Fe content but to the absence of a Fe shoot signal (LODIS), and was associated with the up-regulation of Fe acquisition genes. The possible relationship between GSNOR(GSNO) and ethylene is discussed.

Keywords: ethylene, glutathione (GSH), iron, long distance iron signal (LODIS), nitric oxide (NO), phloem, *S*-nitrosoglutathione (GSNO), *S*-nitrosoglutathione reductase (GSNOR)

INTRODUCTION

Iron (Fe) is abundant in most soils, mainly as Fe^{3+}, although its availability to plants is low, especially in calcareous soils (Römheld and Marschner, 1986). Based on the mechanisms used by plant roots to facilitate mobilization and uptake of Fe, plants are classified into Strategy I species and Strategy II species (Römheld and Marschner, 1986; Ivanov et al., 2012; Kobayashi and Nishizawa, 2012). Dicots, such as *Arabidopsis* and pea (*Pisum sativum*), are Strategy I species and reduce Fe^{3+} to Fe^{2+}, by means of a ferric reductase (encoded by *FRO2* in *Arabidopsis*) at the root surface, prior to its subsequent uptake through a Fe^{2+} transporter (encoded by *IRT1* in *Arabidopsis*; Ivanov et al., 2012; Kobayashi and Nishizawa, 2012). When grown under Fe deficiency, Strategy I species develop several physiological and morphological responses, mainly in roots, which favor Fe acquisition and are generally known as Fe deficiency responses. Among the physiological responses are the up-regulation of the ferric reductase and the Fe^{2+} transporter genes, as well as many other Fe-related genes (Ivanov et al., 2012; Kobayashi and Nishizawa, 2012; Brumbarova et al., 2015; Lucena et al., 2015). In the last years, several transcription factors (TFs) that participate in the activation of these genes have been found (Ivanov et al., 2012; Kobayashi and Nishizawa, 2012; Brumbarova et al., 2015; Zhang et al., 2015; Li et al., 2016; Liang et al., 2017). In *Arabidopsis*, the master regulator of most of the Fe-related genes is FIT (bHLH29), homolog of the tomato FER gene (Bauer et al., 2007 and references therein). The FIT regulatory network comprises other bHLH TFs of the Ib subgroup, such as bHLH38, bHLH39, bHLH100, and bHLH101. All of them have redundant functions and can interact with FIT to form heterodimers that activate the expression of the Fe acquisition genes *FRO2* and *IRT1* (Yuan et al., 2008; Wang et al., 2013; Brumbarova et al., 2015). FIT is induced in roots in response to Fe deficiency while the other Ib bHLH genes cited above are induced in both roots and leaves in response to Fe deficiency (Brumbarova et al., 2015 and references therein). Lately, it has been found that, under Fe-deficiency conditions, IVc subgroup bHLH TFs, like bHLH105 and bHLH115, activate the expression of FIT/bHLH38/39/100/101 (Zhang et al., 2015; Li et al., 2016; Liang et al., 2017).

The regulation of the above TFs and genes is not totally understood, but several works support a role for hormones and signaling molecules in the activation of FIT (and other Ib bHLH TFs) and, consequently, in the up-regulation of the ferric reductase and the Fe^{2+} transporter genes. Among them are auxin, ethylene, salicylic acid, nitric oxide (NO), sucrose, and glutathione (GSH). All of them increase in Fe-deficient roots although their precise roles and interactions are not totally known (Zaharieva and Abadía, 2003; Zaharieva et al., 2004; Lucena et al., 2006, 2015; Graziano and Lamattina, 2007; Waters et al., 2007; Bacaicoa et al., 2009, 2011; Chen et al., 2010; García et al., 2010, 2011; Lingam et al., 2011; Meiser et al., 2011; Romera et al., 2011, 2017; Koen et al., 2012; Yang et al., 2014; Shanmugam et al., 2015; Lin et al., 2016; Shen et al., 2016; Li and Lan, 2017; Kailasam et al., 2018). There are also some hormones, such as cytokinins and jasmonates, that have been involved in the suppression of Fe deficiency responses (Séguéla et al., 2008; Maurer et al., 2011). Besides the activation of Fe-related genes, auxin, ethylene, and NO have also been involved in the regulation of morphological responses to Fe deficiency, such as the development of subapical root hairs (Romera et al., 2011, 2017; Lucena et al., 2015; Li and Lan, 2017). Additionally, ethylene is involved in restricting the suberization of the endodermis under Fe deficiency (Barberon et al., 2016), and NO and GSH are involved in improving Fe availability inside plants (Graziano et al., 2002; Ramírez et al., 2013).

In a previous work, García et al. (2011) showed that ethylene can induce NO accumulation in the subapical region of the roots, where most Fe responses are located. On the other hand, they found that NO can upregulate many ethylene synthesis and signaling genes in roots. This mutual and positive influence between ethylene and NO has also been described in the development of root hairs under Mg deficiency (Liu et al., 2017) and in other physiological processes (García et al., 2011 and references therein; Lin et al., 2013). Both ethylene and NO greatly activate the expression of Fe acquisition genes in plants grown with low levels of Fe (or without Fe), but have much less effect in plants grown with high levels of Fe (Lucena et al., 2006; Graziano and Lamattina, 2007; Chen et al., 2010; García et al., 2011). Similar results have also been found when other activators of Fe acquisition genes, like auxin (Chen et al., 2010) or sucrose (Lin et al., 2016), have been applied to plants grown with different Fe levels. All these results suggest that the up-regulation of Fe acquisition genes does not solely depend on hormones and signaling molecules (such as ethylene, auxin, sucrose, or NO), that would act as activators, but also on the internal Fe content of plants, that would act as a repressor (Lucena et al., 2006; García et al., 2011, 2013; Romera et al., 2011). However, different results suggest that total Fe in roots is not the repressor of Fe acquisition genes. As examples, *Arabidopsis opt3, frd3, nas4x-1* and *bts3* mutants, *Arabidopsis AtHSCB* overexpressing lines, tomato *chln* mutant, and pea *dgl* and *brz* mutants, all of them present constitutive activation of Fe acquisition genes when grown under Fe sufficiency despite the high accumulation of Fe inside their roots (García et al., 2013 and references therein; Romera et al., 2015; Leaden et al., 2016; Hindt et al., 2017; Khan et al., 2018). Several of the above genotypes are affected, either directly or indirectly, in the transport of Fe through the phloem, which suggests that phloem Fe could be a key factor in the repression of Fe acquisition genes (García et al., 2013; Khan et al., 2018). In any case, there is no doubt that shoots play a very important role in the regulation of Fe acquisition genes in roots (García et al., 2013 and references therein; Mendoza-Cózatl et al., 2014; Zhai et al., 2014; Gayomba et al., 2015). In accordance with this, Khan et al. (2018) have recently demonstrated that the leaf vasculature respond to Fe deficiency considerably faster than roots, and Kumar et al. (2017) have found, by using reciprocal shoot/root grafts between *Arabidopsis ysl1ysl3* double mutant and WT plants, that the ability to express the Fe deficiency responses depends on the genotype of the shoot.

OPT3 (OligoPeptide Transporter3) is the main transporter implicated in the loading of shoot Fe into the phloem (Mendoza-Cózatl et al., 2014; Zhai et al., 2014; Kumar et al., 2017;

Khan et al., 2018). In supporting this view, it should be noted that the foliar application of Fe did not inhibit the expression of Fe acquisition genes in Fe-deficient *Arabidopsis opt3-2* roots while it did in Fe-deficient *Arabidopsis* WT roots (García et al., 2013). Furthermore, phloem sap measurements in *opt3* mutants show a 50% reduction in Fe content (Khan et al., 2018). *OPT3* is expressed in the plasma membrane of phloem cells, mainly in shoots, and its shoot-specific expression is sufficient to complement the Fe-deficiency response in *opt3-2* roots (Mendoza-Cózatl et al., 2014; Zhai et al., 2014; Gayomba et al., 2015). These results suggest that OPT3 plays an important role in the iron-signaling network between leaves and roots (García et al., 2013; Mendoza-Cózatl et al., 2014; Zhai et al., 2014; Gayomba et al., 2015). The precise substrate of the OPT3 transporter is not yet clear. Zhai et al. (2014) found that OPT3 can transport Fe^{2+} ions when expressed in *Xenopus* oocytes. However, while Wintz et al. (2003) found that OPT3 was able to rescue the *fet3fet4* strain of yeast, impaired in Fe uptake, Mendoza-Cózatl et al. (2014) found that not. Even if OPT3 transports Fe ions, these ions should be chelated in the phloem sap due to the poor solubility of Fe at the alkaline pH of this fluid (Gutiérrez-Carbonell et al., 2015). Although OPT3 does not mediate GSH transport in *S. cerevisiae* (Zhai et al., 2014), other OPT transporters do (Lubkowitz, 2011 and references therein; Zhang et al., 2016 and references therein). Consequently, some proposed chelating agents of Fe are GSH-derived compounds, like *S*-nitrosoglutathione (GSNO) or nitrosyl-iron complexes (NICs, formed from the interaction of Fe, NO and thiols); also peptides and proteins (Krüger et al., 2002; Ramírez et al., 2011; Rahmanto et al., 2012; Darbani et al., 2013; García et al., 2013; Buet and Simontacchi, 2015). Based on these findings, we suggest the name LODIS (LOng Distance Iron Signal) for the shoot Fe signal related to OPT3 and moving through the phloem, which causes the repression of Fe acquisition genes in roots. Although the LODIS nature is still unknown, it is possible to investigate its consequences by comparing the LODIS-deficient mutant *opt3-2* and the WT cultivar Columbia, and by comparing plants treated or not with foliar application of Fe.

Another important question, which remains unsolved, is how the Fe status is perceived by the roots. At this point, it has been proposed that Fe (probably, LODIS or a LODIS-derived signal) could be sensed by the BRUTUS (BTS) protein in Strategy I plants (Kobayashi and Nishizawa, 2014). BTS is a homolog of HRZs, known Fe sensors in rice (Kobayashi and Nishizawa, 2014). The current data suggests that BTS acts as a negative regulator of Fe responses (Zhang et al., 2015; Hindt et al., 2017). This would explain why Fe-sufficient *bts-2* and *bts-3* roots present higher expression of Fe acquisition genes than Fe-sufficient WT roots (Zhang et al., 2015; Hindt et al., 2017).

To integrate both positive and negative signals in the regulation of Fe acquisition genes in roots, Lucena et al. (2006) proposed a model that implicated both LODIS and ethylene in such a regulation. Subsequently, this model has been extended to other positive signals besides ethylene, like NO and auxin (García et al., 2011; Romera et al., 2011, 2017). According to this model, auxin/ethylene/NO would act as activators of the expression of Fe acquisition genes in roots, while LODIS would act to repress their expression (García et al., 2011; Romera et al., 2011, 2017). This model does not exclude the role of other positive and negative signals (most of them reviewed by García et al., 2015; Romera et al., 2017). The way LODIS represses the expression of Fe acquisition genes is not totally known, but several results suggest that it could negatively affect ethylene action. García et al. (2013) found that ACC up-regulated the expression of Fe acquisition genes when applied to roots of Fe-deficient plants but not when applied simultaneously with foliar Fe. This result suggests that LODIS could block ethylene action, but does not preclude an additional negative effect of LODIS on ethylene production.

One of the objectives of this work was to study the role of LODIS on ethylene synthesis in roots. For this, we determined 1-aminocyclopropane-1-carboxylic acid (ACC) concentration and the expression of the key ethylene synthesis genes *SAM1*, *ACS6*, and *ACO2* in roots of *Arabidopsis* WT Columbia plants subjected to different Fe treatments that alter LODIS content. It should be noted that ACC content and the expression of the above ethylene synthesis genes increase under Fe deficiency (García et al., 2010; Gutiérrez-Carbonell et al., 2015; Lucena et al., 2015 and references therein; Ye et al., 2015; Romera et al., 2017 and references therein). In a parallel study, similar determinations were done in the *Arabidopsis* LODIS-deficient mutant *opt3-2*, and in other *Arabidopsis* mutants that behave like LODIS-deficient, such as *frd3-3* and *nas4x-1*. All of these mutants have constitutive activation of Fe acquisition genes when grown under Fe sufficient conditions (see section "Materials and Methods"; Rogers and Guerinot, 2002; Klatte et al., 2009; García et al., 2013). A second objective of this work was to study the possible relationship of *S*-nitrosoglutathione reductase (GSNOR) with Fe deficiency and, more specifically, with LODIS. Both GSH and NO increase in roots under Fe deficiency and have been implicated in the activation of Fe responses (Zaharieva and Abadía, 2003; Zaharieva et al., 2004; Graziano and Lamattina, 2007; Bacaicoa et al., 2009; Chen et al., 2010; García et al., 2011; Koen et al., 2012; Shanmugam et al., 2015; Kailasam et al., 2018). However, *S*-nitrosoglutathione (GSNO), the most abundant low-molecular-weight *S*-nitrosothiol in plants (Liu et al., 2018), and which is derived from GSH and NO (Corpas et al., 2013), decreases under Fe deficiency in *Arabidopsis* roots (Shanmugam et al., 2015; Kailasam et al., 2018). Since GSNOR regulates GSNO content by decomposing it to oxidized glutathione (GSSG) and H_3N (Leterrier et al., 2011; Corpas et al., 2013), we wanted to know whether GSNOR increases in roots under Fe deficiency. For this, we determined GSNOR expression and activity under Fe deficiency and also under different Fe treatments and genetic backgrounds that could influence LODIS levels.

The results show that ethylene (ACC and the expression of ethylene synthesis genes) and GSNOR (expression and activity) increase under conditions that restrict LODIS accumulation in roots, such as Fe deficiency in WT or Fe sufficiency in the LODIS-deficient mutant *opt3-2*, while they decrease under conditions that favor its accumulation, such as Fe sufficiency or foliar application of Fe in WT. The up-regulation of GSNOR under Fe deficiency in the WT suggests that lower GSNO levels in roots could be a prerequisite for the up-regulation of ethylene synthesis and, consequently, for that of Fe acquisition genes.

MATERIALS AND METHODS

Plant Materials, Growth Conditions, and Treatments

To study the role of LODIS on ethylene and GSNOR in roots, wild-type *Arabidopsis* [*Arabidopsis thaliana* (L.) Heynh ecotype Columbia] and pea [*Pisum sativum* L. cv. Sparkle] plants were used. Additionally, we used some mutants that show constitutive up-regulation of Fe acquisition genes when grown under Fe-sufficient conditions and that are, or behave like, LODIS-deficient (García et al., 2013 and references therein). These mutants were *Arabidopsis opt3-2*, *frd3-3* and *nas4x-1*, and pea *dgl* (Sparkle [*dgl*,*dgl*]). *OPT3* is expressed mainly in shoots, where it could act as a transporter involved in the loading of Fe^{2+} ions into the phloem (Stacey et al., 2008; Zhai et al., 2014; see **Figure 12**). The *Arabidopsis frd3-3* mutant is impaired in xylem Fe transport (Rogers and Guerinot, 2002; Roschzttardtz et al., 2011; Gayomba et al., 2015) but, as a consequence, it is also defective in the transport of Fe from shoots to roots through the phloem (it behaves like LODIS-deficient), since less Fe gets into leaves to enter the phloem (Lucena et al., 2006; see **Figure 12**). The *Arabidopsis nas4x-1* mutant is defective in the synthesis of NA, which is involved in Fe loading and unloading of the phloem (Klatte et al., 2009; Schuler et al., 2012). Both *frd3-3* and *nas4x-1* mutants show chlorosis when grown under Fe-sufficient conditions (Lucena et al., 2006; Klatte et al., 2009). In relation to the pea *dgl* mutant, the specific gene related to this mutation has not been identified yet. However, several results suggest that the *dgl* mutant phenotype may be related to defects in phloem Fe transport since it behaves like a LODIS-deficient mutant (García et al., 2013; Romera et al., 2015). Although the *dgl* mutant originated from the DGV (Dippes Gelbe Viktoria) cultivar, we used a near isogenic line homozygous for the *dgl* mutation that was introgressed into the Sparkle cultivar and described here as Sparkle [*dgl*, *dgl*] (Marentes and Grusak, 1998).

Arabidopsis and pea plants were grown on aerated nutrient solution in a growth chamber, as previously described (Lucena et al., 2006, 2007). When appropriate, plants were transferred to the different treatments. The treatments imposed were: **+Fe**: nutrient solution with 40 μM Fe-EDDHA, except for pea WT Sparkle, that was 20 μM Fe-EDDHA, and for pea *dgl*, that was 3 μM Fe-EDDHA (this mutant grows adequately with 2–3 μM Fe-EDDHA concentration but presents symptoms of Fe toxicity when grown with higher levels of Fe; Romera et al., 2015); **−Fe**: nutrient solution without Fe during different times (from 6 to 72 h, depending on experiments); **−Fe+foliarFe**: −Fe treatment during 2 or 3 days and $FeSO_4$ application to leaves during the last 24 h; **−P**: nutrient solution without P during 2 days; **−S**: nutrient solution without S during 2 days. It should be noted that, in our experimental conditions, the expression of Fe acquisition genes and the ferric reductase activity was weak after 24 h of Fe deficiency and reached their maximum after 48 h of Fe deficiency. $FeSO_4$ was dissolved in deionized water (1.8 mM) and Tween 20 was added as surfactant. Leaves were sprayed once until total moistening. After treatments, root ferric reductase activity was determined as described previously (Lucena et al., 2006). Finally, the roots were collected and kept at −80°C for subsequent analysis of ACC and mRNA levels. In some experiments, GSNOR activity, GSNO and GSH were determined in fresh roots.

ACC Determination

The extraction, purification and quantification of ACC was carried out using the method described by Mora et al. (2012). Briefly, ACC of roots was extracted with 20 μl of d_4ACC [3 μg/mL in acetonitrile/acetic acid 0.2% (90/10)] and 3 ml of MeOH/H_2O/HCOOH (15/4/1, v/v/v) at −20°C. Purification was carried out using a Strata C18-E cartridge (Ref 8B-S001-FBJ, Phenomenex, Torrance, CA, United States) preconditioned with 4 ml of methanol and 2 ml of MeOH/H_2O/HCOOH (15/4/1, v/v/v). Finally, the eluted fraction was centrifuged (10,000 rpm, 8 min) and injected in the LC/MS/MS systems, and ACC was quantified by HPLC linked to a 3200 QTRAP LC/MS/MS system (Applied Biosystems/MDS Sciex, Ontario, Canada), equipped with a turbo ion spray interface.

GSNOR Activity Determination

GSNOR activity was assayed spectrophotometrically at 25°C by monitoring the oxidation of NADH at 340 nm as described by Sakamoto et al. (2002). The root extracts were incubated in an assay mixture containing 20 mM TRIS-HCl (pH 8.0), 0.2 mM NADH, and 0.5 mM EDTA, and the reaction was started by adding GSNO (Calbiochem) to the mixture at a final concentration of 400 μM. The activity was expressed as nmol NADH consumed min^{-1} mg^{-1} protein (ε_{340} = 6.22 mM^{-1} cm^{-1}).

Quantification of GSNO and GSH by Liquid Chromatography Electrospray Ionization Mass Spectrometry (LC–ES/MS)

Arabidopsis samples (300 mg) were ground using a mortar and pestle in the presence of 1 ml of 0.1 M HCl. Homogenates were centrifuged at 15,000 *g* for 20 min at 4°C. The supernatants were collected and filtered through 0.22-mm polyvinylidene fluoride filters and immediately analyzed. All procedures were carried out at 4°C and were protected from light to avoid potential degradation of the analytes (GSNO and GSH). The LC–ES/MS system consisted of a Waters Allience 2695 HPLC system connected to a Micromass Quattro micro API triple quadrupole mass spectrometer, both obtained from the Waters Corporation. HPLC was carried out using an Atlantis® T3 3 μm 2.1 mm × 100 mm Column obtained from the Waters Corporation. The Micromass Quattro Micro API mass spectrometer was used in positive electrospray ionization mode for detection and quantification of GSNO and GSH (Airaki et al., 2011; Leterrier et al., 2012).

qRT-PCR Analysis

Roots were ground to a fine powder with a mortar and pestle in liquid nitrogen. Total RNA was extracted using the Tri Reagent solution (Molecular Research Center, Inc., Cincinnati, OH, United States) according to the manufacturer's

instructions. M-MLV reverse transcriptase (Promega, Madison, WI, United States) was used to generate cDNA from 3 μg of DNase-treated root RNA as the template and random hexamers as the primers.

The study of gene expression by qRT-PCR was performed by using a qRT-PCR Bio-Rad CFX connect thermal cycler and the following amplification profile: initial denaturation and polymerase activation (95°C for 3 min), amplification and quantification repeated 40 times (90°C for 10 s, 57°C for 15 s and 72°C for 30 s), and a final melting curve stage of 65 to 95°C with increment of 0.5°C for 5 s, to ensure the absence of primer dimer or non-specific amplification products. PCR reactions were set up in 20 μl of SYBR Green Bio-RAD PCR Master Mix, following the manufacturer's instructions. Controls containing water instead of cDNA were included to check for contamination in the reaction components. Gene-specific primers (**Table 1**) were designed by using the Primer-BLAST software from the NCBI site. Standard dilution curves were performed for each primer pair to confirm appropriate efficiency of amplification (E = 100 ± 10%). Constitutively expressed *SAND1* and *YLS8* genes, which do not respond to changes in the Fe conditions (Han et al., 2013), were used as reference genes to normalize qRT-PCR results. The relative expression levels were calculated from the threshold cycles (Ct) values and the primer efficiencies by the Pfaffl method (Pfaffl, 2001). Each PCR analysis was conducted on three biological replicates and each PCR reaction repeated twice.

Statistical Analysis

All experiments were repeated at least twice and representative results are presented. The values of qRT-PCR represent the mean ± SE of three independent biological replicates. The values of other determinations (ACC, GSNO, GSH, ferric reductase activity, GSNOR activity) represent the mean ± SE of six replicates. Within each gene or genotype, different letters indicate significant differences ($P < 0.05$) among treatments using one-way analysis of variance (ANOVA) followed by a Duncan's multiple range test (i.e., **Figures 1**, **2**, **6**). Dunnett's test was also used when one or several mutants were compared with the WT for the +Fe treatment (i.e., **Figures 2**, **3**) and when different treatments were compared with a control (i.e., **Figures 3**, **9**). In this latter case, ** indicate significant differences ($P < 0.05$).

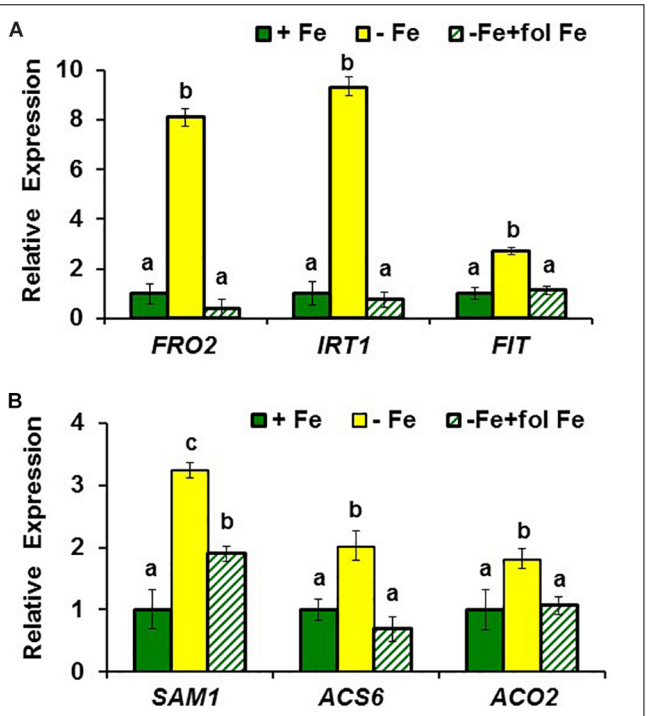

FIGURE 1 | Effect of Fe deficiency and foliar application of Fe on the expression of **(A)** Fe acquisition genes *FRO2*, *IRT1,* and *FIT*; and **(B)** ethylene synthesis genes *SAM1*, *ACS6* and *ACO2*, in roots of *Arabidopsis* WT Columbia plants. Plants were grown in nutrient solution with Fe (+Fe). Some of them were transferred to nutrient solution without Fe 3 days before harvest (–Fe). Half of the –Fe plants were sprayed with Fe 24 h before harvest (–Fe+fol Fe). Relative expression was calculated in relation to +Fe. Data represent the mean ± SE of three independent biological replicates. Within each gene, bars with different letters indicate significant differences ($P < 0.05$).

TABLE 1 | Primer pairs for *Arabidopsis* genes.

Gene	Sequence 5′–3′
AtFRO2 (At1g01580)	**Forward:** TGGTTGCCACATCTGCGTAT **Reverse:** TCGATATGGTGTGGCGACTT
AtIRT1 (At4g19690)	**Forward:** TGTCTCTTTTGCAATCTGTCCA **Reverse:** AGGAGCTCCAACACCAATCA
AtFIT (At2g28160)	**Forward:** CCCTGTTTCATAGACGAGAACC **Reverse:** TTCATCTTCTTCACCACCGGC
AtbHLH38 (At3g56970)	**Forward:** AAAATGTGTGCATTAGTCCCTT **Reverse:** AGTCTGTGGTACCGTCAATTCAA
AtGSNOR1 (At3g56980)	**Forward:** GGTCTCTTTCCTTGTATTCTAG **Reverse:** GCATTCACGACACTCAGCTTG
AtSAM1 (At1g02500)	**Forward:** TAATCTCCCATCGAAGCAGCAG **Reverse:** CAACTTTGCTGTCAGGGTCTTG
AtACO2 (At1g62380)	**Forward:** AGCAACCCTCTCTCATTCTACA **Reverse:** AGCTTGGACAAGTCTACTACTGG
AtACS6 (At4g11280)	**Forward:** ATTGTCTAAAATCGCCTCCGGT **Reverse:** CCACAAAGCTGATTTTCAGCGA
AtEIN2 (At5g03280)	**Forward:** ATTCGCACTGATGGGTCTTCTT **Reverse:** CCAAAGATGGCGAACAAATGGT
AtEIN3 (At3g20770)	**Forward:** GTCCAGAGCAACCAAACCTCTA **Reverse:** TGTTTCCTGGGAACTGGAGATG
AtEIL1 (At2g27050)	**Forward:** CCATCTCTGAAGTTGTGGGGAT **Reverse:** ACCACAATCAAGAACAGAGCCT

RESULTS

Effect of LODIS on Ethylene Synthesis in Roots

To observe whether LODIS affects ethylene synthesis in roots, we determined ACC (ethylene precursor) concentration and the expression of several genes implicated in ethylene synthesis (*SAM1*, *ACS6,* and *ACO2*; García et al., 2010) in roots of *Arabidopsis* WT Columbia plants grown under different Fe treatments that could affect LODIS accumulation: with Fe (LODIS sufficient), without Fe (LODIS deficient), and without Fe but with Fe sprayed on leaves (LODIS sufficient). The

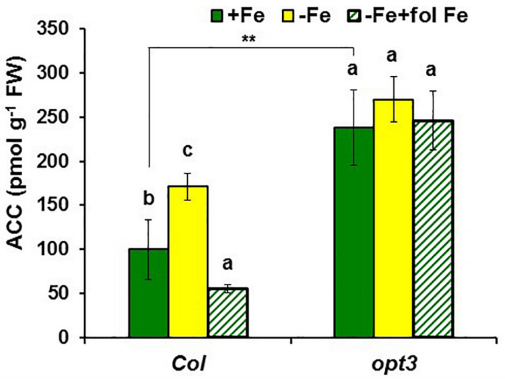

FIGURE 2 | Effect of Fe deficiency and foliar application of Fe on ACC content in roots of *Arabidopsis* WT Columbia and *opt3-2* mutant plants. Treatments as in **Figure 1**. Data represent the mean ± SE of six replicates. Within each genotype, bars with different letters indicate significant differences ($P < 0.05$). Significant difference between the +Fe treatment from *opt3-2* and Col is also indicated: $^{**}P < 0.05$.

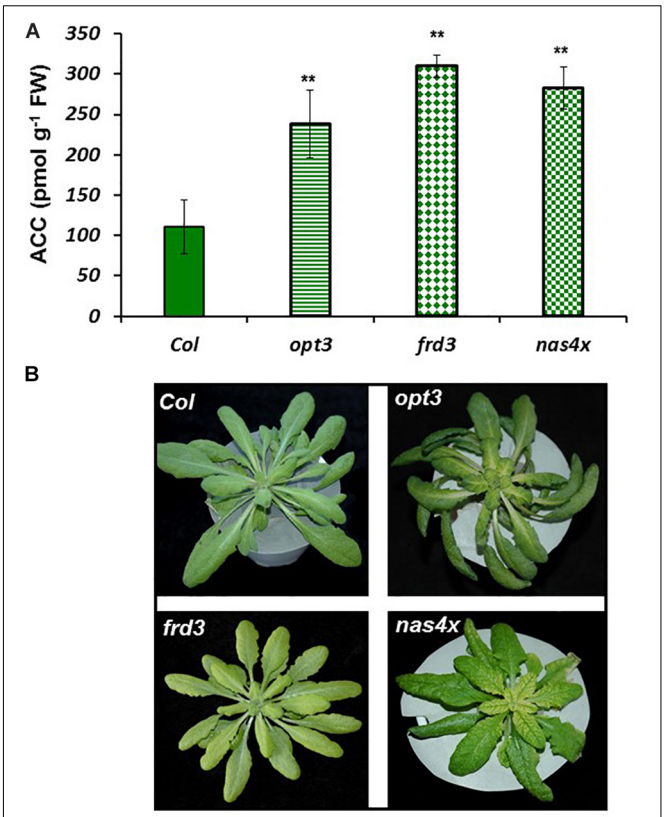

FIGURE 3 | ACC concentration in Fe-sufficient roots **(A)** and shoot appearance **(B)** of *Arabidopsis* WT Columbia and *opt3-2*, *frd3-3,* and *nas4x-1* mutant plants. Note the chlorosis in the *frd3-3* and *nas4x-1* mutants. Plants were grown in nutrient solution with Fe. Data represent the mean ± SE of six replicates. Significant differences from Col are indicated: $^{**}P < 0.05$.

expression of all the ethylene synthesis genes studied and ACC production greatly increased (sometimes, more than 2-fold) in Fe-deficient Columbia roots, in parallel to the expression of the key Fe acquisition genes *FRO2*, *IRT1,* and *FIT* (**Figures 1**, **2**). On the other hand, the foliar application of Fe to Fe-deficient Columbia plants greatly repressed the expression of Fe acquisition (**Figure 1A**) and ethylene synthesis genes (**Figure 1B**), and ACC production (**Figure 2**), which suggests that LODIS inhibits ethylene synthesis. This inhibitory effect of LODIS was further supported by the fact that the foliar application of Fe did not significantly inhibit ACC production in the *Arabidopsis* LODIS-deficient mutant *opt3-2* (**Figure 2**; García et al., 2013; Zhai et al., 2014). This mutant also showed higher ACC concentration in Fe-sufficient roots compared to the WT Columbia (**Figure 2**), which suggests that total Fe in roots does not control ethylene synthesis. Similar higher ACC levels were found in Fe-sufficient roots of other *Arabidopsis* mutants that behave like LODIS-deficient (*frd3-3* and *nas4x-1*) and that present constitutive activation of Fe acquisition genes under Fe-sufficiency (**Figure 3A**; García et al., 2013; see section "Materials and Methods").

It should be noted that, although the *frd3-3* and *opt3-2* mutants usually accumulate more metals than the WT cultivar (Rogers and Guerinot, 2002; Stacey et al., 2008), neither of them showed any symptom of metal toxicity in our experimental conditions (**Figure 3B**). The *frd3-3* and *nas4x-1* mutants showed chlorosis, as expected (**Figure 3B**; see section "Materials and Methods").

The higher ACC content in Fe-sufficient *opt3-2* roots than in Columbia roots (**Figure 2**) was correlated with higher expression of the ethylene synthesis genes *SAM1*, *ACS6* and *ACO2*, and of the ethylene signaling genes *EIN2*, *EIN3* and *EIL1*, in the mutant (from 5- to 30-fold; **Figure 4**). Collectively, these results suggest that ethylene (synthesis and signaling) drastically increases under low LODIS accumulation in roots (i.e., Fe deficiency in WT or Fe sufficiency in the LODIS-deficient mutant *opt3-2*).

Effect of LODIS on GSNOR Expression and Activity in Roots

To study the possible relationship of GSNOR with Fe deficiency, we analyzed GSNOR expression and activity under different Fe treatments and genetic backgrounds that could influence LODIS levels. The results showed that *GSNOR1* expression increased (more than 10-fold) under Fe deficiency in roots of the WT cultivar Columbia (**Figure 5A**). This up-regulation of *GSNOR1* occurred very quickly, after few hours of Fe depletion, and slightly before the up-regulation of the main regulator of the Fe deficiency responses, *FIT* (**Figure 5B**), other Fe acquisition genes (*bHLH38*, *IRT1*, *FRO2*; **Figures 5C–E**), and the enhancement of ferric reductase activity (**Figure 5F**). In agreement with the *GSNOR1* up-regulation, the GSNOR activity significantly increased (approximately 50%) in Fe-deficient Columbia roots (**Figure 6**). This activity was restored to normal level upon foliar application of Fe (**Figure 6**), which suggests that it could be inhibited by the accumulation of LODIS in roots. To further confirm this possibility, we compared *GSNOR1* expression in Fe-sufficient WT and *opt3-2* roots. As shown in **Figure 7**, *GSNOR1* expression was much higher (more than 50-fold) in Fe-sufficient *opt3-2* roots (LODIS-deficient)

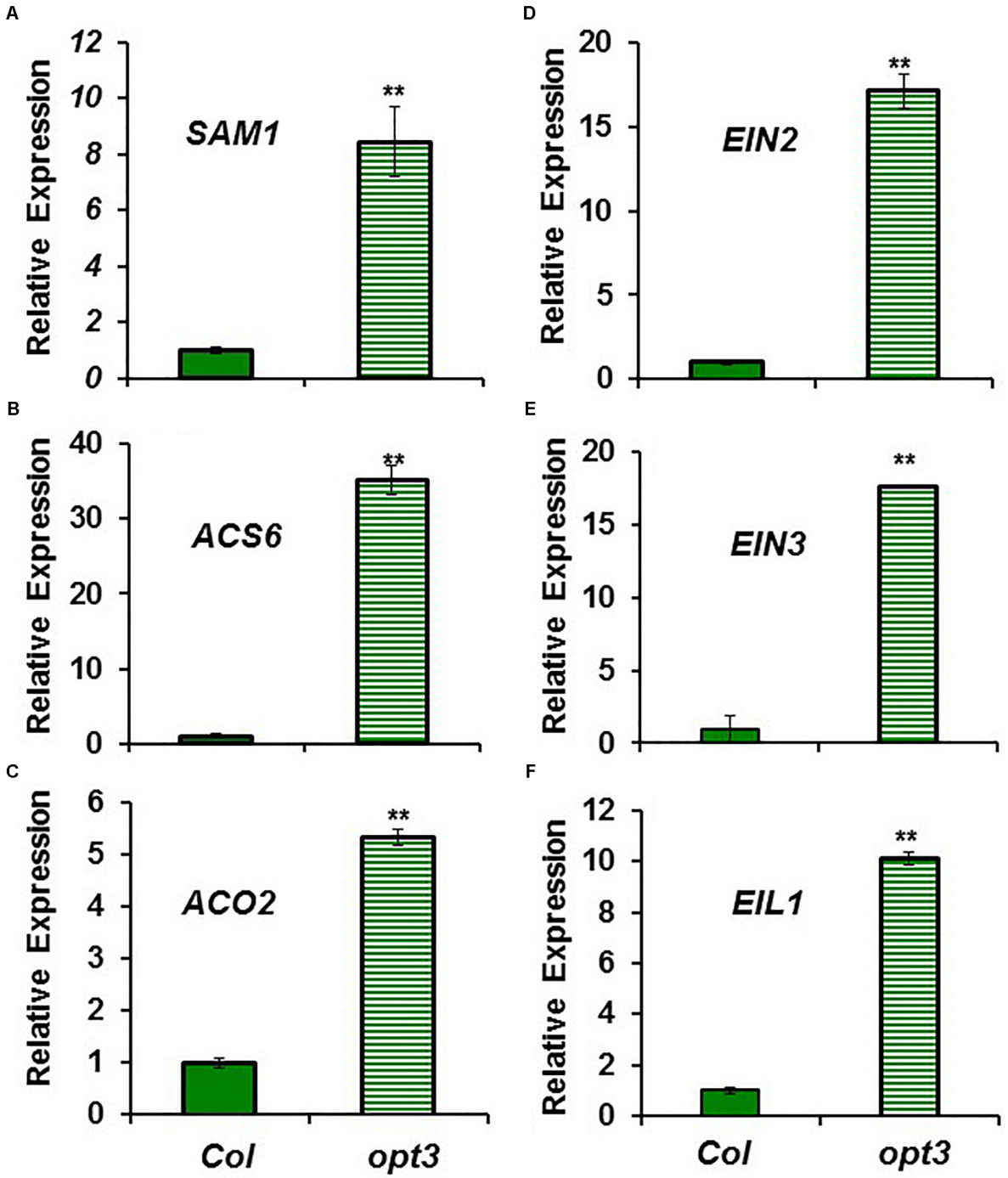

FIGURE 4 | Expression of ethylene synthesis genes **(A)** *SAM1*, **(B)** *ACS6* and **(C)** *ACO2,* and ethylene signaling genes **(D)** *EIN2*, **(E)** *EIN3* and **(F)** *EIL1,* in Fe-sufficient roots of *Arabidopsis* WT Columbia and *opt3-2* mutant plants. Plants were grown in nutrient solution with Fe. Relative expression was calculated in relation to Col. Data represent the mean ± SE of three independent biological replicates. Significant differences between *opt3-2* and Col are indicated: $^{**}P < 0.05$.

than in Fe-sufficient Columbia roots, which suggests that its expression depends on LODIS and not on total root Fe content. The up-regulation of *GSNOR1* expression also occurred under other nutrient deficiencies, such as P deficiency and S deficiency (**Figure 8**). Furthermore, *GSNOR1* expression was up-regulated by ACC treatment in Fe-sufficient Columbia roots (**Figure 9**).

In addition to GSNOR, we also determined GSNO concentration in roots of *Arabidopsis* WT Columbia and *opt3-2* plants subjected to different Fe treatments. The results

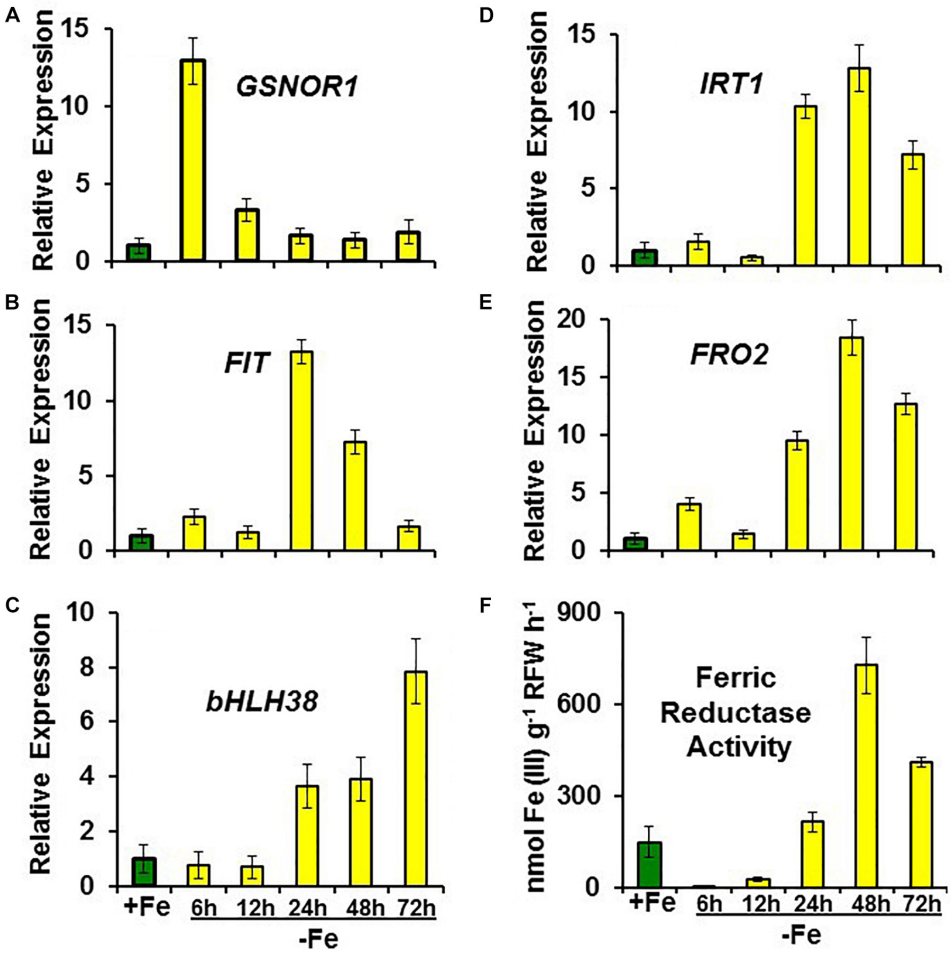

FIGURE 5 | Time course experiment of the effect of Fe deficiency on the expression of **(A)** *GSNOR1*, Fe acquisition genes **(B)** *FIT*, **(C)** *bHLH38*, **(D)** *IRT1* and **(E)** *FRO2*), and on **(F)** ferric reductase activity, in roots of *Arabidopsis* WT Columbia plants. Plants were grown in nutrient solution with Fe (+Fe). Some of them were transferred to nutrient solution without Fe (–Fe) 6, 12, 24, 48, or 72 h before determination of ferric reductase activity or harvest. For genes, data represent the mean ± SE of three independent biological replicates. Relative expression was calculated in relation to +Fe. For ferric reductase activity, data represent the mean ± SE of six replicates.

showed a decrease of approximately 30% of GSNO content in Fe-deficient WT roots and, by contrast, a great increase upon foliar application of Fe (**Figure 10**). GSNO also decreased in Fe-deficient *opt3-2* roots but was less affected by the foliar application of Fe (**Figure 10**). The lower GSNO content in Fe-deficient roots could be explained by the higher GSNOR expression and activity in these roots (**Figures 5**, **6**). In supporting this view, Fe-sufficient *opt3-2* roots, which had higher *GSNOR* expression than Fe-sufficient WT roots (**Figure 7**), had lower GSNO content (approximately 50%; **Figure 10**). Similar results were also found with the pea LODIS-deficient mutant *dgl* and its WT cultivar Sparkle. As shown in **Figure 11**, GSNO content also decreased in Fe-deficient Sparkle roots (approximately 25%) and, similarly to *opt3-2*, GSNO content was lower in Fe-sufficient *dgl* roots (approximately 40%) than in Fe-sufficient Sparkle roots.

Collectively, all these results suggest that GSNOR (expression and activity) increases, and consequently GSNO decreases, under low LODIS accumulation in roots (i.e., Fe deficiency in WT or Fe sufficiency in LODIS-deficient mutants).

Effect of Fe Deficiency on GSH Content in Roots and Leaves of WT and *opt3-2* Mutant Plants

In our experimental conditions, GSH greatly increased in Fe-deficient WT roots but hardly in Fe-deficient *opt3-2* roots (**Table 2**). In leaves, the most noticeable result was the higher GSH content in the *opt3-2* mutant in relation to Columbia under Fe sufficiency (**Table 2**).

DISCUSSION

Ethylene increases in Fe-deficient roots, where it activates the expression of key Fe acquisition genes (reviewed in Lucena et al., 2015; Li and Lan, 2017; Romera et al., 2017). A signal

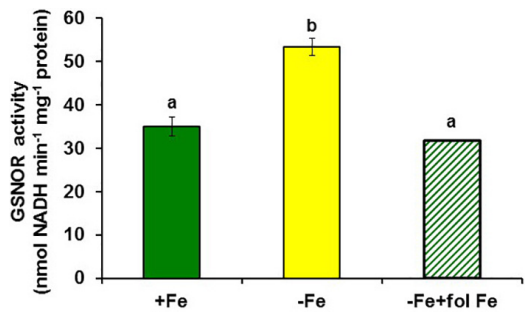

FIGURE 6 | Effect of Fe deficiency and foliar application of Fe on GSNOR activity in roots of *Arabidopsis* WT Columbia plants. Plants were grown in nutrient solution with Fe (+Fe) and some of them were transferred to nutrient solution without Fe 2 days before harvest (–Fe). Half of the –Fe plants were sprayed with Fe 24 h before harvest (–Fe+fol Fe). Data represent the mean ± SE of six replicates. Bars with different letters indicate significant differences ($P < 0.05$).

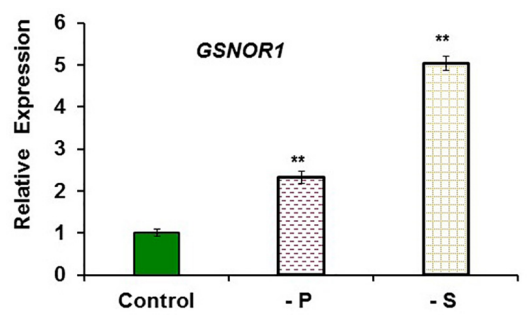

FIGURE 8 | Effect of P or S deficiency on *GSNOR1* expression in roots of *Arabidopsis* WT Columbia plants. Plants were grown in complete nutrient solution (Control). Some of them were transferred to nutrient solution without P (–P) or without S (–S) during the last 2 days. Relative expression was calculated in relation to Control. Data represent the mean ± SE of three independent biological replicates. Significant differences from the Control treatment are indicated: $^{**}P < 0.05$.

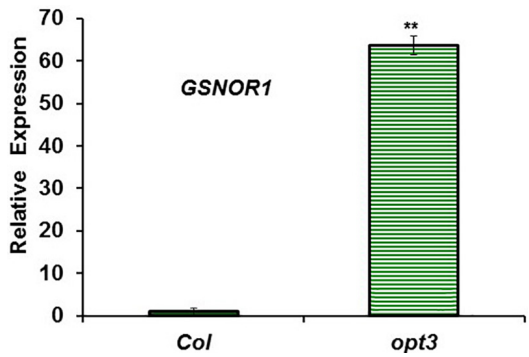

FIGURE 7 | *GSNOR1* expression in roots of Fe-sufficient *Arabidopsis* WT Columbia and *opt3-2* mutant plants. Plants were grown in nutrient solution with Fe. Relative expression was calculated in relation to Col. Data represent the mean ± SE of three independent biological replicates. Significant difference between *opt3-2* and Col is indicated: $^{**}P < 0.05$.

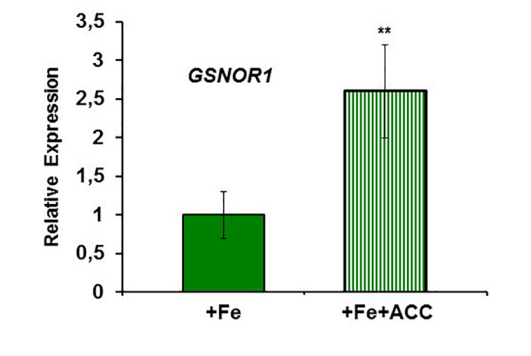

FIGURE 9 | Effect of ACC on *GSNOR1* expression in roots of *Arabidopsis* WT Columbia plants. Plants were grown in nutrient solution with 40 μM Fe (+Fe) and half of them treated with 1 μ M ACC, final concentration (+Fe+ACC), 24 h before harvest. Relative expression was calculated in relation to +Fe. Data represent the mean ± SE of three independent biological replicates. Significant differences from the +Fe treatment are indicated: $^{**}P < 0.05$.

related to phloem Fe, LODIS, blocks this activating effect (García et al., 2013). However, it is not known whether LODIS could affect ethylene synthesis in roots. Results presented in this work (**Figures 1**, **2**, **3A**, **4**) support that LODIS does affect ethylene synthesis. The foliar application of Fe greatly decreased the expression of Fe acquisition and ethylene synthesis genes (**Figure 1**), and ACC production (**Figure 2**), in Fe-deficient WT Columbia roots. However, in Fe-deficient roots of the LODIS-deficient mutant *opt3-2* (García et al., 2013; Mendoza-Cózatl et al., 2014; Zhai et al., 2014), foliar application of Fe had almost no effect on ACC content of roots (**Figure 2**). Moreover, the expression of several ethylene synthesis and signaling genes was much higher in Fe-sufficient *opt3-2* roots than in Fe-sufficient Columbia roots (**Figure 4**). In the same way, Fe-sufficient roots of *opt3-2* and other *Arabidopsis* mutants that behave as LODIS-deficient, such as *frd3-3* and *nas4x-1* (see section "Materials and Methods"), had greater ACC content than Fe-sufficient Columbia roots (**Figures 2**, **3A**). All these results suggest that ethylene synthesis (and signaling) in roots does not depend on total root Fe content (these mutants accumulate high levels of Fe inside roots under Fe sufficiency; García et al., 2013 and references therein) but on LODIS levels, that depend on the OPT3 transporter.

Since heavy metals can enhance ethylene production and the expression of ethylene signaling genes (Keunen et al., 2016), it can be argued that the higher ACC content and the higher expression of ethylene-related genes in Fe-sufficient *opt3-2* roots (and in Fe-sufficient *frd3-3* and *nas4x-1* roots) could be caused by the high accumulation of metals described in some of these mutants. Against this argument, we have to say that, in our experiments, plants were grown with low levels of metals and they did not present leaf toxicity symptoms (**Figure 3B**). Moreover, after the work of Vert et al. (2002) it is known that the accumulation of metals in mutants that present constitutive activation of *IRT1* expression, such as *opt3-2* (Stacey et al., 2008) and *frd3* (Rogers and Guerinot, 2002), is mainly due to the broad substrate range

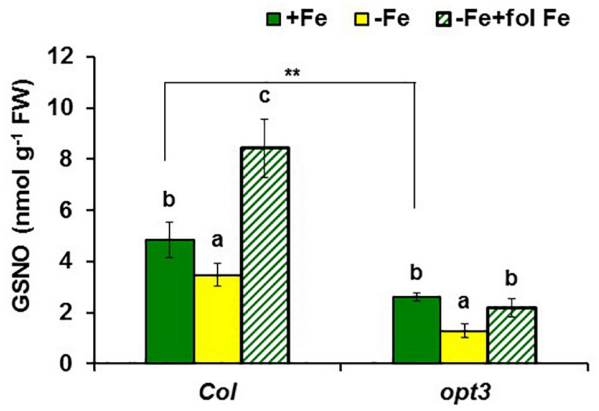

FIGURE 10 | Effect of Fe deficiency and foliar application of Fe on GSNO content in roots of *Arabidopsis* WT Columbia and *opt3-2* mutant plants. Plants were grown in nutrient solution with Fe (+Fe). Some of them were transferred to nutrient solution without Fe 2 days before harvest (–Fe). Half of the –Fe plants were sprayed with Fe 24 h before harvest (–Fe+fol Fe). Data represent the mean ± SE of six replicates. Within each genotype, bars with different letters indicate significant differences ($P < 0.05$). Significant difference between the +Fe treatment from *opt3-2* and Col is also indicated: $^{**}P < 0.05$.

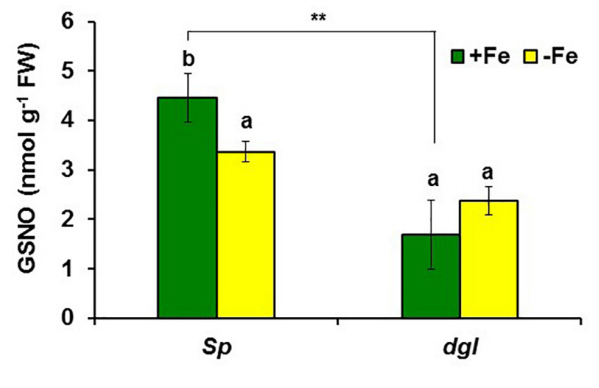

FIGURE 11 | Effect of Fe deficiency on GSNO content in roots of pea WT Sparkle and *dgl* mutant plants. Plants were grown in nutrient solution with Fe (+Fe) and half of them were transferred to nutrient solution without Fe 2 days before harvest (–Fe). Data represent the mean ± SE of six replicates. Within each genotype, bars with different letters indicate significant differences ($P < 0.05$). Significant difference between the +Fe treatment from *dgl* and Sparkle is also indicated: $^{**}P < 0.05$.

of this transporter. IRT1 can transport several divalent metals, besides Fe^{2+}, such as Mn^{2+}, Zn^{2+}, or Cd^{2+} (Korshunova et al., 1999; Lucena et al., 2006). Since *IRT1* expression is activated by ethylene (García et al., 2010; Lingam et al., 2011; Blum et al., 2014; Marín-de la Rosa et al., 2014), the most probable sequence is: (1) enhanced ethylene production → (2) activation of *IRT1* expression → (3) accumulation of metals, and not: (1) accumulation of metals → (2) enhanced ethylene production → (3) activation of *IRT1* expression. No accumulation of metals would occur without IRT1 activity. In supporting this view, it should be noted that the inhibition of ethylene synthesis with cobalt, a potent ethylene inhibitor, drastically inhibited *IRT1* expression and the accumulation of metals in tomato plants (Lucena et al., 2006) and in pea *brz* mutant plants (also named E107, has constitutive activation of Fe responses; Romera et al., 1996, 2015). Taken together, all these results suggest that ethylene is necessary for *IRT1* up-regulation and, consequently, for the acquisition and accumulation of metals. This does not discard that, if plants accumulate high levels of metals, they could cause a further increase of ethylene production, but as a later side effect.

Similarly to ethylene, GSH (**Table 2**) and NO also increase in Fe-deficient WT roots, where they have been implicated in the activation of Fe deficiency responses (Zaharieva and Abadía, 2003; Zaharieva et al., 2004; Graziano and Lamattina, 2007; Bacaicoa et al., 2009; Chen et al., 2010; García et al., 2011; Koen et al., 2012; Shanmugam et al., 2015; Kailasam et al., 2018). However, results in this work show that GSNO content in WT roots, in contrast to its precursors GSH and NO, decreases upon Fe deficiency (**Figures 10**, **11**), which agrees with previous results (Shanmugam et al., 2015; Kailasam et al., 2018). Since GSNOR reduces GSNO to GSSG and other byproducts, like hydroxylamine and H_3N (Leterrier et al., 2011; Corpas et al., 2013; Kubienová et al., 2014), we wanted to know whether GSNOR increases in Fe deficient roots. In fact, *GSNOR1* expression and activity in roots increased early after Fe deficiency and slightly before the up-regulation of Fe acquisition genes (**Figures 5**, **6**). This suggests that GSNOR could be responsible for the lower GSNO contents found in Fe-deficient WT roots (**Figures 10**, **11**; Shanmugam et al., 2015; Kailasam et al., 2018). *GSNOR1* is highly responsive to the Fe status of the plant but, as for ethylene (see above), the results indicate that its up-regulation does not depend on the total root Fe content but on LODIS levels. First, the foliar application of Fe greatly increased GSNO content in Fe-deficient Columbia roots (probably by decreasing GSNOR activity, as seen in **Figure 6**) but hardly in Fe-deficient roots of the LODIS-deficient mutant *opt3-2* (**Figure 10**), which is impaired in the movement of Fe from shoots to

TABLE 2 | Effect of Fe deficiency on GSH (glutathione) concentration in roots and leaves of *Arabidopsis* WT Columbia and *opt3-2* mutant plants.

Compound	Genotype	Roots		Leaves	
		+Fe	−Fe	+Fe	−Fe
GSH (nmol·g^{-1}FW)	Col	53 ± 4	144 ± 1**	146 ± 10	137 ± 8
	opt3-2	43 ± 9	60 ± 15	286 ± 12	138 ± 3**

Plants were grown in nutrient solution with Fe (+Fe) and half of them transferred to nutrient solution without Fe (−Fe) during the last 2 days. Data represent the mean ± SE of six replicates. Significant differences from the +Fe treatment are indicated: $^{**}P < 0.01$.

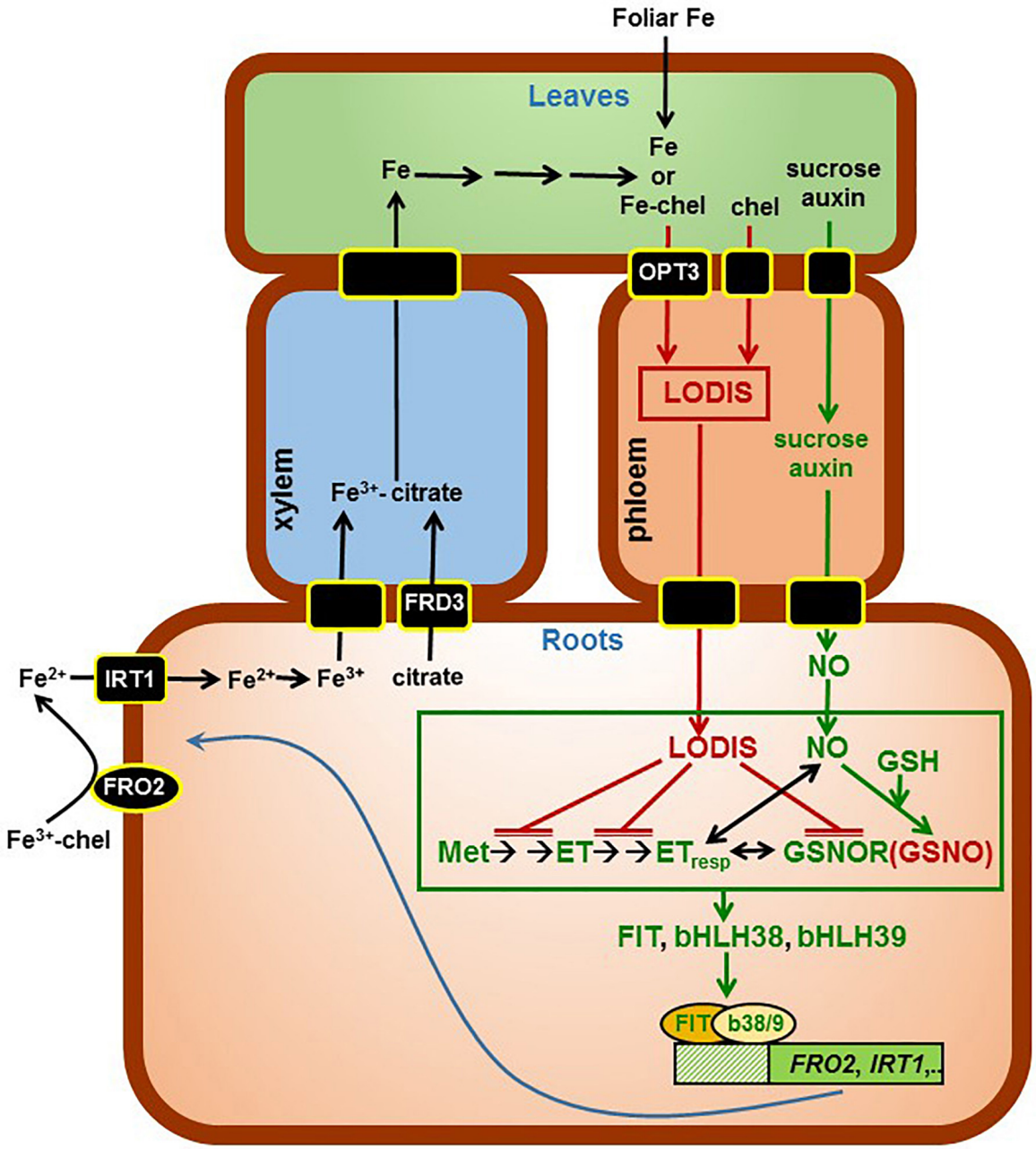

FIGURE 12 | Working Model to explain the role of LODIS on the regulation of Fe acquisition genes. Once inside roots, Fe is translocated to leaves through the xylem, bound to citrate (provided by the FRD3 transporter). In shoots, some Fe (either as free ions or in chelated form) can enter the phloem through the OPT3 transporter, and moves back to roots bound to a chelating agent (forming LODIS). In roots, LODIS could negatively affect ethylene synthesis and signaling, and GSNOR expression and/or activity, which can lead to enhanced GSNO. Besides LODIS, which would act as a repressor of Fe responses, some other shoot signals, like sucrose and auxin, would act as activators of Fe responses through NO (Lin et al., 2016). The possible relationship of ethylene, NO, GSH, GSNOR, and GSNO is depicted in more detail in **Figure 13**. In green are components whose expression, activity and/or content is known to increase under Fe deficiency while in red are components whose expression, activity, and/or content is known to increase under Fe sufficiency. chel, chelating agent; GSH, glutathione; GSNO, *S*-nitrosogluthatione; GSNOR, GSNOR reductase; ET, ethylene; ETresp, ethylene response; Met, methionine (→: promotion; $\bar{T}$: inhibition).

roots (García et al., 2013; Mendoza-Cózatl et al., 2014; Zhai et al., 2014). Second, Fe-sufficient *opt3-2* roots presented much higher *GSNOR1* expression (and less GSNO content) than Fe-sufficient Columbia roots (**Figures 7**, **10**). Similarly, a lower GSNO content was found in Fe-sufficient roots of the pea LODIS-deficient mutant *dgl* than in Fe-sufficient roots of its WT Sparkle (**Figure 11**). All these results clearly suggest that GSNOR expression (and consequently GSNO content)

does not depend on total root Fe content but on LODIS levels.

The results described above clearly show that the higher NO accumulation found in Fe-deficient WT roots (Graziano and Lamattina, 2007; Chen et al., 2010; García et al., 2011) is associated with lower GSNO contents (**Figures 10**, **11**). Similar results have been found by others in roots of *Arabidopsis* plants subjected to Fe deficiency (Shanmugam et al., 2015; Kailasam et al., 2018), to arsenic stress (Leterrier et al., 2012) or to Cd stress (Liu et al., 2018). In the two latter cases, the lower GSNO levels have been associated with a higher GSNOR activity (Leterrier et al., 2012; Liu et al., 2018), which also occurs under other abiotic stress conditions (Corpas et al., 2008; Airaki et al., 2012; Kubienová et al., 2014; Cheng et al., 2015). In relation to Cd stress, it is important to mention that Cd can cause Fe deficiency (Alcántara et al., 1994 and references therein) and induce Fe deficiency responses (Yoshihara et al., 2006). In our work, besides Fe deficiency, *GSNOR1* expression also increased under P or S deficiency (**Figure 8**), which indicates that GSNOR could be implicated in the responses to different nutritional deficiencies. The higher NO accumulation associated with a lower GSNO content in Fe-deficient roots suggests that NO and GSNO do not have the same exact roles, probably because they have different lifetime and location. NO lifetime is relatively short (less than 10 s) while GSNO is a relatively stable store for NO and might constitute a vehicle for its long-distance transport (Corpas et al., 2011; Malik et al., 2011), mediating a signaling function throughout a process of *S*-transnitrosation between GSNO and proteins (Corpas et al., 2013). In relation to their location, both NO and GSNO can present different cellular and intracellular location (Malik et al., 2011; Shi et al., 2015). NO production is associated with phloem cells (Corpas et al., 2004; Gaupels et al., 2008) and, since the GSNOR protein is also located in the phloem (Rustérucci et al., 2007), it is possible that GSNO could be a vehicle to transmit the NO-signal out of the phloem. In agreement with the distinct role of NO and GSNO, Yun et al. (2016) have found that both of them act differently in the responses associated with plant immunity. In relation to Fe deficiency responses in dicot plants, Kailasam et al. (2018) have recently shown, by using chemical screening, that GSNO probably affects the regulation of Fe acquisition genes through FIT while NO could affect them through other TFs, such as bHLH38 and bHLH39. It should be noted that the SKB1 protein, implicated in *bHLH38* and *bHLH39* expression (Fan et al., 2014), can be nitrosylated (Hu et al., 2015). In this way, it is possible that GSNO, through the nitrosylation/de-nitrosylation of SKB1, could affect the expression of these Ib bHLH TFs (Fan et al., 2014; Lucena et al., 2015). In supporting this view, *bHLH38*, *bHLH39,* and *bHLH100* are up-regulated in leaves of the *Arabidopsis gsnor1-3* mutant, which has altered GSNO content (Xu et al., 2013).

Results in this work, along with previous results (García et al., 2013), suggest that LODIS can inhibit both ethylene synthesis and signaling, and GSNOR expression and activity in roots (see Working Model in **Figure 12**). The inhibition of GSNOR would increase GSNO content in roots, which agrees with the higher GSNO contents found in Fe-sufficient WT roots or in roots of Fe-deficient WT plants treated with foliar Fe (**Figures 10**, **11**; Shanmugam et al., 2015; Kailasam et al., 2018). After all these results, several questions arise: what is the nature of LODIS?; is there any relationship between GSNO(NO), GSH and ethylene?; is there any relationship between GSNO(NO)/ethylene and the putative Fe sensor BTS? In relation to the nature of LODIS, it is unknown at present. Although Zhai et al. (2014) found that OPT3 can transport Fe^{2+} ions when expressed in *Xenopus* oocytes, the substrate of OPT3 remains controversial because the Fe transport function of OPT3 could not be confirmed in other experiments (Mendoza-Cózatl et al., 2014). Even if Fe enters the phloem through OPT3 as free ions, it would be difficult for Fe to move in this way, and probably the Fe ions would be chelated (**Figure 12**; see section "Introduction"). OPT3 does not mediate GSH transport in *S. cerevisiae* (Zhai et al., 2014), as other OPT transporters did (Zhang et al., 2016 and references therein). However, the higher leaf GSH content found in the *opt3-2* mutant in relation to Columbia, under Fe sufficiency (**Table 2**) or under Cd treatment (Akmakjian, 2011), supports the idea of LODIS being a compound related, directly or indirectly, to GSH, such as GS-Fe-NO or NICs (Ramírez et al., 2011; Rahmanto et al., 2012; Darbani et al., 2013; Buet and Simontacchi, 2015). Nonetheless, this idea deserves further research.

In relation to the possible interactions between GSNO(NO), GSH and ethylene, it should be said that, besides the mutual and positive influence between NO and ethylene already described in previous works (**Figure 13**; García et al., 2011; Romera et al., 2011; Liu et al., 2017), GSNO(NO), GSH and ethylene could also interact at other levels. GSH can enhance ethylene production by affecting some ethylene synthesis enzymes (Datta et al., 2015). On the other hand, the relationship between GSNO and ethylene can be feasible because both GSNOR (Rustérucci et al., 2007; see above) and several ethylene synthesis enzymes, like 5-methilthioribose kinase (induced in Fe-deficient roots; García et al., 2010; Romera et al., 2017 and references therein), are located in the phloem (Pommerrenig et al., 2011). Moreover, enzymes implicated in ethylene synthesis, such as SAM synthetases (also named methionine adenosyltransferases; Sauter et al., 2013), can be inhibited by *S*-nitrosylation (Lindermayr et al., 2006; Freschi, 2013). Since GSNO has been implicated in the reversible *S*-nitrosylation of proteins (Malik et al., 2011; Begara-Morales et al., 2015; Zaffagnini et al., 2016), it is possible that higher GSNO levels (such as those found in Fe-sufficient WT roots: **Figures 10**, **11**) could contribute to *S*-nitrosylation of ethylene synthesis enzymes and, consequently, to the inhibition of ethylene synthesis (**Figure 13**). By contrast, lower GSNO levels (such as those found in Fe-deficient WT roots or in Fe-sufficient *opt3-2* and *dgl* roots: **Figures 10**, **11**) could contribute to de-nitrosylation of ethylene synthesis enzymes and, consequently, to promotion of ethylene synthesis (**Figures 1B**, **2**). In supporting this view, silencing *GSNOR* in *Nicotiana attenuata*, which leads to higher GSNO content, decreased the herbivore-induced accumulation of ethylene (Wünsche et al., 2011). Reciprocally to the possible

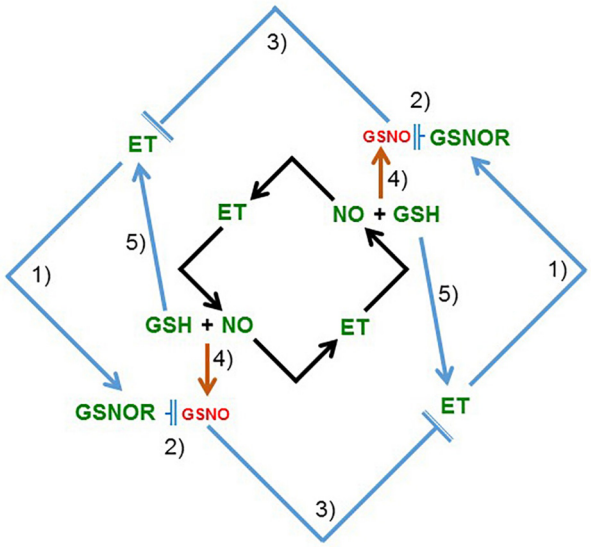

FIGURE 13 | Model to explain the relationship between ethylene and NO, and between ethylene and GSNOR (GSNO), in roots. In previous works, and also in this work (see **Figure 2** and **Table 2**), it has been shown that ethylene, NO, and GSH increase in Fe-deficient roots of dicot plants (see section "Introduction"). Moreover, it has been shown that ethylene can influence NO accumulation in roots and vice versa (black arrows; García et al., 2011; Liu et al., 2017). In this work, it has been found that ethylene and GSNOR increase under low LODIS accumulation in roots (see **Figure 12**). After that, a new model, complementary of the previous one, is proposed (blue arrows) suggesting mutual possible interactions among ethylene, GSNOR, GSH and NO: (1) ethylene can upregulate GSNOR (see **Figure 9**); (2) GSNOR can decrease GSNO (Corpas et al., 2013); (3) Low GSNO can unblock ethylene synthesis since nitrosylation of SAM synthetase by GSNO can inhibit ethylene synthesis (Lindermayr et al., 2006; Freschi, 2013; see section "Discussion"); (4) GSNO derives from NO and GSH (Corpas et al., 2013); (5) GSH can enhance ethylene production (Datta et al., 2015). In green are components whose expression, activity and/or content is known to increase under Fe deficiency while in red are components whose content is known to decrease under Fe deficiency. GSH, glutathione; GSNO, *S*-nitrosoglutathione; GSNOR, GSNO reductase; ET, ethylene; NO, nitric oxide (→: promotion; $\bar{T}$: inhibition).

influence of GSNO(NO) on ethylene synthesis, ethylene (ACC) could decrease GSNO content by activating *GSNOR1* expression (**Figures 9**, **13**). *GSNOR1* expression is also influenced by other hormones, such as salicylic acid which activates it or jasmonic acid which down-regulates it (Díaz et al., 2003). Very recently, it has been found that ethylene (ACC) can increase NO content by activating enzymes involved in its synthesis, such as nitrate reductase and nitric oxide synthase-like (Liu et al., 2017). This would imply that ethylene could simultaneously increase NO accumulation and decrease GSNO content (**Figure 13**).

Finally, in the relationship between GSNO(NO)/ethylene and the putative Fe sensor BTS, some results suggest that the BTS protein could act upstream of ethylene. The *SAM1* gene, encoding a SAM synthetase (involved in ethylene synthesis; Sauter et al., 2013), is up-regulated in the *bts-3* mutant (Hindt et al., 2017). In the same way, several genes whose expression is activated by ethylene, such as *FIT*, *bHLH38*, *bHLH39*, *MYB72*, *BGLU42*, *FRO2*, *IRT1*, *FRD3,* and *NAS2* (García et al., 2010), are up-regulated in *bts-3* roots under Fe-sufficient conditions (Hindt et al., 2017). In rice, roots from HRZ-knockdown plants have higher jasmonate content than the WT ones when grown under Fe sufficiency (Kobayashi et al., 2016). All these results suggest that BTS/HRZs may act as sensors of LODIS, as suggested by Kobayashi and Nishizawa (2014), and depending on its binding state could then affect the synthesis of hormones, like ethylene or jasmonate.

CONCLUSION

The results presented in this work, along with already published results, suggest that shoots, through LODIS, play an important role in the regulation of Fe acquisition genes in roots, which is depicted in the Working Model of **Figure 12**. According to this model, under Fe sufficiency, sufficient Fe goes to leaves and enters the phloem to form LODIS, which travels to roots and represses ethylene synthesis and signaling, and *GSNOR* expression and activity, which leads to increased GSNO content. GSNO(NO), GSH, and ethylene can interact in different ways (see above paragraph and **Figure 13**). Moreover, a high GSNO content can compromise auxin signaling and transport (Shi et al., 2015), which is important because auxin has also been involved in the regulation of Fe responses, where is intimately interrelated with ethylene and NO (Chen et al., 2010; Romera et al., 2011, 2017). Under Fe deficiency, the lack of LODIS derepresses ethylene synthesis and signaling, and *GSNOR* expression and activity, which leads to decreased GSNO content. All this would cause the up-regulation of Fe acquisition genes.

This working model could open the way to better understand the role of shoots and roots in the regulation of Fe deficiency responses. According to this model, LODIS would have a double role in the regulation of Fe acquisition genes, by controlling both ethylene synthesis and signaling (**Figure 12**). This double role of LODIS would explain why the ethylene overproducer mutant *eto* and the treatments with ethylene did not activate the expression of Fe acquisition genes when plants are grown with high levels of Fe (Lucena et al., 2015): despite high ethylene levels, LODIS would block ethylene action. All the results discussed in this work imply that the relationship of GSH, NO and GSNO with ethylene, with GSNOR, with LODIS and with the expression of Fe acquisition genes is complex and deserves further research.

AUTHOR'S NOTE

A very recent work by Grillet et al. (2018) shows that some peptides (IRON MAN or IMA peptides) associated with the phloem, and preferentially expressed in leaves, could be implicated in the regulation of Fe responses in roots. The upregulation of Fe responses in lines overexpressing genes encoding these peptides and their ability to bind Fe^{2+} suggest that these peptides could act either as activators (unbound IMA peptides) or repressors (IMA peptides bound to Fe) of the

responses. Perhaps LODIS is related to the ratio between IMA peptides bound to Fe and unbound IMA peptides.

AUTHOR CONTRIBUTIONS

FR and MG designed the experiments after discussions with PB, RP-V, and EA. MG and CL conducted the laboratory work. FC and MG determined GSNOR, GSNO, and GSH. ÁZ, EB, and JG-M determined ACC. FR, MG, RP-V, and EA wrote the manuscript that was improved by the other authors.

FUNDING

This work was supported by the European Regional Development Fund from the European Union, the 'Ministerio de Economía y Competitividad' (Projects AGL2013-40822-R and AGL2015-65104-P) and the 'Junta de Andalucía' (Research Groups AGR115, BIO159, and BIO192).

ACKNOWLEDGMENTS

We thank Dr. Brian M. Waters, of the University of Nebraska (Lincoln, NE, United States), for the English correction and valuable suggestions in the editing of the manuscript. We thank Dr. Michael Grusak for providing seeds of the Sparkle [dgl,dgl] mutant, the Arabidopsis Biological Resource Center for providing seeds of the *frd3-3* mutant and Dr. Stacey for providing seeds of the *opt3-2* mutant. We also thank Inmaculada Montilla and Carmelo Ruíz-Torres for their excellent technical support.

REFERENCES

Airaki, M., Leterrier, M., Mateos, R. M., Valderrama, R., Chaki, M., Barroso, J. B., et al. (2012). Metabolism of reactive oxygen species and reactive nitrogen species in pepper (*Capsicum annuum* L.) plants under low temperature stress. *Plant Cell Environ.* 35, 281–295. doi: 10.1111/j.1365-3040.2011.02310.x

Airaki, M., Sánchez-Moreno, L., Leterrier, M., Barroso, J. B., Palma, J. M., and Corpas, F. J. (2011). Detection and quantification of S-nitrosoglutathione (GSNO) in pepper (*Capsicum annuum* L.) plant organs by LC-ES/MS. *Plant Cell Physiol.* 52, 2006–2015. doi: 10.1093/pcp/pcr133

Akmakjian, G. Z. (2011). *Long-Distance Cadmium Transport and Regulation of Heavy Metal Stress Responses in Arabidopsis thaliana.* Master Science thesis, University of California, San Diego, CA.

Alcántara, E., Romera, F. J., De La Guardia, M. D., and Cañete, M. (1994). Effects of heavy metals on both induction and function of root Fe(III) reductase in Fe-deficient cucumber (*Cucumis sativus* L.) plants. *J. Exp. Bot.* 281, 1893–1898. doi: 10.1093/jxb/45.12.1893

Bacaicoa, E., Mora, V., Zamarreño, A. M., Fuentes, M., Casanova, E., and García-Mina, J. M. (2011). Auxin: a major player in the shoot-to-root regulation of root Fe-stress physiological responses to Fe deficiency in cucumber plants. *Plant Physiol. Biochem.* 49, 545–556. doi: 10.1016/j.plaphy.2011.02.018

Bacaicoa, E., Zamarreño, A. M., Leménager, D., Baigorri, R., and García-Mina, J. M. (2009). Relationship between the hormonal balance and the regulation of iron deficiency stress responses in cucumber. *J. Am. Soc. Hortic. Sci.* 134, 589–601.

Barberon, M., Vermeer, J. E. M., De Bellis, D., Wang, P., Naseer, S., Andersen, T. G., et al. (2016). Adaptation of root function by nutrient-induced plasticity of endodermal differentiation. *Cell* 164, 1–13. doi: 10.1016/j.cell.2015.12.021

Bauer, P., Ling, H. Q., and Guerinot, M. L. (2007). Fit, the FER-like iron deficiency induced transcription factor in *Arabidopsis*. *Plant Physiol. Biochem.* 45, 260–261. doi: 10.1016/j.plaphy.2007.03.006

Begara-Morales, J. C., Sánchez-Calvo, B., Chaki, M., Mata-Pérez, C., Valderrama, R., Padilla, M. N., et al. (2015). Differential molecular response of monodehydro- ascorbate reductase and glutathione reductase by nitration and S-nitrosylation. *J. Exp. Bot.* 66, 5983–5996. doi: 10.1093/jxb/erv306

Blum, A., Brumbarova, T., Bauer, P., and Ivanov, R. (2014). Hormone influence on the spatial regulation of IRT1 expression in iron-deficient *Arabidopsis thaliana* roots. *Plant Signal. Behav.* 9:e28787. doi: 10.4161/psb.28787

Brumbarova, T., Bauer, P., and Ivanov, R. (2015). Molecular mechanisms governing *Arabidopsis* iron uptake. *Trends Plant Sci.* 20, 124–133. doi: 10.1016/j.tplants.2014.11.004

Buet, A., and Simontacchi, M. (2015). Nitric oxide and plant iron homeostasis. *Ann. N. Y. Acad. Sci.* 1340, 39–46. doi: 10.1111/nyas.12644

Chen, W. W., Yang, J. L., Qin, C., Jin, C. W., Mo, J. H., Ye, T., et al. (2010). Nitric oxide acts downstream of auxin to trigger root ferric-chelate reductase activity in response to iron deficiency in *Arabidopsis thaliana*. *Plant Physiol.* 154, 810–819. doi: 10.1104/pp.110.161109

Cheng, T., Chen, J., Ef, A., Wang, P., Wang, G., Hu, X., et al. (2015). Quantitative proteomics analysis reveals that S-nitrosoglutathione reductase (GSNOR) and nitric oxide signaling enhance poplar defense against chilling stress. *Planta* 242, 1361–1390. doi: 10.1007/s00425-015-2374-5

Corpas, F. J., Alché, J. D., and Barroso, J. B. (2013). Current overview of S-nitrosoglutathione (GSNO) in higher plants. *Front. Plant Sci.* 4:126. doi: 10.3389/ fpls.2013.00126 doi: 10.3389/fpls.2013.00126

Corpas, F. J., Barroso, J. B., Carreras, A., Quirós, M., León, A. M., Romero-Puertas, M. C., et al. (2004). Cellular and subcellular localization of endogenous nitric oxide in young and senescent pea plants. *Plant Physiol.* 136, 2722–2733. doi: 10.1104/pp.104.042812

Corpas, F. J., Chaki, M., Fernández-Ocaña, A., Valderrama, R., Palma, J. M., Carreras, A., et al. (2008). Metabolism of reactive nitrogen species in pea plants under abiotic stress conditions. *Plant Cell Physiol.* 49, 1711–1722. doi: 10.1093/pcp/pcn144

Corpas, F. J., Leterrier, M., Valderrama, R., Airaki, M., Chaki, M., Palma, J. M., et al. (2011). Nitric oxide imbalance provokes a nitrosative response in plants under abiotic stress. *Plant Sci.* 181, 604–611. doi: 10.1016/j.plantsci.2011.04.005

Darbani, B., Briat, J. F., Holm, P. B., Husted, S., Noeparvar, S., and Borg, S. (2013). Dissecting plant iron homeostasis under short and long-term iron fluctuations. *Biotechnol. Adv.* 31, 1292–1307. doi: 10.1016/j.biotechadv.2013.05.003

Datta, R., Kumar, D., Sultana, A., Hazra, S., Bhattacharyya, S., and Chattopadhyay, S. (2015). Glutathione regulates 1-Aminocyclopropane-1-Carboxylate synthase transcription via WRKY33 and 1-Aminocyclopropane-1-Carboxylate Oxidase by modulating messenger RNA stability to induce ethylene synthesis during stress. *Plant Physiol.* 169, 2963–2981. doi: 10.1104/pp.15.01543

Díaz, M., Achkor, H., Titarenko, E., and Martínez, M. C. (2003). The gene encoding glutathione-dependent formaldehyde dehydrogenase/GSNO reductase is responsive to wounding, jasmonic acid and salicylic acid. *FEBS Lett.* 543, 136–139. doi: 10.1016/S0014-5793(03)00426-5

Fan, H., Zhang, Z., Wang, N., Cui, Y., Sun, H., Liu, Y., et al. (2014). SKB1/PRMT5-mediated histone H4R3 dimethylation of Ib subgroup bHLH genes negatively regulates iron homeostasis in *Arabidopsis thaliana*. *Plant J.* 77, 209–221. doi: 10.1111/tpj.12380

Freschi, L. (2013). Nitric oxide and phytohormone interactions: current status and perspectives. *Front. Plant Sci.* 4:398. doi: 10.3389/fpls.2013.00398

García, M. J., Lucena, C., Romera, F. J., Alcántara, E., and Pérez-Vicente, R. (2010). Ethylene and nitric oxide involvement in the up-regulation of key genes related to iron acquisition and homeostasis in *Arabidopsis*. *J. Exp. Bot.* 61, 3885–3899. doi: 10.1093/jxb/erl189

García, M. J., Romera, F. J., Lucena, C., Alcántara, E., and Pérez-Vicente, R. (2015). Ethylene and the regulation of physiological and morphological responses to nutrient deficiencies. *Plant Physiol.* 169, 51–60. doi: 10.1104/pp.15.00708

García, M. J., Romera, F. J., Stacey, M. G., Stacey, G., Villar, E., Alcántara, E., et al. (2013). Shoot to root communication is necessary to control the expression of iron-acquisition genes in strategy I plants. *Planta* 237, 65–75. doi: 10.1007/s00425-012-1757-0

García, M. J., Suárez, V., Romera, F. J., Alcántara, E., and Pérez-Vicente, R. (2011). A new model involving ethylene, nitric oxide and Fe to explain the regulation of Fe-acquisition genes in Strategy I plants. *Plant Physiol. Biochem.* 49, 537–544. doi: 10.1016/j.plaphy.2011.01.019

Gaupels, F., Furch, A. C. U., Will, T., Mur, L. A. J., Kogel, K. H., and van Bel, A. J. E. (2008). Nitric oxide generation in *Vicia faba* phloem cells reveals them to be sensitive detectors as well as possible systemic transducers of stress signals. *New Phytol.* 178, 634–646. doi: 10.1111/j.1469-8137.2008.02388.x

Gayomba, S. R., Zhai, Z., Jung, H., and Vatamaniuk, O. K. (2015). Local and systemic signaling of iron status and its interactions with homeostasis of other essential elements. *Front. Plant Sci.* 6:716. doi: 10.3389/fpls.2015.00716

Graziano, M., Beligni, M. V., and Lamattina, L. (2002). Nitric oxide improves internal iron availability in plants. *Plant Physiol.* 130, 1852–1859. doi: 10.1104/pp.009076

Graziano, M., and Lamattina, L. (2007). Nitric oxide accumulation is required for molecular and physiological responses to iron deficiency in tomato roots. *Plant J.* 52, 949–960. doi: 10.1111/j.1365-313X.2007.03283.x

Grillet, L., Lan, P., Li, W., Mokkapati, G., and Schmidt, W. (2018). Iron man, a ubiquitous family of peptides that control iron transport in plants. *bioRxiv* [Preprint]. doi: 10.1101/351635

Gutiérrez-Carbonell, E., Lattanzio, G., Albacete, A., Ríos-Ruiz, J. J., Kehr, J., Abadía, A., et al. (2015). Effects of Fe deficiency on the protein profile of *Brassica napus* phloem sap. *Proteomics* 15, 3835–3853. doi: 10.1002/pmic.201400464

Han, B., Yang, Z., Samma, M. K., Wang, R., and Shen, W. (2013). Systematic validation of candidate reference genes for qRT-PCR normalization under iron deficiency in *Arabidopsis*. *Biometals* 26, 403–413. doi: 10.1007/s10534-013-9623-5

Hindt, M. N., Akmakjian, G. Z., Pivarski, K. L., Punshon, T., Baxter, I., Salt, D. E., et al. (2017). Brutus and its paralogs, BTS LIKE1 and BTS LIKE2, encode important negative regulators of the iron deficiency response in *Arabidopsis thaliana*. *Metallomics* 9, 876–890. doi: 10.1039/c7mt00152e

Hu, J., Huang, X., Chen, L., Sun, X., Lu, C., Zhang, L., et al. (2015). Site-specific nitrosoproteomic identification of endogenously S-nitrosylated proteins in *Arabidopsis*. *Plant Physiol.* 167, 1731–1746. doi: 10.1104/pp.15.00026

Ivanov, R., Brumbarova, T., and Bauer, P. (2012). Fitting into the harsh reality: regulation of iron-deficiency responses in dicotyledonous plants. *Mol. Plant* 5, 27–42. doi: 10.1093/mp/ssr065

Kailasam, S., Wang, Y., Lo, J. C., Chang, H. F., and Yeh, K. C. (2018). S-nitrosoglutathione works downstream of nitric oxide to mediate iron deficiency signaling in *Arabidopsis. Plant J.* 94, 157–168. doi: 10.1111/tpj.13850

Keunen, E., Schellingen, K., Vangronsveld, J., and Cuypers, A. (2016). Ethylene and metal stress: small molecule, big impact. *Front. Plant Sci.* 7:23. doi: 10.3389/fpls.2016.00023

Khan, M. A., Castro-Guerrero, N. A., McInturf, S. A., Nguyen, N. T., Dame, A. N., Wang, J., et al. (2018). Changes in iron availability in *Arabidopsis* are rapidly sensed in the leaf vasculature and impaired sensing leads to opposite transcriptional programs in leaves and roots. *Plant Cell Environ.* doi: 10.1111/pce.13192 [Epub ahead of print].

Klatte, M., Schuler, M., Wirtz, M., Fink-Straube, C., Hell, R., and Bauer, P. (2009). The analysis of *Arabidopsis* nicotianamine synthase mutants reveals functions for nicotianamine in seed iron loading and iron deficiency responses. *Plant Physiol.* 150, 257–271. doi: 10.1104/pp.109.136374

Kobayashi, T., Itai, R. N., Senoura, T., Oikawa, T., Ishimaru, Y., Ueda, M., et al. (2016). Jasmonate signaling is activated in the very early stages of iron deficiency responses in rice roots. *Plant Mol. Biol.* 91, 533–547. doi: 10.1007/s11103-016-0486-3

Kobayashi, T., and Nishizawa, N. K. (2012). Iron uptake, translocation, and regulation in higher plants. *Annu. Rev. Plant Biol.* 63, 131–152. doi: 10.1146/annurev-arplant-042811-10552

Kobayashi, T., and Nishizawa, N. K. (2014). Iron sensors and signals in response to iron deficiency. *Plant Sci.* 224, 36–43. doi: 10.1016/j.plantsci.2014.04.002

Koen, E., Szymańska, K., Klinguer, A., Dobrowolska, G., Besson-Bard, A., and Wendehenne, D. (2012). Nitric oxide and glutathione impact the expression of iron uptake- and iron transport-related genes as well as the content of metals in *A. thaliana* plants grown under iron deficiency. *Plant Signal. Behav.* 7, 1246–1250. doi: 10.4161/psb.21548

Korshunova, Y. O., Eide, D., Clark, W. G., Guerinot, M. L., and Pakarasi, H. B. (1999). The IRT1 protein from *Arabidopsis thaliana* is a metal transporter with a broad substrate range. *Plant Mol. Biol.* 40, 37–44. doi: 10.1023/A:1026438615520

Krüger, C., Berkowitz, O., Stephan, U. W., and Hell, R. (2002). A metal-binding member of the late embryogenesis abundant family transports iron in the phloem of *Ricinus communis* L. *J. Biol. Chem.* 277, 25062–25069. doi: 10.1074/jbc.M201896200

Kubienová, L., Tichá, T., Jahnová, J., Luhová, L., Mieslerová, B., and Petřívalský, M. (2014). Effect of abiotic stress stimuli on S-nitrosoglutathione reductase in plants. *Planta* 239, 139–146. doi: 10.1007/s00425-013-1970-5

Kumar, R. K., Chu, H. H., Abundis, C., Vasques, K., Rodriguez, D. C., Chia, J. C., et al. (2017). Iron-nicotianamine transporters are required for proper long distance iron signaling. *Plant Physiol.* 175, 1254–1268. doi: 10.1104/pp.17.00821

Leaden, L., Pagani, M. A., Balparda, M., Busi, M. V., and Gomez-Casati, D. F. (2016). Altered levels of AtHSCB disrupts iron translocation from roots to shoots. *Plant Mol. Biol.* 92, 613–628. doi: 10.1007/s11103-016-0537-9

Leterrier, M., Airaki, M., Palma, J. M., Chaki, M., Barroso, J. B., and Corpas, F. J. (2012). Arsenic triggers the nitric oxide (NO) and S-nitrosoglutathione (GSNO) metabolism in *Arabidopsis*. *Environ. Pollut.* 166, 136–143. doi: 10.1016/j.envpol.2012.03.012

Leterrier, M., Chaki, M., Airaki, M., Valderrama, R., Palma, J. M., Barroso, J. B., et al. (2011). Function of S-nitrosoglutathione reductase (GSNOR) in plant development and under biotic/abiotic stress. *Plant Signal. Behav.* 6, 789–793. doi: 10.4161/psb.6.6.15161

Li, W., and Lan, P. (2017). The understanding of the plant iron deficiency responses in strategy I plants and the role of ethylene in this process by omic approaches. *Front. Plant Sci.* 8:40. doi: 10.3389/fpls.2017.00040

Li, X., Zhang, H., Ai, Q., Liang, G., and Yu, D. (2016). Two bHLH transcription factors, bHLH34 and bHLH104, regulate iron homeostasis in *Arabidopsis thaliana*. *Plant Physiol.* 170, 2478–2493. doi: 10.1104/pp.15.01827

Liang, G., Zhang, H., Li, X., Ai, Q., and Yu, D. (2017). bHLH transcription factor bHLH115 regulates iron homeostasis in *Arabidopsis thaliana*. *J. Exp. Bot.* 68, 1743–1755. doi: 10.1093/jxb/erx043

Lin, X. Y., Ye, Y. Q., Fan, S. K., Jin, C. W., and Zheng, S. J. (2016). Increased sucrose accumulation regulates iron-deficiency responses by promoting auxin signaling in *Arabidopsis* plants. *Plant Physiol.* 170, 907–920. doi: 10.1104/pp.15.01598

Lin, Y., Yang, L., Paul, M., Zu, Y., and Tang, Z. (2013). Ethylene promotes germination of *Arabidopsis* seed under salinity by decreasing reactive oxygen species: evidence for the involvement of nitric oxide simulated by sodium nitroprusside. *Plant Physiol. Biochem.* 73, 211–218. doi: 10.1016/j.plaphy.2013.10.003

Lindermayr, C., Saalbach, G., Bahnweg, G., and Durner, J. (2006). Differential inhibition of *Arabidopsis* methionine adenosyltransferases by protein S-nitrosylation. *J. Biol. Chem.* 281, 4285–4291. doi: 10.1074/jbc.M511635200

Lingam, S., Mohrbacher, J., Brumbarova, T., Potuschak, T., Fink-Straube, C., Blondet, E., et al. (2011). Interaction between the bHLH transcription factor FIT and the Ethilene Insensitive3/ Ethylene Insensitive3-like1 reveals molecular linkage between the regulation of iron acquisition and ethylene signaling in *Arabidopsis*. *Plant Cell* 23, 1815–1829. doi: 10.1105/tpc.111.084715

Liu, M., Liu, X. X., He, X. L., Liu, L. J., Wu, H., Tang, C. X., et al. (2017). Ethylene and nitric oxide interact to regulate the magnesium deficiency-induced root hair development in *Arabidopsis*. *New Phytol.* 213, 1242–1256. doi: 10.1111/nph.14259

Liu, S., Yang, R., Tripathi, D. K., Li, X., He, W., Wu, M., et al. (2018). The interplay between reactive oxygen and nitrogen species contributes in the regulatory mechanism of the nitro-oxidative stress induced by cadmium in *Arabidopsis*. *J. Hazard. Mater.* 344, 1007–1024. doi: 10.1016/j.jhazmat.2017.12.004

Lubkowitz, M. (2011). The oligopeptide transporters: a small gene family with a diverse group of substrates and functions? *Mol. Plant* 4, 407–415. doi: 10.1093/mp/ssr004

Lucena, C., Romera, F. J., García, M. J., Alcántara, E., and Pérez-Vicente, R. (2015). Ethylene participates in the regulation of Fe deficiency responses in Strategy I plants and in rice. *Front. Plant Sci* 6:1056. doi: 10.3389/fpls.2015.01056

Lucena, C., Romera, F. J., Rojas, C. L., García, M. J., Alcántara, E., and Pérez-Vicente, R. (2007). Bicarbonate blocks the expression of several genes involved in the physiological responses to Fe deficiency of Strategy I plants. *Funct. Plant Biol.* 34, 1002–1009. doi: 10.1071/FP07136

Lucena, C., Waters, B. M., Romera, F. J., García, M. J., Morales, M., Alcántara, E., et al. (2006). Ethylene could influence ferric reductase, iron transporter and

H+-ATPase gene expression by affecting FER (or FER-like) gene activity. *J. Exp. Bot.* 57, 4145–4154. doi: 10.1093/jxb/erl189

Malik, S. I., Hussain, A., Yun, B. W., Spoel, S. H., and Loake, G. J. (2011). GSNOR-mediated de-nitrosylation in the plant defence response. *Plant Sci.* 181, 540–544. doi: 10.1016/j.plantsci.2011.04.004

Marentes, E., and Grusak, M. A. (1998). Mass determination of low-molecular-weight proteins in phloem sap using matrix-assisted laser desorption/ionisation time-of-flight mass spectrometry. *J. Exp. Bot.* 49, 903–911.

Marín-de la Rosa, N., Sotillo, B., Miskolczi, P., Gibbs, D. J., Vicente, J., Carbonero, P., et al. (2014). Large-scale identification of gibberellin-related transcription factors defines group VII Ethylene Response Factors as functional DELLA partners. *Plant Physiol.* 166, 1022–1032. doi: 10.1104/pp.114.244723

Maurer, F., Müller, S., and Bauer, P. (2011). Suppression of Fe deficiency gene expression by jasmonate. *Plant Physiol. Biochem.* 49, 530–536. doi: 10.1016/j.plaphy.2011.01.025

Meiser, J., Lingam, S., and Bauer, P. (2011). Post-transcriptional regulation of the Fe deficiency bHLH transcription factor FIT is affected by iron and nitric oxide. *Plant Physiol.* 157, 2154–2166. doi: 10.1104/pp.111.183285

Mendoza-Cózatl, D. G., Xie, Q., Akmakjian, G. Z., Jobe, T. O., Patel, A., Stacey, M. G., et al. (2014). OPT3 is a component of the iron-signaling network between leaves and roots and misregulation of opt3 leads to an over-accumulation of cadmium in seeds. *Mol. Plant* 7, 1455–1469. doi: 10.1093/mp/ssu067

Mora, V., Baigorri, R., Bacaicoa, E., Zamarreño, A. M., and García-Mina, J. M. (2012). The humic acid-induced changes in the root concentration of nitric oxide, IAA and ethylene do not explain the changes in root architecture caused by humic acid in cucumber. *Environ. Exp. Bot.* 76, 24–32. doi: 10.1016/j.envexpbot.2011.10.001

Pfaffl, M. W. (2001). A new mathematical model for relative quantification in real-time RT-PCR. *Nucleic Acids Res.* 29:e45. doi: 10.1093/nar/29.9.e45

Pommerrenig, B., Feussner, K., Zierer, W., Rabinovych, V., Klebl, F., Feussner, I., et al. (2011). Phloem-specific expression of Yang cycle genes and identification of novel Yang cycle enzymes in Plantago and *Arabidopsis*. *Plant Cell* 23, 1904–1919. doi: 10.1105/tpc.110.079657

Rahmanto, Y. S., Kalinowski, D. S., Lane, D. J. R., Lok, H. C., Richardson, V., and Richardson, D. R. (2012). Nitrogen monoxide (NO) storage and transport by dinitrosyl-dithiol-iron complexes: long-lived NO that is trafficked by interacting proteins. *J. Biol. Chem.* 287, 6960–6968. doi: 10.1074/jbc.R111.329847

Ramírez, L., Bartoli, C. G., and Lamattina, L. (2013). Glutathione and ascorbic acid protect *Arabidopsis* plants against detrimental effects of iron deficiency. *J. Exp. Bot.* 64, 3169–3178. doi: 10.1093/jxb/ert153

Ramírez, L., Simontacchi, M., Murgia, I., Zabaleta, E., and Lamattina, L. (2011). Nitric oxide, nitrosyl iron complexes, ferritin and frataxin: a well equipped team to preserve plant iron homeostasis. *Plant Sci.* 181, 582–592. doi: 10.1016/j.plantsci.2011.04.006

Rogers, E. E., and Guerinot, M. L. (2002). FRD3, a member of the multidrug and toxin efflux family, controls iron deficiency responses in *Arabidopsis*. *Plant Cell* 14, 1787–1799. doi: 10.1105/tpc.001495

Romera, F. J., García, M. J., Alcántara, E., and Pérez-Vicente, R. (2011). Latest findings about the interplay or auxin, ethylene and nitric oxide in the regulation of Fe deficiency responses by Strategy I plants. *Plant Signal. Behav.* 6, 167–170. doi: 10.4161/psb.6.1.14111

Romera, F. J., Lucena, C., García, M. J., Alcántara, E., and Pérez-Vicente, R. (2015). "Regulation of Fe deficiency responses in wt pea and some of its mutants (brz and dgl)," in *Pisum sativum: Cultivation, Functional Properties and Health Benefits*, ed. S. Becket (New York, NY: Nova Science Publishers Inc.), 1–20.

Romera, F. J., Lucena, C., García, M. J., Alcántara, E., and Pérez-Vicente, R. (2017). "The role of ethylene and other signals in the regulation of Fe deficiency responses by dicot plants," in *Stress Signaling in Plants: Genomics and Proteomics Perspectives*, Vol. 2, ed. M. Sarwat (Dordrecht: Springer), 277–300.

Romera, F. J., Welch, R. M., Norvell, W. A., and Schaefer, S. C. (1996). Iron requirement for and effects of promoters and inhibitors of ethylene action on stimulation of Fe(llI)-chelate reductase in roots of Strategy I species. *Biometals* 9, 45–50. doi: 10.1007/BF00188089

Römheld, V., and Marschner, H. (1986). Mobilization of iron in the rhizosphere of different plant species. *Adv. Plant Nutr.* 2, 155–204.

Roschzttardtz, H., Séguéla-Arnaud, M., Briat, J. F., Vert, G., and Curie, C. (2011). The FRD3 citrate effluxer promotes iron nutrition between simplistically disconnected tissues throughout *Arabidopsis* development. *Plant Cell* 23, 2725–2737. doi: 10.1105/tpc.111.088088

Rustérucci, C., Espunya, M. C., Díaz, M., Chabannes, M., and Martínez, M. C. (2007). S-nitrosoglutathione reductase affords protection against pathogens in *Arabidopsis*, both locally and systemically. *Plant Physiol.* 143, 1282–1292. doi: 10.1104/pp.106.091686

Sakamoto, A., Ueda, M., and Morikawa, H. (2002). *Arabidopsis* glutathione-dependent formaldehyde dehydrogenase is an S-nitrosoglutathione reductase. *FEBS Lett.* 515, 20–24. doi: 10.1016/S0014-5793(02)02414-6

Sauter, M., Moffatt, B., Saechao, M. C., Hell, R., and Wirtz, M. (2013). Methionine salvage and S-adenosylmethionine: essential links between sulfur, ethylene and polyamine biosynthesis. *Biochem. J.* 451, 145–154. doi: 10.1042/BJ20121744

Schuler, M., Rellán-Álvarez, R., Fink-Straube, C., Abadía, J., and Bauer, P. (2012). Nicotianamine functions in the phloem-based transport of iron to sink organs, in pollen development and pollen tube growth in *Arabidopsis*. *Plant Cell* 24, 2380–2400. doi: 10.1105/tpc.112.099077

Séguéla, M., Briat, J. F., Vert, G., and Curie, C. (2008). Cytokinins negatively regulate the root iron uptake machinery in *Arabidopsis* through a growth-dependent pathway. *Plant J.* 55, 289–300. doi: 10.1111/j.1365-313X.2008.03502.x

Shanmugam, V., Wang, Y. W., Tsednee, M., Karunakaran, K., and Yeh, K. C. (2015). Glutathione plays an essential role in nitric oxide-mediated iron-deficiency signaling and iron-deficiency tolerance in *Arabidopsis*. *Plant J.* 84, 464–477. doi: 10.1111/tpj.13011

Shen, C., Yang, Y., Liu, K., Zhang, L., Guo, H., Sun, T., et al. (2016). Involvement of endogenous salicylic acid in iron-deficiency responses in *Arabidopsis*. *J. Exp. Bot.* 67, 4179–4193. doi: 10.1093/jxb/erw196

Shi, Y. F., Wang, D. L., Wang, C., Culler, A. H., Kreiser, M. A., Suresh, J., et al. (2015). Loss of GSNOR1 function leads to compromised auxin signaling and polar auxin transport. *Mol. Plant* 8, 1350–1365. doi: 10.1016/j.molp.2015.04.008

Stacey, M. G., Patel, A., McClain, W. E., Mathieu, M., Remley, M., Rogers, E. E., et al. (2008). The *Arabidopsis* AtOPT3 protein functions in metal homeostasis and movement of iron to developing seeds. *Plant Physiol.* 146, 589–601. doi: 10.1104/pp.107.108183

Vert, G., Grotz, N., Dedaldechamp, F., Gaymard, F., Guerinot, M. L., Briat, J. F., et al. (2002). IRT1, an *Arabidopsis* transporter essential for iron uptake from the soil and for plant growth. *Plant Cell* 14, 1223–1233. doi: 10.1105/tpc.001388

Wang, N., Cui, Y., Liu, Y., Fan, H., Du, J., Huang, Z., et al. (2013). Requirement and functional redundancy of Ib subgroup bHLH proteins for iron deficiency responses and uptake in *Arabidopsis thaliana*. *Mol. Plant* 6, 503–513. doi: 10.1093/mp/sss089

Waters, B. M., Lucena, C., Romera, F. J., Jester, G. G., Wynn, A. N., Rojas, C. L., et al. (2007). Ethylene involvement in the regulation of the H^+-ATPase CsHA1 gene and of the new isolated ferric reductase CsFRO1 and iron transporter CsIRT1 genes in cucumber plants. *Plant Physiol. Biochem.* 45, 293–301. doi: 10.1016/j.plaphy.2007.03.011

Wintz, H., Fox, T., Wu, Y. Y., Feng, V., Chen, W., Chang, H. S., et al. (2003). Expression profiles of *Arabidopsis thaliana* in mineral deficiencies reveal novel transporters involved in metal homeostasis. *J. Biol. Chem.* 278, 47644–47653. doi: 10.1074/jbc.M309338200

Wünsche, H., Baldwin, I. T., and Wu, J. (2011). S-nitrosoglutathione reductase (GSNOR) mediates the biosynthesis of jasmonic acid and ethylene induced by feeding of the insect herbivore *Manduca sexta* and is important for jasmonate-elicited responses in *Nicotiana attenuata*. *J. Exp. Bot.* 62, 4605–4616. doi: 10.1093/jxb/err171

Xu, S., Guerra, D., Lee, U., and Vierling, E. (2013). S-nitrosoglutathione reductases are low-copy number, cysteine-rich proteins in plants that control multiple developmental and defense responses in *Arabidopsis*. *Front. Plant Sci.* 4:430. doi: 10.3389/fpls.2013.00430

Yang, Y., Ou, B., Zhang, J., Si, W., Gu, H., Qin, G., et al. (2014). The *Arabidopsis* mediator subunit MED16 regulates iron homeostasis by associating with EIN3/EIL1 through subunit MED25. *Plant J.* 77, 838–851. doi: 10.1111/tpj.12440

Ye, L., Li, L., Wang, L., Wang, S., Li, S., Du, J., et al. (2015). MPK3/MPK6 are involved in iron deficiency-induced ethylene production in *Arabidopsis*. *Front. Plant Sci.* 6:953. doi: 10.3389/fpls.2015.00953

Yoshihara, T., Hodoshima, H., Miyano, Y., Shoji, K., Shimada, H., and Goto, F. (2006). Cadmium inducible Fe deficiency responses observed from macro and

molecular views in tobacco plants. *Plant Cell Rep.* 25, 365–373. doi: 10.1007/s00299-005-0092-3

Yuan, Y. X., Wu, H. L., Wang, N., Li, J., Zhao, W. N., Du, J., et al. (2008). FIT interacts with AtbHLH038 and AtbHLH039 in regulating iron uptake gene expression for iron homeostasis in *Arabidopsis*. *Cell Res.* 18, 385–397. doi: 10.1038/cr.2008.26

Yun, B. W., Skelly, M. J., Yin, M., Yu, M., Mun, B. G., Lee, S. U., et al. (2016). Nitric oxide and S-nitrosoglutathione function additively durin plant immunity. *New Phytol.* 211, 516–526. doi: 10.1111/nph.13903

Zaffagnini, M., DeMia, M., Morisse, S., Di Giacinto, N., Marchand, C. H., Maes, A., et al. (2016). Protein S-nitrosylation in photosynthetic organisms: a comprehensive overview with future perspectives. *Biochim. Biophys. Acta* 1864, 952–966. doi: 10.1016/j.bbapap.2016.02.006

Zaharieva, T. B., and Abadía, J. (2003). Iron deficiency enhances the levels of ascorbate, glutathione and related enzymes in sugar beet roots. *Protoplasma* 221, 269–275. doi: 10.1007/s00709-002-0051-6

Zaharieva, T. B., Gogorcena, Y., and Abadía, J. (2004). Dynamics of metabolic responses to iron deficiency in sugar beet roots. *Plant Sci.* 166, 1045–1050. doi: 10.1016/j.plantsci.2003.12.017

Zhai, Z., Gayomba, S. R., Jung, H., Vimalakumari, N. K., Piñeros, M., Craft, E., et al. (2014). OPT3 is a phloem-specific iron transporter that is essential for systemic iron signaling and redistribution of iron and cadmium in *Arabidopsis*. *Plant Cell* 26, 2249–2264. doi: 10.1105/tpc.114.123737

Zhang, J., Liu, B., Li, M., Feng, D., Jin, H., Wang, P., et al. (2015). The bHLH transcription factor bHLH104 interacts with IAA-Leucine Resistant3 and modulates iron homeostasis in *Arabidopsis*. *Plant Cell* 27, 787–805. doi: 10.1105/tpc.114.132704

Zhang, Z., Xie, Q., Jobe, T. O., Kau, A. R., Wang, C., Li, Y., et al. (2016). Identification of AtOPT4 as a plant glutathione transporter. *Mol. Plant* 9, 481–484. doi: 10.1016/j.molp.2015.07.013

Conflict of Interest Statement: The authors declare that the research was conducted in the absence of any commercial or financial relationships that could be construed as a potential conflict of interest.

frontiers in Plant Science

ORIGINAL RESEARCH
published: 13 November 2018
doi: 10.3389/fpls.2018.01641

Differential Diel Translation of Transcripts With Roles in the Transfer and Utilization of Iron-Sulfur Clusters in Arabidopsis

*Hongliang Zhang and Ute Krämer**

Molecular Genetics and Physiology of Plants, Faculty of Biology and Biotechnology, Ruhr University Bochum, Bochum, Germany

Iron-sulfur (Fe-S) clusters are evolutionarily ancient ubiquitous protein cofactors which have mostly catalytic functions but can also have structural roles. In *Arabidopsis thaliana*, we presently know a total of 124 Fe-S metalloproteins that are encoded in the genome. Fe-S clusters are highly sensitive to oxidation. Therefore, we hypothesized that Fe-S cluster protein biogenesis is adjusted following the daily rhythms in metabolism driven by photosynthesis at the whole-plant, organ, cellular and sub-cellular levels. It had been concluded previously that little such regulation occurs at the transcript level among the genes functioning in Fe-S cluster assembly. As an initial step toward testing our hypothesis, we thus addressed the diel time course of the translation state of relevant transcripts based on publicly available genome-wide microarray data. This analysis can answer whether the translation of the pool of transcripts of a given gene is temporarily either enhanced or suppressed, and when during the day. Thirty-three percent of the transcripts with functions in Fe-S cluster assembly exhibited significant changes in translation state over a diurnal time course, compared to 26% of all detected transcripts. These transcripts comprised functions in all three steps of cluster assembly including persulfide formation, Fe-S cluster formation and Fe-S cluster transfer to target apoproteins. The number of Fe-S cluster carrier/transfer functions contributed more than half of these transcripts, which reached maxima in translation state either during the night or the end of the night. Similarly, translation state of mitochondrial frataxin and ferredoxin, which are thought to contribute Fe and electrons during cluster formation, peaked during the night. By contrast, translation state of chloroplast SUFE2 in persulfide formation and cytosolic Fe-S cluster formation scaffold protein NBP35 reached maxima in translation state during the day. Among the transcripts encoding target Fe-S cluster-utilizing proteins, 19% exhibited diurnal variation in translation state. Day-time maxima of translation state were most common among these transcripts, with none of the maxima during the night (ZT18). We conclude that diurnal regulation of translation state is important in metalloprotein biogenesis. Future models of Fe-S protein biogenesis require more comprehensive data and will have to accommodate diurnal dynamics.

Keywords: translatome, microarray, diurnal, metalloprotein, Fe, Zn, Mn, Cu

OPEN ACCESS

Edited by:
Manuel González-Guerrero, Universidad Politécnica de Madrid (UPM), Spain

Reviewed by:
Ping Lan, Institute of Soil Science (CAS), China
Marinus Pilon, Colorado State University, United States
Louis Grillet, Academia Sinica, Taiwan

***Correspondence:**
Ute Krämer
Ute.Kraemer@ruhr-uni-bochum.de;
Ute.Kraemer@rub.de

Specialty section:
This article was submitted to Plant Nutrition, a section of the journal Frontiers in Plant Science

Received: *07 August 2018*
Accepted: *22 October 2018*
Published: *13 November 2018*

Citation:
Zhang H and Krämer U (2018) Differential Diel Translation of Transcripts With Roles in the Transfer and Utilization of Iron-Sulfur Clusters in Arabidopsis. Front. Plant Sci. 9:1641. doi: 10.3389/fpls.2018.01641

INTRODUCTION

Across all groups of biological organisms, proteins that can bind one or several iron-sulfur (Fe-S) cluster cofactors *in vivo* (Fe-S proteins) fulfill central cellular biochemical functions. Several types exist of protein-bound Fe-S clusters, based on chemical structures and oxidation states. Among these, cubane [4Fe–4S] and rhombic [2Fe–2S] are the most widespread Fe–S clusters, containing ferrous or ferric $Fe^{(+II)}$ or $^{(+III)}$ and sulfide $S^{(-II)}$ (Lill, 2009; Balk and Schaedler, 2014). Disruption of Fe-S protein biogenesis has been associated with serious diseases in human and animals (Lill, 2009; Wachnowsky et al., 2017). For example, frataxin is thought to function as the iron donor for the mitochondrial Isu1 scaffold protein complex in Fe-S cluster assembly in human. Depletion of frataxin causes the neurodegenerative disease Friedreich's ataxia, attributed to defective Fe–S protein activity and iron accumulation (Campuzano et al., 1996; Rötig et al., 1997).

In plants, Fe-S proteins are abundant in mitochondria and chloroplasts, for example in respiratory and photosynthetic electron transfer chains (Blaby-Haas and Merchant, 2013; Couturier et al., 2013), and Fe-S cluster assembly occurs in both of these organelles (Balk and Schaedler, 2014). Notably, the metabolism, repair and epigenetic modification of DNA all depend on Fe-S protein functions (Buzas et al., 2014; Zhang, 2015). The catalytic subunits of eukaryotic DNA polymerases α, δ, ε, and ζ contain [4Fe-4S] cofactors that are required for protein-protein interactions in the active protein complex (Netz et al., 2012). In Arabidopsis, Fe-S cluster-binding residues are conserved in these proteins, namely POLA1, POLD1, POLE1A/POL2A, POLE1B/POL2B, and REV3, the catalytic subunit of DNA polymerase ζ (Shultz et al., 2007; **Supplementary Dataset 1**). Moreover, proteins of the Demeter (DME) family contain a [4Fe-4S] cofactor and function in the demethylation and base excision repair of DNA (Choi et al., 2002; Wöhrmann et al., 2012; Buzas, 2016). Expanding from the list of Fe-S proteins updated in 2010 (Balk and Pilon, 2011), a total of 124 genes encoding proteins that contain Fe-S clusters are presently known in Arabidopsis (**Supplementary Dataset 1**).

The biosynthesis of Fe-S proteins requires cellular Fe-S cluster assembly. The first knowledge on Fe-S assembly pathways was obtained in *Escherichia coli* and *Azotobacter vinelandii* (Lill, 2009). Subsequent work revealed that genes encoding Fe-S assembly proteins are well conserved from prokaryotes to eukaryotes (Balk and Lobréaux, 2005; Lill, 2009; Py and Barras, 2010). In recent years, an increasing number of proteins of the Fe-S cluster assembly pathways were characterized employing mutants of *A. thaliana* (Couturier et al., 2013; Balk and Schaedler, 2014), and yet, our present knowledge in plants still relies to a large degree on inference from other model organisms. In plants, there are three cellular pathways of Fe-S cluster biogenesis. These are the Sulfur mobilization (SUF) pathway in plastids, the Iron Sulfur Cluster (ISC) pathway in mitochondria, and Cytosolic Iron-sulfur protein Assembly (CIA) pathway in the cytosol. Although each of these Fe-S cluster assembly pathways involves different proteins, all three of them proceed according to common biosynthetic principles (**Figure 1**). First, cysteine is metabolized by cysteine desulfurase to generate a persulfide (protein-S-S-H) at the active site of the enzyme. Subsequently, a terminal sulfane S^0 of this persulfide is transferred to a scaffold protein complex, followed by the reduction to sulfide (S^{-II}). The integration of iron on the scaffold protein results in the formation of the Fe-S cluster. Finally, the assembled Fe-S cluster is transferred to target apoproteins via carrier/transfer proteins. Based on three excellent reviews (Balk and Pilon, 2011; Couturier et al., 2013; Balk and Schaedler, 2014), we have assembled a list of 49 *A. thaliana* genes encoding proteins involved in Fe-S cluster assembly (**Supplementary Dataset 2**). Note that some of these Fe-S cluster assembly proteins bind Fe-S clusters themselves, mostly Fe-S scaffold and carrier/transfer proteins.

Although we have good knowledge of the Fe-S protein biogenesis machinery, we know comparably little about the regulation of Fe-S protein biogenesis. The Fe-S protein biogenesis machinery of bacteria involves transcriptional regulators, such as Fur, OxyR and IscR. For example, under oxidative stress, OxyR activates the expression of the *suf* operon in *E. coli* (Roche et al., 2013). However, none of the known bacterial regulators of Fe-S protein biogenesis has any orthologs in a plant or an algal genome (Couturier et al., 2013), suggesting that plants utilize different regulatory mechanisms. Protein-bound Fe-S clusters can be destroyed by oxygen or reactive oxygen species (ROS), such as hydrogen peroxide or nitric oxide (Beinert et al., 1997). Free Fe^{2+} released from Fe-S clusters can catalyze the Fenton reaction, which generates even more ROS (Halliwell and Gutteridge, 1992; Ravet et al., 2009). Transcript levels of few genes encoding Fe–S cluster assembly proteins respond to oxidative stress, nutritional iron deficiency, and heavy metal excess, in plants (Liang et al., 2014) (see also Discussion). Overall there is only little environment-dependent regulation in plants of Fe-S cluster assembly at the transcript level (Balk and Schaedler, 2014).

In plants, contrasting photosynthetic activity between day and night confers a diel rhythm in plant metabolism as well as in the generation of ROS, primarily locally in chloroplasts but also across cells, tissues and organs of plants (Lai et al., 2012; Sierla et al., 2013; Trotta et al., 2014). Plants are capable of regulatory adjustment to these fluctuations, which can be controlled by light, stress, metabolic state or the circadian clock (Lai et al., 2012; Sierla et al., 2013; Trotta et al., 2014). Surprisingly, it was noted that Fe-S cluster assembly – a potentially highly ROS-sensitive process – exhibits no diurnal profile of regulation at the transcript level (Balk and Schaedler, 2014). Consequently, Fe-S protein biogenesis of plants is either sufficiently ROS-insensitive, or alternatively it could be diurnally controlled at a different level of regulation.

To examine whether Fe-S protein biogenesis is diurnally regulated at the level of translational regulation, we re-analyzed published microarray-based diurnal translatome data (Missra et al., 2015). Accordingly, subsets of Fe-S cluster assembly and Fe-S utilizing proteins are under pronounced translational control. Among these, the translation of transcripts encoding Fe-cluster assembly proteins tended to peak at night while the translation of the majority of transcripts encoding Fe cluster-utilizing proteins reached a minimum. We conclude that the diurnal regulation of metalloprotein biogenesis deserves to be addressed in a

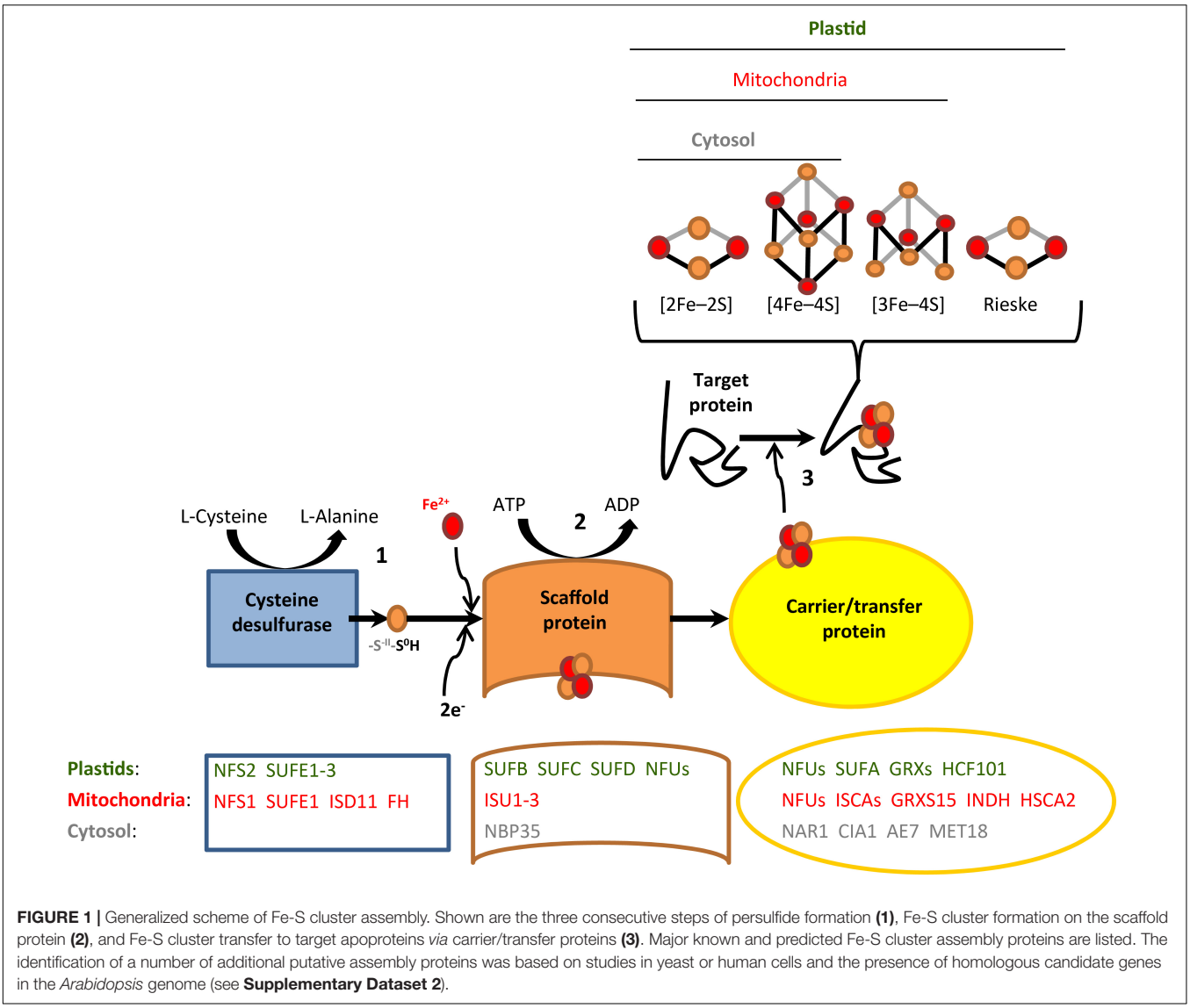

FIGURE 1 | Generalized scheme of Fe-S cluster assembly. Shown are the three consecutive steps of persulfide formation **(1)**, Fe-S cluster formation on the scaffold protein **(2)**, and Fe-S cluster transfer to target apoproteins *via* carrier/transfer proteins **(3)**. Major known and predicted Fe-S cluster assembly proteins are listed. The identification of a number of additional putative assembly proteins was based on studies in yeast or human cells and the presence of homologous candidate genes in the *Arabidopsis* genome (see **Supplementary Dataset 2**).

more quantitative and comprehensive translatome sequencing approach.

MATERIALS AND METHODS

Diel translatome time course data from ATH1 GeneChip microarray hybridization was taken from Missra et al. (2015) (**Figure 2**). Briefly, RNA was fractionated into non-polysomal (NP), small polysomal (SP), and large polysomal (LP) fractions using sucrose density centrifugation. In these fractions, the mRNA molecules were estimated to be bound by two and seven ribosomes on average so that SP and LP fractions were weighted by 2 and 7, respectively (Missra et al., 2015). The translation state (TL) of a given mRNA was approximated as follows: TL = (2 × SP + 7 × LP)/(NP + SP + LP), resulting in a global maximum TL of 6.48 and a minimum TL of 0.46. We additionally estimated relative rates of protein biosynthesis (PBR) for each protein across the diel time course by multiplying translation state with transcript levels (PBR = TL× TX, whereby TX = NP + SP + LP) as given in Missra et al. (2015). This calculation is based on the assumption that there is a correlation between the amount of ribosome-associated mRNA and its rate of translation, which is a simplification. The authors made no adjustment for global oscillation of TL across all expressed genes, which peaked at noon (ZT6; ∼ 0.8) and was minimal at the end of the night (ZT0; ∼ 0.68). Following the strategy employed by Missra et al. (2015), transcripts concluded to exhibit diel variation of TL fulfilled one of three criteria: ΔTL (difference between maximum and minimum average TL of three replicates) > 0.7, or ANOVA (Analysis Of Variance) $P < 0.05$, or Significance Analysis of Microarrays (SAM) with a collective FDR < 0.10 (Tusher et al., 2001).

For analyzing the TL of Fe-S proteins and Fe-S assembly proteins in this study, we first assembled a list of 124 Fe-S cluster-containing proteins (**Supplementary Dataset 1**) and 49

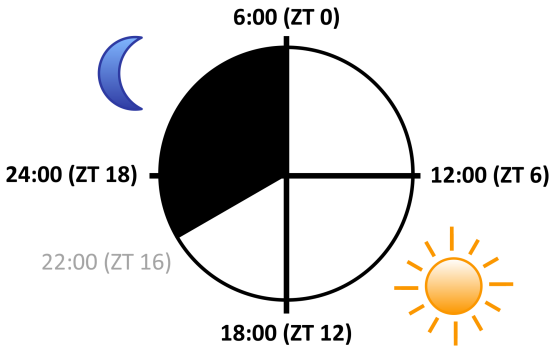

FIGURE 2 | Sampling scheme over the diurnal cycle. *Arabidopsis* seedlings were grown on agar-solidified full-strength MS media in petri dishes at constant temperature of 22°C in 16 h light (white; light intensity 80 μmol m^{-2} s^{-1})/8 h dark (black) cycles for 10 days, and harvested at ZT 0, ZT 6, ZT 12, and ZT 18, respectively (black, bold fonts; ZT: Zeitgeber Time). Diagram represents the sampling design of Missra et al. (2015).

Fe-S assembly proteins (**Supplementary Dataset 2**) identified in *A. thaliana* so far, expanding from previous work (Balk and Pilon, 2011; Couturier et al., 2013; Balk and Schaedler, 2014). Then, the translatome data of the genes in the two lists of Fe-S proteins and Fe-S assembly proteins were extracted from **Supplementary Dataset 1** of the original publication (Missra et al., 2015) as shown in **Supplementary Datasets 3**, **4** of this publication. Note that we consider as Fe-S cluster-utilizing proteins (**Supplementary Dataset 4**) only those Fe-S cluster-containing proteins that are not involved in Fe-S cluster assembly (**Supplementary Dataset 3**). Translatome data were further analyzed by using the software Genesis 1.7.6 (Sturn et al., 2002). First, translatome data were scaled by the mean center method. That is, for each transcript at each time point, $Z = TL_{ZT0,6,12,or18}$ – average ($TL_{ZT0} + TL_{ZT6} + TL_{ZT12} + TL_{ZT18}$). The purpose of this was to aid visualization of diel cycles of a number of genes together. Subsequently, the transcripts were clustered into different groups by the average linkage clustering method (Sokal and Michener, 1958). Analysis of TL of metalloproteins dependent on cofactors other than Fe-S clusters was done based on manually assembled lists (**Supplementary Dataset 5**). Only the transcripts showing significant diurnal dynamics at the translatome level were used when calculating the proportion of transcripts reaching maximum TL at each time point.

RESULTS

Global Translation Status of Fe-S Proteins and Fe-S Assembly Proteins Over a Diurnal Cycle

According to the previous analysis, out of 12,342 detected transcripts, 3,218 transcripts (26%) varied significantly in their translation state (TL) over a diurnal cycle (**Supplementary Dataset 6**). In this dataset, 39 (out of a total of 49) transcripts encoding Fe-S assembly proteins and 68 (out of 97) transcripts encoding Fe-S cluster-utilizing proteins were detected as expressed (**Supplementary Datasets 3**, **4**). Among these, 13 transcripts encoding Fe-S assembly proteins (33%) and 13 transcripts encoding Fe-S cluster-utilizing proteins (19%) showed diurnal fluctuations in TL (**Table 1**). The apparent over-representation of Fe-S cluster assembly genes among genes with diurnal changes in TL was not statistically significant according to a Fisher's exact test.

Transcripts Encoding Fe-S Assembly Proteins With Diurnal Changes in Translation State

Thirteen transcripts encoding Fe-S assembly proteins varied significantly in their TL over the diurnal cycle. Among these 13 transcripts, 7 correspond to mitochondrial, 5 to plastidic and one to cytosolic proteins. These transcripts clustered into two groups of similar TL profiles over the diurnal cycle (**Figure 3A**). TL of transcripts in the first cluster peaked during and at the end of the night (ZT18 or ZT0). Interestingly, 7 out of 9 transcripts in this group encode proteins associated with Fe-S cluster carriage/transfer, including mitochondrial ISCA2, ISCA4, NFU4, and GRXS15 and chloroplast SUFA, NFU1 and GRXS14. The remaining two transcripts in this cluster encode the candidate Fe donor protein mitochondrial frataxin (FH) and the alpha-helical mitochondrial ferredoxin, respectively. This ferredoxin protein is thought to provide an electron for Fe-S cluster synthesis on ISU1, the major scaffold protein in mitochondria. TL of transcripts in the second cluster peaked during the day (ZT6 or ZT12). Among the four transcripts that reached peak TL during the day, two encode plastidic cysteine desulfurase activators and interactors of CpNifS, namely SUFE2 and SUFE3 (Narayana Murthy et al., 2007). The other two transcripts encode the cytosolic Fe-S assembly scaffold protein NBP35 (Bych et al., 2008; Kohbushi et al., 2009; Bastow et al., 2017), and HSCA2, one of two abundant mitochondrial HSP70-type chaperones which was proposed to function in Fe-S cluster transfer (Balk and Pilon, 2011). The estimation of protein biosynthesis rates (PBR) (**Supplementary Figure 1A** and **Supplementary Dataset 7**) resulted in diel profiles that were similar to TL for most Fe-S assembly proteins, but considerably

TABLE 1 | Extent of diurnal regulation of translation state of Fe-S cluster-related proteins.

	Transcripts detected[a] (number of genes)	Diurnal variation in Translation State (TL)[b] (number of genes)
Fe-S cluster assembly	39	13 (33%)
Fe-S cluster use	68	13 (19%)
All functions	12,342	3,218 (26%)

[a] *Transcript levels detected as present in all ribosome-associated fractions at all four time points (Missra et al., 2015).* [b] *Number counts for transcripts exhibiting significant diurnal variation in TL according to Missra et al. (2015) (see Materials and Methods).*

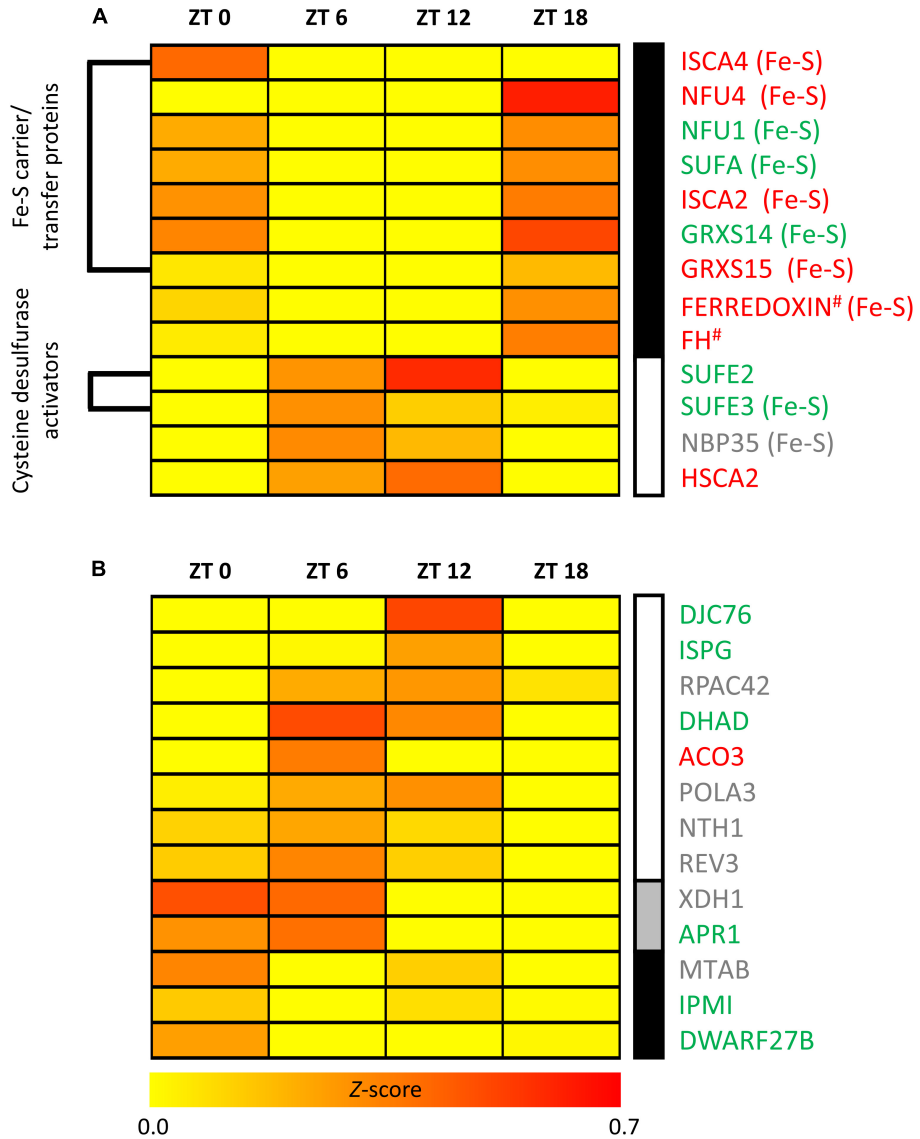

FIGURE 3 | Transcripts encoding Fe-S cluster-related proteins that exhibit significant diurnal variation in translation state. **(A)** Fe-S cluster assembly, **(B)** Fe-S cluster utilization. TL data, scaled by the mean center method for each sampling time point, were analyzed by software Genesis 1.7.6. Subsequently, the identified groups were subjected to average linkage clustering. Clusters are marked by differently shaded vertical bars (right). The translation state represents an estimate of ribosome occupancy per transcript. #Putative assembly protein. Fe-S: indicates the ability to bind an Fe-S cluster in **(A)**.

more diverse than diel TL profiles for Fe-S carrier/transfer proteins (see **Figure 3A**).

Transcripts Encoding Fe-S Proteins With Diurnal Changes in Translation State

Twenty-three transcripts encoding Fe-S proteins varied significantly in TL over the diurnal time course. Among these, 13 transcripts encode Fe-S cluster-utilizing proteins (**Figure 3B**) and 10 transcripts encode Fe-S proteins that are involved in cluster assembly and Fe-S protein biogenesis (**Figure 3A**). The 13 transcripts encoding Fe-S cluster-utilizing proteins comprised 6 plastidic, 4 nuclear, 2 cytosolic, and 1 mitochondrial localized proteins. Proteins detected to exhibit diurnal regulation of TL have various functions, in particular DNA and RNA metabolism as well as isoprenoid and leucine biosynthesis. All except two of these proteins are predicted to bind the most abundant [4Fe-4S] cluster, which is less stable than the [2Fe-2S] cluster. Only DWARF27B, a homolog of a rice β-carotene isomerase protein acting in strigolactone biosynthesis, and Xanthine the dehydrogenase XDH1 bind [2Fe-2S] clusters (Zhang et al., 2012; Balk and Schaedler, 2014). Fe-S cluster-utilizing proteins fell into three groups of differing diel TL profiles (**Figure 3B**). TL of 8 transcripts peaked during the day (ZT6 or ZT12), TL of two transcripts peaked at ZT0 and ZT6, and TL of three transcripts peaked at the end of the night (ZT0) (**Figure 3B**). TL of none

of the Fe-S cluster-utilizing proteins peaked at ZT18 during the night, in contrast to the Fe-S carrier/transfer proteins that exhibited diel TL differences (see **Figure 3A**). When, instead of TL, we considered estimates of PBR, we mostly observed no changes or only minor shifts for few proteins (**Supplementary Figure 1** and **Supplementary Dataset 8**).

Among the transcripts showing diel changes in TL, ten transcripts encode Fe-S proteins that are also involved in Fe-S protein biogenesis (see **Figure 3A**). The TL of 7 of these 10 transcripts peaked during the night (ZT18) and one peaked at the end of the night (ISCA4). Only the cytosolic Fe-S cluster scaffold protein NBP35 and SUFE3 peaked during the daytime.

Transcripts Encoding Proteins Binding Heme and Cationic Fe, Zn, Cu, or Mn With Diurnal Changes in Translation State

To compare Fe-S cluster-containing proteins with other metalloproteins, we determined the proportion showing diurnal variation in TL among proteins binding heme/cytochrome cofactors (29%) and proteins binding cationic Fe (28%), Zn (22%), Cu (30%), or Mn (39%) (**Table 2**). Among these, in comparison to all functions (26%) only Zn-dependent proteins are significantly differently represented, with an underrepresentation in contrast to the trend for over-representation of heme/cytochrome-dependent, Cu-dependent and Mn-dependent proteins. In order to compare the timing of biogenesis of metalloproteins among those exhibiting significant variation in TL over the diurnal cycle, we determined the proportion of transcripts peaking in TL at each time point (**Figure 4**). Whereas TL of 62% of transcripts encoding Fe-S cluster assembly proteins peaked at ZT18, TL of none of the transcripts encoding Fe-S cluster-utilizing proteins peaked at this time point (**Figure 4A**; statistically significantly different from all detected transcripts at $P < 0.01$, Fisher's exact test), in accordance with observations described earlier (see **Figure 3**). The diel TL profile of transcripts encoding heme/cytochrome- as well as Fe, Zn, and Cu cation-binding proteins was similar to that of all detected transcripts, with a maximum of 30–50% peaking at ZT18, a less pronounced secondary maximum of 25–42% peaking at ZT6 and a minimum of 0–17% peaking at ZT12 (**Figures 4A,B**). Notably, none of the transcripts encoding Cu-dependent proteins showed an afternoon peak in TL at ZT12 (statistically significantly different from all detected transcripts, $P < 0.05$, Fisher's exact text), and as many as 50% peaked during the night at ZT18. The diel course of TL of transcripts encoding Mn-dependent proteins differed from that of all others, with a maximum of 39% of proteins peaking at the end of the night (ZT0).

TABLE 2 | Extent of diurnal regulation of translation state of heme/cytochrome and Fe, Zn, Cu, and Mn cation-binding metalloproteins.

	Transcripts detected[a] (number of genes)	Diurnal variation in Translation State (TL)[b] (number of genes)
Fe cation-dependent	192	53 (28%)
Heme-dependent	255	74 (29%)
Zn-dependent	967	216 (22%)*
Cu-dependent	131	39 (30%)
Mn-dependent	46	18 (39%)
All functions	12,342	3,218 (26%)

[a] *Transcript levels detected as present in all ribosome-associated fractions at all four time points (Missra et al., 2015).* [b] *Number counts for transcripts exhibiting significant diurnal variation in TL according to Missra et al. (2015) (see Materials and Methods). *$P < 0.05$ (Pearson Chi-Square test).*

DISCUSSION

Here we addressed the translation state of transcripts encoding Fe-S cluster-binding proteins and other metalloproteins over a diurnal cycle. While this has not been addressed to date, previous studies have addressed the responses of various components in Fe-S cluster assembly to changed environmental conditions.

Besides oxygen (see Introduction), iron and sulfur supply were reported to affect Fe-S cluster biosynthesis. Under iron deficiency conditions, *SUFB* expression is down-regulated in both *A. thaliana* (Xu et al., 2005; Sivitz et al., 2012; Rodríguez-Celma et al., 2013) and in rice (Liang et al., 2014). Corresponding to the decreased transcript level, SUFB protein abundance is also decreased (Hantzis et al., 2018). SUFB is a component of the $SUFBC_2D$ complex which functions as a scaffold protein in the plastidic SUF pathway (Hu et al., 2017). Besides SUFB, the protein abundance of a Fe-S carrier/transfer protein SUFA was decreased under Fe deficiency, whereas *SUFA* transcript abundance was unaffected, suggesting the possibility of regulation at the translational or protein level. Recently, it was reported that S and Fe uptake are closely coordinated (Astolfi et al., 2010; Astolfi et al., 2012; Zuchi et al., 2015). This is not surprising, given that Fe-S clusters are the most abundant among all the Fe-containing cofactors (Forieri et al., 2013; Balk and Schaedler, 2014; Vigani and Briat, 2016). Fe deficiency can result in the down-regulation of transcript levels of *sulfite reductase* (*SiR*). SiR is a protein involved in sulfate assimilation (Forieri et al., 2017), which contains an Fe_4S_4 cluster itself. This response might contribute to a decreased S flux into cysteine, the only S donor for Fe-S cluster biosynthesis (Balk and Schaedler, 2014).

Light is another environmental factor known to enhance the incorporation of Fe-S clusters into Fe-S cluster-utilizing proteins of isolated chloroplasts (Takahashi et al., 1986) as well as the expression of some Fe-S cluster assembly genes. *SUFE1* transcript levels were reported to increase 2.3-fold in the light (Ye et al., 2006), and light-grown plants contained 2.5 times higher SUFE1 protein levels than dark-grown plants. Another study showed that prolonged darkness leads to significant decreases in the protein abundance of several key components in SUF pathway, including GRXS14, NFU2, NFU3, SUFA, and SUFB (Rey et al., 2017).

It was reported that the expression of major Fe homeostasis genes is under circadian regulation, such as *IRT1*, *bHLH39*, and *FER1* (Hong et al., 2013). Regulation of ferritin gene (*AtFER1*, *AtFER3,* and *AtFER4*) expression by the clock was

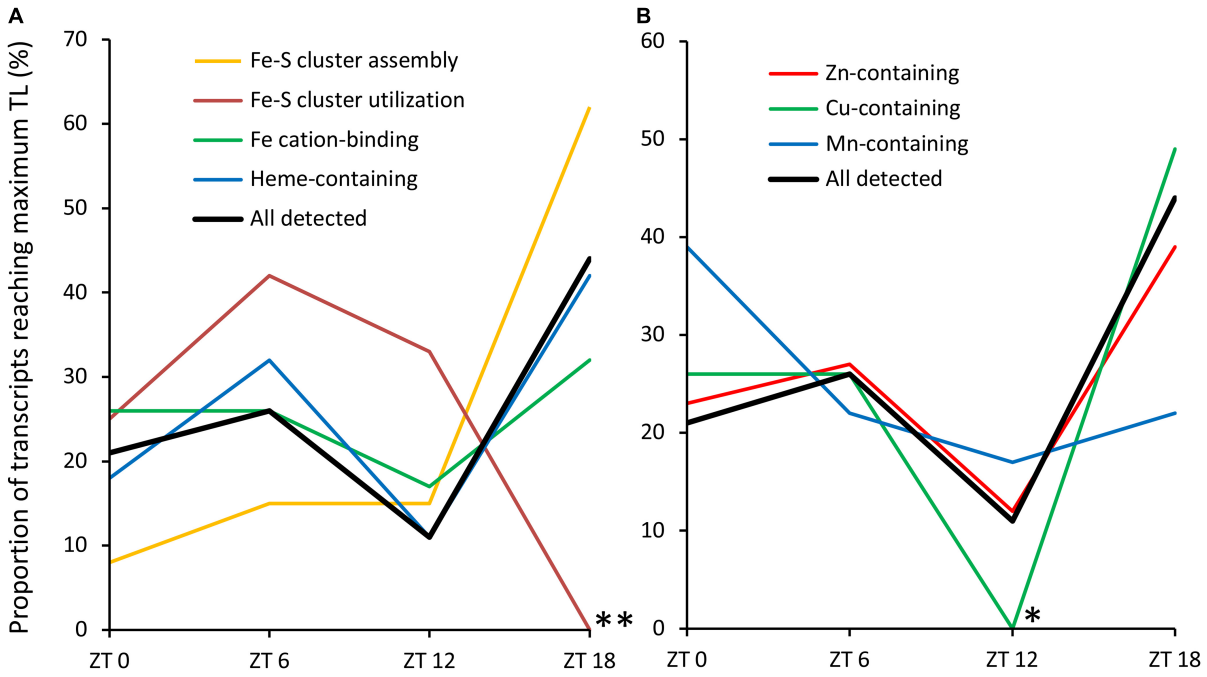

FIGURE 4 | Diurnal TL maxima of transcripts encoding metalloproteins. **(A)** Fe-dependent metalloproteins. **(B)** Other metalloproteins. Only the transcripts showing significant diurnal variation in TL were used in this analysis (see **Tables 1**, **2**). Asterisks mark significant differences from all detected transcripts at the same time point (Fisher's exact test; $*P < 0.05$, $**P < 0.01$).

confirmed by showing that they are direct transcriptional targets of PRR7, a central clock component (Liu et al., 2013). In turn, Fe nutrition status can modulate the plant circadian clock, with period lengthening under Fe-deficient conditions (Chen et al., 2013; Hong et al., 2013; Salomé et al., 2013). We observed no significant diel regulation of translation state of these transcripts (**Supplementary Dataset 9**).

TL of Transcripts Encoding Proteins in Early Steps of Fe-S Cluster Assembly and in Fe-S Cluster Transfer Show Contrary Diurnal Dynamics in Translation State

In our analysis, we separated Fe-S cluster-associated functions into Fe-S cluster assembly and Fe-S cluster utilization. By comparison to all genes detected as expressed, those with functions in Fe-S cluster assembly were slightly, ca. 1.3-fold overrepresented among the genes exhibiting diurnal variation in TL. By contrast, genes associated with Fe-S cluster utilization were slightly, ca. 0.7-fold, underrepresented (**Table 1**). Expanding this analysis, genes encoding Mn-dependent proteins were the most overrepresented, ca. 1.5-fold, among genes exhibiting diurnal variation in TL, followed by genes encoding Cu-dependent proteins (1.2-fold) (**Table 2**). The proportion of genes exhibiting diurnal variation in TL among heme/cytochrome-dependent and Fe cation-dependent proteins was similar to that of all expressed genes. It is important to note that none of these deviations were statistically significant, possibly because of a lack of sensitivity of statistical testing given the small number of genes in each of the functional classes. The only significant difference was an underrepresentation, approximately 0.85-fold, of genes encoding Zn-dependent proteins among those exhibiting significant diurnal variation in TL. The considerably larger number of genes in this class is likely to have facilitated the statistical detection of this effect. This result may reflect the high proportion of transcription factors of overall low abundance among Zn-dependent proteins, by comparison to genes encoding highly abundant proteins functioning in metabolism. Taking these results together, diel dynamics in TL are relevant for all classes of metalloproteins.

However, based on this preliminary analysis, the pervasiveness of such diel dynamics in TL among metalloproteins is similar or only slightly higher than for non-metalloproteins. Moreover, our results suggest differences between different types of metalloproteins and metalloprotein functions, with overall more pronounced diel dynamics in TL among Mn-dependent proteins and Fe-S cluster assembly proteins and overall less diel dynamics in TL among Zn-dependent proteins. Evidently, TL analyzed in this study cannot be seen as a proxy of the overall rate of protein biogenesis (PBR), which is better described by an estimate of the total amount of ribosomal occupancy on transcripts derived from a given gene in the future (e.g., in this study: $PBR_{est} = 2 \times SP + 7 \times LP$). A re-analysis of data shown in **Figure 3** suggested little difference between the diel dynamics in TL and the diel dynamics in PBR (**Supplementary Figure 1**) except for Fe-S carrier/transfer proteins, for which diel PBR profiles were rather variable.

Among the metalloprotein-encoding genes exhibiting diurnal variation in TL, we observed some striking differences in the diel profiles (**Figure 4**). The deviating profiles for Mn and, very pronouncedly, Cu-dependent metalloproteins are consistent with an overall metal-specific differentiation of TL over the diel cycle for these metals. In addition, there was a clear difference between genes encoding Fe-S cluster assembly proteins and those encoding Fe-S cluster-utilizing proteins. More than 60% of the former peaked during the night at ZT18, whereas none of the latter peaked at this time point. Instead, TL of genes encoding Fe-S cluster-utilizing proteins peaked mostly ZT6 (42%) and ZT12 (33%). A possible interpretation of this observation is the occurrence of a temporal gap between the biogenesis of Fe-S clusters and their incorporation into freshly synthesized polypeptide chains of Fe-S cluster-utilizing apo-metalloproteins.

A more detailed examination of the diel TL profiles of Fe-S cluster assembly proteins identified two distinct clusters (**Figure 3A**). The Fe-S assembly proteins in the first cluster, for which TL peaked during the night (ZT18 and to a lesser degree ZT0) mainly participate in the third step of Fe-S cluster protein biogenesis, which is Fe-S cluster transfer to target apoproteins via carrier/transfer proteins (**Figure 1**). By contrast, the three Fe-S cluster assembly proteins SUFE2, SUFE3, and NBP35 in the second cluster, which peaked during the day (ZT12 and ZT6), contribute to the first two steps of Fe-S protein biogenesis, persulfide formation and Fe-S cluster formation on the scaffold protein complex (**Figure 1**). These data suggest that some functions in Fe-S cluster synthesis and Fe-S cluster transfer to apoproteins have opposing diel dynamics of association with ribosomes. Taking all our observations together, the biosynthesis of apometalloproteins that require Fe-S clusters appears to occur preferentially during the day, as well as just before dawn for some cytosolic/nuclear Fe-S proteins (**Figure 3** and **Supplementary Figure 1**).

In contrast to cytoplasmic NBP35, the main scaffold proteins SUFB, C and D of plastids and ISU1 of mitochondria did not show diurnal dynamics at the level of translation state. In the context of the model described above, it is possible that their basal transcript levels and translation states are sufficiently high throughout the day, which can satisfy the need of Fe-S biogenesis even during the peak phase of Fe-S protein synthesis. It is worth noting that besides stimulating the cysteine desulfurase activity of NFS2 alike SUFE2 (SufE activity), SUFE3 possesses quinolinate synthase activity which is required for NAD cofactor synthesis (Narayana Murthy et al., 2007). The quinolinate synthase activity of SUFE3 is dependent on the presence of a highly oxygen-sensitive [4Fe-4S] cluster (Cicchillo et al., 2005; Ollagnier-de Choudens et al., 2005; Narayana Murthy et al., 2007). *SUFE3* cannot complement the embryo lethal phenotype of a *sufe1* knock-out mutant, suggesting the SufE activity of SUFE3 is likely dedicated to Fe-S cluster formation in its own quinolinate synthase domain (Narayana Murthy et al., 2007; Balk and Pilon, 2011).

Three mitochondrial proteins are less easily integrated into the general patterns observed here, frataxin (FH), ferredoxin and HSCA2. FH and ferredoxin are thought to have a role in the second step of Fe-S cluster assembly by analogy to human and yeast (Balk and Schaedler, 2014), but their TLs peak at night alongside the TL of several proteins with Fe-S carrier/transfer functions (see **Figure 3A**, in agreement with **Supplementary Figure 1**). FH was proposed to deliver Fe to ISU1 by direct interaction with the NFS1/ISD11/ISU1 complex in mitochondria (Balk and Schaedler, 2014). An alternative model has also been discussed in which FH promotes the interaction of the cysteine desulfurase NFS1 with the scaffold ISU proteins to favor the sulfur transfer reaction (Couturier et al., 2013). FH was reported to localize to both mitochondria and plastids (Turowski et al., 2015). HSCA1 can functionally complement the yeast *ssq1* knockout mutant and its ATPase activity is enhanced by HSCB and ISU1 (Xu et al., 2009). The role of HSCA2 in Fe-S protein biogenesis remains to be investigated. Additional and more detailed information will be required to test the possible models arising from this study. In particular also, diel variation in TL was only detected for a subset of proteins in each functional class.

Extensive Translational Cycling of Fe-S Transfer/Carrier Proteins May Be Determined by Their Specific Roles

Among the 13 Fe-S assembly proteins cycling in translation state, 7 are Fe-S carrier/transfer proteins. ISCA4, NFU4, GRXS15, and ISCA2 localize in mitochondria, whereas NFU1, SUFA, and GRXS14 are localized in plastids. So far, a number of Fe-S transfer/carrier proteins have been identified in *A. thaliana* and they are thought to form a flexible network for Fe-S cluster delivery (Couturier et al., 2013). The function of some Fe-S transfer/carrier proteins may be redundant, because knock-out mutants for most genes encoding Fe-S transfer/carrier proteins are viable (Couturier et al., 2013). For instance, plants deficient in GRXS14 or GRXS16 did not display any growth defect, whereas the growth rate of plants lacking both was reduced (Rey et al., 2017). However, some reports showed that Fe-S carrier/transfer proteins also have specificity for a particular Fe-S target protein or group of targets (Balk and Schaedler, 2014). For instance, NFU2 and HCF101 are involved in the maturation of one or several proteins belonging to PSI and some other stromal proteins (Lezhneva et al., 2004; Stöckel and Oelmüller, 2004; Touraine et al., 2004; Yabe et al., 2004). Thus, we presently cannot decide whether these 7 translationally cycling Fe-S carrier/transfer proteins may preferentially function in the biogenesis of specific Fe-S proteins.

Another feature of Fe-S carrier/transfer proteins is that they act in different manners depending on their redox environment. Mutants for some genes encoding Fe-S carrier/transfer proteins only showed lethal phenotypes specifically under oxygenic conditions. The maturation of two Fe-S proteins in *E. coli*, IspG and IspH, requires a different combination of Fe-S carrier/transfer protein isoforms under different oxygenic conditions. Under aerobic conditions, it uses IscU, IscA and then ErpA for cluster insertion into apo-IspG and apo-IspH, whereas it uses IscU and either ErpA or IscA under anaerobic conditions (Vinella et al., 2009). Another example is cytoplasmic NAR1 in eukaryotes, an Fe-S carrier/transfer protein in CIA

pathway. NAR1 forms a complex with CIA1, AE7, and MET18 to transfer Fe-S clusters from the scaffold protein NBP35 to target apoproteins. Interestingly, *nar1* mutants in plants, yeast, and nematodes display phenotypes only under normal oxygen pressure but not under low oxygen pressure (Fujii et al., 2009; Mondy et al., 2014). Therefore, the function of some Fe-S carrier/transfer proteins has a close relationship with the oxygen levels *in vivo* and *in vitro*, which might explain the existence of extensive cycling of TL of Fe-S transfer/carrier proteins over the diurnal cycle as observed here.

Open Questions and Prospects

Here we report that the TL of subsets of Fe-S assembly and Fe-S utilizing proteins, as well as of other metalloproteins, vary over a diurnal cycle. It was concluded earlier that Fe-S assembly proteins are not diurnally regulated at the transcript level (Balk and Schaedler, 2014). But there is no investigation so far into whether the rates of Fe-S protein biosynthesis are under circadian or diurnal regulation. Knowledge on the regulation of Fe-S protein biogenesis in plants grown under various regimes of temperature and photoperiod would also help us better understand the mechanisms of *de novo* synthesis or repair of Fe-S clusters (Couturier et al., 2013).

Although much progress was made in elucidating the Fe-S protein biogenesis machinery in plants in the past decades, we are still lacking plant-specific knowledge on the function of a number of predicted Fe-S cluster assembly proteins. Another issue is that the environment-dependent regulation of Fe-S cluster protein biogenesis is largely unknown. Initially, it is important to understand whether and how Fe-S cluster assembly proteins and Fe-S cluster-utilizing proteins are regulated at the transcript, translational and protein levels under various environmental conditions, such as iron and sulfur starvation and other environmental stresses known to enhance internal levels of ROS.

CONCLUSION

We assessed the translation state of Fe-S and other metal-dependent proteins genome-wide over a diurnal cycle through the re-analysis of a published microarray dataset. Our analysis suggested that there are notable and complex diel dynamics. Overall, translation state of Fe-S cluster assembly proteins peaked in the middle and at the end of the night (ZT0 and ZT18). Notably, translation state of none of the Fe-S cluster-utilizing proteins peaked during the night, and instead peaked during the day (ZT6 and ZT12). Finally, we observed a trend for peaks in translation state of transcripts encoding proteins requiring different metals at different times of the day. These observations were made only for subsets of proteins of each group. While the biological implications of these observations deserve further study, the diurnal regulation of metalloprotein biogenesis at the level of translational regulation is substantial and should be addressed in a more quantitative and comprehensive study. RNA sequencing-based methods are now available to address this biological question with far higher accuracy (Juntawong et al., 2014).

AUTHOR CONTRIBUTIONS

HZ performed all data analysis, wrote first draft of manuscript and edited manuscript. UK conceived study and edited manuscript.

FUNDING

This work was funded by the Deutsche Forshcungsgemeinschaft in SPP1927 Iron-Sulfur for Life.

ACKNOWLEDGMENTS

We thank Dr. Janneke Balk, JIC Norwich, for repeated sharing of information.

SUPPLEMENTARY MATERIAL

The Supplementary Material for this article can be found online at: https://www.frontiersin.org/articles/10.3389/fpls.2018.01641/full#supplementary-material

REFERENCES

Astolfi, S., Zuchi, S., Hubberten, H. M., Pinton, R., and Hoefgen, R. (2010). Supply of sulphur to S-deficient young barley seedlings restores their capability to cope with iron shortage. *J. Exp. Bot.* 61, 799–806. doi: 10.1093/jxb/erp346

Astolfi, S., Zuchi, S., Neumann, G., Cesco, S., Di Toppi, L. S., and Pinton, R. (2012). Response of barley plants to Fe deficiency and Cd contamination as affected by S starvation. *J. Exp. Bot.* 63, 1241–1250. doi: 10.1093/jxb/err344

Balk, J., and Lobréaux, S. (2005). Biogenesis of iron-sulfur proteins in plants. *Trends Plant Sci.* 10, 324–331. doi: 10.1016/j.tplants.2005.05.002

Balk, J., and Pilon, M. (2011). Ancient and essential: the assembly of iron-sulfur clusters in plants. *Trends Plant Sci.* 16, 218–226. doi: 10.1016/j.tplants.2010.12.006

Balk, J., and Schaedler, T. A. (2014). Iron cofactor assembly in plants. *Annu. Rev. Plant Biol.* 65, 125–153. doi: 10.1146/annurev-arplant-050213-035759

Bastow, E. L., Bych, K., Crack, J. C., Le Brun, N. E., and Balk, J. (2017). NBP35 interacts with DRE2 in the maturation of cytosolic iron-sulphur proteins in *Arabidopsis thaliana*. *Plant J.* 89, 590–600. doi: 10.1111/tpj.13409

Beinert, H., Holm, R. H., and Münck, E. (1997). Iron-sulfur clusters: nature's modular, multipurpose structures. *Science* 277, 653–659. doi: 10.1126/science.277.5326.653

Blaby-Haas, C. E., and Merchant, S. S. (2013). Iron sparing and recycling in a compartmentalized cell. *Curr. Opin. Microbiol.* 16, 677–685. doi: 10.1016/j.mib.2013.07.019

Buzas, D. M. (2016). Emerging links between iron-sulfur clusters and 5-methylcytosine base excision repair in plants. *Genes Genet. Syst.* 91, 51–62. doi: 10.1266/ggs.16-00015

Buzas, D. M., Nakamura, M., and Kinoshita, T. (2014). Epigenetic role for the conserved Fe-S cluster biogenesis protein AtDRE2 in *Arabidopsis thaliana*. *Proc. Natl. Acad. Sci. U.S.A.* 111, 13565–13570. doi: 10.1073/pnas.1404058111

Bych, K., Netz, D. J. A., Vigani, G., Bill, E., Lill, R., Pierik, A. J., et al. (2008). The essential cytosolic iron-sulfur protein Nbp35 acts without Cfd1 partner in the green lineage. *J. Biol. Chem.* 283, 35797–35804. doi: 10.1074/jbc.M807303200

Campuzano, V., Montermini, L., Molto, M. D., Pianese, L., Cossee, M., Cavalcanti, F., et al. (1996). Friedreich's ataxia: autosomal recessive disease caused by an intronic GAA triplet repeat expansion. *Science* 271, 1423–1427. doi: 10.1126/science.271.5254.1423

Chen, Y.-Y., Wang, Y., Shin, L.-J., Wu, J.-F., Shanmugam, V., Tsednee, M., et al. (2013). Iron is involved in the maintenance of circadian period length in *Arabidopsis*. *Plant Physiol.* 161, 1409–1420. doi: 10.1104/pp.112.212068

Choi, Y., Gehring, M., Johnson, L., Hannon, M., Harada, J. J., Goldberg, R. B., et al. (2002). DEMETER, a DNA glycosylase domain protein, is required for endosperm gene imprinting and seed viability in *Arabidopsis*. *Cell* 110, 33–42. doi: 10.1016/S0092-8674(02)00807-3

Cicchillo, R. M., Tu, L., Stromberg, J. A., Hoffart, L. M., Krebs, C., and Booker, S. J. (2005). *Escherichia coli* quinolinate synthetase does indeed harbor a [4Fe-4S] cluster. *J. Am. Chem. Soc.* 127, 7310–7311. doi: 10.1021/ja051369x

Couturier, J., Touraine, B., Briat, J.-F., Gaymard, F., and Rouhier, N. (2013). The iron-sulfur cluster assembly machineries in plants: current knowledge and open questions. *Front. Plant Sci.* 4:259. doi: 10.3389/fpls.2013.00259

Forieri, I., Sticht, C., Reichelt, M., Gretz, N., Hawkesford, M. J., Malagoli, M., et al. (2017). System analysis of metabolism and the transcriptome in *Arabidopsis thaliana* roots reveals differential co-regulation upon iron, sulfur and potassium deficiency. *Plant Cell Environ.* 40, 95–107. doi: 10.1111/pce.12842

Forieri, I., Wirtz, M., and Hell, R. (2013). Toward new perspectives on the interaction of iron and sulfur metabolism in plants. *Front. Plant Sci.* 4:357. doi: 10.3389/fpls.2013.00357

Fujii, M., Adachi, N., Shikatani, K., and Ayusawa, D. (2009). [FeFe]-hydrogenase-like gene is involved in the regulation of sensitivity to oxygen in yeast and nematode. *Genes Cells* 14, 457–468. doi: 10.1111/j.1365-2443.2009.01282.x

Halliwell, B., and Gutteridge, J. M. C. (1992). Biologically relevant metal ion-dependent hydroxyl radical generation. An update. *FEBS Lett.* 307, 108–112. doi: 10.1016/0014-5793(92)80911-Y

Hantzis, L. J., Kroh, G. E., Jahn, C. E., Cantrell, M., Peers, G., Pilon, M., et al. (2018). A program for iron economy during deficiency targets specific Fe proteins. *Plant Physiol.* 176, 596–610. doi: 10.1104/pp.17.01497

Hong, S., Kim, S. A., Guerinot, M. L., and McClung, C. R. (2013). Reciprocal interaction of the circadian clock with the iron homeostasis network in *Arabidopsis*. *Plant Physiol.* 161, 893–903. doi: 10.1104/pp.112.208603

Hu, X., Kato, Y., Sumida, A., Tanaka, A., and Tanaka, R. (2017). The SUFBC2D complex is required for the biogenesis of all major classes of plastid Fe-S proteins. *Plant J.* 90, 235–248. doi: 10.1111/tpj.13483

Juntawong, P., Girke, T., Bazin, J., and Bailey-Serres, J. (2014). Translational dynamics revealed by genome-wide profiling of ribosome footprints in *Arabidopsis*. *Proc. Natl. Acad. Sci. U.S.A.* 111, E203–E212. doi: 10.1073/pnas.1317811111

Kohbushi, H., Nakai, Y., Kikuchi, S., Yabe, T., Hori, H., and Nakai, M. (2009). *Arabidopsis* cytosolic Nbp35 homodimer can assemble both [2Fe-2S] and [4Fe-4S] clusters in two distinct domains. *Biochem. Biophys. Res. Commun.* 378, 810–815. doi: 10.1016/j.bbrc.2008.11.138

Lai, A. G., Doherty, C. J., Mueller-Roeber, B., Kay, S. A., Schippers, J. H. M., and Dijkwel, P. P. (2012). Circadian clock-associated 1 regulates ROS homeostasis and oxidative stress responses. *Proc. Natl. Acad. Sci. U.S.A.* 109, 17129–17134. doi: 10.1073/pnas.1209148109

Lezhneva, L., Amann, K., and Meurer, J. (2004). The universally conserved HCF101 protein is involved in assembly of [4Fe-4S]-cluster-containing complexes in *Arabidopsis thaliana* chloroplasts. *Plant J.* 37, 174–185. doi: 10.1046/j.1365-313X.2003.01952.x

Liang, X., Qin, L., Liu, P., Wang, M., and Ye, H. (2014). Genes for iron-sulphur cluster assembly are targets of abiotic stress in rice, *Oryza sativa*. *Plant Cell Environ.* 37, 780–794. doi: 10.1111/pce.12198

Lill, R. (2009). Function and biogenesis of iron-sulphur proteins. *Nature* 460, 831–838. doi: 10.1038/nature08301

Liu, T., Carlsson, J., Takeuchi, T., Newton, L., and Farré, E. M. (2013). Direct regulation of abiotic responses by the *Arabidopsis* circadian clock component PRR7. *Plant J.* 76, 101–114. doi: 10.1111/tpj.12276

Missra, A., Ernest, B., Lohoff, T., Jia, Q., Satterlee, J., Ke, K., et al. (2015). The circadian clock modulates global daily cycles of mRNA ribosome loading. *Plant Cell* 27, 2582–2599. doi: 10.1105/tpc.15.00546

Mondy, S., Lenglet, A., Cosson, V., Pelletier, S., Pateyron, S., Gilard, F., et al. (2014). GOLLUM [FeFe]-hydrogenase-like proteins are essential for plant development in normoxic conditions and modulate energy metabolism. *Plant Cell Environ.* 37, 54–69. doi: 10.1111/pce.12128

Narayana Murthy, U. M., Ollagnier-de-Choudens, S., Sanakis, Y., Abdel-Ghany, S. E., Rousset, C., Ye, H., et al. (2007). Characterization of *Arabidopsis thaliana* SufE2 and SufE3: functions in chloroplast iron-sulfur cluster assembly and NAD synthesis. *J. Biol. Chem.* 282, 18254–18264. doi: 10.1074/jbc.M701428200

Netz, D. J. A., Stith, C. M., Stümpfig, M., Köpf, G., Vogel, D., Heide, M., et al. (2012). Eukaryotic DNA polymerase require an iron-sulfur cluster for the formation of active complexes. *Nat. Chem. Biol.* 8, 125–132. doi: 10.1038/nchembio.721

Ollagnier-de Choudens, S., Loiseau, L., Sanakis, Y., Barras, F., and Fontecave, M. (2005). Quinolinate synthetase, an iron-sulfur enzyme in NAD biosynthesis. *FEBS Lett.* 579, 3737–3743. doi: 10.1016/j.febslet.2005.05.065

Py, B., and Barras, F. (2010). Building Fe–S proteins: bacterial strategies. *Nat. Rev. Microbiol.* 8, 436–446. doi: 10.1038/nrmicro2356

Ravet, K., Touraine, B., Boucherez, J., Briat, J. F., Gaymard, F., and Cellier, F. (2009). Ferritins control interaction between iron homeostasis and oxidative stress in *Arabidopsis*. *Plant J.* 57, 400–412. doi: 10.1111/j.1365-313X.2008.03698.x

Rey, P., Becuwe, N., Tourrette, S., and Rouhier, N. (2017). Involvement of *Arabidopsis* glutaredoxin S14 in the maintenance of chlorophyll content. *Plant Cell Environ.* 40, 2319–2332. doi: 10.1111/pce.13036

Roche, B., Aussel, L., Ezraty, B., Mandin, P., Py, B., and Barras, F. (2013). Iron/sulfur proteins biogenesis in prokaryotes: formation, regulation and diversity. *Biochim. Biophys. Acta* 1827, 923–937. doi: 10.1016/j.bbabio.2012.12.010

Rodríguez-Celma, J., Pan, I. C., Li, W., Lan, P., Buckhout, T. J., and Schmidt, W. (2013). The transcriptional response of *Arabidopsis* leaves to Fe deficiency. *Front. Plant Sci.* 4:276. doi: 10.3389/fpls.2013.00276

Rötig, A., de Lonlay, P., Chretien, D., Foury, F., Koenig, M., Sidi, D., et al. (1997). Aconitase and mitochondrial iron–sulphur protein deficiency in Friedreich ataxia. *Nat. Genet.* 17, 215–217. doi: 10.1038/ng1097-215

Salomé, P. A., Oliva, M., Weigel, D., and Krämer, U. (2013). Circadian clock adjustment to plant iron status depends on chloroplast and phytochrome function. *EMBO J.* 32, 511–523. doi: 10.1038/emboj.2012.330

Shultz, R. W., Tatineni, V. M., Hanley-Bowdoin, L., and Thompson, W. F. (2007). Genome-wide analysis of the core DNA replication machinery in the higher plants *Arabidopsis* and rice. *Plant Physiol.* 144, 1697–1714. doi: 10.1104/pp.107.101105

Sierla, M., Rahikainen, M., Salojärvi, J., Kangasjärvi, J., and Kangasjärvi, S. (2013). Apoplastic and chloroplastic redox signaling networks in plant stress responses. *Antioxid. Redox Signal.* 18, 2220–2239. doi: 10.1089/ars.2012.5016

Sivitz, A. B., Hermand, V., Curie, C., and Vert, G. (2012). *Arabidopsis* bHLH100 and bHLH101 control iron homeostasis via a FIT-independent pathway. *PLoS One* 7:e44843. doi: 10.1371/journal.pone.0044843

Sokal, R. R., and Michener, C. D. (1958). A statistical method for evaluating systematic relationship. *Univ. Kansas Sci. Bull.* 28, 1409–1438.

Stöckel, J., and Oelmüller, R. (2004). A novel protein for photosystem I biogenesis. *J. Biol. Chem.* 279, 10243–10251. doi: 10.1074/jbc.M309246200

Sturn, A., Quackenbush, J., and Trajanoski, Z. (2002). Genesis: cluster analysis of microarray data. *Bioinformatics* 18, 207–208. doi: 10.1093/bioinformatics/18.1.207

Takahashi, Y., Mitsui, A., Hase, T., and Matsubara, H. (1986). Formation of the iron-sulfur cluster of ferredoxin in isolated chloroplasts. *Proc. Natl. Acad. Sci. U.S.A.* 83, 2434–2437.

Touraine, B., Boutin, J. P., Marion-Poll, A., Briat, J. F., Peltier, G., and Lobréaux, S. (2004). Nfu2: a scaffold protein required for [4Fe-4S] and ferredoxin iron-sulphur cluster assembly in *Arabidopsis* chloroplasts. *Plant J.* 40, 101–111. doi: 10.1111/j.1365-313X.2004.02189.x

Trotta, A., Rahikainen, M., Konert, G., Finazzi, G., and Kangasjarvi, S. (2014). Signalling crosstalk in light stress and immune reactions in plants. *Philos. Trans. R. Soc. B Biol. Sci.* 369:20130235. doi: 10.1098/rstb.2013.0235

Turowski, V. R., Aknin, C., Maliandi, M. V., Buchensky, C., Leaden, L., Peralta, D. A., et al. (2015). Frataxin is localized to both the chloroplast

and mitochondrion and is involved in chloroplast Fe-S protein function in *Arabidopsis*. *PLoS One* 10:e0141443. doi: 10.1371/journal.pone.0141443

Tusher, V. G., Tibshirani, R., and Chu, G. (2001). Significance analysis of microarrays applied to the ionizing radiation response. *Proc. Natl. Acad. Sci. U.S.A.* 98, 5116–5121. doi: 10.1073/pnas.091062498

Vigani, G., and Briat, J.-F. (2016). Impairment of respiratory chain under nutrient deficiency in plants: does it play a role in the regulation of iron and sulfur responsive genes? *Front. Plant Sci.* 6:1185. doi: 10.3389/fpls.2015.01185

Vinella, D., Brochier-Armanet, C., Loiseau, L., Talla, E., and Barras, F. (2009). Iron-sulfur (Fe/S) protein biogenesis: phylogenomic and genetic studies of A-type carriers. *PLoS Genet.* 5:e1000497. doi: 10.1371/journal.pgen.1000497

Wachnowsky, C., Fidai, I., and Cowan, J. A. (2017). Iron–sulfur cluster biosynthesis and trafficking – impact on human disease conditions. *Metallomics* 10, 9–29. doi: 10.1039/C7MT00180K

Wöhrmann, H. J. P., Gagliardini, V., Raissig, M. T., Wehrle, W., Arand, J., Schmidt, A., et al. (2012). Identification of a DNA methylation-independent imprinting control region at the *Arabidopsis* MEDEA locus. *Genes Dev.* 26, 1837–1850. doi: 10.1101/gad.195123.112

Xu, X. M., Adams, S., Chua, N. H., and Møller, S. G. (2005). AtNAP1 represents an atypical SufB protein in *Arabidopsis* plastids. *J. Biol. Chem.* 280, 6648–6654. doi: 10.1074/jbc.M413082200

Xu, X. M., Lin, H., Latijnhouwers, M., and Møller, S. G. (2009). Dual localized AtHscB involved in iron sulfur protein biogenesis in *Arabidopsis*. *PLoS One* 4:e7662. doi: 10.1371/journal.pone.0007662

Yabe, T., Morimoto, K., Kikuchi, S., Nishio, K., Terashima, I., and Nakai, M. (2004). The *Arabidopsis* chloroplastic NifU-like protein CnfU, which can act as an iron-sulfur cluster scaffold protein, is required for biogenesis of ferredoxin and photosystem I. *Plant Cell* 16, 993–1007. doi: 10.1105/tpc.020511

Ye, H., Abdel-Ghany, S. E., Anderson, T. D., Pilon-Smits, E. A. H., and Pilon, M. (2006). CpSufE activates the cysteine desulfurase CpNifS for chloroplastic Fe-S cluster formation. *J. Biol. Chem.* 281, 8958–8969. doi: 10.1074/jbc.M512737200

Zhang, B., Crack, J. C., Subramanian, S., Green, J., Thomson, A. J., Le Brun, N. E., et al. (2012). Reversible cycling between cysteine persulfide-ligated [2Fe-2S] and cysteine-ligated [4Fe-4S] clusters in the FNR regulatory protein. *Proc. Natl. Acad. Sci. U.S.A.* 109, 15734–15739. doi: 10.1073/pnas.1208787109

Zhang, C. (2015). Involvement of iron-containing proteins in genome integrity in *Arabidopsis thaliana*. *Genome Integr.* 6:2. doi: 10.4103/2041-9414.155953

Zuchi, S., Watanabe, M., Hubberten, H.-M., Bromke, M., Osorio, S., Fernie, A. R., et al. (2015). The interplay between sulfur and iron nutrition in tomato. *Plant Physiol.* 169, 2624–2639. doi: 10.1104/pp.15.00995

Conflict of Interest Statement: The authors declare that the research was conducted in the absence of any commercial or financial relationships that could be construed as a potential conflict of interest.

frontiers in Plant Science

MINI REVIEW
published: 21 November 2018
doi: 10.3389/fpls.2018.01706

Plant Frataxin in Metal Metabolism

Diego F. Gomez-Casati, Maria V. Busi and Maria A. Pagani*

Centro de Estudios Fotosintéticos y Bioquímicos (CEFOBI-CONICET), Universidad Nacional de Rosario, Rosario, Argentina

Frataxin is a highly conserved protein from prokaryotes to eukaryotes. Several functions related to iron metabolism have been postulated for this protein, including Fe-S cluster and heme synthesis, response to oxidative damage and oxidative phosphorylation. In plants, the presence of one or two isoforms of this protein with dual localization in mitochondria and chloroplasts has been reported. Frataxin deficiency affects iron metabolism in both organelles, leading to an impairment of mitochondrial respiration, and chlorophyll and photosynthetic electron transport deficiency in chloroplasts. In addition, plant frataxins can react with Cu^{2+} ions and dimerize, which causes the reduction of free Cu ions. This could provide an additional defense mechanism against the oxidation of Fe-S groups by Cu ions. While there is a consensus on the involvement of frataxin in iron homeostasis in most organisms, the interaction of plant frataxins with Cu ions, the presence of different isoforms, and/or the localization in two plant organelles suggest that this protein might have additional functions in vegetal tissues.

Keywords: frataxin, iron, copper, Fe-S clusters, metal homeostasis

OPEN ACCESS

Edited by:
Felipe Klein Ricachenevsky, Universidade Federal de Santa Maria, Brazil

Reviewed by:
Khurram Bashir, RIKEN, Japan
Daniel H. Gonzalez, National University of the Littoral, Argentina
Joaquin Medina, Centro de Biotecnología y Genómica de Plantas (CBGP), Spain

****Correspondence:***
Diego F. Gomez-Casati
gomezcasati@cefobi-conicet.gov.ar

Specialty section:
This article was submitted to Plant Nutrition, a section of the journal Frontiers in Plant Science

Received: *30 May 2018*
Accepted: *02 November 2018*
Published: *21 November 2018*

Citation:
Gomez-Casati DF, Busi MV and Pagani MA (2018) Plant Frataxin in Metal Metabolism. Front. Plant Sci. 9:1706. doi: 10.3389/fpls.2018.01706

IRON FUNCTIONS IN PLANTS, UPTAKE AND DISTRIBUTION

Iron is an essential element for almost all life forms. It is part of cofactors that carry out electron transfer functions, and is involved in chemical transitions (e.g., hydroxylations), hydration and dehydration reactions and radical-mediated rearrangements. Iron also participates in oxygen sensing and transport, and regulation of protein stability (Connorton et al., 2017). Iron is essential for plant growth but, at the same time, is highly reactive and toxic via the Fenton reaction. Thus, plants tightly control iron homeostasis and react to both deficiency and overload of iron. Photosynthetic organisms are distinguished by a high iron requirement for the function of both mitochondria and chloroplasts. These organelles are thought to play a major role in the iron metabolism of the plant cell because this metal/ion serves as an essential cofactor for many enzymes involved in the mitochondrial respiratory chain and electron transfer in the chloroplastic photosynthetic complexes (Morrissey and Guerinot, 2009).

Plants mainly acquire iron from the rhizosphere. Although iron is one of the most abundant metals in the land surface, its availability for plant roots is very low, dependent on the soil reduction potential and pH. In soils that are aerobic or at higher pH, Fe is readily oxidized and is thus predominately in the form of insoluble ferric Fe(III) oxides. At lower pH, the ferric ion is freed from the oxide and becomes more available for uptake. Thirty percent of the world's land for cultivation is too alkaline for optimal plant growth – the most common problem is iron deficiency. Many plant foods like rice, maize, and wheat constitute poor sources of dietary iron (Takahashi et al., 2001; Walker and Connolly, 2008; Morrissey and Guerinot, 2009).

Iron uptake in plants has classically been divided into Strategy I (reducing, dicotyledonous and non-graminaceous monocots) and Strategy II (chelating, graminaceous monocots), the main

difference being the oxidation state of the iron (Romheld and Marschner, 1986). In the rhizosphere, iron is mostly found as ferric oxyhydrates of very low solubility. The participation of FRO2 (Ferric Reduction Oxidase 2), IRT1 (Iron-Regulated Transporter 1) and AHA2 (a proton pump located in plasma membrane) has been reported in Strategy I in tomato and *Arabidopsis thaliana*. Phytosiderophores (plant-derived small organic molecules with a high affinity for iron) and oligopeptide transporters participate in Strategy II in rice, maize and barley (including the iron-siderophore transporters YS1, first characterized in maize, and YSL15 in rice) (Higuchi et al., 1999; Curie et al., 2001; Inoue et al., 2009; Nozoye et al., 2011). Rice is particular among monocots because it uses Strategy II to acquire Fe from rhizosphere but also has the Strategy I-like system (Ishimaru et al., 2006). Under flooded conditions, when Fe(II) is more stable and abundant, rice also absorbs Fe(II) directly via OsIRT1 (Oryza sativa IRT1) and OsNRAMPs (Natural Resistance Associated Macrophage Proteins) (Takahashi et al., 2011). It has been reported that IRT1 has a major role in the regulation of plant iron homeostasis and it is essential for plant growth under iron-limited conditions (Vert et al., 2002). IRT1 undergoes ubiquitin-dependent endocytosis to prevent the uptake of other divalent metals such as Mn, Zn, and Co (Barberon et al., 2014; Dubeaux et al., 2015). In addition, other transporters such as several NRAMPs also participate in the uptake of iron, but as a low-affinity systems (Curie et al., 2000; Castaings et al., 2016).

Several phenylpropanoid-pathway enzymes are upregulated under iron deficiency in *Arabidopsis* such as PAL1, PAL2 (two Phe ammonia-lyases), 4CL1 and 4CL2 (two 4-coumarate:CoA ligases), the ABC transporter PDR9 (responsible for coumarin secretion into the rhizosphere) and MAT3 (an enzyme that produces *S*-adenosyl methionine which is involved in coumarin biosynthesis) (Lan et al., 2011; Rodriguez-Celma et al., 2013; Mai et al., 2016). It has been demonstrated that the phenolic compounds secreted facilitate Fe(III) availability for the FRO2 reductase to generate Fe(II) which is transported by IRT1 (Fourcroy et al., 2016). This suggests that these phenolic compounds are important in/for Strategy I iron uptake and are also involved in iron mobilization from insoluble pools (soil) or root apoplast (Fourcroy et al., 2014; Schmid et al., 2014). The catecholic coumarins found at the highest levels in the exudates of iron-deficient wild-type *Arabidopsis* are esculetin, fraxetin, scopoletin, and sideretin (Fourcroy et al., 2014; Schmid et al., 2014). Fraxetin is the major coumarin exuded into the rhizosphere in response to iron deficiency in alkaline conditions, while sideretin is exuded in acidic conditions. Fraxetin and sideretin are synthesized from scopoletin by hydroxylases [2-ODD (S8H)], which generates fraxetin, and a cytochrome P450 (CYP82C4), which oxidizes fraxetin to generate sideretin) and both compounds efficiently mobilize and reduce insoluble Fe(III), rescuing the chlorotic phenotypes (Rajniak et al., 2018). To date, most efforts in understanding soil iron-uptake limitations have focused on the role of soil pH and have ignored other potentially relevant factors such as interactions with soil organic matter or other metals such as Zn(II) or Mn(II) (Rajniak et al., 2018).

Because of its low solubility and high toxicity, iron must form complexes with chelators to be translocated without causing damage by redox reactions (Dubeaux et al., 2015). One of the complexes necessary for transport by the symplast occurs between the reduced form of iron (Fe^{2+}) and nicotianamine, a non-protein amino acid produced by nicotianamine synthase (Inoue et al., 2003; Klatte et al., 2009; Rellan-Alvarez et al., 2010), which also chelates other divalent cations (e.g., Zn^{2+}). Once iron has passed the endodermis, it is taken into the xylem to reach the shoot. The dominant form of iron in the xylem is Fe^{3+} bound to citrate and, therefore, the flow of citrate is essential for iron translocation (Rellan-Alvarez et al., 2010). This translocation is mediated by the efflux transporter FRD3 in *Arabidopsis* (Green and Rogers, 2004) and its ortholog FRDL1 in rice (Yokosho et al., 2016).

The leaves are the main receptor organ for iron because they are where it is needed for photosynthesis. Here, iron re-enters the symplast by the action of FRO proteins (Finazzi et al., 2015; Bashir et al., 2016). Subsequently, it can be remobilized and arrives at other sink organs through the phloem, where it is mainly transported as Fe(II)- nicotianamine complexes. In *Arabidopsis*, OPT3 (of the oligopeptide transporter family protein) is involved in this process (Mendoza-Cozatl et al., 2014; Zhai et al., 2014). The seed is considered the final destination of iron, where iron reserves are fundamental for germination. The YSL transporters are involved in the iron loading of the seeds (Le Jean et al., 2005).

Mitochondria and chloroplasts represent major iron sinks within cells, as iron is required for the proper functioning of the respiratory chain and photosynthetic protein complexes. The mechanisms by which Fe is obtained by chloroplasts and mitochondria are not as well-known as iron uptake at the root epidermis. There is evidence of reduction-based mechanisms for chloroplast and mitochondria Fe-acquisition, since the presence of FRO7 and FRO3/FRO8 has been reported in each organelle (Jeong et al., 2008). A mitochondrial iron transporter, which belongs to the mitochondrial carrier family (MCF) also present in yeast, zebrafish, humans, and *Drosophila*, was identified in rice and named MIT (Bashir et al., 2011). The protein PIC1 (Permease In Chloroplasts 1) was the first molecular component involved in plastid Fe-transport identified in *Arabidopsis* and tobacco (Duy et al., 2007; Gong et al., 2015). In addition, other proteins are supposed to participate in Fe transport across the chloroplast envelope, including two transporters from the yellow stripe 1-like family, YSL4 and YSL6, which have been characterized as potential plastid Fe-efflux transporters in *Arabidopsis* (Divol et al., 2013). However, in summary, mitochondrial and chloroplast iron transport is till far from being completely deciphered, nor it is understood their cross talk regarding iron homeostasis.

BIOSYNTHESIS OF IRON COFACTORS: THE PARTICIPATION OF FRATAXIN

Iron is an important component of Fe-S clusters found in many ferrosulfoproteins. Three different systems capable of mediating

Fe-S cluster assembly have been identified: NIF (nitrogen fixation) found in azeotropic bacteria, SUF (mobilization of sulfur) found in archaea, bacteria and plastids, and ISC (iron-sulfur cluster) present in bacteria and mitochondria (Romheld and Marschner, 1983; Patzer and Hantke, 1999; Dos Santos et al., 2004; Lill and Muhlenhoff, 2008; Morrissey and Guerinot, 2009; Balk and Pilon, 2011). These systems have in common three steps: (i) the production of sulfur from cysteine, catalyzed by a cysteine desulfurase; (ii) the assembly of Fe-S clusters onto scaffold proteins; and (iii) the transfer of the mature Fe-S cluster into an apoprotein. It has been reported that a small mitochondrial protein, frataxin, could be involved in several steps of this process (Balk and Lobreaux, 2005; Lill and Muhlenhoff, 2008; Lillig and Lill, 2009; Balk and Pilon, 2011; Turowski et al., 2012).

Frataxin is a nuclear-encoded mitochondrial protein whose deficiency is the cause of Friedreich's ataxia, a hereditary cardio- and neurodegenerative disease in humans. This protein plays a role in Fe-S cluster biosynthesis, protection against oxidative stress and iron metabolism. Frataxin is highly conserved throughout evolution, being present in humans, plants, flies, worms, and bacteria (Gibson et al., 1996; Babcock et al., 1997; Adinolfi et al., 2002; Busi and Gomez-Casati, 2012; Han et al., 2017). Some hints about frataxin function can be gleaned from the evolutionary record (Morrissey and Guerinot, 2009). The appearance of frataxin in eukaryotes occurred about the time of the endosymbiotic event creating mitochondria from the purple bacterial ancestor, and it was probably acquired by mitochondria together with other components of the *ISC* operon (Waters et al., 2007; Morrissey and Guerinot, 2009). Different organisms developed mechanisms to avoid the toxicity of free metal ions that allow the control of their uptake, storage and release. It was postulated that frataxin potentially fulfills some of these functions (Busi and Gomez-Casati, 2012).

In 2004, we identified the first frataxin protein in a photosynthetic organism, *A. thaliana* (Busi et al., 2004, 2006). The functionality of AtFH was assessed by complementation of a yeast frataxin-null mutant, suggesting that AtFH was involved in plant mitochondrial respiration and stress responses (Busi et al., 2004). In agreement with this hypothesis, AtFH-deficient plants presented retarded growth, showed an increment of reactive oxygen species (ROS) and an induction of oxidative stress markers. Interestingly, we also found an increment of aconitase and succinate dehydrogenase-2 (SDH2-1) transcripts, both coding for mitochondrial Fe-S-containing proteins. The reduction of the activities of both enzymes indicates that AtFH also participates in Fe-S cluster assembly or the insertion of Fe-S clusters into apoproteins, possibly in cooperation with other proteins such as Nfs1, HscB, Isd11, and Isu (among others), by the formation of a multiprotein complex (Gonzalez-Cabo et al., 2005; Busi et al., 2006; Maliandi et al., 2007; Shan et al., 2007; Shan and Cortopassi, 2012; Turowski et al., 2012; Leaden et al., 2014; **Figure 1**). Consistent with the essential role of AtFH in cellular function is the observation that homozygous null mutants result in a lethal phenotype (Busi et al., 2004, 2006; Vazzola et al., 2007; Martin et al., 2009). Our data also substantiate the hypothesis that AtFH, apart from its role in protecting bioavailable iron within mitochondria and the biogenesis of Fe-S groups, plays a role in the biosynthesis of heme in plants (Maliandi et al., 2011). We have shown, by *in vitro* experiments, that AtFH catalyzes the formation of heme when it is incubated with Fe(II) and protoporphyrin IX (Armas et al., 2019). Despite plant ferrochelatases are only present in chloroplasts (Lister et al., 2001; Masuda et al., 2003), a modest but detectable ferrochelatase activity has been observed in plant mitochondria (Cornah et al., 2002), pointing toward frataxin as the enzyme responsible for the reaction in this organelle.

We have reported that in *Arabidopsis*, AtFH is dual-targeted to mitochondria and chloroplasts (Turowski et al., 2015) and its deficiency alters the normal functioning of chloroplasts by affecting the levels of Fe, chlorophyll, and Fe-S proteins, suggesting that AtFH plays a role as a modulator of both the mitochondrial ISC and chloroplast SUF systems (Turowski et al., 2015; **Figure 1**). In AtFH deficient plants, we also found a reduction of about 40% in ferredoxin levels and about 30% in nitrite reductase (a chloroplastic Fe-S-containing protein) activity (Turowski et al., 2015). Thus, it is possible that plant frataxins play similar roles in the two organelles, as iron donors, regulating the activity of Fe-S proteins, and, possibly, modulating the activity of the ISC and SUF systems.

Although we identified only one frataxin gene in *A. thaliana*, other plants could have at least two isoforms (Murgia et al., 2009). Recently, we reported the presence of two functional frataxin isoforms in *Zea mays*, ZmFH-1 and ZmFH-2, located in both, mitochondria and chloroplasts (Buchensky et al., 2017). The biochemical, biophysical and physiological studies showed some differences between the two isoforms in protection against oxidants, aggregation state and expression patterns. ZmFH-1 showed to be more efficient against oxidative damage and it is expressed in a higher extent in almost all tissues respect to ZmFH-2. Furthermore, ZmFH-2 undergoes some conformational changes when exposed to air, possibly due to a C-terminal extension that could give high thermodynamic stability to the protein in comparison to ZmFH-1 (Buchensky et al., 2017; Sanchez et al., 2018). These results suggest that the two proteins play similar but not identical roles in plant cell metabolism.

In some cases, frataxin assembly seems to be a consequence of iron incorporation into the protein. The assembly of yeast frataxin, for instance, seems to be driven by iron oxidation and accumulation by iron core formation, whereas iron core degradation results in protein disassembly (Adamec et al., 2000; Aloria et al., 2004). Human frataxin assembly has been proposed to be a means of detoxifying redox-active iron. However, in the case of human frataxin, iron does not seem to be the main factor for assembly and it was postulated that the assembly is a physiological property of the protein that allows it to perform diverse cellular functions (O'Neill et al., 2005a,b).

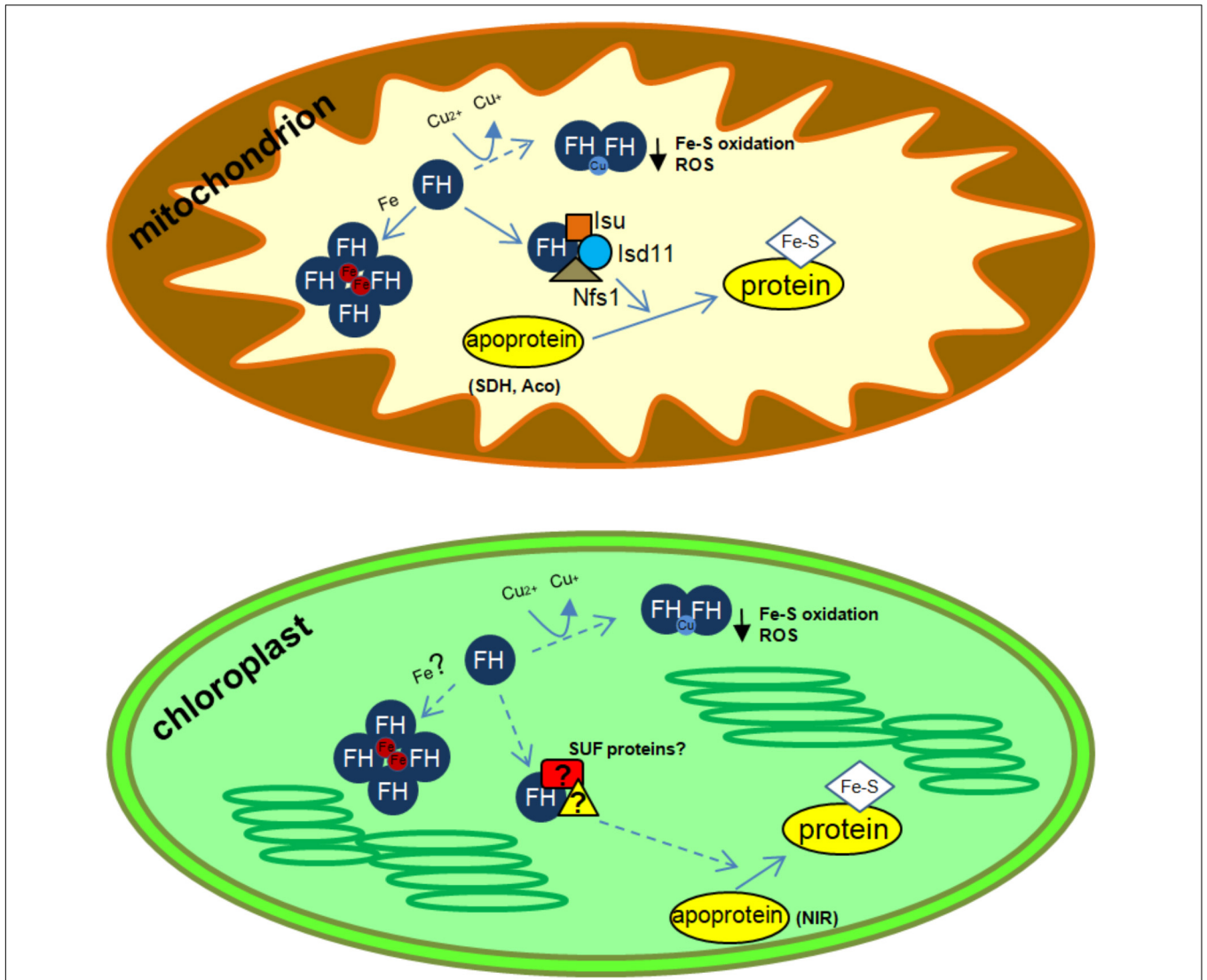

FIGURE 1 | Schematics of possible frataxin functions in plant organelles. ROS, reactive oxygen species; SDH, succinate dehydrogenase; Aco, aconitase; NIR, nitrite reductase. In mitochondria, frataxin increase Nfs1 activity and could also be involved in several additional functions related to iron and copper metabolism (iron storage, Fe-S protein maturation and prevention of ROS formation after Cu reduction). In chloroplasts, frataxin could be involved in metal metabolism and Fe-S synthesis, possibly by the interaction with proteins from the SUF system. In addition, frataxin could also be involved in Cu reduction and response to Fe-S cluster oxidation and in the prevention of ROS accumulation. Known frataxin functions are indicated with solid arrows, whereas possible functions are indicated with dashed arrows.

FRATAXIN AND COPPER

Cu is a trace element necessary for many different processes in plants. More than 50% of Cu present in plants is found in chloroplasts, which underscores the need for Cu in photosynthesis (Raldugina et al., 2016). The major Cu protein is plastocyanin, which is an essential component of the electron transport chain of photosystem I (Schubert et al., 2002; Kramer and Clemens, 2006). Plant mitochondria also require Cu for the assembly and function of cytochrome *c* oxidase, the terminal enzyme of the respiratory chain, among other Cu proteins (Garcia et al., 2014). Nevertheless, free copper ions are dangerous inside cells since they can directly attack functional sites in proteins or induce ROS production through Fenton and Haver–Weiss reactions (Halliwell, 2006). As a result, many protective mechanisms exist, such as Cu metallochaperones (Robinson and Winge, 2010), low molecular weight thiol ligands such as glutathione, and the mitochondrial anionic compound known as copper ligand (or CuL) described in yeast (Cobine et al., 2004). Still, Cu is toxic when present in excess, probably because these housekeeping defense mechanisms are overwhelmed.

Copper toxicity has classically been associated with ROS production and oxidative damage. However, more recent evidence shows that damage and inhibition of Fe-S metabolism is the more likely initial manifestation of Cu toxicity (Dupont et al., 2011). Dehydratase family enzymes are rapidly inactivated

upon exposure of *Escherichia coli* cells to low micromolar copper levels due to the displacement of iron atoms from their solvent-exposed Fe-S clusters (Macomber et al., 2007). Copper stress in *Bacillus subtilis* leads to enhanced expression of Fe-S cluster scaffold (SufU) and many Fe-S proteins, as well as iron and sulfur uptake pathways (Chillappagari et al., 2010). Additional work performed *in vitro* confirms that mammalian ISCA1/2 and GLRX5 Fe-S clusters are destabilized by the presence of Cu(I) (Brancaccio et al., 2017).

De novo Fe-S cluster biogenesis in plants occurs in chloroplasts and mitochondria and as we mentioned above, plant frataxins are located in both organelles (Turowski et al., 2015; Buchensky et al., 2017). We have shown that frataxins can react *in vitro* with the free cupric ion to give the cuprous form (Sanchez et al., 2018). In this reaction, the conserved cysteine residue of frataxin is oxidized forming a disulfide bridge with another frataxin unit (Buchensky et al., 2017). Moreover, plant frataxins oxidized and in their dimeric form (AtFH and ZmFH2) can bind free Cu(I) ions (Sanchez et al., 2018). Frataxin oxidation and the resulting dimerization might be necessary to bring together enough ligands for the cuprous ion. Cu(I) binding sites are dominated by amino acids with sulfur ligands like cysteine and methionine, but histidine can also bind Cu(I), although less tightly. The cuprous ion is coordinated by 2, 3, or 4 ligands, and proteins involved in copper resistance tend to have a coordination environment of low affinity and high coordination number (usually 4) (Rubino and Franz, 2012). AtFH and ZmFH-2 contain three histidine and two methionine residues (the cysteine residue is oxidized and unable to bind copper). Among the potential plant frataxin Cu(I) ligands, two histidine residues are relatively close (seven and eight amino acids apart in ZmFH-2 and AtFH, respectively). In this manner, a plant frataxin dimer might fulfill the requirements of four low-affinity ligands for a Cu(I) ion. The reaction observed *in vitro* might reasonably occur *in vivo*, with concomitant reduction of free copper ions, hence protecting the Fe-S clusters in plants. In this way, frataxins could comprise an additional defense for Fe-S clusters in the presence of excess copper (**Figure 1**).

There is additional evidence from different organisms that frataxin might be involved in copper metabolism. Friedreich's ataxia patients show altered Cu distribution in the dentate nucleus of the central nervous system (Koeppen et al., 2012), and in the *Drosophila* model of the disease there is a generalized increase in copper content (Soriano et al., 2016), as there is in mitochondria of yeast frataxin-null mutants (Han et al., 2017). Moreover, in frataxin knockdown flies, treatment with copper chelators improved their impaired motor performance without altering the iron accumulation phenotype, implying a direct role of Cu in the pathophysiology of the disease (Soriano et al., 2016).

Saccharomyces cerevisiae frataxin-null mutants are more sensitive to Cu than wild-type cells (Foury and Cazzalini, 1997; Han et al., 2017) and in anaerobic growth conditions, in which little oxygen is available for ROS generation, copper accumulation and its toxicity increases (Strain and Culotta, 1996; Outten et al., 2001). Ha-Duong and coworkers have shown that yeast frataxin can bind Cu(II) and Cu(I) ions, with higher affinities than iron (Han et al., 2017). Thus, we might assume that yeast frataxin protects Fe-S clusters from copper toxicity by preventing free Cu ions from interacting with them in the same way we have suggested for plant frataxins. Yeast complementation assays with plant frataxins support this hypothesis. *Arabidopsis* and maize frataxins can completely restore the ability of a *S. cerevisiae* frataxin-null strain to grow in high copper medium (Sanchez et al., 2018), which led us to infer that plant and yeast frataxins might perform similar and conserved molecular functions in copper metabolism.

AUTHOR CONTRIBUTIONS

DG-C, MB, and MP collaborated in the writing of the manuscript.

FUNDING

This work was supported by grants from ANPCyT (PICT 2014-2184/2016-350/2016-0264). DG-C, MB, and MP are research members of CONICET.

REFERENCES

Adamec, J., Rusnak, F., Owen, W. G., Naylor, S., Benson, L. M., Gacy, A. M., et al. (2000). Iron-dependent self-assembly of recombinant yeast frataxin: implications for Friedreich ataxia. *Am. J. Hum. Genet.* 67, 549–562. doi: 10.1086/303056

Adinolfi, S., Trifuoggi, M., Politou, A. S., Martin, S., and Pastore, A. (2002). A structural approach to understanding the iron-binding properties of phylogenetically different frataxins. *Hum. Mol. Genet.* 11, 1865–1877. doi: 10.1093/hmg/11.16.1865

Aloria, K., Schilke, B., Andrew, A., and Craig, E. A. (2004). Iron-induced oligomerization of yeast frataxin homologue Yfh1 is dispensable in vivo. *EMBO Rep.* 5, 1096–1101. doi: 10.1038/sj.embor.7400272

Armas, A. M., Balparda, M., Terenzi, A., Busi, M. V., Pagani, M. A., and Gomez-Casati, D. F. (2019). Ferrochelatase activity of plant frataxin. *Biochimie* 156, 118–122. doi: 10.1016/j.biochi.2018.10.009

Babcock, M., De Silva, D., Oaks, R., Davis-Kaplan, S., Jiralerspong, S., Montermini, L., et al. (1997). Regulation of mitochondrial iron accumulation by Yfh1p, a putative homolog of frataxin. *Science* 276, 1709–1712. doi: 10.1126/science.276.5319.1709

Balk, J., and Lobreaux, S. (2005). Biogenesis of iron-sulfur proteins in plants. *Trends Plant Sci.* 10, 324–331. doi: 10.1016/j.tplants.2005.05.002

Balk, J., and Pilon, M. (2011). Ancient and essential: the assembly of iron-sulfur clusters in plants. *Trends Plant Sci.* 16, 218–226. doi: 10.1016/j.tplants.2010.12.006

Barberon, M., Dubeaux, G., Kolb, C., Isono, E., Zelazny, E., and Vert, G. (2014). Polarization of IRON-REGULATED TRANSPORTER 1 (IRT1) to the plant-soil interface plays crucial role in metal homeostasis. *Proc. Natl. Acad. Sci. U.S.A.* 111, 8293–8298. doi: 10.1073/pnas.1402262111

Bashir, K., Ishimaru, Y., Shimo, H., Nagasaka, S., Fujimoto, M., Takanashi, H., et al. (2011). The rice mitochondrial iron transporter is essential for plant growth. *Nat. Commun.* 2:322. doi: 10.1038/ncomms1326

Bashir, K., Rasheed, S., Kobayashi, T., Seki, M., and Nishizawa, N. K. (2016). Regulating subcellular metal homeostasis: the key to crop improvement. *Front. Plant Sci.* 7:1192. doi: 10.3389/fpls.2016.01192

Brancaccio, D., Gallo, A., Piccioli, M., Novellino, E., Ciofi-Baffoni, S., and Banci, L. (2017). [4Fe-4S] cluster assembly in mitochondria and its impairment by copper. *J. Am. Chem. Soc.* 139, 719–730. doi: 10.1021/jacs.6b09567

Buchensky, C., Sanchez, M., Carrillo, M., Palacios, O., Capdevila, M., Dominguez-Vera, J. M., et al. (2017). Identification of two frataxin isoforms in *Zea mays*: structural and functional studies. *Biochimie* 140, 34–47. doi: 10.1016/j.biochi.2017.06.011

Busi, M. V., and Gomez-Casati, D. F. (2012). Exploring frataxin function. *IUBMB Life* 64, 56–63. doi: 10.1002/iub.577

Busi, M. V., Maliandi, M. V., Valdez, H., Clemente, M., Zabaleta, E. J., Araya, A., et al. (2006). Deficiency of *Arabidopsis thaliana* frataxin alters activity of mitochondrial Fe-S proteins and induces oxidative stress. *Plant J.* 48, 873–882. doi: 10.1111/j.1365-313X.2006.02923.x

Busi, M. V., Zabaleta, E. J., Araya, A., and Gomez-Casati, D. F. (2004). Functional and molecular characterization of the frataxin homolog from *Arabidopsis thaliana*. *FEBS Lett.* 576, 141–144. doi: 10.1016/j.febslet.2004.09.003

Castaings, L., Caquot, A., Loubet, S., and Curie, C. (2016). The high-affinity metal transporters NRAMP1 and IRT1 team up to take up iron under sufficient metal provision. *Sci. Rep.* 6:37222. doi: 10.1038/srep37222

Chillappagari, S., Seubert, A., Trip, H., Kuipers, O. P., Marahiel, M. A., and Miethke, M. (2010). Copper stress affects iron homeostasis by destabilizing iron-sulfur cluster formation in *Bacillus subtilis*. *J. Bacteriol.* 192, 2512–2524. doi: 10.1128/JB.00058-10

Cobine, P. A., Ojeda, L. D., Rigby, K. M., and Winge, D. R. (2004). Yeast contain a non-proteinaceous pool of copper in the mitochondrial matrix. *J. Biol. Chem.* 279, 14447–14455. doi: 10.1074/jbc.M312693200

Connorton, J. M., Balk, J., and Rodriguez-Celma, J. (2017). Iron homeostasis in plants - a brief overview. *Metallomics* 9, 813–823. doi: 10.1039/c7mt00136c

Cornah, J. E., Roper, J. M., Pal Singh, D., and Smith, A. G. (2002). Measurement of ferrochelatase activity using a novel assay suggests that plastids are the major site of haem biosynthesis in both photosynthetic and non-photosynthetic cells of pea (*Pisum sativum* L.). *Biochem. J.* 362, 423–432. doi: 10.1042/bj3620423

Curie, C., Alonso, J. M., Le Jean, M., Ecker, J. R., and Briat, J. F. (2000). Involvement of NRAMP1 from *Arabidopsis thaliana* in iron transport. *Biochem. J.* 347(Pt 3), 749–755. doi: 10.1042/bj3470749

Curie, C., Panaviene, Z., Loulergue, C., Dellaporta, S. L., Briat, J. F., and Walker, E. L. (2001). Maize yellow stripe1 encodes a membrane protein directly involved in Fe(III) uptake. *Nature* 409, 346–349. doi: 10.1038/35053080

Divol, F., Couch, D., Conejero, G., Roschzttardtz, H., Mari, S., and Curie, C. (2013). The *Arabidopsis* YELLOW STRIPE LIKE4 and 6 transporters control iron release from the chloroplast. *Plant Cell* 25, 1040–1055. doi: 10.1105/tpc.112.107672

Dos Santos, P. C., Dean, D. R., Hu, Y., and Ribbe, M. W. (2004). Formation and insertion of the nitrogenase iron-molybdenum cofactor. *Chem. Rev.* 104, 1159–1173. doi: 10.1021/cr020608l

Dubeaux, G., Zelazny, E., and Vert, G. (2015). Getting to the root of plant iron uptake and cell-cell transport: polarity matters! *Commun. Integr. Biol.* 8:e1038441. doi: 10.1080/19420889.2015.1038441

Dupont, C. L., Grass, G., and Rensing, C. (2011). Copper toxicity and the origin of bacterial resistance–new insights and applications. *Metallomics* 3, 1109–1118. doi: 10.1039/c1mt00107h

Duy, D., Wanner, G., Meda, A. R., Von Wiren, N., Soll, J., and Philippar, K. (2007). PIC1, an ancient permease in Arabidopsis chloroplasts, mediates iron transport. *Plant Cell* 19, 986–1006. doi: 10.1105/tpc.106.047407

Finazzi, G., Petroutsos, D., Tomizioli, M., Flori, S., Sautron, E., Villanova, V., et al. (2015). Ions channels/transporters and chloroplast regulation. *Cell Calcium* 58, 86–97. doi: 10.1016/j.ceca.2014.10.002

Fourcroy, P., Siso-Terraza, P., Sudre, D., Saviron, M., Reyt, G., Gaymard, F., et al. (2014). Involvement of the ABCG37 transporter in secretion of scopoletin and derivatives by *Arabidopsis* roots in response to iron deficiency. *New Phytol.* 201, 155–167. doi: 10.1111/nph.12471

Fourcroy, P., Tissot, N., Gaymard, F., Briat, J. F., and Dubos, C. (2016). Facilitated Fe nutrition by phenolic compounds excreted by the *Arabidopsis* ABCG37/PDR9 transporter requires the IRT1/FRO2 high-affinity root Fe^{2+} transport system. *Mol. Plant* 9, 485–488. doi: 10.1016/j.molp.2015.09.010

Foury, F., and Cazzalini, O. (1997). Deletion of the yeast homologue of the human gene associated with Friedreich's ataxia elicits iron accumulation in mitochondria. *FEBS Lett.* 411, 373–377. doi: 10.1016/S0014-5793(97)00734-5

Garcia, L., Welchen, E., and Gonzalez, D. H. (2014). Mitochondria and copper homeostasis in plants. *Mitochondrion* 19(Pt B), 269–274. doi: 10.1016/j.mito.2014.02.011

Gibson, T. J., Koonin, E. V., Musco, G., Pastore, A., and Bork, P. (1996). Friedreich's ataxia protein: phylogenetic evidence for mitochondrial dysfunction. *Trends Neurosci.* 19, 465–468. doi: 10.1016/S0166-2236(96)20054-2

Gong, X., Guo, C., Terachi, T., Cai, H., and Yu, D. (2015). Tobacco PIC1 mediates iron transport and regulates chloroplast development. *Plant Mol. Biol. Rep.* 33, 401–413. doi: 10.1007/s11105-014-0758-5

Gonzalez-Cabo, P., Vazquez-Manrique, R. P., Garcia-Gimeno, M. A., Sanz, P., and Palau, F. (2005). Frataxin interacts functionally with mitochondrial electron transport chain proteins. *Hum. Mol. Genet.* 14, 2091–2098. doi: 10.1093/hmg/ddi214

Green, L. S., and Rogers, E. E. (2004). *FRD3* controls iron localization in Arabidopsis. *Plant Physiol.* 136, 2523–2531. doi: 10.1104/pp.104.045633

Halliwell, B. (2006). Reactive species and antioxidants. Redox biology is a fundamental theme of aerobic life. *Plant Physiol.* 141, 312–322. doi: 10.1104/pp.106.077073

Han, T. H. L., Camadro, J. M., Santos, R., Lesuisse, E., El Hage Chahine, J. M., and Ha-Duong, N. T. (2017). Mechanisms of iron and copper-frataxin interactions. *Metallomics* 9, 1073–1085. doi: 10.1039/c7mt00031f

Higuchi, K., Suzuki, K., Nakanishi, H., Yamaguchi, H., Nishizawa, N. K., and Mori, S. (1999). Cloning of nicotianamine synthase genes, novel genes involved in the biosynthesis of phytosiderophores. *Plant Physiol.* 119, 471–480. doi: 10.1104/pp.119.2.471

Inoue, H., Higuchi, K., Takahashi, M., Nakanishi, H., Mori, S., and Nishizawa, N. K. (2003). Three rice nicotianamine synthase genes, OsNAS1, OsNAS2, and OsNAS3 are expressed in cells involved in long-distance transport of iron and differentially regulated by iron. *Plant J.* 36, 366–381. doi: 10.1046/j.1365-313X.2003.01878.x

Inoue, H., Kobayashi, T., Nozoye, T., Takahashi, M., Kakei, Y., Suzuki, K., et al. (2009). Rice OsYSL15 is an iron-regulated iron(III)-deoxymugineic acid transporter expressed in the roots and is essential for iron uptake in early growth of the seedlings. *J. Biol. Chem.* 284, 3470–3479. doi: 10.1074/jbc.M806042200

Ishimaru, Y., Suzuki, M., Tsukamoto, T., Suzuki, K., Nakazono, M., Kobayashi, T., et al. (2006). Rice plants take up iron as an Fe^{3+}-phytosiderophore and as Fe^{2+}. *Plant J.* 45, 335–346. doi: 10.1111/j.1365-313X.2005.02624.x

Jeong, J., Cohu, C., Kerkeb, L., Pilon, M., Connolly, E. L., and Guerinot, M. L. (2008). Chloroplast Fe(III) chelate reductase activity is essential for seedling viability under iron limiting conditions. *Proc. Natl. Acad. Sci. U.S.A.* 105, 10619–10624. doi: 10.1073/pnas.0708367105

Klatte, M., Schuler, M., Wirtz, M., Fink-Straube, C., Hell, R., and Bauer, P. (2009). The analysis of Arabidopsis nicotianamine synthase mutants reveals functions for nicotianamine in seed iron loading and iron deficiency responses. *Plant Physiol.* 150, 257–271. doi: 10.1104/pp.109.136374

Koeppen, A. H., Ramirez, R. L., Yu, D., Collins, S. E., Qian, J., Parsons, P. J., et al. (2012). Friedreich's ataxia causes redistribution of iron, copper, and zinc in the dentate nucleus. *Cerebellum* 11, 845–860. doi: 10.1007/s12311-012-0383-5

Kramer, U., and Clemens, S. (2006). Functions and homeostasis of zinc, copper, and nickel in plants. *Curr. Genet.* 14, 215–271. doi: 10.1007/4735_96

Lan, P., Li, W., Wen, T. N., Shiau, J. Y., Wu, Y. C., Lin, W., et al. (2011). iTRAQ protein profile analysis of Arabidopsis roots reveals new aspects critical for iron homeostasis. *Plant Physiol.* 155, 821–834. doi: 10.1104/pp.110.169508

Le Jean, M., Schikora, A., Mari, S., Briat, J. F., and Curie, C. (2005). A loss-of-function mutation in AtYSL1 reveals its role in iron and nicotianamine seed loading. *Plant J.* 44, 769–782. doi: 10.1111/j.1365-313X.2005.02569.x

Leaden, L., Busi, M. V., and Gomez-Casati, D. F. (2014). The mitochondrial proteins AtHscB and AtIsu1 involved in Fe-S cluster assembly interact with the Hsp70-type chaperon AtHscA2 and modulate its catalytic activity. *Mitochondrion* 19(Pt B), 375–381. doi: 10.1016/j.mito.2014.11.002

Lill, R., and Muhlenhoff, U. (2008). Maturation of iron-sulfur proteins in eukaryotes: mechanisms, connected processes, and diseases. *Annu. Rev. Biochem.* 77, 669–700. doi: 10.1146/annurev.biochem.76.052705.162653

Lillig, C. H., and Lill, R. (2009). Lights on iron-sulfur clusters. *Chem. Biol.* 16, 1213–1214. doi: 10.1016/j.chembiol.2009.12.005

Lister, R., Chew, O., Rudhe, C., Lee, M. N., and Whelan, J. (2001). *Arabidopsis thaliana* ferrochelatase-I and -II are not imported into *Arabidopsis* mitochondria. *FEBS Lett.* 506, 291–295. doi: 10.1016/S0014-5793(01)02925-8

Macomber, L., Rensing, C., and Imlay, J. A. (2007). Intracellular copper does not catalyze the formation of oxidative DNA damage in *Escherichia coli*. *J. Bacteriol.* 189, 1616–1626. doi: 10.1128/JB.01357-06

Mai, H. J., Pateyron, S., and Bauer, P. (2016). Iron homeostasis in *Arabidopsis thaliana*: transcriptomic analyses reveal novel FIT-regulated genes, iron deficiency marker genes and functional gene networks. *BMC Plant Biol.* 16:211. doi: 10.1186/s12870-016-0899-9

Maliandi, M. V., Busi, M. V., Clemente, M., Zabaleta, E. J., Araya, A., and Gomez-Casati, D. F. (2007). Expression and one-step purification of recombinant *Arabidopsis thaliana* frataxin homolog (AtFH). *Protein Expr. Purif.* 51, 157–161. doi: 10.1016/j.pep.2006.06.007

Maliandi, M. V., Busi, M. V., Turowski, V. R., Leaden, L., Araya, A., and Gomez-Casati, D. F. (2011). The mitochondrial protein frataxin is essential for heme biosynthesis in plants. *FEBS J.* 278, 470–481. doi: 10.1111/j.1742-4658.2010.07968.x

Martin, M., Colman, M. J., Gomez-Casati, D. F., Lamattina, L., and Zabaleta, E. J. (2009). Nitric oxide accumulation is required to protect against iron-mediated oxidative stress in frataxin-deficient Arabidopsis plants. *FEBS Lett.* 583, 542–548. doi: 10.1016/j.febslet.2008.12.039

Masuda, T., Suzuki, T., Shimada, H., Ohta, H., and Takamiya, K. (2003). Subcellular localization of two types of ferrochelatase in cucumber. *Planta* 217, 602–609. doi: 10.1007/s00425-003-1019-2

Mendoza-Cozatl, D. G., Xie, Q., Akmakjian, G. Z., Jobe, T. O., Patel, A., Stacey, M. G., et al. (2014). OPT3 is a component of the iron-signaling network between leaves and roots and misregulation of OPT3 leads to an over-accumulation of cadmium in seeds. *Mol. Plant* 7, 1455–1469. doi: 10.1093/mp/ssu067

Morrissey, J., and Guerinot, M. L. (2009). Iron uptake and transport in plants: the good, the bad, and the ionome. *Chem. Rev.* 109, 4553–4567. doi: 10.1021/cr900112r

Murgia, I., Tarantino, D., and Soave, C. (2009). Mitochondrial iron metabolism in plants: frataxin comes into play. *Plant Soil* 325, 5–14. doi: 10.1007/s11104-009-0038-6

Nozoye, T., Nagasaka, S., Kobayashi, T., Takahashi, M., Sato, Y., Sato, Y., et al. (2011). Phytosiderophore efflux transporters are crucial for iron acquisition in graminaceous plants. *J. Biol. Chem.* 286, 5446–5454. doi: 10.1074/jbc.M110.180026

O'Neill, H. A., Gakh, O., and Isaya, G. (2005a). Supramolecular assemblies of human frataxin are formed via subunit-subunit interactions mediated by a non-conserved amino-terminal region. *J. Mol. Biol.* 345, 433–439.

O'Neill, H. A., Gakh, O., Park, S., Cui, J., Mooney, S. M., Sampson, M., et al. (2005b). Assembly of human frataxin is a mechanism for detoxifying redox-active iron. *Biochemistry* 44, 537–545.

Outten, F. W., Huffman, D. L., Hale, J. A., and O'halloran, T. V. (2001). The independent cue and cus systems confer copper tolerance during aerobic and anaerobic growth in *Escherichia coli*. *J. Biol. Chem.* 276, 30670–30677. doi: 10.1074/jbc.M104122200

Patzer, S. I., and Hantke, K. (1999). SufS is a NifS-like protein, and SufD is necessary for stability of the [2Fe-2S] FhuF protein in *Escherichia coli*. *J. Bacteriol.* 181, 3307–3309.

Rajniak, J., Giehl, R. F. H., Chang, E., Murgia, I., Von Wiren, N., and Sattely, E. S. (2018). Biosynthesis of redox-active metabolites in response to iron deficiency in plants. *Nat. Chem. Biol.* 14, 442–450. doi: 10.1038/s41589-018-0019-2

Raldugina, G. N., Krasavina, M. S., Lunkova, N. F., and Burmistrova, N. A. (2016). "Transgenesis in plant metal interaction: emerging remediation techniques," in *Resistance of Plants to Cu Stress*, ed. P. Ahmad (Berlin: Elsevier), 69–114. doi: 10.1016/B978-0-12-803158-2.00004-7

Rellan-Alvarez, R., Giner-Martinez-Sierra, J., Orduna, J., Orera, I., Rodriguez-Castrillon, J. A., Garcia-Alonso, J. I., et al. (2010). Identification of a tri-iron(III), tri-citrate complex in the xylem sap of iron-deficient tomato resupplied with iron: new insights into plant iron long-distance transport. *Plant Cell Physiol.* 51, 91–102. doi: 10.1093/pcp/pcp170

Robinson, N. J., and Winge, D. R. (2010). Copper metallochaperones. *Annu. Rev. Biochem.* 79, 537–562. doi: 10.1146/annurev-biochem-030409-143539

Rodriguez-Celma, J., Lin, W. D., Fu, G. M., Abadia, J., Lopez-Millan, A. F., and Schmidt, W. (2013). Mutually exclusive alterations in secondary metabolism are critical for the uptake of insoluble iron compounds by Arabidopsis and *Medicago truncatula*. *Plant Physiol.* 162, 1473–1485. doi: 10.1104/pp.113.220426

Romheld, V., and Marschner, H. (1983). Mechanism of iron uptake by peanut plants : I. Fe reduction, chelate splitting, and release of phenolics. *Plant Physiol.* 71, 949–954. doi: 10.1104/pp.71.4.949

Romheld, V., and Marschner, H. (1986). Evidence for a specific uptake system for iron phytosiderophores in roots of grasses. *Plant Physiol.* 80, 175–180. doi: 10.1104/pp.80.1.175

Rubino, J. T., and Franz, K. J. (2012). Coordination chemistry of copper proteins: how nature handles a toxic cargo for essential function. *J. Inorg. Biochem.* 107, 129–143. doi: 10.1016/j.jinorgbio.2011.11.024

Sanchez, M., Palacios, O., Buchensky, C., Sabio, L., Gomez-Casati, D. F., Pagani, M. A., et al. (2018). Copper redox chemistry of plant frataxins. *J. Inorg. Biochem.* 180, 135–140. doi: 10.1016/j.jinorgbio.2017.11.020

Schmid, N. B., Giehl, R. F., Doll, S., Mock, H. P., Strehmel, N., Scheel, D., et al. (2014). Feruloyl-CoA 6′-hydroxylase1-dependent coumarins mediate iron acquisition from alkaline substrates in Arabidopsis. *Plant Physiol.* 164, 160–172. doi: 10.1104/pp.113.228544

Schubert, M., Petersson, U. A., Haas, B. J., Funk, C., Schroder, W. P., and Kieselbach, T. (2002). Proteome map of the chloroplast lumen of *Arabidopsis thaliana*. *J. Biol. Chem.* 277, 8354–8365. doi: 10.1074/jbc.M108575200

Shan, Y., and Cortopassi, G. (2012). HSC20 interacts with frataxin and is involved in iron-sulfur cluster biogenesis and iron homeostasis. *Hum. Mol. Genet.* 21, 1457–1469. doi: 10.1093/hmg/ddr582

Shan, Y., Napoli, E., and Cortopassi, G. (2007). Mitochondrial frataxin interacts with ISD11 of the NFS1/ISCU complex and multiple mitochondrial chaperones. *Hum. Mol. Genet.* 16, 929–941. doi: 10.1093/hmg/ddm038

Soriano, S., Calap-Quintana, P., Llorens, J. V., Al-Ramahi, I., Gutierrez, L., Martinez-Sebastian, M. J., et al. (2016). Metal homeostasis regulators suppress FRDA phenotypes in a *Drosophila* model of the disease. *PLoS One* 11:e0159209. doi: 10.1371/journal.pone.0159209

Strain, J., and Culotta, V. C. (1996). Copper ions and the regulation of *Saccharomyces cerevisiae* metallothionein genes under aerobic and anaerobic conditions. *Mol. Gen. Genet.* 251, 139–145.

Takahashi, M., Nakanishi, H., Kawasaki, S., Nishizawa, N. K., and Mori, S. (2001). Enhanced tolerance of rice to low iron availability in alkaline soils using barley nicotianamine aminotransferase genes. *Nat. Biotechnol.* 19, 466–469. doi: 10.1038/88143

Takahashi, R., Ishimaru, Y., Senoura, T., Shimo, H., Ishikawa, S., Arao, T., et al. (2011). The OsNRAMP1 iron transporter is involved in Cd accumulation in rice. *J. Exp. Bot.* 62, 4843–4850. doi: 10.1093/jxb/err136

Turowski, V. R., Aknin, C., Maliandi, M. V., Buchensky, C., Leaden, L., Peralta, D. A., et al. (2015). Frataxin is localized to both the chloroplast and mitochondrion and is involved in chloroplast Fe-S protein function in Arabidopsis. *PLoS One* 10:e0141443. doi: 10.1371/journal.pone.0141443

Turowski, V. R., Busi, M. V., and Gomez-Casati, D. F. (2012). Structural and functional studies of the mitochondrial cysteine desulfurase from *Arabidopsis thaliana*. *Mol. Plant* 5, 1001–1010. doi: 10.1093/mp/sss037

Vazzola, V., Losa, A., Soave, C., and Murgia, I. (2007). Knockout of frataxin gene causes embryo lethality in *Arabidopsis*. *FEBS Lett.* 581, 667–672. doi: 10.1016/j.febslet.2007.01.030

Vert, G., Grotz, N., Dedaldechamp, F., Gaymard, F., Guerinot, M. L., Briat, J. F., et al. (2002). IRT1, an Arabidopsis transporter essential for iron uptake from the soil and for plant growth. *Plant Cell* 14, 1223–1233. doi: 10.1105/tpc.001388

Walker, E. L., and Connolly, E. L. (2008). Time to pump iron: iron-deficiency-signaling mechanisms of higher plants. *Curr. Opin. Plant Biol.* 11, 530–535. doi: 10.1016/j.pbi.2008.06.013

Waters, B. M., Lucena, C., Romera, F. J., Jester, G. G., Wynn, A. N., Rojas, C. L., et al. (2007). Ethylene involvement in the regulation of the H(+)-ATPase CsHA1

gene and of the new isolated ferric reductase CsFRO1 and iron transporter CsIRT1 genes in cucumber plants. *Plant Physiol. Biochem.* 45, 293–301. doi: 10.1016/j.plaphy.2007.03.011

Yokosho, K., Yamaji, N., and Ma, J. F. (2016). OsFRDL1 expressed in nodes is required for distribution of iron to grains in rice. *J. Exp. Bot.* 67, 5485–5494. doi: 10.1093/jxb/erw314

Zhai, Z., Gayomba, S. R., Jung, H. I., Vimalakumari, N. K., Pineros, M., Craft, E., et al. (2014). OPT3 is a phloem-specific iron transporter that is essential for systemic iron signaling and redistribution of iron and cadmium in *Arabidopsis*. *Plant Cell* 26, 2249–2264. doi: 10.1105/tpc.114.123737

Conflict of Interest Statement: The authors declare that the research was conducted in the absence of any commercial or financial relationships that could be construed as a potential conflict of interest.

frontiers in Plant Science

ORIGINAL RESEARCH
published: 15 January 2019
doi: 10.3389/fpls.2018.01985

The Diverse Iron Distribution in Eudicotyledoneae Seeds: From Arabidopsis to Quinoa

*Miguel Angel Ibeas[1], Susana Grant-Grant[1], Maria Fernanda Coronas[1], Joaquín Ignacio Vargas-Pérez[1], Nathalia Navarro[1], Isidro Abreu[2], Hiram Castillo-Michel[3], Natalia Avalos-Cembrano[1], Julio Paez Valencia[4], Fernanda Perez[5], Manuel González-Guerrero[2] and Hannetz Roschzttardtz[1]**

[1] Facultad de Ciencias Biológicas, Pontificia Universidad Católica de Chile, Santiago, Chile, [2] Centro de Biotecnología y Genómica de Plantas (UPM-INIA), Universidad Politécnica de Madrid, Madrid, Spain, [3] ID21, European Synchrotron Radiation Facility (ESRF), Grenoble, France, [4] Department of Botany, University of Wisconsin–Madison, Madison, WI, United States, [5] Departamento de Ecología, Pontificia Universidad Católica de Chile, Santiago, Chile

OPEN ACCESS

Edited by:
Felipe Klein Ricachenevsky, Universidade Federal de Santa Maria, Brazil

Reviewed by:
Louis Grillet, Academia Sinica, Taiwan
Paloma Koprovski Menguer, John Innes Centre (JIC), United Kingdom

***Correspondence:**
Hannetz Roschzttardtz
hroschzttardtz@bio.puc.cl

Specialty section:
This article was submitted to Plant Nutrition, a section of the journal Frontiers in Plant Science

Received: *30 August 2018*
Accepted: *20 December 2018*
Published: *15 January 2019*

Citation:
Ibeas MA, Grant-Grant S, Coronas MF, Vargas-Pérez JI, Navarro N, Abreu I, Castillo-Michel H, Avalos-Cembrano N, Paez Valencia J, Perez F, González-Guerrero M and Roschzttardtz H (2019) The Diverse Iron Distribution in Eudicotyledoneae Seeds: From Arabidopsis to Quinoa. Front. Plant Sci. 9:1985. doi: 10.3389/fpls.2018.01985

Seeds accumulate iron during embryo maturation stages of embryogenesis. Using *Arabidopsis thaliana* as model plant, it has been described that mature embryos accumulate iron within a specific cell layer, the endodermis. This distribution pattern was conserved in most of the analyzed members from Brassicales, with the exception of the basal *Vasconcellea pubescens* that also showed elevated amounts of iron in cortex cells. To determine whether the *V. pubescens* iron distribution was indicative of a wider pattern in non-Brassicales Eudicotyledoneae, we studied iron distribution pattern in different embryos belonging to plant species from different Orders from Eudicotyledoneae and one basal from Magnoliidae. The results obtained indicate that iron distribution in *A. thaliana* embryo is an extreme case of apomorphic character found in Brassicales, not-extensive to the rest of Eudicotyledoneae.

Keywords: apomorphy, Arabidopsis, quinoa, embryo, iron, phylogeny

INTRODUCTION

Increased iron content in seeds is an important agronomic trait. This is due to the relevance of this element in seed production (Marschner, 2005; Roschzttardtz et al., 2011), embryo development, and seedling germination and growth (Lanquar et al., 2005; Kim et al., 2006), as well as in human nutrition (Murgia et al., 2012). In spite of this essential role, the prevalent low iron bioavailability in the soil of most of the main agricultural areas of the world, limits plant productivity, fertility, and even germination rates (Guerinot and Yi, 1994). Consequently, a substantial effort has been dedicated to unraveling the molecular bases controlling iron homeostasis, how plants incorporate and distribute iron throughout their organs, and how iron is stored in the seeds (Walker and Waters, 2011; Kobayashi and Nishizawa, 2012; Grillet et al., 2014; Flis et al., 2016; Tsai and Schmidt, 2017).

Iron distribution in seeds has been studied in monocots and Eudicotyledoneae. Using rice and wheat as models it was concluded that most of the iron in monocot plants is stored in the aleurone layer (Iwai et al., 2012; De Brier et al., 2016). In Eudicotyledoneae, the majority of work has been carried out in Arabidopsis. It has been estimated that approximately 50% of the seed iron content

is stored in endodermal cells (Roschzttardtz et al., 2009; Schnell Ramos et al., 2013). Results from experiments using multiple iron-imaging methods showed that the vast majority of the seed embryo iron is located in vacuoles (Kim et al., 2006; Roschzttardtz et al., 2009; Schnell Ramos et al., 2013). This is in contrast to other plant tissues in which iron has also been detected in plastids, associated with ferritin, and in nucleoli (Roschzttardtz et al., 2011, 2013).

Iron accumulates steadily in the endodermal vacuole during the maturation stage of embryo development, and is subsequently used during post-germinative growth (Lanquar et al., 2005; Roschzttardtz et al., 2009). The defects shown by the *vit1* and *nramp3 nramp4* mutants under iron deficiency conditions suggest that proper iron storage seems essential for seed germination and post-germinative growth (Lanquar et al., 2005; Kim et al., 2006; Mary et al., 2015). These mutant plants are defective in iron loading into the vacuoles of endodermal cells during embryo maturation, a process mediated by the transporter AtVIT1 (VACUOLAR IRON TRANSPORTER1) (Kim et al., 2006); or in iron recovery from vacuoles in these cells via the AtNRAMP3 and AtNRAMP4 (NATURAL RESISTANCE ASSOCIATED MACROPHAGE PROTEIN3 and 4) transporters during germination (Lanquar et al., 2005).

Closely related Brassicaceae embryos accumulate iron very similarly to Arabidopsis, i.e., in vacuoles of cells surrounding the embryo provasculature (Ibeas et al., 2017). However, reports on another Eudicotyledoneae, the legume *Phaseolus vulgaris*, showed broader iron localization. While iron hotspots were detected in cotyledons in a pattern resembling the provasculature, the metal was also evenly distributed in the rest of the organ (Cvitanich et al., 2010). This alternative way of accumulating iron in the seed could indicate that the storage of this nutrient in Eudicotyledoneae is more diverse than what has been reported to date. Considering the importance of Eudicotyledoneae as crops, and the need to improve the iron content in the edible parts (DeFries et al., 2015), we set to study iron distribution in embryos from a wide range of orders belonging to dicotyledonous plants. Our results show that the iron distribution pattern in the Arabidopsis embryo is not extended to all Eudicotyledoneae, it rather seems to be a derived character only observed in the Brassicaceae family. We also found that Caryophyllales has a distinct iron distribution pattern and that iron loading during *Chenopodium quinoa* seed development is different than what we had previously observed in Brassicaceae (Ibeas et al., 2017), suggesting there might be different strategies for the storage of iron in these seeds.

MATERIALS AND METHODS

Plant Material and Growth Conditions

Most of the seeds used in this study were purchased at a local market or harvested in public gardens. Some seeds were collected in the field and identified before being deposited in the herbarium at the Departamento de Ecología, Pontificia Universidad Católica de Chile. The list of species used in this study is in **Supplementary Table S1**. *C. quinoa* plants were grown on soil in a greenhouse at 23°C under long-day condition (16-h/8-h day/night cycle).

Histochemical Staining of Iron With Perls/DAB Method

Seed embryos from the species indicated in **Supplementary Table S1** or *C. quinoa* seeds at different developmental stages were isolated and fixed with 2% *w*/*v* paraformaldehyde in 1 mM phosphate buffer pH 7.0 for 45 min. The following steps were performed according to Roschzttardtz et al. (2009) and Ibeas et al. (2017).

Synchrotron μ-XRF

Quinoa seeds were embedded in OCT (Optimal Cutting Temperature) resin and plunge-frozen in isopentane chilled in liquid nitrogen. Longitudinal sections (30 μm) were prepared using a cryomicrotome (Leica, RM2265-LN22) at –50°C and immediately imaged at beamline ID21 at the ESRF (European Synchrotron Radiation Facility, Grenoble, France). Elemental distribution was mapped by micro X-ray fluorescence (μXRF) under cryogenic conditions (Cotte et al., 2017). The beam was focused with the use of KB mirrors to a size of 0.5 × 0.9 μm^2 (V × H). The fluorescence signal was detected using an 80 mm^2 active area SGX Si drift detector with a Be window. Two photodiodes were used to measure the incident and transmitted beam intensities. Scans were acquired with an energy of 7.2 keV (Fe k-edge) with a dwell time of 100 ms per pixel, and a pixel size of 2 μm × 2 μm. RGB color maps and Fe, Mn, and P elemental maps were created using PyMca software (Soléa et al., 2007).

Phylogenetic Analysis

A phylogenetic tree of the species in the data set was assembled using the phylogeny of angiosperms at family level, from the Angiosperm Phylogeny Group (The Angiosperm Phylogeny Group et al., 2016). To resolve relationships within Brassicaceae we followed Guo et al. (2017), which uses 77 protein coding regions. Branch lengths were set to 1.0. Species were assigned to four categories according to Fe location in seed embryos: endodermis; inner layers of cortex, external cortex or protodermis. Ancestral states of iron location were reconstructed using Mesquite (Maddison and Maddison, 2007) based on one−parameter model.

RESULTS

Differences in Iron Distribution in Embryos of the Order Brassicales

Analyses on species from the Brassicaceae family showed that their embryos have similar subcellular iron distribution in cotyledons and hypocotyl (Ibeas et al., 2017). In *Arabidopsis thaliana*, *Camelina sativa, Nasturtium officinale, Lepidium sativum*, and *Brassica napus* dry seed embryos, iron accumulates in the vacuoles of cells surrounding the provasculature. Some differences in the number of cells that store iron were observed in the hypocotyl: while Arabidopsis only presented a one cell layer,

the other species have two or more (Roschzttardtz et al., 2009; Ibeas et al., 2017).

We extended this study to members of other families within the Brassicales order. We performed Perls/DAB staining on *Cleome hassleriana* (Cleomaceae Family) and *Capparis spinosa* (Capparaceae Family). Embryo sections revealed that iron accumulates in cells that surround the provasculature in a similar manner as embryos from Brassicaceae species (**Figure 1**). Some differences were observed in *C. spinosa*, where a group of cells between provasculature regions in cotyledons showed iron accumulation in vacuoles (**Supplementary Figure S1**). Surprisingly, when analyzing the member of the Caricaceae family *V. pubescens* (a more ancestral Brassicales), we observed that several cortex cells accumulate iron. This pattern sets it apart from the rest of Brassicales embryos studied to date and suggests that Brassicaceae embryo cortex cells may also accumulate iron (**Figure 1**).

Iron Distribution in Embryos From Different Orders of Eudicotyledoneae

To inquire whether the observation that *V. pubescencs* has a differential iron distribution is an exception or an ancestral trait lost at some point in the Brassicales order, Perls/DAB analyses were carried out in embryos from six representative Eudicotyledoneae Orders (Sapindales, Rosales, Zygophyllales, Solanales, Asterales, and Caryophyllales) and one basal specie from Magnoliidae (Magnoliales). Interestingly, the analysis of embryos from those orders showed that iron accumulates in several cell layers including endodermis and cortex cells. In some cases, iron was also detected in the protodermis (Solanales, Asterales, and Magnoliales; **Figure 2**). These results indicate that the Arabidopsis embryo has an uncommon iron distribution compared to embryos of seed plants from other Orders of the Eudicotyledoneae class. Moreover, a more detailed analysis of *Porlieria chilensis* Perls/DAB-stained section shows that iron also seems to accumulate extracellularly, in what might be described as the cortex apoplast (**Figure 2**).

Iron Distribution in Caryophyllales Embryos

In order to evaluate iron distribution in species from other orders, seed embryos of several species belonging to Caryophyllales were used to determine whether iron distribution might differ within the same order. **Figure 3A** shows embryos from *Fagopyrum esculentum*, *C. quinoa* and *Phytolacca dioica*. In all cases, embryos were isolated and fixed, and then thin sections were analyzed, in particular hypocotyl and cotyledon. Using Perls/DAB staining we found that in all the species analyzed, iron was present in several embryo cell types, including endodermis and cortex cells. This result indicates that this pattern of iron distribution

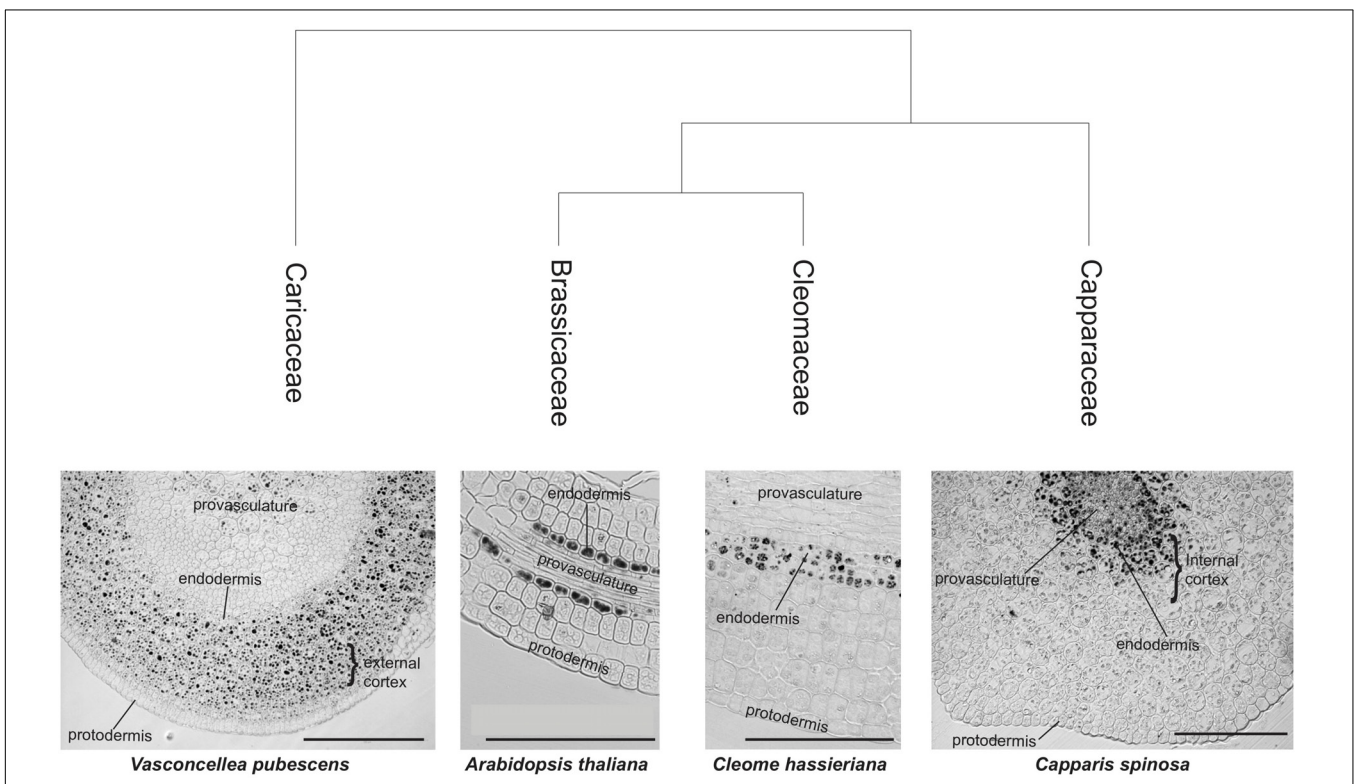

FIGURE 1 | Iron distribution in Brassicales embryos. Iron distribution in hypocotyls of four Brassicales species were mapped on the phylogenetic tree modified from Hall et al. (2004). The analysis of sections using Perls/DAB of Brassicaceae family species was previously described in Ibeas et al. (2017). Iron is accumulated, in addition to endodermis, in the cortex cells (internal cortex, close to endodermis, and close to the protodermis, external cortex). A section of *A. thaliana* hypocotyl stained with Perls/DAB is shown. Bars in panels correspond to 100 μm.

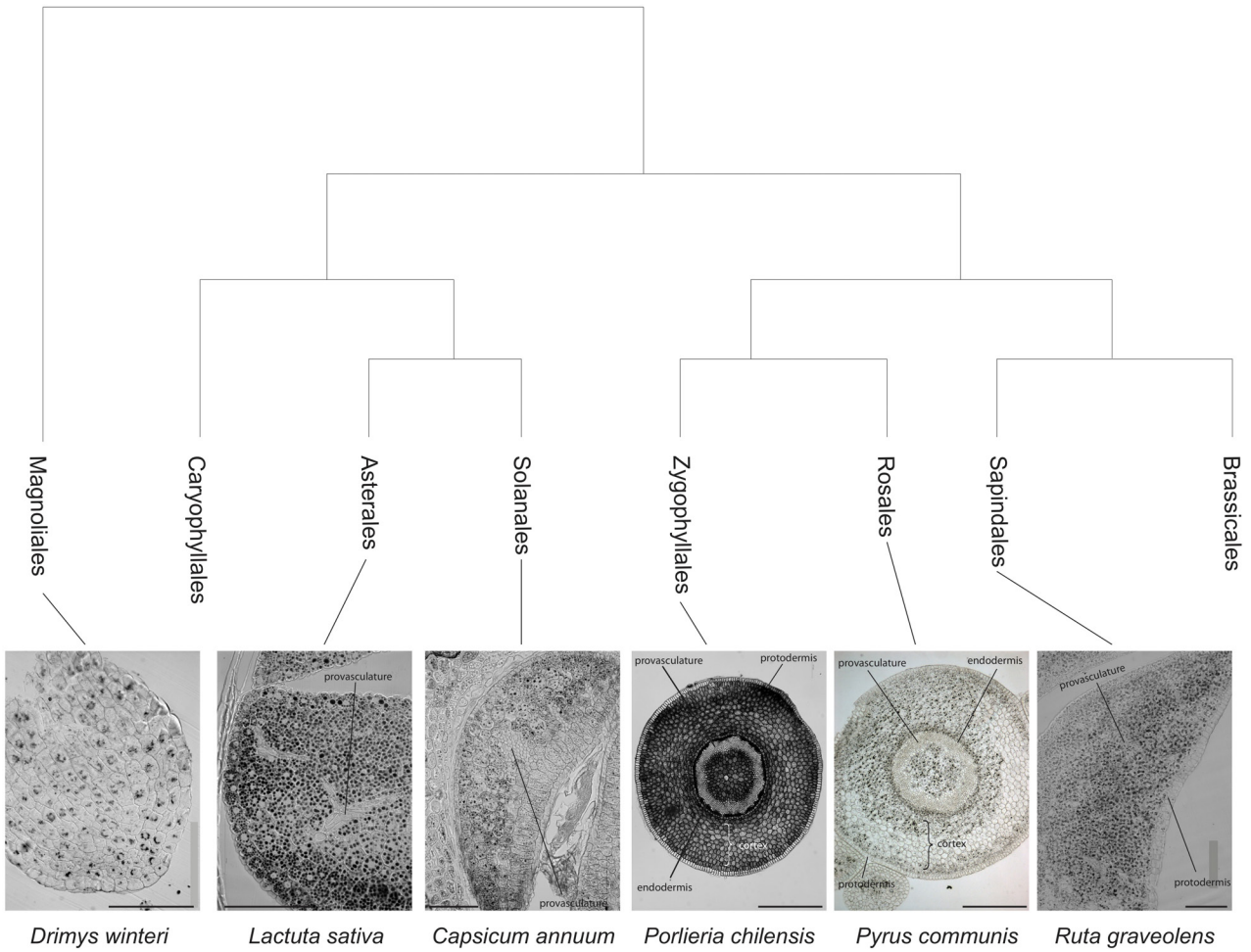

FIGURE 2 | Iron distribution in Eudicotyledoneae mature embryos. Iron distribution was revealed by Perls/DAB staining of hypocotyls (*Porlieria chilensis* and *Pyrus communis*) or cotyledons sections (*Ruta graveolens*, *Capsicum annuum*, and *Lactuca sativa*). The phylogenetic tree was assembled from The Angiosperm Phylogeny Group et al. (2016). Bars in panels correspond to 100 μm.

is conserved within this order (**Figure 3A**). We also analyzed embryos from *Spinacia oleracea, Beta vulgaris,* and *Rheum rhabarbarum* (**Supplementary Table S1**).

Next, we used synchrotron-based micro X-ray fluorescence (SμXRF) to independently confirm iron distribution using Perls/DAB staining in *C. quinoa* seeds. Dry seeds were sectioned and analyzed by S-μXRF, showing iron accumulation in several cell layers in hypocotyl but excluding provasculature (**Figure 3B**). S-μXRF also showed Mn accumulation in several cell layers of *C. quinoa* hypocotyl (probably cortex) in contrast with the restricted localization of Mn in the subepidermal layer of plant model *A. thaliana* (Kim et al., 2006; Punshon et al., 2012; Schnell Ramos et al., 2013; Eroglu et al., 2017).

Iron Distribution During *Chenopodium quinoa* Seed Development

Previously, our group reported for the first time that some Brassicaceae species accumulate iron in two embryo cell types (endodermis and one cell layer of cortex). We also showed that in early stages of *B. napus* seed development, iron accumulates in nuclei of the free cell endosperm and in all embryo cell types. Later, iron is relocated to cytoplasmic structures, and finally, at the mature stage, iron is accumulated in vacuoles of the endodermis and cortex (Ibeas et al., 2017).

Because the iron distribution pattern in Caryophyllales is different from the pattern described above, we used *C. quinoa* as a model to study iron localization during seed development. *C. quinoa* is an emerging crop that has potential health benefits and an exceptional nutritional value. We analyzed four different stages of seed maturation in *C. quinoa*: early stages (between 3 and 7 days postanthesis), an intermediate stage (14 days postanthesis/cotyledon stage) and a late stage (21 days postanthesis/mature stage). In order to describe the seed structures where iron accumulates before being loaded into the embryo, we used whole seeds including seed coat, perisperm and embryo in our analyses.

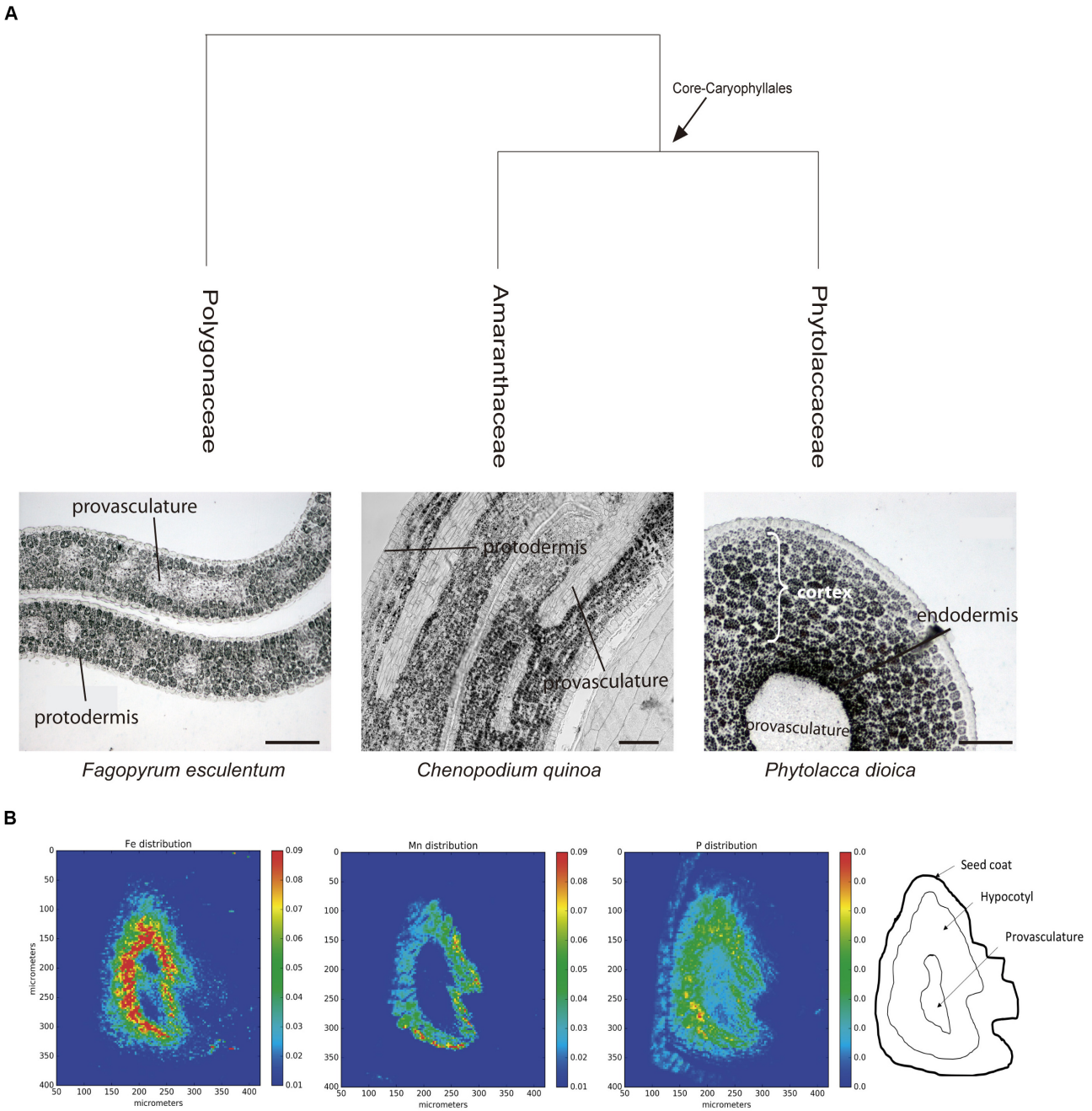

FIGURE 3 | (A) Iron distribution in Caryophyllales mature embryos. Perls/DAB stained embryo sections from polygonaceae, amaranthaceae, and phytolaccaceae families (*Fagopyrum esculentum*, *Chenopodium quinoa*, and *Phytolacca dioica*, respectively). Bars in panels correspond to 50 μm. **(B)** Iron detection in hypocotyl Quinoa dry seed section using synchrotron-based micro X-ray fluorescence (SμXRF). P, Mn, and Fe distribution are shown.

Analysis of seed sections containing early embryo developmental stages revealed that there are no detectable iron pools in seed coat, perisperm or embryos (**Figure 4**). In seeds containing embryos at the cotyledon stage iron is detected inside the nuclei and in structures surrounding the nuclei (**Figures 5A,B**). Interestingly, longitudinal sections of the entire seed showed detectable iron pools in the integuments. Strong iron staining was observed in cytoplasmic structures (**Figures 5C,D**). In order to confirm the subcellular compartments that accumulate iron we performed Perls/DAB and Toluidine blue staining on the same sections. The zoom of specific cells in **Figures 5B,D**, show that iron localizes in nuclei and cytoplasmic structures in the embryo. Moreover, there is strong iron staining in cytoplasmic structures in the integuments.

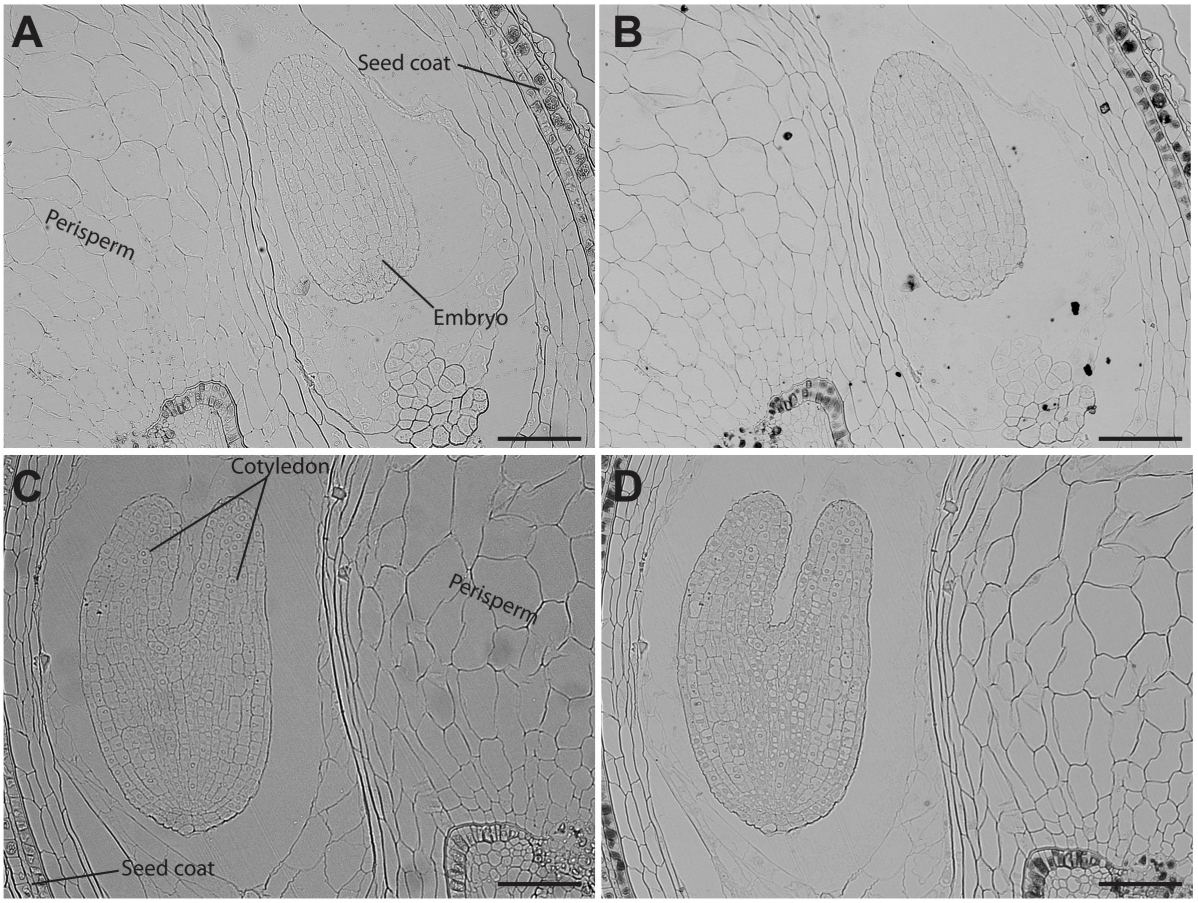

FIGURE 4 | Iron distribution in *C. quinoa* seeds in early developmental stages. *C. quinoa* seeds 3 and 7 days postanthesis were collected from fruits, embedded in Technovit resin, sectioned (3 μm) and then stained with Perls/DAB **(B,D)**. Unstained sections were used as control **(A,C)**. The scale bar represents 100 μm.

In mature seeds, iron is no longer localized in nuclei (**Figure 6**). At this stage, iron is detected in several embryonic cell types, including endodermis and cortex cells of cotyledons and hypocotyl (**Figures 6B,D**). Perls/DAB and Toluidine blue staining show that iron pools do not localize in nuclei in cotyledon and hypocotyl cells (Zoom in **Figures 6B,D**).

DISCUSSION

Dietary iron deficiency is a major issue for human health, affecting more than 2 billion people around the world (Murgia et al., 2012). Seeds are a pivotal source of iron for humans and animals (Roschzttardtz et al., 2017). Therefore, understanding the molecular mechanisms involved in iron loading and distribution in seeds is critical for the development of biotechnological approaches to improve seed iron content. Generation of biofortified crops could be a financially sound strategy to deliver nutrients to the population, as an alternative to the continuous governmental investment in fortification and supplementation programs (DeFries et al., 2015). Thus, genetic biofortification of staple crops could result in an environmentally friendly and cost-effective strategy for the improvement of nutritional health (Guerinot and Yi, 1994).

Pioneer studies, using SμXRF and a histochemical method for iron detection in plant tissues (Perls/DAB stain), showed that iron accumulates in the vacuoles of the endodermis cell layer of *A. thaliana* mature embryos (Kim et al., 2006; Roschzttardtz et al., 2009; Eroglu et al., 2017; Ibeas et al., 2017). While this distribution pattern is conserved in the rest of the Brassicaceae family (Ibeas et al., 2017), it is not present in legumes (Cvitanich et al., 2010). These observations suggest that embryos may have multiple ways to store iron. Consequently, by exploring this diversity, we should be able to propose suitable models to dissect the molecular mechanisms of seed iron storage and eventually translate these findings to crops of commercial and nutritional value. Toward this end, we used Perls/DAB staining to determine iron distribution in several plant species along the Eudicotyledoneae phylogeny. As a result, we obtained the first phylogenetic study of iron distribution in plant seed embryos. The results indicate that seed embryos belonging to different Eudicotyledoneae orders accumulate iron in several cell layers, with more diversity that what can be

inferred by simply using Arabidopsis as model. In particular, cortex cells accumulate iron in all the embryo species analyzed except for Brassicales families Capparaceae, Cleomaceae and Brassicaceae. These results strongly suggest that iron distribution in cortex cells in embryos from Eudicotyledoneae embryo plants is a conserved characteristic from a phylogenetic point of view. We used S-μXRF as a second and independent method to confirm that in quinoa embryos, iron accumulates in several cell layers including the cortex and endodermis cells (**Figure 3B**).

Quinoa seed has high nutritional value and has recently started to be used as a novel functional food (Abugoch, 2009). This plant contains 15 mg of iron per 100 g of seeds, covering the daily iron needs of infants and adults (National Academy Press, 2001; Konishi et al., 2004). We evaluated iron accumulation during *C. quinoa* seed development and found that it does not accumulate iron in any seed tissue during the early developmental stages (**Figure 4**). This is in contrast with what was previously described for *B. napus* seeds, in which strong iron staining was observed in the nuclei of the free cell endosperm surrounding the embryo, and also in several cell layers of the embryo at the torpedo stage (Ibeas et al., 2017). This discovery opens new questions on the mechanisms of iron distribution and accumulation in these seeds, and will be used as the basis for the development of biotechnological strategies to increase total iron content in seeds for human consumption.

A side finding of this work is the broad distribution of Mn in the embryo of *C. quinoa* hypocotyl (**Figure 3B**), compared to the restricted location of Mn in the hypocotyl subepidermal tissue of *A. thaliana* embryos (Kim et al., 2006; Punshon et al., 2012; Schnell Ramos et al., 2013; Eroglu et al., 2017). It has recently been shown that mutations in the genes *cax1cax3* (Punshon et al., 2012), *mtp8* and *vit1* (Eroglu et al., 2017) cause a broad distribution of Mn indicating that they are responsible for this localization. As proposed for iron, this finding will open new strategies for the development of Mn fortified seeds.

In addition to Brassicales, our analyses also showed that at least some Zygophyllales, such as *P. chilensis*, also have an unusual iron distribution. In this case, iron is distributed inside and outside the cells (apoplast). This iron pool would necessarily be accumulated in a different manner from the vacuolar-located. For instance, there would be no need for particular metal transporters as is the case for Arabidopsis (Lanquar et al., 2005; Kim et al., 2006). It would also be interesting to determine the

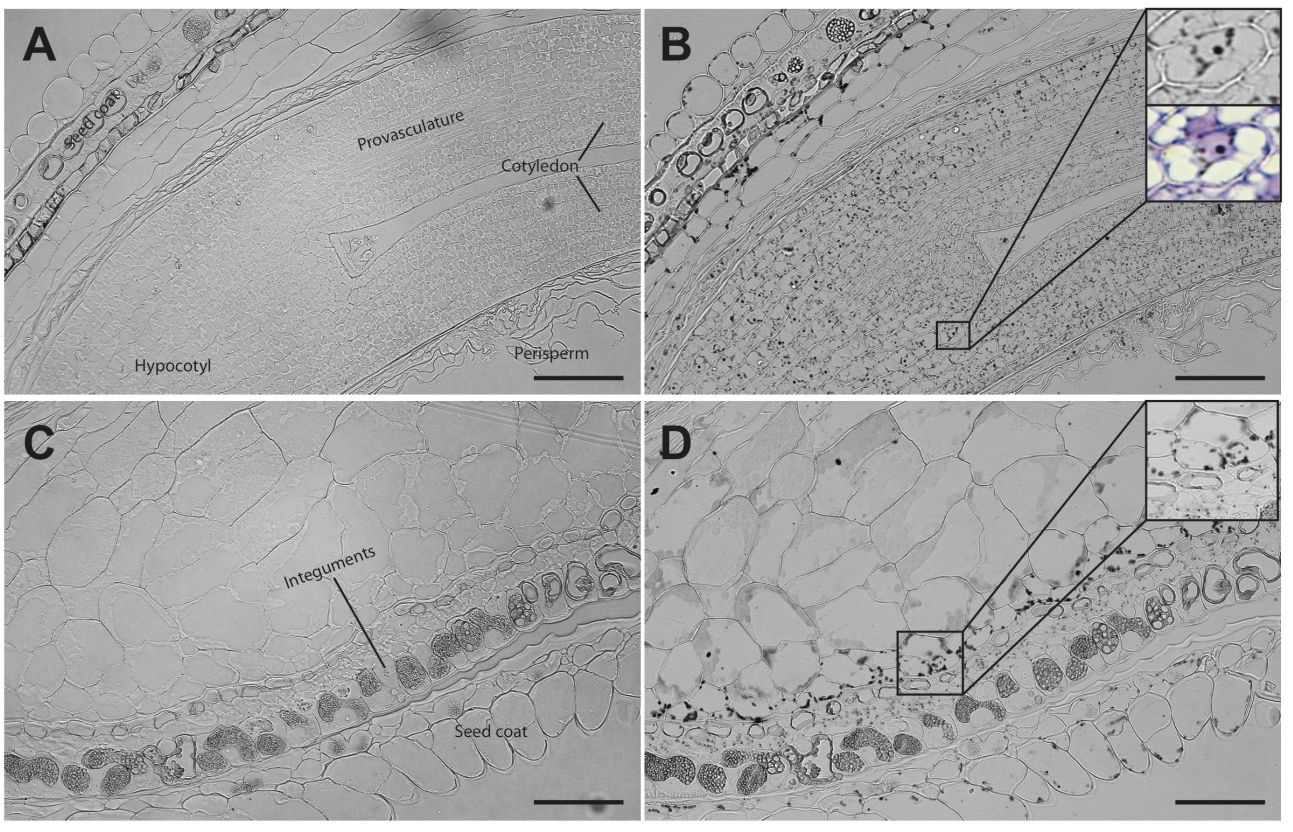

FIGURE 5 | Iron distribution in *C. quinoa* seeds at cotyledon stage. *C. quinoa* seeds at the cotyledon stage (14 days postanthesis) dissected from fruits were embedded in Technovit resin, sectioned (3 μm) and then stained with Perls/DAB **(B**,**D)**. In **B** the zoom shows iron accumulation into and around the nuclei. In **B** and **D** toluidine blue was used to show different cell structures. Unstained sections were used as control **(A**,**C)**. The scale bar represents 100 μm.

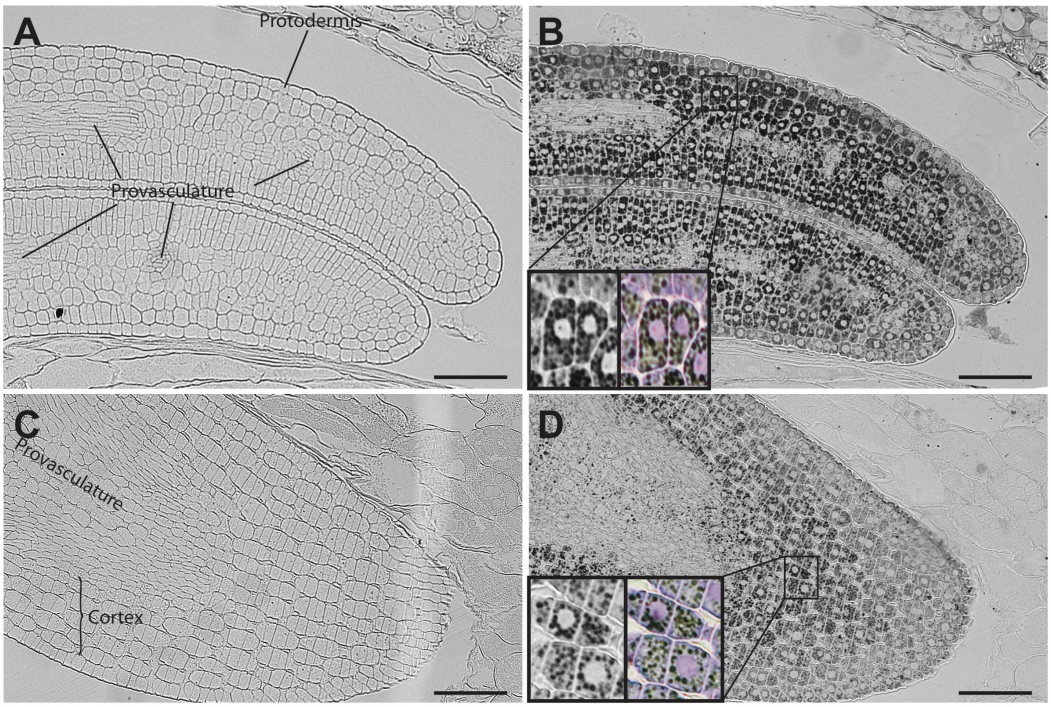

FIGURE 6 | Iron distribution in *C. quinoa* seeds at mature embryo stage. *C. quinoa* seeds at the mature embryo stage, before seed desiccation stage (21 days postanthesis), were collected from fruits, embedded in Technovit resin and sectioned (3 μm). The sections were then stained with Perls/DAB **(B**,**D)**. Cotyledons and hypocotyl are shown in **A**,**B** and **C**,**D**, respectively. The zoom in **B** and **D** show iron accumulation in cell structures different from nuclei. Perls/DAB and Toluidine blue were used in order to reveal different cell structures. Unstained sections were used as control **(A**,**C)**. The scale bar represents 100 μm.

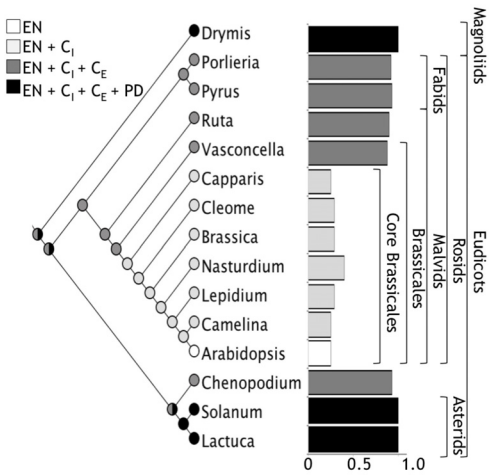

FIGURE 7 | A global view of iron distribution in embryos. Phylogenetic tree showing all the species analyzed in this study. Colors of circles indicate type of cells that accumulate iron in the hypocotyl. White, only endodermis; light gray, endodermis + internal cortex (C_I); dark gray, endodermis + internal cortex + external cortex (C_E); black, endodermis + internal cortex + external cortex + protodermis (PD). Cortex cell are defined as the cell layers that are between the endodermis and the protodermis, we refer as internal cortex the cell layers than are near to the endodermis. Ratio of number of cells where iron is accumulated versus total number of cell layers from the endodermis to the protodermis for embryos from different orders are indicated in bars. Colors of bars correspond to the same code described above.

iron ligands, and how assimilable it is.Further analyses of this and other Zygophyllales species will be carried out to ascertain the extension of this phenotype and to determine its molecular bases.

Regarding the widespread use of Arabidopsis as a Eudicotyledoneae model plant for iron nutrition, our results show that iron distribution in Arabidopsis embryos is not a widely conserved character in Eudicotyledoneae seed embryos and it corresponds to an apomorphic character. Ancestral reconstruction of the phylogeny of angiosperms with Maximum Parsimony or Maximum Likelihood indicated that the embryo of the ancestor of Brassicales, and probably of all Eudicotyledoneae, accumulates iron in several layers of the cortex (**Figure 7**). The loss of iron in the outer layers of the cortex evolved in the core of Brassicales, whereas the ability to accumulate iron only in endodermis is a derived trait of Arabidopsis. According to Beilstein et al. (2010), the apomorphy described in our study emerged between 120 and 70 Mya. In our opinion, Brassicales seeds could be used to evaluate molecular mechanisms involved in iron accumulation in the cortex cells, using information obtained from other species described in this article.

These results also open new questions on the mechanisms involved in iron accumulation and remobilization in cortex and protodermis cells, during embryogenesis and seed germination, respectively. From an evolutionary point of view, it will be

interesting to study which competitive advantage determined the selection of this iron distribution in Brassicales species.

AUTHOR CONTRIBUTIONS

MI, SG-G, JV-P, NN, and HR performed the embryo dissections and Perls/DAB staining. IA, HC-M, and MG-G performed the SμXRF analysis. FP performed the phylogenetic analysis. All authors participated in the writing of the manuscript.

FUNDING

This work was funded by FONDECYT 1160334 (Chilean Government) to HR. Ph.D. students' work was supported by Conicyt-Chile grants 21160350 (to MI), 21170951 (to SG-G), and 21151344 (to JV-P).

ACKNOWLEDGMENTS

The authors are greatly indebted to Dr. Xavier Jordana, María Isabel Gómez and Dr. Juan Keymer for its continued support and encouragement. *Vasconcellea pubescens* seeds were kindly provided by Dr. Maria José Letelier and Dr. Sebastián Godoy.

SUPPLEMENTARY MATERIAL

The Supplementary Material for this article can be found online at: https://www.frontiersin.org/articles/10.3389/fpls.2018.01985/full#supplementary-material

REFERENCES

Abugoch, L. (2009). *Advances in Food and Nutrition Research*. Amsterdam: Elsevier Inc., 58.

Beilstein, M., Nagalingum, N., Clements, M., Manchester, S., and Mathews, S. (2010). Dated molecular phylogenies indicate a miocene origin for *Arabidopsis thaliana*. *Proc. Natl. Acad. Sci. U.S.A.* 107, 18724–18728. doi: 10.1073/pnas.0909766107

Cotte, M., Pouyet, E., Salomé, M., Rivard, C., De Nolf, W., Castillo-Michel, H., et al. (2017). The ID21 X-ray and infrared microscopy beamline at the ESRF: status and recent applications to artistic materials. *J. Anal. At. Spectrom.* 32, 477–493. doi: 10.1039/C6JA00356G

Cvitanich, C., Przybyłowicz, W., Urbanski, D., Jurkiewicz, A., Mesjasz-Przybyłowicz, J., Blair, M., et al. (2010). Iron and ferritin accumulate in separate cellular locations in Phaseolus seeds. *BMC Plant Biol.* 10:26. doi: 10.1186/1471-2229-10-26

De Brier, N., Gomand, S., Donner, E., Paterson, D., Smolders, E., Delcour, J., et al. (2016). Element distribution and iron speciation in mature wheat grains (*Triticum aestivum* L.) using synchrotron X-ray fluorescence microscopy mapping and X-ray absorption near-edge structure (XANES) imaging. *Plant Cell Environ.* 39, 1835–1847. doi: 10.1111/pce.12749

DeFries, R., Fanzo, J., Remans, R., Palm, C., Wood, S., and Anderman, T. L. (2015). Global nutrition. metrics for land-scarce agriculture. *Science* 349, 238–240. doi: 10.1126/science.aaa5766

Eroglu, S., Giehl, R. F. H., Meier, B., Takahashi, M., Terada, Y., Ignatyev, K., et al. (2017). Metal tolerance protein 8 mediates manganese homeostasis and iron reallocation during seed development and germination. *Plant Physiol.* 174, 1633–1647. doi: 10.1104/pp.16.01646

Flis, P., Ouerdane, L., Grillet, L., Curie, C., Mari, S., and Lobinski, R. (2016). Inventory of metal complexes circulating in plant fluids: a reliable method based on HPLC coupled with dual elemental and high-resolution molecular mass spectrometric detection. *New Phytol.* 211, 1129–1141. doi: 10.1111/nph.13964

Grillet, L., Ouerdane, L., Flis, P., Hoang, M., Isaure, M., Lobinski, R., et al. (2014). Ascorbate efflux as a new strategy for iron reduction and transport in plants. *J. Biol. Chem.* 289, 2515–2525. doi: 10.1074/jbc.M113.514828

Guerinot, M., and Yi, Y. (1994). Iron: nutritious, noxious, and not readily available. *Plant Physiol.* 104, 815–820. doi: 10.1104/pp.104.3.815

Guo, X., Hao, G., Zhang, L., Mao, K., Wang, X., Zhang, D., et al. (2017). Plastome phylogeny and early diversification of Brassicaceae. *BMC Genomics* 18:176. doi: 10.1186/s12864-017-3555-3

Hall, J., Iltis, H., and Sytsma, K. (2004). Molecular phylogenetics of core brassicales, placement of orphan genera rmblingia, forchhammeria, tirania, and character evolution. *Syst. Bot.* 29, 654–669. doi: 10.1600/0363644041744491

Ibeas, M., Grant-Grant, S., Navarro, N., Perez, M., and Roschzttardtz, H. (2017). Dynamic subcellular localization of iron during embryo development in Brassicaceae seeds. *Front. Plant Sci.* 8:2186. doi: 10.3389/fpls.2017.02186

Iwai, T., Takahashi, M., Oda, K., Terada, Y., and Yoshida, K. (2012). Dynamic changes in the distribution of minerals in relation to phytic acid accumulation during rice seed development. *Plant Physiol.* 160, 2007–2014. doi: 10.1104/pp.112.206573

Kim, S., Punshon, T., Lanzirotti, A., Li, L., Alonso, J., Ecker, J., et al. (2006). Localization of iron in Arabidopsis seed requires the vacuolar membrane transporter VIT1. *Science* 314, 1295–1298. doi: 10.1126/science.1132563

Kobayashi, T., and Nishizawa, N. (2012). Iron uptake, translocation, and regulation in higher plants. *Annu. Rev. Plant Biol.* 63, 131–152. doi: 10.1146/annurev-arplant-042811-105522

Konishi, Y., Hirano, S., Tsuboi, H., and Wada, M. (2004). Distribution of minerals in quinoa (*Chenopodium quinoa* Willd.) seeds. *Biosci. Biotechnol. Biochem.* 68, 231–234. doi: 10.1271/bbb.68.231

Lanquar, V., Lelièvre, F., Bolte, S., Hamès, C., Alcon, C., Neumann, D., et al. (2005). Mobilization of vacuolar iron by AtNRAMP3 and AtNRAMP4 is essential for seed germination on low iron. *EMBO J.* 24, 4041–4051. doi: 10.1038/sj.emboj.7600864

Maddison, W., and Maddison, D. (2007). *Mesquite: A Modular System for Evolutionary Analysis, Version 2.0*.

Marschner, H. (2005). *Mineral Nutrition of Higher Plants*, 2nd Edn. Orlando: Academic Press, 889.

Mary, V., Schnell, M., Gillet, C., Socha, A., Giraudat, J., Agorio, A., et al. (2015). Bypassing iron storage in endodermal vacuoles rescues the iron mobilization defect in the natural resistance associated-macrophage protein3 natural resistance associated-macrophage protein4 double mutant. *Plant Physiol.* 169, 748–759. doi: 10.1104/pp.15.00380

Murgia, I., Arosio, P., Tarantino, D., and Soave, C. (2012). Biofortification for combating 'hidden hunger' for iron. *Trends Plant Sci.* 17, 47–55. doi: 10.1016/j.tplants.2011.10.003

National Academy Press. (2001). *Dietary Reference Intakes for Vitamin A, Vitamin K, Arsenic, Boron, Chromium, Copper, Iodine, Iron, Manganese, Molybdenum, Nickel, Silicon, Vanadium, and Zinc*. Washington, DC: National Academy Press.

Punshon, T., Hirschi, K., Yang, J., Lanzirotti, A., Lai, B., and Guerinot, M. L. (2012). The role of CAX_1 and CAX_3 in elemental distribution and abundance in Arabidopsis seed. *Plant Physiol.* 158, 352–362. doi: 10.1104/pp.111.184812

Roschzttardtz, H., Bustos, S., Coronas, M. F., Ibeas, M. A., Grant-Grant, S., and Vargas-Pérez, J. (2017). Increasing provasculature complexity in the arabidopsis embryo may increase total iron content in seeds: a hypothesis. *Front. Plant Sci.* 8:960. doi: 10.3389/fpls.2017.00960

Roschzttardtz, H., Conejero, G., Curie, C., and Mari, S. (2009). Identification of the endodermal vacuole as the iron storage compartment in the Arabidopsis embryo. *Plant Physiol.* 151, 1329–1338. doi: 10.1104/pp.109.144444

Roschzttardtz, H., Conéjéro, G., Divol, F., Alcon, C., Verdeil, J.-L., Curie, C., et al. (2013). New insights into Fe localization in plant tissues. *Front. Plant Sci.* 4:350. doi: 10.3389/fpls.2013.00350

Roschzttardtz, H., Grillet, L., Isaure, M., Conejero, G., Ortega, R., and Curie, C. (2011). Plant cell nucleolus as a hot spot for iron. *J. Biol. Chem.* 286, 27863–27866. doi: 10.1074/jbc.C111.269720

Schnell Ramos, M., Khodja, H., Mary, V., and Thomine, S. (2013). Using μPIXE for quantitative mapping of metal concentration in *Arabidopsis thaliana* seeds. *Front. Plant Sci.* 4:168. doi: 10.3389/fpls.2013.00168

Soléa, V. A., Papillona, E., Cottea, M., Walterb, P., and Susini, J. (2007). A multiplatform code for the analysis of energy-dispersive X-ray fluorescence spectra. *Spectrochim. Acta* 62, 63–68. doi: 10.1016/j.sab.2006.12.002

The Angiosperm Phylogeny Group, Chase, M. W., Christenhusz, M. J. M., Fay, M. F., Byng, J. W., and Judd, W. S. (2016). An update of the angiosperm phylogeny group classification for the orders and families of flowering plants: APG IV. *Bot. J. Linn. Soc.* 181, 1–20. doi: 10.1016/j.jep.2015.05.035

Tsai, H., and Schmidt, W. (2017). One way. or another? Iron uptake in plants. *New Phytol.* 214, 500–505. doi: 10.1111/nph.14477

Walker, E., and Waters, B. (2011). The role of transition metal homeostasis in plant seed development. *Curr. Opin. Plant Biol.* 14, 318–324. doi: 10.1016/j.pbi.2011.03.025

Conflict of Interest Statement: The authors declare that the research was conducted in the absence of any commercial or financial relationships that could be construed as a potential conflict of interest.

Advantages of publishing in Frontiers

OPEN ACCESS
Articles are free to read for greatest visibility and readership

FAST PUBLICATION
Around 90 days from submission to decision

HIGH QUALITY PEER-REVIEW
Rigorous, collaborative, and constructive peer-review

TRANSPARENT PEER-REVIEW
Editors and reviewers acknowledged by name on published articles

Frontiers
Avenue du Tribunal-Fédéral 34
1005 Lausanne | Switzerland

Visit us: www.frontiersin.org
Contact us: info@frontiersin.org | +41 21 510 17 00

REPRODUCIBILITY OF RESEARCH
Support open data and methods to enhance research reproducibility

DIGITAL PUBLISHING
Articles designed for optimal readership across devices

FOLLOW US
@frontiersin

IMPACT METRICS
Advanced article metrics track visibility across digital media

EXTENSIVE PROMOTION
Marketing and promotion of impactful research

LOOP RESEARCH NETWORK
Our network increases your article's readership